NOTICE

The quality of this microform is heavily dependent upon the quality of the original thesis submitted for microfilming. Every effort has been made to ensure the highest quality of reproduction possible.

If pages are missing, contact the university which granted the degree.

Some pages may have indistinct print especially if the original pages were typed with a poor typewriter ribbon or if the university sent us an inferior photocopy.

Reproduction in full or in part of this microform is governed by the Canadian Copyright Act, R.S.C. 1970, c. C-30, and subsequent amendments.

AVIS

La qualité de cette microforme dépend grandement de la qualité de la thèse soumise au microfilmage. Nous avons tout fait pour assurer une qualité supérieure de reproduction.

S'il manque des pages, veuillez communiquer avec l'université qui a conféré le grade

La qualité d'impression de certaines pages peut laisser à désirer, surtout si les pages originales ont été dactylographiées à l'aide d'un ruban usé ou si l'université nous a fait parvenir une photocopie de qualité inférieure

La reproduction, même partielle, de cette microforme est soumise à la Loi canadienne sur le droit d'auteur, SRC 1970, c. C-30, et ses amendements subséquents

WORK HARDENING, STRENGTH, RESTORATIVE MECHANISMS, AND DUCTILITY IN THE HOT WORKING OF 300 SERIES STAINLESS STEELS

Norman Daniel Ryan

A Thesis

in

The Department

of

Mechanical Engineering

Presented in Partial Fulfillment of the Requirements
for the Degree of Doctor of Philosophy at
Concordia University
Montréal, Québec, Canada

March 1989

ISBN 0-315-49112-4

ABSTRACT

Work Hardening, Strength, Restorative Mechanisms, and
Ductility in the Hot Working of 300 Series Stainless Steels

Norman Daniel Ryan, Ph.D.
Concordia University, 1989

Stress-strain curves, generated through continuous and multistage torsion tests of as-cast 304, 316, 317 and homogenized 301, 304, 316 and 317 γ stainless steels in the range of 1200-900^{o}C and 0.1 to 5.0 s^{-1}, were analyzed with respect to the characteristics of work hardening, dynamic and static recovery, dynamic and static recrystallization, and ductility. Work hardening was related to the Kocks-Mecking model where the saturation stress is due to dynamic recovery DRV. The associated enthalpy which rose across the deformation range attaining a maximum at the highest temperature, was in close agreement with the constant activation energy determined by sinh analysis. This activation energy was corrected upwards in consideration of deformational heating.

Dynamic softening mechanisms were extensively analyzed through examination of the flow curves, with conclusions based upon mechanical data being confirmed by optical metallographic methods. Upon attaining a critical strain, dynamic recrystallization DRX was initiated, producing a peak at approximately 30% DRX and then softening to a steady state regime where 99% DRX had taken place. The rate of dynamic softening was determined by means of the Avrami equation. The critical stress and strain for subgrain formation and for DRX were determined from changes in slope of the strain hardening-flow stress θ-σ curves. A transition from multiple peak grain coarsening to single peak grain refinement behavior was observed and analyzed. The peak strain was shown to be a function of the Zener-Hollomon

the deformation conditions. Both the DRV subgrain size and DRX grain size were found to be functions of the steady state flow stress.

Static restorative mechanisms were examined by mechanical metallographic methods and favorably compared with other work. Fractional softening was due to both static recovery SRV and recrystallization SRX. The kinetics were analyzed through use of the Avrami equation. At low strains, the time for 50% SRX was a strong function of strain to the -2 power. In addition, the temperature compensated time for SRX depended upon the three-eighths power of the Zener-Hollomon parameter for both isothermal and declining temperature T multistage tests.

A time-to-fracture criterion was shown to qualitatively represent the hot ductility which rose with increases in both temperature and strain rate for those alloys with low solute, but decreased with increasing strain rate for the high Mo bearing alloys. The as-cast alloys had considerably lower ductility than the homogenized alloys, this being due to the presence of delta ferrite. Due to the retarding effects of the static restorative processes, the hot ductility augmented considerably as temperature and holding time were increased.

Simulation of a cross country mill showed that the multistage flow curves increased as strain rate rose and as interval time and T declined, particularly below 1050^{o}C. Due to incomplete softening during each interval, accumulated strain was instrumental in raising the flow stress in a pass well above that determined by simple continuous deformation. Since the time between successive planetary rolls is insufficient for any restorative mechanisms to operate, the power requirements for the planetary hot rolling mill were determined from continuous flow curves. The results favorably agreed with similar mills installed in both Canada and Japan.

ACKNOWLEDGEMENTS

The author wishes to express his sincere appreciation and gratitude to his advisor Professor H.J. McQueen for his astute advice and continual encouragement through the entire research programme. In addition, he thanks Professor E. Evanglista for his cooperation in creating a summer 'stage' at the University of Ancona, Italy where the electron microscopy was performed.

The author would like to thank Professor J.J. Jonas and Dr. S. Yue of McGill University for liberal use of the hot torsion machine for the testing of the 250 specimens used in this extensive research. In addition, he recognizes the assistance of J. Bowles in optical metallography, of H. Eli with drawings, of P. McQueen with torsion testing, of G. Flicker in literature research, and of I.C. Smith with word processing.

Having received all materials from Atlas Steels of Tracy, Quebec, he wishes to thank the administration for their cordial relationship and expediency in the supply of both specimens and materials. Furthermore, he acknowledges with gratitude the financial support received from the Natural Sciences and Engineering Research Council of Canada and Fonds pour la Formation des Chercheurs et l'Aide à la Recherche.

TABLE OF CONTENTS

LIST OF FIGURES

LIST OF TABLES

LIST OF SYMBOLS

a	intercept of Z dependence of steady state subgrain size, Eqn. 12
a_o	proportionality constant, σ_c/σ_p, Eqn. 33
a'	intercept of Z dependence of as-quenched hardness, Eqn. 14
b	coefficient of Z dependence of subgrain size, Eqn. 12
b_o	intercept of subgrain size dependence on Z, Fig. 70a
b'	as-quenched hardness coefficient of Z dependence, Eqn. 14
c	power for McQueen-Cingara flow curve modelling, Eqn. 31
c_o	coefficient of σ_s dependence of subgrain size, Fig. 70a
d_s	steady state subgrain size, Eqns. 11-13
h	coefficient of d_s dependence of as-quenched hardness, Eqn. 13
h_i	initial slab thickness in planetary rolling, Fig. 82
h_f	final sheet thickness in planetary rolling, Fig. 82
k_s	power of σ_s dependence of DRX grain size, Eqn. 50
k_M	power of σ_s dependence of MRX grain size, Eqn. 51
k_{DRX}	time constant of the Avrami equation for DRX, Eqns. 10, 34
k_{SRX}	time constant of the Avrami equation for SRX, Eqns. 23, 25
k'	Elfmark σ_s power of σ_s dependence of ε_f, Eqn. 39
k_p	mean pass flow stress, Fig. 38
k'_p	mean flow stress for each planetary roll, Eqn. 54
m	strain rate sensitivity, Eqn. 3
ms	metallic solute, Fig. 13
m'_o	material power constant in Sellars flow curve modelling, Eqn. 32
m''_o	material power constant in Sellars flow curve modelling, Eqn. 33
m'	subgrain size power in lation to as-quenched hardness, Eqn. 13
n	stress exponent of hyperbolic function, Eqn. 17
n_f	stress exponent for fracture, Eqn. 35
n_{DRX}	stress exponent for DRX, Eqn. 46
n^D	Elfmark Z exponent, Eqn. 48, Fig. 44a
n'	strain hardening coefficient, Eqn. 3
n''	stress exponent of power law, Eqn. 15
p	subgrain size stress exponent, Fig. 70a
q	Elfmark power of W_{DRX} dependence of $\varepsilon_f Z_{DRX}^{-1}$, Eqn. 49, Fig. 44b

q_o	power of d_s dependence of σ_s, Fig. 69
r	power of solute dependence of Q_{HW}, Eqn. 56
r_c	rolling reduction in continuous rolling, Fig. 38
r_e	radial distance from axis of specimen, Eqn. 2
r_p	rolling reduction in planetary mill, Fig. 82
r_T	total reduction in planetary mill, Fig. 82
r'	power of D_s dependence of σ_s, Eqn. 8, Fig. 63
r'_o	power of D_{MRX} dependence of σ_s, Fig. 63
r''	power of Z dependence of D_s, Eqn. 9
s_o	specific heat, Eqn. 5
t	time for any given percentage of DRX, Eqn. 45
t_c	time for the initiation of DRX, Fig. 22
t'	time for any given percentage of SRX, Eqn. 27
t_{DRX}	time for 99% dynamic recrystallization, Eqn. 40
t_f	time to fracture, Eqn. 35, 47
t_i	holding time after ith pass, Figs. 36-38
t_0	Sandberg-Sandstrom characteristic time for SRX, Eqn. 27
$t_{0.5}$	time for 0.5 volume fraction of SRX, Eqn. 24
v.f.	volume fraction, Fig. 21
A	material constant, hyperbolic sine function, Eqn. 17
A_f	material fracture constant, hyperbolic sine function, Eqn. 35
A_{DRX}	material constant, dynamic recrystallization, Eqn. 46
A_{SRX}	material constant, static recrystallization, Eqn. 24
AL	athermal limit, Fig. 19
A^D	material constant for W_{DRX} dependence on Z, Eqn. 48, Fig. 44
A'_Z	coefficient of Z dependence of σ_p, Fig. 16
A'	material constant, power law, Eqn. 15
A'_{SRX}	coefficient of Z dependence of $W_{0.5}$, Fig. 33
A''	material constant, exponential function, Eqn. 16
A''_f	material fracture constant, exponential function, Eqn. 47
A_o	Gittins-Sellars material constant for fracture, Eqns. 35, 36
A'_o	inverse of material constant A in Eqn. 38
A'_s	coefficient of $\dot{\varepsilon}$ dependence of σ^*_s, Figs. 8, 9
A_e	coefficient of $\dot{\varepsilon}$ dependence of Γ_e, Fig. 3
A_p	material constant for peak strain calculation, Eqn. 44

B	coefficient of D_s dependence of σ_s, Eqn. 8
B_{DRX}	coefficient of σ_s dependence of D_s, Eqn. 50
B_o	Sellars material constant for flow curve modelling, Eqn. 32
B'_o	Sellars constant for flow curve modelling with DRX, Eqn. 33
B'	coefficient of Z dependence of D_s, Eqn. 9
B''	material constant, relating σ_s to d_s, Eqn. 11
B''_{q0}	coefficient of σ_s dependence of d_s, Fig. 69
C	as-cast material
C'	Sellars material constant, Eqn. 32
C_1	Roberts material constant in flow curve modelling, Eqn. 34
C_2	Roberts material constant in flow curve modelling, Eqn. 3
C_P	Sims geometrical function for rolling, ref. 281
C_{DRX}	constant ($k_{DRX}K(1-X_{DRX})$ from differentiation of Avrami equation, Eqn. 58, Fig. 28
Cr_{eq}	Cr + 1.37Mo + 1.5Si + 2Nb + 3Ti (wt.%), ref. 109
D_0	original grain size, Eqns. 44, 58
D_s	steady state DRX grain size, Eqns. 8, 9, 50
D_{MRX}	metadynamically recrystallized grain size, Fig. 63
D_{SRX}	statically recrystallized grain size, Fig. 60
DRV	dynamic recovery
DRX	dynamic recrystallization
E	Elfmark coefficient of Z dependence of ε_f, Eqn. 39
E'	Elfmark material constant for ε_f as a function of Z, Eqn. 41
F	coefficient of solute dependence of Q_{HW}, Eqn. 56
FS	fractional softening, Fig. 37
FS_i	FS after the i'th pass in the i'th interval, Eqn. 26
G_T	total torque in the planetary rolling mill, Eqn. 55
GB	grain boundary
HSLA	high strength low alloy steel
H_o	annealed hardness, Eqn. 13
H_v	as-quenched Vickers hardness, Eqns. 13, 14
ΔH	Kocks-Mecking analysis activation enthalpy, Eqn. 22
J_P	Sims stress function for rolling, ref. 281
K	constant where $K = \beta_{DRX} D_0$, Eqn. 57
L_e	gage length of specimen, Eqn. 1

M_{MRX}	coefficient of σ_s dependence of D_{MRX}, Eqn. 51
MRX	metadynamic recrystallization
Ni_{eq}	Ni + 0.31Mn + 22C + 14.2N + Cu (wt.%), ref. 109
P	extrusion pressure, Fig. 12
P_p	roll separating force in planetary rolling, Fig. 85
P_T	total roll separating force for the planetary mill, Eqn. 55
P_o	the slope of $1/\sigma_s^*$ versus $d(1/\sigma)/d\theta$, Eqns. 7, 30, 34
Q_f	activation energy for fracture, Eqn. 35
Q_{CRX}	activation energy for initiation of DRX, Fig. 30
Q_{HW}	activation energy for hot working (σ_p), Eqn. 17
Q_{HWC}	activation energy corrected for deformational heating, Fig. 20
Q_{SRX}	activation energy for static recrystallization, Eqn. 24
R	gas constant, Eqns. 15-17
R′	specimen effective radius, Eqn. 4
R_e	specimen radius at periphery, Eqns. 1-3
R'_e	Cr_{eq}/Ni_{eq} ratio
R_b	radius of backup roll in planetary mill, Eqn. 55
R_c	radius of constellation of planetary rolling mill, Fig. 82
R_A	reduction in area, Eqn. 42
R_p	radius of a planetary roll, Eqn. 55
R'_p	radius of deformed planetary roll, Fig. 85
S	solute content, weight percent, Eqn. 56
SFE	stacking fault energy
SRV	static recovery
SRX	static recrystallization
T	temperature
T′	Tanaka's characteristic temperature, Eqns. 19, 20
T_m	melting temperature
T_i	temperature at unloading, ith pass, Figs. 72, 76
T_{i+1}	temperature at reloading, (i+1)th pass, Figs. 72, 76
ΔT	adiabatic temperature increase, Eqn. 5
TEM	transmission electron microscopy
W	homogeneous worked material
W_{DRX}	temperature-compensated time to 99% DRX, Eqn. 40
X	material distance into bite of planetary mill, Fig. 82

X_{DRX}	volume fraction of dynamic recrystallization, Eqn. 10
X_{SRX}	volume fraction of static recrystallization, Eqns. 23, 25
Y	slab half-thickness in planetary rolling, Fig. 82
ΔY	draft in planetary rolling, Fig. 82
Z	Zener-Hollomon parameter, T-compensated strain rate, Eqns. 15-18
Z_c	critical value of Z for grain refinement (given D_0), Fig. 62
Z_f	Zener-Hollomon parameter for fracture, Eqn. 36
Z_{DRX}	Zener-Hollomon parameter for 99% DRX, Eqn. 39
Z_L	upper limit of Z parameter for the initiation of DRX, Fig. 21
	constant, $\alpha = \beta/n$
α_1	subtended angle at the point of mean strain rate, Eqn. 55
β	constant in exponential function, $\beta=\alpha n$, Eqn. 16
β_{DRX}	Avrami grain size constant, dynamic recrystallization, Eqn. 10
β_{SRX}	Avrami grain size constant, static recrystallization, Eqn. 23
β_f	fracture grain size constant, exponential function, Eqn. 47
β''	Sellars grain size constant for flow curve modelling, Eqn. 33
γ	austenite phase
γ'	surface energy of the fractured surface, Eqn. 37
γ_e	shear strain, Eqn. 1
δ	ferrite phase
ε	equivalent surface strain
ε_c	critical strain for the initiation of DRX, Eqn. 34, Figs, 22, 24
ε_f	fracture strain, Eqns. 39, 41, 49
ε_i	pass strain, Figs. 36, 72, 74, 76
ε_p	peak strain, Eqn. 44, Fig. 26
ε_s	strain for the onset of steady state, Fig. 26
ε_x	the time for the first wave of DRX ($\varepsilon_s-\varepsilon_p$), Fig. 23
ε_{SF}	strain for subgrain formation, Fig. 36
ε_T	total strain in planetary rolling, Fig. 82
$\dot{\varepsilon}$	equivalent strain rate, Eqns. 15-17
$\dot{\varepsilon}_i$	pass strain rate, Figs. 72-81
$\dot{\varepsilon}_m$	strain rate for athermal behavior, Fig. 9
$\dot{\varepsilon}_o$	constant related to σ^*_{so}, Eqn. 21
$\dot{\varepsilon}'_o$	unit parameter for strain rate, Eqn. 20
θ	strain hardening rate, Eqn. 6

θ_e	angle of twist, Eqn. 1
θ_0	maximum work hardening rate, at σ=o, Eqn. 6
θ_1	angle of the planetary roll bite, Eqn. 55
θ_{II}	strain hardening rate during stage II
λ	strain rate in rolling, Fig. 82
μ	shear modulus, Eqn. 37
ν	Poisson ratio, Eqn. 37
π	3.14159
ρ	density, Eqn. 5
σ	equivalent flow stress, Eqns. 30, 34
σ_c	critical stress for initiation of DRX, Fig. 5
σ_f	fracture stress, Eqns. 35, 36
σ_p	peak flow stress, Eqns. 15-17
σ_s	steady state flow stress, Eqn. 8
σ^*_{sm}	saturation stress for experimental athermal behavior, Fig. 9
$\Delta\sigma$	difference in flow curve modelled for DRX from that for DRV alone, Eqn. 33
σ_m	maximum flow stress in a multistage pass, Fig. 75
σ_{mi}	flow stress of the ith pass, Eqn. 26
σ_{yo}	original yield stress, Eqns. 26, 32
σ_{SF}	flow stress for subgrain formation, Fig. 5
$\sigma_{y(i+1)}$	reloading yield stress in (i+1)th pass, Eqns. 26, 29
σ'_{yi}	unloading yield stress at T_i, Eqn. 29
$\sigma'_{y(1+1)}$	yield stress of recrystallized material on reloading at T_{i+1}, Eqn. 29
σ^*_s	saturation stress, Eqns. 6, 7, 21, 22
σ^*_{so}	maximum saturation stress, at zero k, Eqns. 21, 22
τ	shear stress, Eqn. 2
τ_R	shear stress at surface of specimen with radius R, Eqn. 3
$\tau_{R'}$	surface shear stress of specimen with effective radius, Eqn. 4
ϕ	specimen diameter, Fig. 1
ω_b	angular velocity of the planetary mill backup rolls, Eqn. 55
Γ	stacking fault energy constant, Eqns. 21, 22
Γ_e	torque, Eqns. 2, 3, 4

CHAPTER 1: INTRODUCTION

Since the highly corrosion resistant austenitic stainless steels have excellent formability and weldability, they are used extensively for domestic and industrial applications. Furthermore, they retain toughness and ductility over a broad range of temperatures. While these alloys are more expensive than carbon steels, ferritic stainless types, and aluminum, they have a higher strength-to-weight ratio, so that less material is required, particularly when used for structures or pressure-vessel work. These alloys also allow less material to provide the corrosion resistance necessary for the life of the product. Moreover in architecture, these alloys require virtually no maintenance and are far more aesthetic than most other materials. Since the use of the γ stainless steels for the manufacture of components is ever expanding into the areas of nuclear power, water pollution control, transportation and food processing, it was important that a thorough study of their hot working characteristics be undertaken.

To that end, types 301, 304, 316, and 317 were investigated. Since these alloys are continuously cast, they were tested in that condition and also examined in the homogenized worked condition. The alloys were characterized through two hundred and fifty tests performed under isothermal and iso-strain rate conditions in the range 900 to 1200^{o}C and 0.1 to 5 s^{-1} on a hydraulic computer-controlled torsion machine capable of high strains. These experiments included continuous tests to fracture and interrupted tests which simulate multistage rolling. Work hardening,

dynamic and static restoration and fracture mechanisms were examined. In addition, an analysis of their microstructure by optical and electron microscopy was performed to develop a better understanding of their mechanical and metallurgical responses to hot working with a view to optimize their processing and mechanical properties.

In order to optimize the calculations of the mean flow stress which is required to determine the force and simultaneous power requirements for the hot working of these austenitic stainless steels, constitutive equations were developed. From copious data in the literature, reliable values of constants were established so that with only knowledge of the metallic solute and original grain size, estimates of the peak stress which favorably compare with measured values can be determined. Since cracking, commonly at the rolled edges, has a deleterious effect upon product quality, further constitutive equations were derived which allow the forming limit to be established for any hot deformation conditions.

Before proceeding with a thorough exposition of the present work, an extensive review of the literature associated with the above ideas will be reported. A logical sequence of the test procedures and resulting scientific findings will be presented. Finally, the significance of these results to the theory of hot deformation will be explained and conclusions will be drawn.

CHAPTER 2

REVIEW OF PREVIOUS WORK

2.1 HOT WORKABILITY TESTING

2.1.1 INDUSTRIAL APPLICATION

In order to attain the most economic hot forming of alloys, it is advisable to determine the strength, ductility and microstructural changes through continuous isothermal tests. Furthermore, to reduce the expense of trial and error methods of improving product quality in hot working, physical simulations in the laboratory with maintainenance of rigid control over all variables at both the plasto-mechanical and microstructural levels, are recommended (1-37). Simulation of multistage hot forming processes are performed mathematically with the models being primarily computer analyses (30, 31). Several of these modelling projects have realized accurate predictions of the roll separating force and power requirements of a roll pass schedule in multistage rolling (32-37) and single pass planetary rolling of several steels (1, 38, 39).

2.1.2 TYPES OF TESTING METHODS

In order to further understanding of the hot deformation behavior of γ stainless alloys, a wide variety of tests have been carried out. While they have been performed in tension, compression and torsion, they have all been primarily used to examine hot strength, softening modes, hot ductility, microstructural evolution and multistage behavior (5-9, 11, 15-18, 22, 24, 30, 31, 34, 36, 40-43). Each of these modes have both benefits and disadvantages which are discussed below.

The test method should be chosen for its ability to determine the flow stress and fracture strain under the desired conditions of temperature,

strain rate, and amount of deformation which can be considerable, as in planetary rolling (1, 38, 39). In addition, the test should allow the accurate simulation of interrupted rolling schedules (1-37). Finally, the test method should allow rapid quenching which retains the microstructure for examination at room temperature by optical metallography and electron microscopy.

2.1.3 TENSION AND COMPRESSION

The strain and strain rates attainable with conventional tensile testing equipment are inadequate for hot working studies. This mode has a serious deficiency because necking commences at strains much lower than those attainable in forming and prevents multistage testing in simulation of industrial rolling schedules (40-45). Conventional axisymmetric compression testing suffers similar problems with respect to strain rate. This problem is overcome by the use of the cam plastometer. While this mode of testing is homogeneous to about 0.7, friction at the anvils results in barrelling which limits the strain to about 2.0. While the alloy's resistance to hoop cracking can be examined, the fracture strain is not determined directly. Since the area under compression and thus the friction remains constant, plane strain compression is superior to the former mode in that deformation is possible to a strain of approximately 5.0. The major disadvantage of this testing method is the inhomogeneity caused by frictional effects which vary with the ratio of anvil width to specimen height (43-45).

2.1.4 TORSION

In the torsion test, the mode of deformation is pure shear in which twisting at a constant speed produces a constant true strain and strain

rate which decreases linearly from periphery to the center of the specimen (1, 42, 43). This gradient is mathematically corrected in the calculation of these values. The specimen can be subjected to extremely high strains without any frictional problems or geometrical instability prior to fracture which makes it suitable for multistage simulation (41-43, 46-56). During the torsion test, the specimen has an initial tendency to lengthen, but it later shortens. If constrained, the latter behavior imposes axial tensile stresses which reduce the fracture strain by enlarging any cracks developed

The equations for converting torque, Γ_e, and rotation, θ_e, into shear stress, τ, and shear strain, γ_e, for a solid specimen of radius, R_e, and length, L_e, are (42, 43, 46, 49, 50, 52, 55):

$$\gamma_e = R_e \, \theta_e / L_e \qquad (1)$$

$$\Gamma_e = 2 \, \pi \int_0^{R_e} \tau \, r_e^2 \, dr, \qquad (2)$$

where r_e is the radial distance from the axis. The shear stress is zero at the center of the specimen and increases linearly with the radius as a result of both strain hardening coefficient n' and strain rate sensitivity m. Considering this gradient across the specimen with radius R, where τ depends upon both the strain, ε, and strain rate, $\dot{\varepsilon}$, the following equation is derived (42, 43, 49, 55, 56):

$$\tau_R = \Gamma_e \, (\, 3 + n' + m \,) / \, 2\pi \, R_e^3, \qquad (3)$$

τ_R is the shear stress at the surface and n' and m are the slopes of the plots of log Γ_e versus log ε and log Γ_e versus log $\dot{\varepsilon}$, respectively. During hot working, n' becomes zero at the flow curve peak and steady state (42, 49-52, 56). The following alternate analysis has been used by Cole and Richardson (57) in order to avoid the use of n' and m in the calculation of

the shear stress. An effective radius, R', is used which for solid specimens is 0.724 R'. The following equation:

$$\tau_{R'} = 3\ \Gamma_e\ /\ 2\ \pi\ R'^3 \qquad (4)$$

calculates the shear stress which approximates that determined by the previous equation (52, 57). In order to compare with the normal effective flow stress and strain derived by tensile and compression testing, the equivalent stress σ and strain ϵ equal $\sqrt{3}\tau$ and $\gamma_e/\sqrt{3}$, respectively according to von Mises theory. In order to avoid the problem of the gradient, hollow specimens can be used but such thin tubes tend to buckle at relatively low strains (58-62).

2.1.5 RELATIVE ADVANTAGES OF TORSION

Considering these three testing modes, the hot torsion test has become the preferred technique for testing and optimizing hot working behavior because no geometrical instability occurs during deformation (36, 43, 49). In particular, it is capable of simulating a rolling schedule with several passes by providing interruptions where the specimen is unloaded and held for a prescribed period of time (1-6, 8-19, 24-31). The microstructures near the surface must be examined in chord or tangential section, in order to correlate with surface $\dot{\epsilon}$ and σ. Because of the gradient, room temperature mechanical properities cannot be determined except by hardness testing.

2.1.6 DEFORMATIONAL HEATING

As in all working operations, deformational heating occurs during all testing modes. It increases with the product of the stress and the strain without considering any temperature loss due to radiation or conduction. As $\dot{\epsilon}$ increases, the time for the removal of this heat is reduced and the

conditions approach adiabatic. This adiabatic temperature increase is determined by the following equation (46, 63-78):

$$\Delta T = \int_{o}^{\varepsilon} \sigma_p \, d\varepsilon / s_o \rho, \qquad (5)$$

where the specific heat s_o = 0.14 J/m^3 and the density ρ = 7.9 x 10^3 kg/m^3 for austenitic stainless steels (79, 80). At high $\dot{\varepsilon}$ with associated high σ, the temperature of the gage section increases substantially which leads to a marked fall in flow stress. At low $\dot{\varepsilon}$ and low T, the heat production is slow and the surface temperature may remain nearly constant. Rise in T increases as the gage length/radius ratio becomes larger (51). Adiabatic heating must be considered when ductility is high because the real T at fracture may be higher than the nominal one, hence ε_f may be lower at the nominal T.

2.2 STRENGTH AND MICROSTRUCTURAL CHANGES DURING HOT WORKING

2.2.1 FLOW CURVE SHAPE

Throughout the hot working of alloys, the increase in dislocation density is counteracted by the softening processes of dynamic recovery, DRV, and dynamic recrystallization, DRX (30, 34, 36, 42, 49, 52-54, 74, 76-78, 81-92). If DRV is the only restoration mechanism, σ increases progressively up to a steady state flow stress, σ_s, which is determined by the balance of the work hardening and restoration effects (82-92). Aluminum and ferritic steels exhibit this behavior (82, 83, 93-95). DRV proceeds more slowly in the face-centered-cubic austenitic stainless steel, so that the dislocation density attains a sufficiently high value for the initiation of DRX. As a result, the flow curve exhibits a characteristic maximum followed by a decrease to the onset of a steady state regime as a result of the reduced strength of the new grains (90-92, 96-101).

2.2.2 COMPOSITIONAL EFFECTS

The solutes in γ stainless steels can be divided into three classes. The ferrite-stabilizing elements, silicon and molybdenum, having a greater degree of atomic mismatch, give rise to significant solid solution hardening. Nickel, manganese and chromium, the substitutional austenite-forming elements, have respectively low, medium and high effects (31, 89, 102, 103). Of the interstitially dissolved elements, carbon and nitrogen, the latter gives rise to considerable strengthening, whereas the former rise to softening due to an increase in vacancy diffusion and dynamic recovery (82, 83). They both have great strengthening effect at low T where carbides or nitrides have precipitated (104). While many elements augment the strength of γ stainless steels, some have a negative effect upon hot ductility. For example, molybdenum, oxygen and nitrogen produce deleterious effects upon the hot ductility of types 316 and 317 stainless steels (42, 57, 103-108).

2.2.3 DELTA FERRITE EFFECTS

While δ-ferrite increases the strength, it decreases significantly the ductility (102, 109). The amount of ferrite is primarily determined by the segregation of the alloying elements during solidification which occurs in the primary ferritic or austenitic mode. In the former, ferrite nucleates and later austenite begins to grow on the ferritic dendrites resulting in an intimate network of two phases. The γ grain boundaries, GB, are free of ferrite but contain other impurities (110-112).

In ferritic freezing, the elements nickel, manganese, and molybdenum segregate to the melt, while chromium does not segregate at all. In austenitic freezing, chromium and molybdenum segregate to the melt, while nickel is enriched in the austenite dendrites. Ultimately, δ phase may

segregate with other impurities to the austenite GB, where it is much more deleterious (110-112). However, the δ also leads to corrugated GB and to enhanced SRX in multistage forming, both of which raise ε_f. The change between ferritic and austenitic freezing occurs at Cr to Ni equivalents ratio just below or equal to 1.5 (109).

2.2.4 WORK HARDENING BEHAVIOR

Work hardening which commences with yielding continues throughout deformation being continually reduced by DRV. An analysis of the flow curves reveals its behavior up to the peak strain, σ_p, where restoration finally balances the effects of work hardening. When the strain hardening rate ($\theta = d\sigma/d\varepsilon$) is developed as a function of the flow stress, the curves for all deformation conditions diverge from a common intercept designated as θ_0 at $\sigma = 0$ and consist of two distinct linear segments (113-123). Firstly, θ decreases linearly with the flow stress over a significant range of the σ-ε curve from θ_0 to where subgrain formation begins ($\varepsilon \approx 0.1$) (124-126). The θ-σ curve gradually changes to a lower slope, linear segment. Finally, the curve drops to $\theta = 0$ at σ_p, the point of inflection indicating that DRX has become operative at σ_c. An extrapolation of the second linear portion to $\theta = 0$ determines the value of the saturation stress, σ_s^*, which would be the limit of the steady state regime due to DRV alone in the absence of DRX (113, 122, 123).

The strain hardening rate at any given stress, σ, within the region where only DRV is operative is described by the following linear equation (101, 113, 114):

$$\theta = \theta_0 (1 - \sigma/\sigma_s^*). \qquad (6)$$

With the exception of small strains, θ is related to $1/\sigma$ with the slope

increasing systematically with T and $\dot{\varepsilon}$. These relationships result in the following expression for the work hardening rate:

$$\theta = P_o (\sigma^*_i/\sigma - 1), \qquad (7)$$

where P_o, the slope of $1/\sigma^*_i$ versus $d(1/\sigma)/d\theta$, is relatively well described by a straight line passing through the origin (101).

2.2.5 SATURATION STRESS AND DEPENDENCE ON T

The extrapolation of slopes in a logarithmic plot of σ^*_i versus T for a given alloy, converge to a saturation stress at zero K. This saturation stress with a maximum value of σ^*_{io} falls with increasing T, and logarithmically rises with increasing $\dot{\varepsilon}$ to a maximum independent of temperature (120). Furthermore, it also rises with decreasing stacking fault energy SFE, which is exhibited by the high Mo bearing 317 with the lowest SFE of the alloys examined. Consequently, the existence of this saturation stress is a basic characteristic of work hardening and DRV (113-115, 117, 119, 122, 123).

2.3 RESTORATION PROCESSES

2.3.1 REDUCTION OF θ BY DYNAMIC RECOVERY

The alloy at the start of deformation experiences extensive work hardening θ_{II}, being constant during stage II because there is no DRV (20, 113-115, 117, 119). But as deformation proceeds through stage III, θ decreases rapidly due to DRV. The DRV results from climb and glide of the dislocations. Insofar as DRV involves climb of edge dislocations, it has the same T dependence as diffusion of vacancies and is found only at T high enough for the atoms to have sufficient vibrational energy to enable vacancies to migrate rapidly (88).

According to McQueen (82, 83, 86, 88, 95, 117), as work hardening

builds up the dislocation density, the DRV proceeds by the dislocations either annihilating each other or forming combinations and rearranging into low energy sub-boundaries (86-90). This simultaneous work hardening and DRV continues up to where these mechanisms equalize. In alloys where recovery proceeds rapidly, the flow stress increases monotonically to a steady state value which is determined by a balance between the accumulation and elimination of dislocations. During steady state, the dynamic stability of the equiaxed subgrain structure with unvarying dimensions and misorientation, is maintained by sub-boundaries continually being unravelled and reknitted (86, 88, 90, 95, 117).

2.3.2 DYNAMIC RECRYSTALLIZATION BEHAVIOR

At room temperature, stacking faults are prevalent in austenitic stainless steels indicative of low SFE (127-131). The lower the SFE, the greater the separation between the partial dislocations (65). Consequently at high T, cross slip and climb are inhibited and DRV is slow. As a result deformation leads to the development of a dislocation substructure in which the subgrain boundaries remain tangled, not forming regular arrays as observed in alloys with rapid DRV. Because of the limited DRV, sufficiently high local differences in dislocation density arise to nucleate DRX during deformation (34, 84, 86, 97, 99, 101, 131). The original grain boundaries constitute the principal sites where DRX nucleation occurs partly by bulging of the GB and partly from cells of high misorientation (132). The boundaries of annealing twins are also nucleation sites. As deformation proceeds, the original grain boundary sites are exhausted with formation of a complete necklace (84, 98-100). The reaction proceeds via nucleation at the interface between the recrystallized and unrecrystallized material,

thus forming necklaces of new grains at the periphery of old grains until they are consumed (99, 100). Obviously, the rate of DRX decreases strongly with an increase in the original grain size D_0 (34, 84, 86, 97, 99, 101).

2.3.3 CRITICAL STRAIN FOR DRX INITIATION

When the strain reaches about 0.1 and as marked by the end of the first linear segment of the θ-σ plot, subgrains commence to form (119, 122, 123). At a somewhat higher stress and dislocation density, a critical strain for DRX is attained (30, 31, 34, 36, 76, 77, 84-91, 93, 97, 99, 133, 134); this is marked by the downward inflection in the θ-σ curve (Sec. 2.2.4). Shortly, DRX acting in conjunction with DRV counterbalances the strain hardening. With steady state deformation continuing until fracture, the DRX grains repeatedly reform remaining almost equiaxed and containing a DRV substructure (34, 74, 84, 86, 90-92, 97-100, 117, 131, 132, 135, 149). The DRV substructure which develops in the DRX grains as they deform has a dimension consistent with the stress and subgrain diameter in the original elongated grains before the peak (87).

2.3.4 CYCLES OF DYNAMIC RECRYSTALLIZATION

According to Luton and Sellars (97), a single peak arises at high $\dot{\varepsilon}$ and low T because the strain interval over which the first cycle of recrystallization occurs is much larger than ε_c. That is, DRX nucleates in the new grains when they reach ε_c giving rise to a grain refined microstructure. Several cycles of recrystallization overlap, thereby giving rise to continual recrystallization (34, 84, 86, 97, 99, 136, 137). Nevertheless, in such circumstance the first cycle of DRX comes to an end at the onset of steady state, ε_s. At low $\dot{\varepsilon}$ and high T, one cycle of DRX comes to an end without a second starting so that strain hardening takes

place once again until a new wave of DRX causes repetition of softening. As further waves of DRX occur, the process becomes sufficiently out of phase in different local regions to make DRX effectively continual, thereby resulting in a steady state flow stress (34, 135-137). The slow nucleation behavior results in grain coarsening. The critical condition Z_c for transition from single to multiple-peak behavior is $D_s < D_o/2$, where D_s is the steady state grain size associated with Z_c (136-138); grain coarsening occurs with discrete DRX cycles at low Z and grain refinement from overlapping DRX waves.

The DRX grain size D_s is uniquely determined by the steady state flow stress, σ_s being represented by an equation of the form (138-140):

$$\sigma_s = BD_s^{-r'} , \qquad (8)$$

where B is a constant and the value of the constant, r', varies between 0.75 and 0.80 (31, 84, 86, 89, 90, 99,101, 131, 136). The variation in DRX grain diameter with Z is expressed by the following equation:

$$D_S = B'Z^{r''} \qquad (9)$$

where B' and r'' are constants, with r'' having a value of about 0.2 for γ stainless steels (132, 138).

2.3.5 VOLUME FRACTION RECRYSTALLIZED

The progress of DRX can be measured from its initiation at ε_c up to 99% DRX which is achieved at the onset of steady state. The volume fraction recrystallized, X_{DRX}, as a function of strain can be fitted to the Avrami equation (30, 31, 99, 100, 141):

$$X_{DRX} = 1 - \exp [-\beta_{DRX} (\varepsilon - \varepsilon_c)^{k_{DRX}}], \qquad (10)$$

where β_{DRX} and k_{DRX} are constants. While k_{DRX} is essentially constant, β_{DRX} increases as $\dot{\varepsilon}$ falls, T rises and D_0 decreases (101, 142-144). Nucleation

proceeds rapidly after the critical strain, but starts to slow down as space along the grain boundaries significantly diminishes. The old boundaries become saturated at a low fraction (20-40%) of DRX with the result that another necklace begins to form at the boundary between old and new grains. With the last 10% of recrystallization taking place at the center of the old grain, the difficulty of nucleation results in it taking about one third of the total time (134).

2.3.6 DYNAMICALLY RECOVERED SUBSTRUCTURE IN DRX GRAINS

While DRX becomes the predominant softening mode during steady state, DRV continues to produce an equiaxed substructure with misorientations between 1 and 2 degrees (86-90). As substantiated by transmission electron microscopy, subgrain size, d_s, is a strong function of σ_s with the relationship :

$$\sigma_s = B'' d_s^{-1}. \qquad (11)$$

The similarity of this equation for DRV subgrains and Eqn 8 for DRX grains is the result of the former defining the nucleation of the latter (23, 145-149). As expected from the constitutive equation described shortly, the subgrain diameter varies uniformly with the deformation conditions Z, according to the relation (31, 84, 86, 87, 89, 90, 99, 232, 136):

$$d_S^{-1} = a + b \log Z. \qquad (12)$$

2.3.7 EFFECT OF SUBSTRUCTURE UPON PRODUCT QUALITY

The as-quenched substructure of an alloy influences its room temperature strength. Therefore, the as-quenched hardness, H_v, as a function of the subgrain size is expressed by the following equation (22, 88, 132, 149-152):

$$H_v = H_0 + h\, d_s^{-m'}, \qquad (13)$$

where H_0 is the annealed hardness, h is a constant and m' equals 1.5. The hardness of alloys undergoing DRX increases with rising Z as a result of increasing dislocation density. Consequently, hardness is related to log Z through the expression (22, 88, 149-152):

$$H_v = a' + b' \log Z. \qquad (14)$$

The significantly lower hardness values after hot working than those after cold working are indicative of the low density substructures arising from the softening effects of both DRV and DRX.

2.4. STRENGTH CONSTITUTIVE EQUATIONS

2.4.1 STRESS - STRAIN-RATE AND ARRHENIUS FUNCTIONS

Sellars and Tegart (131) stated that independent of whether restoration proceeds by DRV alone or in conjunction with DRX, the $\dot{\varepsilon}$ and T dependence of the peak stress, σ_p, during hot working can be described by relationships successfully used to express creep behavior at low (Eqn. 15) and high stresses (Eqn. 16) respectively (20, 31, 34, 96, 101, 131, 153-155):

$$A' \sigma_p^{n''} = \dot{\varepsilon} \exp (Q_{HW}/RT) = Z \qquad (15)$$

$$A'' (\beta\sigma_p) = \dot{\varepsilon} \exp (Q_{HW}/RT) = Z \qquad (16)$$

where A', A'', β, n'', Q_{HW} and R are constants. The Zener Hollomon parameter Z describes the deformation conditions in terms of a T-compensated $\dot{\varepsilon}$. These equations can be combined into the following equation which accurately accomodates all flow stress values (20, 34, 131, 153-155):

$$A [\sinh (\alpha\sigma_p)]^n = \dot{\varepsilon} \exp (Q_{HW}/RT) = Z \qquad (17)$$

This reduces to the previous equations at low ($\alpha\sigma < 0.8$) and high ($\alpha\sigma > 1.2$) stresses respectively, with the constants $A' = A\ \alpha^n$, $A'' = A\ 2^n$ and $\beta = \alpha n$ (34, 154, 155), n being the stress exponent, and R is the gas

constant. Q_{HW} is the activation energy which is related to an activated event in the hot working process.

There is interest in the T dependence of different phenomenological features of the deformation in addition to that of the peak flow stress. Equation 17 above is generally found to be satisfactory for determining the activation energy at other defined points along the flow curve, these being the yield stress, the critical stress/strain for DRX, and the onset of steady state and the fracture point. Since Q_{HW} of alloys undergoing DRX is about 30% greater than that for self diffusion, a correlation of creep and hot working data is clearly not feasible (20, 83, 84, 86, 131, 156). The principal reason for this is that creep is controlled by DRV and DRX is not usually found. From Eqn. 17, a unique peak flow stress can be calculated by the following equation (157):

$$\sigma_p = (1/\alpha) \ln \{ (Z/A)^{1/n} + [(Z/A)^{2/n} + 1)^{1/2} \} \quad (18)$$

The Q_{HW} and n values collected for many steel compositions are presented in Tables 1-4 (49, 57, 63, 76, 77, 119, 126, 152, 158-195).

2.4.2 TANAKA'S FORMULATION AND THE CHARACTERISTIC TEMPERATURE

In order to eliminate the constant A which varies considerably with composition, Tanaka (196) developed an equation which involves a characteristic temperature, T', which is defined by:

$$T' = Q_{HW} / (R \ln A). \quad (19)$$

This was shown to be constant for each alloy grade. The original hyperbolic sine function is modified to the form:

$$\sigma_p = (1/\alpha) \sinh^{-1}\{(\dot{\varepsilon}/\dot{\varepsilon}_0') \exp [Q_{HW}/R(1/T - 1/T')]\}^{1/n}, \quad (20)$$

where $\dot{\varepsilon}_0' = 1\ s^{-1}$ is a unit parameter for strain rate A new analytical approach to this equation has recently been developed by Cingara et al

TABLE 1 COMPOSITIONS , GRAIN SIZES, STRESS EXPONENTS AND ACTIVATION ENERGIES FOR 304

Steel Condition	C	Mn	P	S	Si	Cr	Mo	Ni	N	O	MET+	D_0x	Mode	n	Q_{HW}	REFERENCE		
			wt.	%					ppm	ppm	%	μm						
304LW	.100	.41	--	--	.45	18.30	--	8.00	-	--	27.16	--	TEN	4.6	381↓	Ikeshima	e	158
304W	.070	.48	--	--	.43	18.60	--	7.70	-	--	27.21	--	ROL	4.7	377↓	Hinkfoth,Konig	f	159
304W	.070	.48	--	--	.43	18.60	--	7.70	-	--	27.21	--	COM	4.4	424	Cook	g	160
304W	.047	.81	.033	.019	.28	18.10	--	8.50	-	--	27.69	--	TOR	4.3	398	Wallquist,Carl.	h	161
304C	.030	.91	.021	.030	.34	17.80	--	9.70	-	(δ=7%)	28.75	--	TOR	4.9	347↓	Gavrila	i	162
304C	.040	.80	.013	.008	.28	17.70	0.04	9.90	490	--	28.75	--	TEN	4.5	396	Dhosi et al.	i'	163
304LW	.030	.91	.021	.030	.34	17.80	--	9.70	-	--	28.75	--	TOR	3.8	404	Gavrila	j	162
304W	.110	1.17	.020	.013	.58	16.55	0.12	9.85	-	(Ti .57)	28.84	--	TOR	4.0	416	Zela et al.	k	164
304W	.062	1.72	.030	.008	.47	18.28	0.28	8.27	590	35	29.02	70	TOR	4.6	393	PRESENT	l	-
304W	.080	1.06	.037	.005	.49	18.37	--	9.16	-	--	29.08	--	COM	4.5	393	Hashizume	m	165
304W	.100	.92	.018	.014	.37	17.80	--	9.50	-	(Ti .57)	29.16	-	TEN	3.5	351↓	Elfmark	n	166
304W	.050	1.07	.029	.003	.53	18.42	0.09	9.14	380	(Cu .05)	29.30	150	TEN	4.6	435	Maki et al.	p	138
304W	.070	1.76	--	--	.82	17.60	0.27	8.52	(Cu .30,Co .17)		29.45	--	TOR	4.3	410	McQueen et al.	q	167
304C	.069	1.76	.020	.002	.68	18.31	0.08	8.68	-	(δ=31%)	29.51	64	TOR	4.5	407	PRESENT	r	-
304W	.042	1.29	.008	.011	.53	18.32	0.01	9.34	240	(Cu .04)	29.56	28	COM	3.8	418	Ahlblom	s	168
304W	.070	.82	.030	.011	.47	17.80	--	10.50	-	--	29.59	--	COM	4.9	398	Zyuzin et al.	t	169
304W	.070	.82	.030	.011	.47	17.80	--	10.50	-	(Ti .20)	29.79	--	COM	3.5	422	Zotyeyev	u	170
304C	.030	.92	.021	.030	.34	17.70	--	11.00	-	(δ=4%)	29.96	--	TOR	4.0	429	Gavrila	v	162
304LW	.030	.92	.021	.030	.34	17.70	--	11.00	-	--	29.96	--	TOR	4.0	431	Gavrila	w	162
304W	.060	1.21	.032	--	.57	18.69	--	9.42	-	--	30.10	--	TEN	5.6↑	391	Inouye	x	171
304W	.060	1.56	.031	.008	.75	18.70	0.22	9.07	271	--	30.33	--	COM	4.4	393	Ouchi & Okita	y	192
304W	.054	1.19	.025	.016	.48	18.29	0.29	10.10	-	--	30.35	--	TEN	3.0↓	425	Nadai,Manjoine	z	63
304W	.090	.95	.018	.021	.64	18.00	--	10.40	-	(Ti .43)	30.42	--	COM	3.3↓	407	Sokolov	A	172
304W	.050	.92	--	--	.11	18.20	0.02	11.30	(Nb .02,Ti .02)		30.67	--	TOR	4.0	402	Müller	B	173
304W	.050	.92	--	--	.11	18.20	0.02	11.30	(Nb .02,Ti .02)		30.67	250	TOR	4.6	410	Barraclough	C	174
304W	.055	1.06	.036	.022	.59	18.20	0.50	10.60	-	(Cu .26)	30.95	--	TOR	4.3	406	Rossard	D	49
304W	.055	1.06	.036	.022	.59	18.20	0.50	10.30	-	(Cu .26)	30.95	--	TOR	4.3	414	Sellars,Tegart	E	175
304W	.110	1.07	.024	.012	.80	18.20	--	10.30	-	(Ti .65)	31.02	--	COM	2.9↓	404	Tarnoyskij et	F	176
304W	.062	1.02	--	--	.17	18.50	0.02	11.40	-	--	31.24	120	TOR	5.8↑	424	Cole,Richard	G	57
304LW	.018	1.20	--	--	.32	18.60	0.19	11.10	60	(Cu .16)	31.57	280	TOR	4.5	415	Carfi et al.	H	119
304LW	.020	1.57	--	--	.47	19.50	--	10.20	-	--	31.74	-	TEN	4.4	424	Bywater,Gladm.	I	177
304C	.030	.91	.021	.030	.35	17.60	--	13.00	-	(δ=0%)	31.86	-	TOR	4.2	431	Gavrila	J	162
304LW	.030	.91	.021	.030	.35	17.60	--	13.00	-	--	31.86	-	TOR	4.1	438↑	Gavrila	K	162
304LW	.026	1.72	.026	.005	.54	19.02	--	10.80	(Cu .07,Nb .06)		31.21	300	TOR	4.7	418	Ohtakara et al.	L	178
304L	.026	1.72	.026	.005	.54	19.02	--	10.80	(Cu .07,Nb .06)		32.21	-	TOR	5.8↑	427	Nakamura et al.	M	179
304W	.084	1.40	.036	.021	.67	18.85	0.47	10.92	-	--	32.32	200	TOR	4.5	398	Hengerer	N	180
304W	.084	1.40	.036	.021	.67	18.85	0.47	10.12	(Cu .26,Ti .57)		32.34	-	TOR	3.4↓	409	Hildebrand	P	181
304L	.013	1.80	.012	.004	.64	19.60	0.03	10.60	380	(Co .07)	32.74	27	TOR	4.6	411	Semiatin,Holbr.	Q	76
304W	.040	1.70	.012	.010	.55	18.23	0.44	12.41	-	--	33.35	-	TOR	4.4	439↑	Radu et al.	R	182
304W	.040	1.90	.017	.017	.67	17.63	1.37	12.64	-	--	34.26	-	TOR	4.2	464↑	Radu et al.	S	182
MEAN	.073	1.15	.025	.016	.48	18.22	0.10	10.17	344	35	30.30	168	-	4.3	410	Q_{HWC} 500 kJ/mol		

+ In increasing order of metallic solute; x cast, dendrite arm spacing; worked, original grain size.
W=Worked, C=As Cast, L=Low Carbon, TOR=Torsion, TEN=Tension, COM=Compression, EXT=Extrusion, ROL=Rolling.

TABLES 2-4 COMPOSITIONS, GRAIN SIZES, STRESS EXPONENTS AND ACTIVATION ENERGIES: 2,301; 3,316; 4,317.

Steel Condition	C	Mn	P	S	Si	Cr	Mo	Ni	N	O	MET†	D_0 x	Mode	n	Q_{HW}	REFERENCE		
			wt. %						ppm	ppm	%	μm						
Table 2: Values for 301																		
301W	.150	.48	.031	.016	.48	16.21	--	7.62	-	-	24.79	--	TOR	3.7	335↓	Elfmark	a	166
301W	.080	1.16	.013	.026	.32	17.44	--	7.37	-	-	26.29	--	EXT	4.4	340↓	McCallum,Cockc.	b	183
301W	.110	1.12	.036	.002	.54	17.12	0.20	7.92	190	43	26.90	66	TOR	4.4	399	PRESENT	c	-
301W	.080	1.10	.009	.014	.93	16.99	0.31	6.96	200	(Al .93)	27.24	--	COM	4.9	437↓	Suzuki et al.	d	184
MEAN	.105	.97	.022	.058	.57	16.94	0.26	7.47	195	(.07)	26.29	66	-	4.3	378	Q_{HWC} 435 kJ/mol		
Table 3: Values for 316																		
316W	.070	.97	.020	.021	.46	17.10	2.48	11.40	-	--	32.41	--	TOR	4.9	444	Gittins et al.	T	185
316C	.068	1.15	.021	.013	.40	16.90	2.35	12.00	(δ=20%,	Ti .22)	32.02	--	TOR	5.0	410↓	Zidek, Kubicko	T'	186
316W	.068	1.15	.021	.013	.40	16.90	2.35	12.00	-	(Ti .22)	32.02	--	TOR	4.5	453	Zidek, Kubicko	U'	186
316W	.068	1.15	.021	.013	.40	16.90	2.35	12.00	-	(Ti .22)	32.02	--	TOR	3.4↓	455	Zela et al.	U	164
316W	.070	1.57	.039	--	.90	17.40	2.60	10.60	-	--	33.07	--	TEN	5.7↓	465	Inouye	V	171
316L	.024	1.50	--	--	.29	16.70	2.61	12.20	390	--	33.32	191	TOR	4.4	450	Barbosa,Sellar.	W	187
316LW	.024	1.50	--	--	.29	16.70	2.61	12.20	-	--	33.32	30		4.5	460	Colas,Sellars	X	77
316W	.090	1.00	.031	.017	.60	17.20	2.30	11.80	-	(Ti .58)	33.48	--	COM	3.8	448	Zyuzin et al.	Y	169
316W	.070	1.34	.010	.008	.67	17.29	2.26	12.04	-	--	33.60	--	COM	4.2	459	Suzuki et al.	Z	184
316LW	.010	1.87	.034	.007	.62	16.40	2.73	12.05	140	37	33.67	60	TOR	4.5	454	PRESENT	A'	-
316W	.070	1.27	.020	.023	.64	17.20	2.92	10.90	(Co .32,Cu	.49)	33.76	--	TOR	4.5	460	Hughes et al.	B'	188
316C	.017	1.60	.022	.007	.52	16.92	2.76	12.42	110	(δ=20%)	34.60	63	TOR	4.5	402↓	PRESENT	C'	-
316W	.040	1.68	--	--	.40	17.00	2.20	12.90	(δ=1.3%,	Ti .42)	34.60	50	TOR	4.8	458	Dragan et al.	D'	189
316LW	.030	1.76	--	--	.70	17.60	2.67	12.80	(δ=3%)	--	34.83	111	TEN	4.8	479	Bywater & Glad	E'	177
316W	.060	1.74	.024	.014	.43	17.93	2.50	12.38	--	--	34.96	50	TOR	5.8↓	481	Young & Sherby	F'	190
316W	.550	1.76	--	--	1.08	17.42	2.14	12.80	--	(Ti .05)	35.25	60	TOR	4.8	499↓	Teodosiu et al.	G'	191
316LW	.020	1.76	--	--	.35	17.40	2.35	13.70	600	--	35.52	80	TOR	4.6	460	Donadille etal.	H'	126
316LW	.030	2.13	.014	.013	.69	17.56	2.73	12.82	--	--	35.93	--	TOR	4.0	479	Radu et al.	I'	182
316LW	.013	1.72	.007	.011	.60	17.38	2.71	13.67	420	--	36.08	--	TEN	4.0	464	Johansson	J'	192
316W	.040	1.39	--	.010	.52	17.60	2.73	13.90	--	(Cu .22)	36.36	--	TOR	2.1↓	498↓	Nikkila	K'	193
316W	.070	1.22	.026	.030	.52	17.04	2.97	15.39	(Ti .57,Cu	.19)	37.90	--	TOR	3.1↓	491↓	Tokarz & Bik	L'	194
MEAN	.048	1.49	.024	.015	.52	17.17	2.32	12.47	332	(.30)	34.27	77	-	4.3	460	Q_{HWC} 570 kJ/mol		
Table 4: Values for 317																		
317LW	.027	1.59	.017	.015	.53	15.80	4.30	14.00	1400	--	36.22	75	COM	4.0	504	Boden	M'	195
317LW	.030	1.60	.015	.015	.51	17.28	3.66	12.85	--	--	35.90	--	TOR	4.5	503	Radu et al.	N'	182
317C	.050	1.46	.015	.023	.51	16.70	4.06	15.00	360	(Cu .110)	37.73	--	TEN	4.5	502	Dhosi et al.	P'	163
317C	.035	1.73	.032	.004	.44	18.60	3.22	13.88	170	(δ=23%)	37.87	72	TOR	4.0	508	PRESENT	Q'	-
317W	.035	1.73	.032	.004	.44	18.60	3.22	13.88	170	(δ=5%) 61	37.87	57	TOR	4.5	496	PRESENT	R'	-
MEAN	.035	1.62	.022	.012	.49	17.40	3.69	13.92	525	61 (.11)	37.12	68	-	4.3	503	Q_{HWC} 615 kJ/mol		

† In increasing order of metallic solute; x cast, dendrite arm spacing; worked, original grain size.
W=Worked, C=As Cast, L=Low Carbon, TOR=Torsion, TEN=Tension, COM=Compression, EXT=Extrusion, ROL=Rolling.

(197) who determined all constants. These constants allow a more precise extrapolation to high $\dot{\varepsilon}$ representative of industrial hot working conditions. These empirical constitutive equations have been found to be reliable for the calculation of force and power requirements of hot working equipment operating at high $\dot{\varepsilon}$ which far exceed those possible by laboratory testing modes.

2.4.3 KOCKS-MECKING ANALYSIS

Based upon the combined effects of work hardening and a variety of mechanisms, the Kocks-Mecking (198) analysis of the T and $\dot{\varepsilon}$ dependence of the flow curve has resulted in the following equation (113, 114):

$$\dot{\varepsilon}/\dot{\varepsilon}_0 = \exp\,[-\Gamma \ln\,(\sigma^*_{s0}/\sigma^*_s)\,/RT] = (\sigma^*_s\,/\sigma^*_{s0}\,)^{\Gamma/RT}, \qquad (21)$$

where $\dot{\varepsilon}_0$ and Γ are constants. The activation enthalpy, ΔH, described by the following equation:

$$\Delta H = \Gamma \ln(\sigma^*_{s0}\,/\sigma^*_s\,), \qquad (22)$$

is strongly stress dependent, increasing with T as σ^*_s declines. The activation entropy alters this to give a constant activation free energy at high T which approximates the Q_{HW} value determined by sinh $\alpha\sigma$ analysis. The term $RT/\Gamma = m$ is the strain rate sensitivity which is the reciprocal of the stress exponent n'' in the power law equation; clearly n'' increases with stress as T is lowered (113, 114).

2.5 MICROSTRUCTURAL CHANGES AFTER HOT WORKING

2.5.1 STATIC RESTORATION PROCESSES

Most hot working processes are performed with passes and interruptions which are defined mainly by the capacity of the shaping equipment and speed of the manipulators. The pause periods between these interruptions vary from several hundred to a few hundredths of a second (22, 24, 30, 36, 89,

91, 92). However, where it is possible the schedule should be designed to control the dynamically and statically produced microstructure which is responsible both for forces in subsequent stages and for product quality (1-37). Between these stages the following microstructural changes take place: SRV and SRX, and grain growth, all of which are a function of time (22, 36, 86, 134, 143. 199). While SRV takes place after deformation by the annihilation of dislocations within the subgrains, SRX takes place by the massive elimination of dislocations by the motion of high angle boundaries (22, 31, 34, 86, 89). Unlike ε_c for DRX which occurs at about 0.65 of the peak stress, the SRX critical strain is much lower between 0.05 and 0.10 (132, 143, 200). If the critical strain is not attained, then softening is only by SRV and saturates at a level of 20-40% (22, 117, 199-202).

2.5.2 STATIC RECRYSTALLIZATION

Static recovery proceeds immediately after deformation, whereas SRX commences only after an incubation period in which time SRV may help create the recrystallization nuclei (22, 86, 89, 106, 199, 201-207). By proceeding first, SRV accounts for between 30 and 40% of the total softening in stainless steel and copper (22, 139, 208-210). Increased ε and $\dot{\varepsilon}$ raise the rate of both these mechanisms because of the increased dislocation density; however, it favors SRX by raising the driving force for nucleation. This stored dislocation energy rises with increasing $\dot{\varepsilon}$ and decreasing T and is strongly dependent upon ε (22, 24, 30, 34, 74, 89, 139, 168, 174, 199). Because nucleation occurs preferentially at grain boundaries, the density of favorable sites increases with decreasing D_0, and hence an augmented rate of static softening (31, 199). Since SRX is a thermally activated process, the temperature of holding after deformation significantly

controls SRV and the rate of SRX. In addition, increasing $\dot{\varepsilon}$ lowers the incubation time for the commencement of SRX (10, 12, 168, 174, 201, 202).

SRX proceeds similarly to DRX by the nucleation of new grains along the grain boundaries (13, 130, 139), but does not form succeeding necklaces of new grains. Because of lower ε_c, there is a lower density of sites along the boundary (84, 100, 205, 209). In addition, there is no concurrent deformation to buildup substructure in the SRX grains and halt growth. As a result, for strains less than ε_c or ε_p these grains are larger than the DRX grains produced after the peak (132, 168, 200, 205).

2.5.3 EFFECTS OF METADYNAMIC RECRYSTALLIZATION

When the strain for interruption exceeds ε_c for DRX, the nuclei existing when deformation stops continue to grow statically. This metadynamic recrystallization, MRX, proceeds very rapidly since there is no need for an incubation period as for nucleation of SRX (13, 132, 168, 201, 202, 205, 208, 209). In spite of this increased rate, MRX usually does not go to completion due to the heterogeneity caused by the repeated cycles of DRX. Unlike DRV which produces a substructure of homogeneous dislocation density, DRX produces a somewhat heterogeneous distribution of dislocation density due to the fact that some regions are deformed almost to ε_c, while others have been partly deformed (30, 31, 34, 86, 89, 90, 132, 205). SRX occurs later in these latter regions with a reduction in the rate. Since there is no additional DRX nuclei once deformation ceases, the MRX grains are larger than the DRX grains (85, 132, 168, 205).

2.5.4 KINETIC EQUATIONS

Since the volume fraction, X_{SRX}, is readily obtainable by optical metallography, its Avrami kinetics can be determined by the following expression (23, 70, 106, 139, 141, 204, 205, 209, 211, 212):

$$X_{SRX} = 1 - \exp(-\beta_{SRX} t^{k_{SRX}}), \qquad (23)$$

where β and k_{SRX} behave similarly as in DRX (Eqn. 10) but have different values (130, 139, 174, 205, 206, 211-214). Since SRX kinetics depend strongly on ε, $\dot{\varepsilon}$, D_0, Z and T, the time for 50% recrystallized is calculated by the following expression (209):

$$t_{0.5} = A_{SRX} \varepsilon^{-2} D_o^2 Z^{-0.375} \exp(Q_{SRX}/RT), \qquad (24)$$

where the powers are constant for γ stainless steel. Once $t_{0.5}$ is known, the grain constant β_{SRX} can be deleted from the Avrami equation, thereby allowing X_{SRX} to be calculated by the following expression (26, 31):

$$X_{SRX} = 1 - \exp\{-0.693 (t/t_{0.5})\}^{k_{SRX}} \qquad (25)$$

2.6 SIMULATION OF INDUSTRIAL PROCESSING

2.6.1 MULTISTAGE PROCESSING

In most hot forming operations where the material undergoes a drastic shape change through a series of deformations, it is advisable that the work hardening, dynamic and static restoration, and fracture mechanisms in conjunction with the microstructural changes be known in order to optimize equipment design and product quality, thereby maintaining competitiveness (1-37). With rest intervals often of varying time as in the plant, interrupted tests to high cumulative ε under both isothermal (1-6, 8-12) and anisothermal (2, 4, 21-28, 30) conditions can be carried out by hot torsion. Multiple stage tests are now used regularly to examine an alloy's softening behavior between passes and flow stress in a subsequent stage.

2.6.2 MULTISTAGE FLOW STRESS

The behavior of the flow curves derived from multistage tests is a sensitive measure of an alloy's structural development. The previous pass has a fundamental influence on the softening in an interval. It may be

augmented by unrecrystallized material which entered the pass from the previous interval (10-12, 21, 22, 26-28, 199, 203, 206). SRV and SRX during the interval lower the flow curve (10, 22, 30, 31, 86, 89, 199, 203, 206, 215). In comparison with the continuous and with the initial flow curves, the shapes after interruption reveal the microstructural states at the end of the interval; this is known as mechanical metallography (199).

2.6.3 ISOTHERMAL INTERRUPTED DEFORMATION

With isothermal interrupted deformations, a specimen is usually deformed at the desired temperature to a given strain after which it is unloaded and held for increasing intervals. Following this, it is reloaded at the same $\dot{\varepsilon}$ and T. When the interval is very short, the reloading flow curve quickly rejoins the continuous curve (10, 19, 22-24, 193, 199, 215). With rising interval, the magnitude of the yield stress on reloading is governed by the microstructural changes brought about by SRV and SRX. When full SRX occurs, the second flow curve becomes almost identical to the first with the difference being attributable to the change of SRX grain diameter, D_{SRX} (10, 22, 199, 215).

2.6.4 DETERMINATION OF STATIC SOFTENING

This fractional softening, FS, in the i'th interval, is evaluated by the following quotient (21-26, 199, 201, 202, 215-219):

$$FS_i = [\sigma_{mi} - \sigma_{y(i+1)}] / [\sigma_{mi} - \sigma_{y0}] \qquad (26)$$

where σ_{y0} is the original yield stress, σ_{mi} is the flow stress of the i'th pass, $\sigma_{y(i+1)}$ is the reloading yield stress. Since FS as defined includes SRV which accounts for approximately 30% of the total softening (22, 139, 201-203), an equation has been developed which separates the SRV from the SRX (24):

$$FS = \{1 - [\ 1\ /\ [1 + (t\ /t_0)]^{1/2}](1 - X_{SRX}) + X_{SRX} \qquad (27)$$

where t is the interval and t_0 is a characteristic time for SRV, related to the interruption strain and temperature. This has been evaluated by Barraclough and Sellars (139), at a strain of 0.25 and expressed by Roberts in the following form (30):

$$FS = 1 - \exp\ (\ -20\ X_{SRX}\ ) - 0.2\ (\ 1 - X_{SRX}\ ) \qquad (28)$$

Through multistage tests, fractional softening can be determined using Eqn. 26 after which X_{SRX} can be calculated from Eqn. 28. Using the time for 50% volume fraction recrystallized, t_0 can be derived from substitution of the values in Eqn. 27 (24).

2.6.5 GRAPHICAL DETERMINATION OF FRACTION RECRYSTALLIZED

A graphical method for direct determination of X_{SRX} from Eqn. 26 employs a special definition of the reloading stress (81, 220). The first flow curve, placed over the reloading flow curve so that their stress maximums coincide at the same ε_i, is back-extrapolated to the line of unloading. To take account of refinement in grain size due to SRX after the first pass, the reloading curve which represents complete SRX is superimposed on to the second flow curve to give a different extrapolation value. It is found that the large grained initial curve underestimates X_{SRX}, while the fine grained reference curve overestimates it. An average of these two values has only a slight error relative to the metallographic results.

2.6.6 SOFTENING MECHANISMS AND ENVELOPE CURVES IN MULTISTAGE TESTS

The static restoration mechanisms operating during an interruption can involve, (a) only SRV, (b) SRV with partial SRX, (c) SRV with complete SRX effecting a grain size varying from finer to coarser than the original, (d) SRV with MRX followed by SRX (10, 12, 22, 36, 199, 201, 202, 215). In

multistage tests, the degree of softening depends not only upon the previous deformation, but on the accumulation of strain which results from incomplete softening between earlier passes. Regions with substructures representing the sum of several preceding passes produce a finer recrystallized grain size (10, 25, 26, 215). This effect becomes more important with high processing rates and low T which are found in the final passes of continuous mills (1-3, 8, 9, 13-19, 36). The presence of solute and precipitate stabilizes the substructure thereby slowing SRV and SRX, particularly with HSLA steels where niobium precipitates significantly decrease SRX at low T (221).

When plotted against accumulated strain, the pattern of successive stress curves influenced by varying degrees of softening or of accumulated strain defines an envelope curve connecting the maxima (10, 12, 19, 36, 199, 215). Short intervals which leave no time for SRX lead to an envelope close to the continuous curve as DRX occurs due to accumulated ε. Limited partial SRX, cooperating with DRX, lowers the pass flow curves and with similar softening in succeeding interruptions develops an envelope curve which is generally lower than the continuous curve. Greater partial SRX moves the pattern towards that described below for complete SRX. Complete SRX to D_0 leads to the repetition of the first flow curve providing a saw-toothed appearance and an envelope curve which is higher than the steady state values of the corresponding continuous curve. While SRX to a finer grain diameter leads to a higher envelope curve, SRX to a coarse grain diameter leads to a low one possibly below the steady state.

2.6.7 ANISOTHERMAL MULTISTAGE SCHEDULES

While the isothermal multistage hot torsion test is an excellent

vehicule for the examination of an alloy's softening behavior (1, 5, 6, 8-12, 14-16, 215, 221), anisothermal testing where the temperature is continually declining is a truer simulation of industrial processes (2-4, 17, 21, 22, 25-28, 30, 31, 35, 36, 199). Likewise, the strain rate is also increasing from pass to pass as the material becomes thinner and moves faster as in continuous hot rolling. The variables controlling the final microstructure are pass ε_i, $\dot{\varepsilon}_i$, interval, t_i and T_i (21, 25-28, 199). Since the temperature at reloading, $T_{(i+1)}$, has decreased from that at unloading, T_i, the equation for calculating FS under isothermal multistage conditions is inadequate. Therefore, the following expression has been developed taking into account declining T and retained strain (21):

$$FS_i = [\sigma_{mi} - \sigma_{y(i+1)} \cdot (\sigma'_{yi}/\sigma'_{y(i+1)})] / (\sigma_{mi} - \sigma'_{yi}) \qquad (29)$$

where $\sigma_{y(i+1)}$ is the yield stress due to incomplete softening and accumulated strain at T_{i+1}. Both σ'_{yi} and $\sigma'_{y(i+1)}$ are the yield stresses of recrystallized metal, one at T_i and the other at $T_{(i+1)}$; these are calculated from the constitutive equations. Under isothermal multistage conditions, where $\sigma'_{yi} = \sigma'_{y(i+1)}$, Eqn. 29 reverts to Eqn. 26.

2.6.8 MATHEMATICAL MODELLING

In most industrial hot rolling, the reductions are below 30% ($\varepsilon \approx 0.2$), and consequently less than ε_c for DRX. Roberts (30) developed the following equation which accurately fits experimental data of alloys with high SFE where DRV rapidly occurs:

$$\sigma^*_s \ln (\sigma^*_s / \sigma) - \sigma = P_o \varepsilon \qquad (30)$$

where σ^*_s and P_o has the same meaning as in Eqn. 7. and Sec. 2.2.4. Since a knowledge of the flow curve occuring before the peak is required for the determination of the mean flow stress, an equation based upon the peak flow stress/peak strain relationship has been developed. This is a practical

method because σ_p and ε_p are readily determinable for the deformation conditions from the constitutive equations. The equation has the following form (197):

$$(\sigma / \sigma_p) = [(\varepsilon / \varepsilon_p) \exp (1 - \varepsilon / \varepsilon_p)]^c, \quad (31)$$

where c is a constant less than unity which rises as Z decreases. This can be used in conjunction with the finite element method where the flow stress at each grid point is a function of ε, $\dot{\varepsilon}$, and T as they develop during processing.

When the total curve is required as in planetary rolling simulation by hot torsion (1), the resultant work hardening and softening determines flow curve shape throughout the steady state regime. The curve with consideration of only the DRV softening kinetics, comforms to the following equation (222):

$$\sigma = \sigma_{y0} + B_0 [1 - \exp (-C'\varepsilon)]^{m'_o}, \quad (32)$$

where σ_{y0}, the initial flow stress and the constants B_0, C', and m'_o all depend upon Z. The gradual softening by DRX, $\Delta\sigma$, from the DRV steady state is described by the Avrami type expression in terms of strain (222):

$$\Delta\sigma = B'_0 \{1 - \exp [-\beta''(\varepsilon - a_o \varepsilon_p) / \varepsilon_p]^{m''_o}, \quad (33)$$

where a, B'_0, β'', and m''_o are constants and $a_o \varepsilon_p$ equals the critical strain for DRX. For high Z (low T and high $\dot{\varepsilon}$), ε_p increases thereby raising the value of $\Delta\sigma$. The entire flow curve can be derived by subtracting $\Delta\sigma$ from the flow stress determined for a given strain by Eqn. 32 (222). Incorporating the same principles into one equation, Roberts (30) proposed the following expression:

$$\sigma = C_1 \varepsilon^{P_o} - C_2 \{ 1 - \exp [-\beta_{DRX} (\varepsilon - \varepsilon_c)^{k_{DRX}} \quad \varepsilon > \varepsilon_c \quad (34)$$

where P_o has the same value as in Eqn. 7, C_1, C_2 are constants and all

other symbols have the same meaning as in Eqn. 10. Recent work by Roberts (30, 31) has been reasonably successful in deriving a series of curves for anisothermal deformation with increasing $\dot{\epsilon}$ and decreasing t_i (219). In addition, comprehensive knowledge of the softening kinetics for anisothermal interruptions is required for accurate curve modelling.

2.7 HOT DUCTILITY

2.7.1 FRACTURE MECHANISM AND EFFECTS OF DRX

Fracture in hot working occurs by w-type cracks forming at triple junctions as a consequence of stress concentrations produced by differential shearing along GB (20, 22, 86, 131, 223-230). In addition, irregularities in the original GB may give rise to pore formation. With continuing deformation these fissures (a) grow by additional shearing, plastic extension and vacancy diffusion along GB and (b) link up to give intergranular fracture. Cracking may also commence at second phase particles depending on their flow behavior relative to the matrix (91).

When DRX is the softening process, grains are being continually nucleated along the existing grain boundaries which causes GB migration away from the fissures preventing their propagation. However, further growth occurs by the fissure capturing a moving grain boundary for a period of time. New fissures can appear and grow along the grain boundaries of the new grains (20, 22, 86, 225-227).

2.7.2 COMPOSITIONAL EFFECTS UPON HOT DUCTILITY

Solid-solution alloying increases the strength and lowers ductility during hot working (22, 34, 89, 101, 131, 229, 230). Solute hardening reduces intergrain accomodation and raises the stress concentrations. In addition, solute obstructs GB migration (106, 131, 231-235). As a result,

fissuration is augmented and fracture occurs at a lower ε. The hot ductility of two-phase stainless steels is significantly reduced (34, 41, 89, 101, 131, 227, 233-242). Nevertheless, there is a ductility trough at about 30vol% δ (173, 243-245), after which the ductility rises. Fracture is initiated by interphase cracking where most of the deformation is concentrated in the austenite (246). Therefore, fracture in as-cast alloys is often initiated in areas of interdendritic segregation where there exists the greatest differences in stress distribution (22, 34, 86, 89, 131, 226, 228, 241).

2.7.3 FRACTURE INHIBITION DEPENDENCE ON T AND $\dot{\varepsilon}$

Many alloys exhibit a ductility peak between low and high $\dot{\varepsilon}$. In the case of low $\dot{\varepsilon}$, when DRV is the only operative softening mechanism, there exists a low $\dot{\varepsilon}$ region where high T mechanisms weaken the grain boundaries through GB sliding. Moreover, the proportion of straining due to GB sliding rises, so that there is more cracking (22, 34, 89, 101, 131, 226, 229, 230). When high $\dot{\varepsilon}$ are applied, impeded recovery and resulting strain hardening reduce grain accomodation leading to high stress concentration between the grains. For $\dot{\varepsilon}$ between these two regions, the DRV is sufficient to give the maximum ductility; as T increases, the peak shifts to higher $\dot{\varepsilon}$ (228, 246-248).

During hot working, a sufficient driving force is required for the initiation of DRX. However, at very low $\dot{\varepsilon}$ where DRV is very active, DRX does not proceed due to an insufficient driving force. At very high $\dot{\varepsilon}$, the critical strain is raised as concurrent straining inhibits nucleation. Consequently, DRX only intervenes at some intermediate $\dot{\varepsilon}$. As T rises, ductility is increased by faster DRX (22, 34, 89, 131, 229, 230) and the

ductility-strain rate maximum to lower $\dot{\varepsilon}$ (247).

2.7.4 FRACTURE CONSTITUTIVE RELATIONSHIP

As in creep, the stress concentrations inducing w-cracking rise with the general stress level. Since the sinh relationship is valid for correlating strength data for hot working, the following strain constitutive equation is used for fracture (34, 131, 249):

$$t_f = A_o(\sinh \alpha\sigma_f)^{-n_f} \exp (Q_f/RT) \qquad (35)$$

Because the lines are parallel in a logarithmic plot of fracture time t_f versus sinh $\alpha\sigma_f$, it is possible to obtain a Q_f from a plot of log $\alpha\sigma_f$ versus 1/T at constant $\dot{\varepsilon}$. The difference in n_f and Q_f values for strength and fracture data is a measure of the strain rate effect. As with strength data, the use of the temperature-compensated parameter (34, 131, 249):

$$Z_f = t_f \exp (-Q_f/RT) = A_0(\sinh \alpha\sigma_f)^{-n_f} \qquad (36)$$

permits the correlation of data for different T and $\dot{\varepsilon}$ on a single straight line.

In consideration of triple point cracking, the time to fracture is dependent on the size of the DRX grains as described by the equation (249, 250):

$$t_f \dot{\varepsilon} = [\gamma' 8\pi (1 - \nu)/ \mu D_s]^{1/2} \qquad (37)$$

where γ' is the surface energy of the fractured surface, ν is the Poisson ratio, μ is the shear modulus and D_s is the diameter of the DRX grains and is taken as the length of the sliding grain boundary. Substitution into Eqn. 37 gives the following equation (249):

$$t_f = [\gamma' 8\pi (1 - \nu)/ \mu] D_s^{-1/2} A_o' [\sinh \alpha\sigma_p]^{-n} (Q_{HW}/RT) \qquad (38).$$

Unfortunalely, the fracture time determined by this equation is 2 to 3 orders of magnitude lower than those measured experimentally. The reason

appears to be the intermittant growth of cracks which are stopped as the grain boundary migrates away from them during DRX. Each time recrystallization occurs, cracks are effectively blunted and stress concentrations must build up on a newly captured grain boundary by sliding before the crack can propagate (249, 250).

2.7.5 DUCTILITY CONSTITUTIVE EQUATION BASED ON RATE OF DRX

From an analysis of Elfmark (251, 252) of the experimental fracture strains, ε_f, and recrystallization kinetics for alloys, the data are fitted by the following equation:

$$\varepsilon_f = E\ Z_{DRX}\ \sigma_s^{-(3+k')}, \qquad (39)$$

where E is a constant, Z_{DRX} is the Zener Hollomon parameter related to the onset of steady state, and k' is derived from a plot of the values of D_s against the respective steady state flow stresses. This indicates the fundamental dependence of ductility upon σ_s, that is, the rate of DRX. Considering the temperature-compensated-time, W_{DRX} for DRX (3, 174, 251,252):

$$W_{DRX} = t_{DRX}\ \exp\ (-Q_{DRX}/RT) \qquad (40),$$

an appropriate equation for the fracture strain in terms of the imposed deformation conditions is derived as:

$$\varepsilon_f = E'\ [\ \dot{\varepsilon}\ \exp\ (Q_{DRX}/RT)]^{-0.2} \qquad (41)$$

where Q_{DRX} is the activation energy for DRX.

2.7.6 HOT DUCTILITY ENHANCEMENT IN MULTISTAGE PROCESSING

During interrupted deformation, structural changes take place which are reflected in the hot ductility. As the interval increases, the ductility also rises due to GB migration during SRX. When the initial interruption ε is large and the interval long, the growth of cracks is

inhibited by the completely recrystallized structure (22, 106, 229, 230). When the interruption ϵ is small and the interval short, the growth of the small fissures is inhibited even by partial recrystallization. However, when due to solute and precipitate effect, large cracks form in the first pass and the amount of recrystallization is insufficient to replace the initial structure, fracture strain is not improved (22, 106, 180, 229, 230, 233).

2.7.7. TORSION/TENSION DUCTILITY COMPARISON

In the tension test the necking instability occurs at the elongation at which the strain hardening rate diminishes to a low level as analyzed by Considére. However, once necking starts, the reduction in area depends most clearly on the fracture mechanism. Intergranular fissures or cracks in brittle segregates or interphase decohesions are opened up by the triaxial tensile stress (34, 246, 253). This is usually represented by the mean stress which is one third of the sum of the principal stresses; as necking occurs, it rises above one third of the tensile stress (42-44).

In torsion there is no basic instability. The above cracks are initiated by the shear strain, but with zero mean stress, they do not grow as rapidly as in tension. Thus in torsion, true fracture strain is usually much higher than that in tension. In primary metal forming, the applied stresses are mainly compressive so that a compressive mean stress retards the opening of cracks. However, friction with the tooling often gives rise to secondary tensile stresses in some regions which can cause cracking especially if associated with non-uniform cooling, for example, edge cracking in rolling (65, 253).

The ductility in tension is measured by the reduction in area, R_A, of

the specimen at fracture; the true strain at which the alloy fractures is given by the following equation (65, 254):

$$\varepsilon_f = \ln (1 / 1- R_A) \qquad (42)$$

At $\varepsilon_f>1$, the ductilities are empirically related by the following expression (254):

$$\varepsilon_f \text{ (torsion)} = [\varepsilon_f\text{(tension)}]^2 \qquad (43)$$

CHAPTER 3

EXPERIMENTAL TECHNIQUES

3.1 EXPERIMENTAL OUTLINE

3.1.1 RESEARCH PROGRAMME

Because of the need for a more thorough understanding, than that appearing in the literature, of the hot deformation characteristics of four common γ stainless steels of similar quality, a comprehensive research programme was undertaken. The heterogeneous as-cast materials which exist at the start of rolling were analyzed to examine their flow curve behavior and microstructural evolution in order to find out the influence of segregated ferrite. The hot working characteristics of the worked homogenized materials were similarly observed to see the influence of the dissolved elements in the absence of δ ferrite.

3.1.2 TESTING OBJECTIVES

In order to accomplish the following research objectives, two hundred and fifty torsion tests were conducted on a computer controlled torsion machine located within the Department of Mining and Metallurgy, McGill University. The following goals were set:

(a) Determination of the flow stress versus strain in the 900-1200^{o}C temperature range at strain rates 0.1 to 5.0 s^{-1}.

(b) Determination of hot ductility by tests to fracture.

(c) Determination of the dynamic structural evolution in specimens deformed to $\varepsilon = 5$.

(d) Analysis of flow curves for the development of constitutive strength and ductility equations.

(e) Analysis of work hardening, DRV and DRX behavior through the use of θ-σ curves.

(f) Examination of DRV and DRX by optical and electron microscopy.

(g) Determination of the room temperature hardness of the retained hot worked substructure.

(h) Examination of SRX through multistage testing with increasing pause times.

(i) Simulation of multistage rolling with declining T.

(j) Mathematical modelling of the high reduction planetary rolling mill.

3.2 MATERIALS

3.2.1 CHEMICAL COMPOSITIONS

The chemical compositions of types 304C, 316C, 317C, 301W, 304W, 316W, and 317W austenitic stainless steels, supplied by Atlas Steels, are presented in Table 5. In addition, the total metallic solutes, S, and D_0 are included.

3.2.2 SPECIMEN PREPARATION

The as-cast specimens were cut from a 127mm thick continuously cast slab with their axes in the casting direction, while the worked material was prepared by soaking at 1200°C forging to 50% reduction, reheating and rolling to 19mm thick plates. Torsion specimens (215, 255) (Fig. 1) from both materials were similarly machined ($2R_e$ = 6.25mm, L_e = 25.4mm) to close tolerances in the gage section with their axes parallel to the casting and rolling directions, respectively. All specimens were annealed in vacuum pouches for 30 minutes at 1050°C and then rapidly quenched in water to avoid the harmful effects of carbide precipitation.

TABLE 5: CHEMICAL COMPOSITIONS (wt.%) FOR WORKED AND AS-CAST ALLOYS*

STEEL CONDITION	C	Mn	P	S	Si	Cr	Mo	Ni	Cu	N_2	O_2	δ^+ stab.	tot.$^+$ sol.	D_o^+	Cr_{eq}^+	Ni_{eq}^+	R'^+_e	δ phase
					wt.%					PPM	PPM	%	%	μm	%	%		%
301 W	.110	1.12	.036	.002	.54	17.12	0.20	7.92	-	190	43	17.3	26.9	66	-	-	-	-
304 W	.062	1.72	.030	.008	.47	18.28	0.28	8.27	-	590	35	18.6	28.9	-	-	-	-	-
304 C	.069	1.76	.020	.002	.68	18.31	0.08	8.68	-	250	-	18.4	27.1	64	19.4	11.1	1.75	31
316 W	.010	1.87	.034	.007	.62	16.40	2.73	12.05	.26	140	37	19.1	31.8	60	-	-	-	-
316 C	.017	1.84	.022	.007	.52	16.92	2.76	12.42	-	110	-	19.1	32.1	63	21.5	13.5	1.59	20
317 W	.035	1.73	.032	.004	.44	18.60	3.22	13.88	-	170	61	21.8	35.7	57	-	-	-	5
317 C	.035	1.73	.032	.004	.44	18.60	3.22	13.88		170	-	21.8	35.7	72	23.4	15.4	1.52	23

*Cast and Worked not the same heats. +D_o initial grain size; for cast, dendrite arm spacing

+δ stabilizers, total solute; Cr_{eq}, Ni_{eq}, R'_e.

3.3 HOT TORSION TESTING

3.3.1 TESTING EQUIPMENT

On a closed-loop servo-controlled hot torsion testing machine (10, 12, 19, 25-28, 35, 215, 255) (Fig. 2), torsional displacements were applied to the test specimen through a rotary hydraulic actuator and measured by a rotary potentiometer. Mounted at the other end of the lathe bed is a strain-gage, torque-cell transducer which measures the force developed in the specimen. The system is capable of speeds from 0-1500 RPM, a maximum torque of 113Nm (1000 inch-pounds) and a maximum of fifty turns which far exceeds the normal ductility. The speed and direction of rotation of the motor is controlled by a servo valve which proportions the hydraulic fluid to the electrical signal magnitude. The control function is generated by a PDP-11/4 mini-computer. While the threaded end of the specimen is secured into the grip mounted on the load cell, the other end is engaged into the rectangular recessed rotating grip. The load cell end of the machine is tightened on the ways just prior to testing in order to avoid axial compression of the specimen; normally, a 2mm clearance was left at the rectangular end to allow for thermal expansion. The specimen was heated in a six element radiant furnace which is capable of temperatures up to 1250^{o}C. The temperature was controlled by a Leeds and Northrop 1300 process programmer. Oxidation of the specimen was prevented by a constant flow of high purity argon inside the furnace. After five minutes homogenization, the specimen was tested to fracture or a fixed strain of 5.

3.3.2 STRESS DETERMINATION

In calculating the equivalent flow stress, σ, from the torque, Γ_e, and the equivalent $\dot{\varepsilon}$, Eqns. 2 and 3 (10, 34, 36, 42, 49, 52, 55, 56, 74, 76,

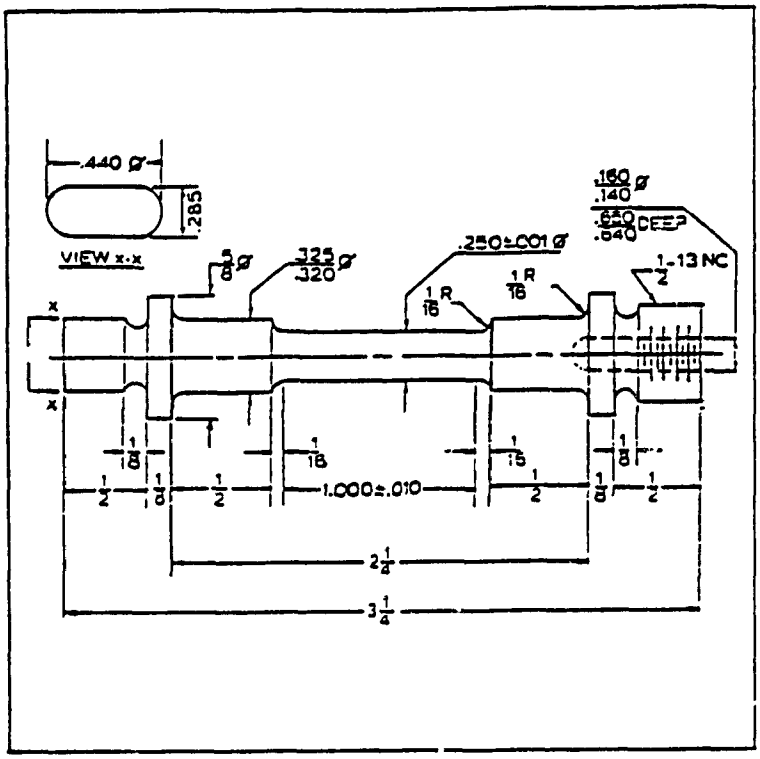

Fig. 1 Test specimen design (dimensions in inches). The gage section has L_c = 25.4mm, R_c = 6.35mm (10, 215, 255).

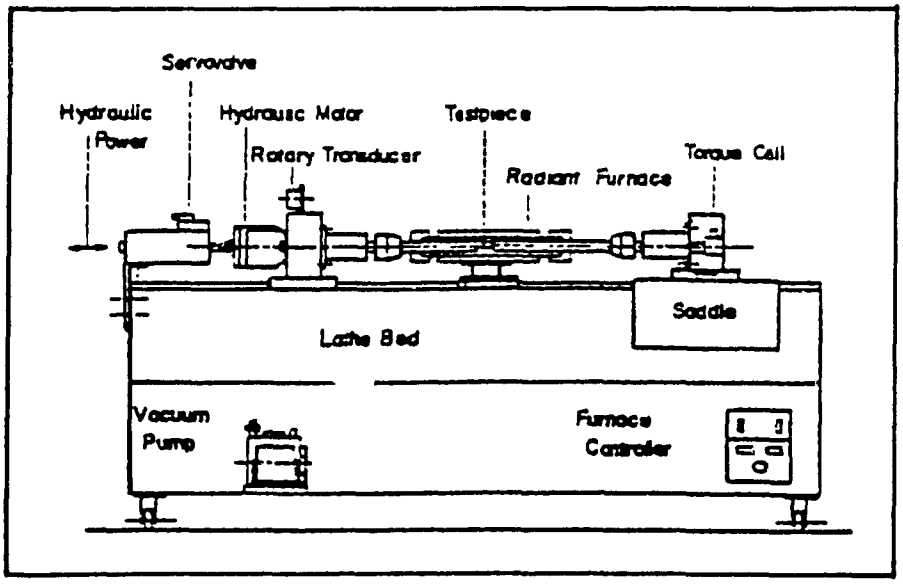

Fig. 2 Closed-loop servo-controlled hot torsion testing machine (10, 12, 19, 25-28, 35, 215, 255).

84, 89, 96, 101, 131, 167, 168, 215, 255) were used. As an approximation, the value of the strain hardening coefficient, n', was taken as zero as it is at σ_p and in the steady state regime. For other points on the curve this represents a small error. The value of the strain rate sensitivity, m, which is the reciprocal of the stress exponent, n'', (10, 34, 36, 49, 52, 55, 56, 74, 84, 89, 101, 131, 215, 255) in the power law, was determined from the slopes of log Γ_e versus log $\dot{\varepsilon}$ depicted in Fig. 3a-d (49, 182, 184). Generally, m decreases as T declines.

3.3.3 MULTISTAGE TESTS FOR STATIC RESTORATION ANALYSIS

In multistage tests, the program provides for pass strain, strain rate, unloading, and interval without change in temperature or removal from the furnace (10, 12, 14, **22, 26, 36** 52, 74, 86, 174, 180, 193, 215). These tests were carried out on all alloys in both the as-cast and worked condition at 0.1 and 1 s^{-1}, 900 and 1000°C and had a constant pass strain of 0.2. In any one series of six passes, the intervals were either 20 or 40s. Any specimen was heated in about 5 minutes by means of a dual-elliptical radiant furnace to the test temperature of either 900 or 1000°C, held for 5 minutes before deforming to a total strain of 1.2. At the end of a test, the specimen was withdrawn from the furnace axially and spray quenched with water within 2 seconds.

In order to analyze the progress of softening with increasing interval, a multistage test was developed which allowed for the determination of static restoration up to the fully recrystallized state. From a review of the literature (168, 174), the times to attain this at 900 and 1000°C (1 s^{-1}) were established and ultimately verified by optical and mechanical metallography (199). The test consisted of a prestrain of 0.4

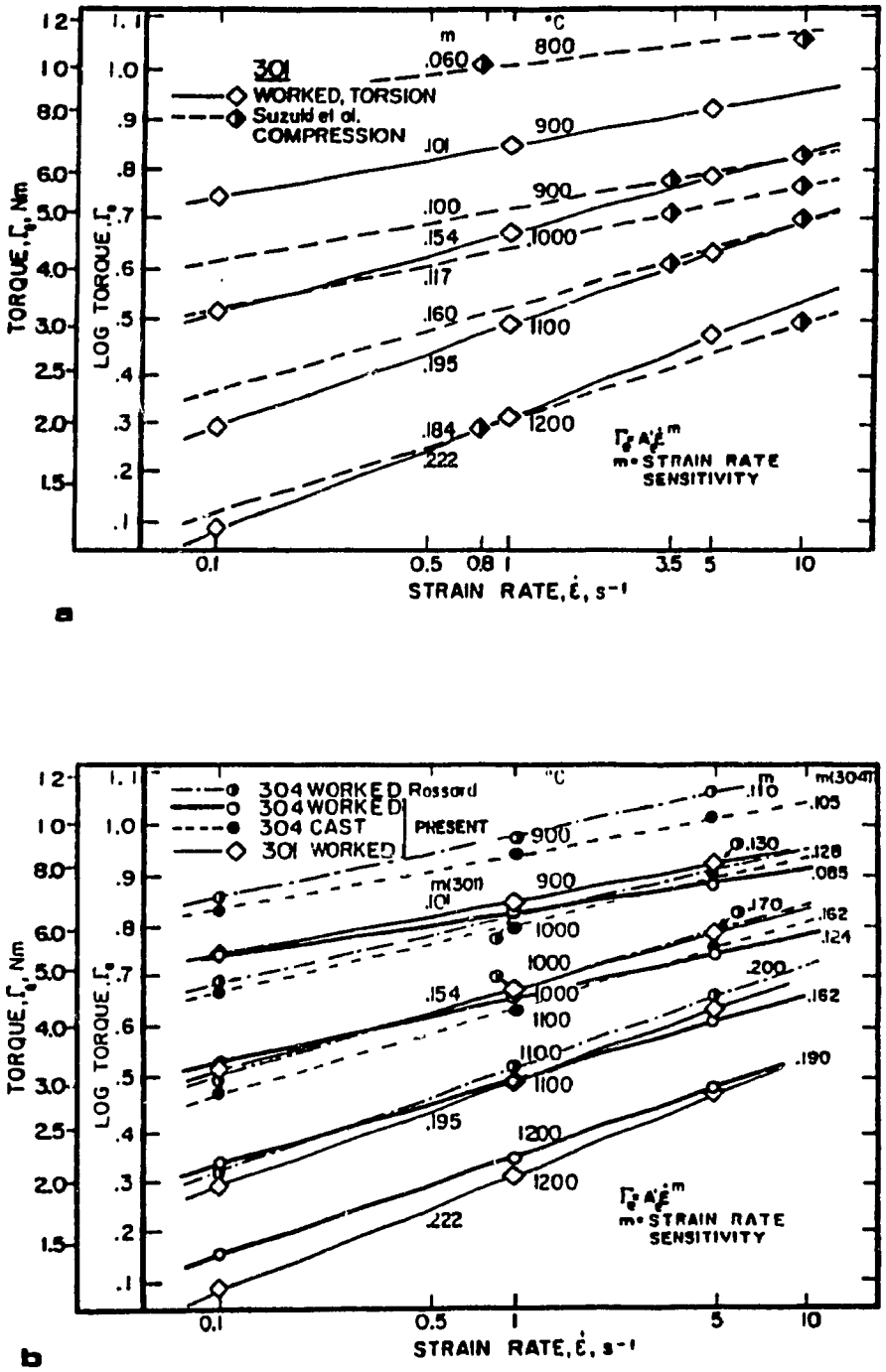

Fig. 3. The strain rate sensitivity m of the torque appears as the slope in this logarithmic plot of Γ_e versus $\dot{\epsilon}$: a) for 301W, b) for 304C and 304W, c) for 316C and 316W, and d) 317C and 317W. Published data are included for comparison (49, 182, 184).

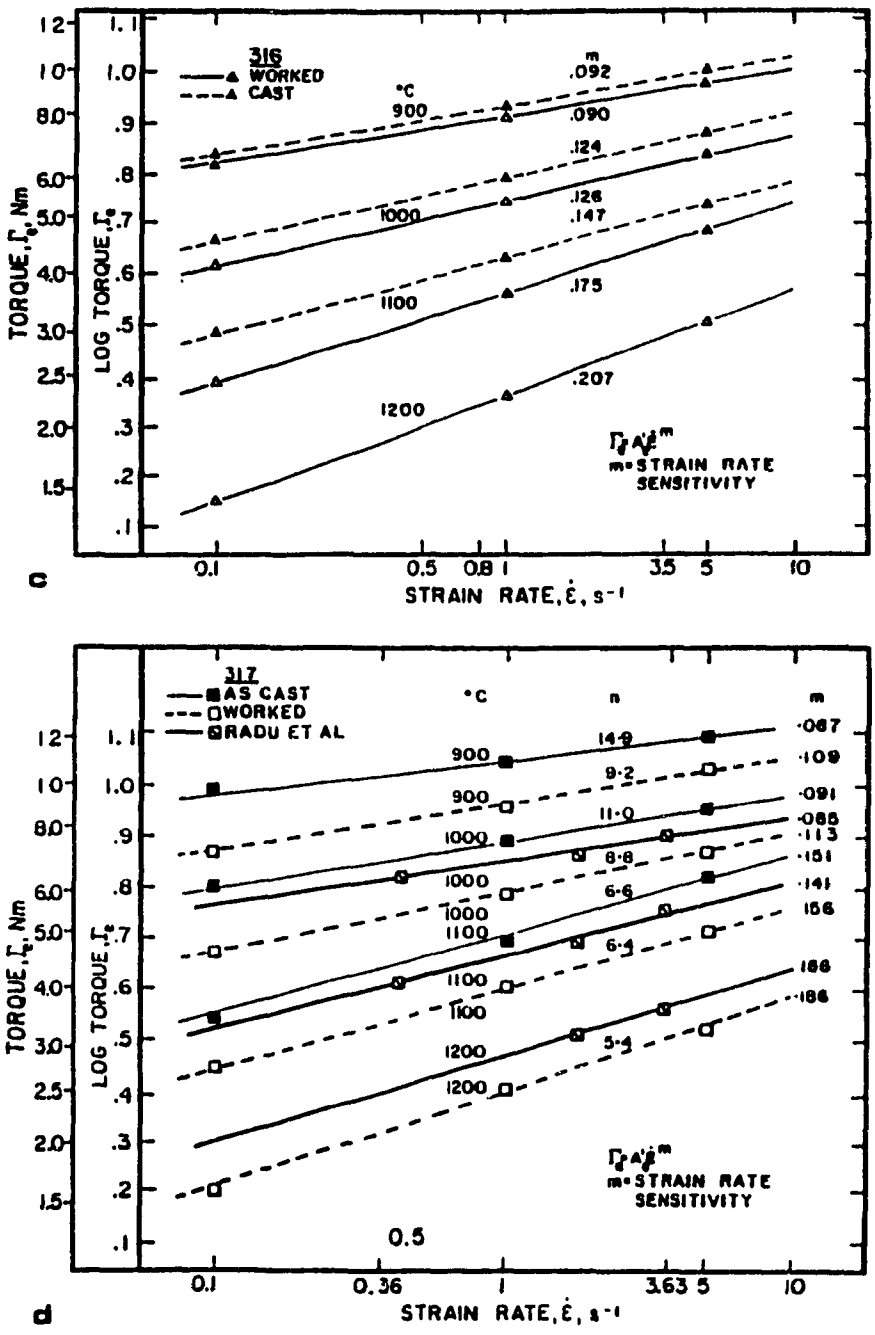

Fig. 3. The strain rate sensitivity m of the torque appears as the slope in this logarithmic plot of Γ_e versus $\dot{\varepsilon}$: c) for 316C and 316W, and d) for 317C and 317W. Published data are included for comparison (182).

and interval for full recrystallization, followed by a pass strain of 0.2 with the subsequent interval programmed to increase in logarithmic increments. The fractional softening for each interval was calculated by Eqn. 26. Using mechanical metallography (199), and conversion from FS to X_{SRX} (Sec. 2.6.4) (24, 30, 139, 174), the sigmoidal S curve was determined in accordance with Eqn. 23 (Sec. 2.5.4).

3.3.4 SIMULATION OF BAR MILL BY MULTISTAGE TESTS

The simulation of a cross country bar mill consisting of seventeen stages in which the pass strain was constant at 0.2 and the interval was either 20 or 40 s was performed on all alloys. The strain rate was controlled in three ways: a) constant at 0.1 s^{-1}, b) constant at 1 s^{-1}, or c) increasing from 0.1 to 2 s^{-1} with T declining from 1203 to 905^{o}C at a constant rate of 0.9^{o}C/s ($\approx$ 50^{o}C/min). The specimen was quenched within 2 s in order to observe microstructural evolution.

3.3.5 PLANETARY ROLLING SIMULATION

While many small planetary rolls deform the slab successively as it is being reduced 93% in one rolling operation (38), the time between each deformation is about two hundredths of a second which is not long enough for any static restoration. Therefore, while this is essentially an interrupted rolling operation, the continuous flow curves and the constitutive equations are used for calculation of forces and instantaneous power requirements (1).

3.4 MICROSTRUCTURAL EXAMINATION

3.4.1 OPTICAL AND ELECTRON MICROSCOPY

Tangential, longitudinal and transverse samples were cut from specimen by means of a slow-running, diamond wafering bladed, cut-off saw,

lubricated with kerosene in order to minimize disturbance of the DRV and DRX microstructures. After mounting, they were prepared by wet grinding with progressively finer silicon carbide papers, 240, 320, 400, and 600 grit. Initial rough polishing was achieved by use of 6 micron diamond paste on a nylon cloth and 1 micron diamond on microcloth. Final polishing was carried out using 0.05μm alumina on microcloth. All samples were chemically etched by immersion at about 20°C for times of 1-3 minutes depending on the deformation conditions with those at the highest T requiring the shortest time. While the etchant for 301 and 304 was 30ml HF, 10ml HNO_3 and 20 ml glycerine, for 316 and 317 it was 10ml HNO_3, 10ml $HC_2H_3O_2$ (acetic acid) and 15ml HCl (256). Grain sizes were determined by the the three circle intercept method in ASTM Standard E112 (257) with the mean intercept being multiplied by 1.68 for determination of the grain diameter (168, 174).

3.4.2 TRANSMISSION ELECTRON MICROSCOPY

In order to observe the DRV effects upon the substructure, slices were cut from tangential sections as for optical observation. These slices for transmission electron microscopy (TEM) were cut, 0.5mm below the surface. After being ground parallel, they were chemically thinned to 50 μm in a solution of 20% perchloric acid in butoxyethanol at -4°C and 18V. Finally, 3mm discs, punched from the slices, were prepared by double-jet thinning with the above solution and operating conditions (258). The TEM microstructural analysis was performed on a CM Philips electron microscope at 125kV. The size of subgrains was measured by the same methods applicable to grains (257).

3.4.3 HARDNESS TESTS

In order to determine the room temperature strength, microhardness

values were acquired from all specimens subjected to continuous deformation and quenching . Due to the surface condition of the gage sections, the Rockwell tester was chosen in preference to the Vickers tester which could not provide accurate readings. Rockwell hardness readings were also obtained from tangential sections, 0.5mm below the surface. The readings from both preparations revealed similar values with negligible variations. The Rockwell superfical number was converted to the Vickers number (259) and plotted for analysis of hardness behavior.

CHAPTER 4

EXPERIMENTAL RESULTS

4.1 FLOW CURVE CHARACTERISTICS

4.1.1 FLOW CURVE SHAPE

Representative flow curves for both as-cast (C) and worked (W) materials deformed in hot torsion are presented in Fig. 4a-d (184, 191). In hot working, the flow curve, after yielding, exhibits simultaneous work hardening and DRV until DRX is initiated at σ_c and ε_c (Secs. 2.2.1-2.2.3). Then, the curve reaches σ_p and ε_p where work hardening and restorative mechanisms equalize. With the latter mechanism becoming predominant, the curve declines to a steady state regime where both DRV and DRX continue to operate in conjunction with deformation until fracture intervenes at σ_f, ε_f. While the 304C, 316C and 317C fractured shortly after the peak at $\varepsilon_f < 2$, the worked alloys, including 301W, fractured at $\varepsilon_f \approx 14$ at high T and low $\dot{\varepsilon}$. While most curves show a single peak, the ones with the lowest value of Z in each case have a periodic form. An extrapolation of any curve beyond σ_c, ε_c to σ_s^*, which is defined below, would be the curve shape due to DRV alone in the absence of DRX. While the ε_c values for 304C, 316C, and 317C alloys were 0.71, 0.66, and 0.72 ε_p, they were lower for the worked at 0.61, 0.64, and 0.65 ε_p, with 301W being 0.67 ε_p. Generally, σ_p and ε_p increase as the deformation T decreases and $\dot{\varepsilon}$ increases.

4.1.2 STRAIN HARDENING θ-σ CURVES ($\theta = d\sigma/d\varepsilon$)

These flow curves have been further analyzed by determining θ as a function of stress up to σ_p, Fig. 5a-h (113, 119, 123, 126, 191, 260) (Secs. 2.2.4- 2.3.1). All generated curves diverge from a common intercept

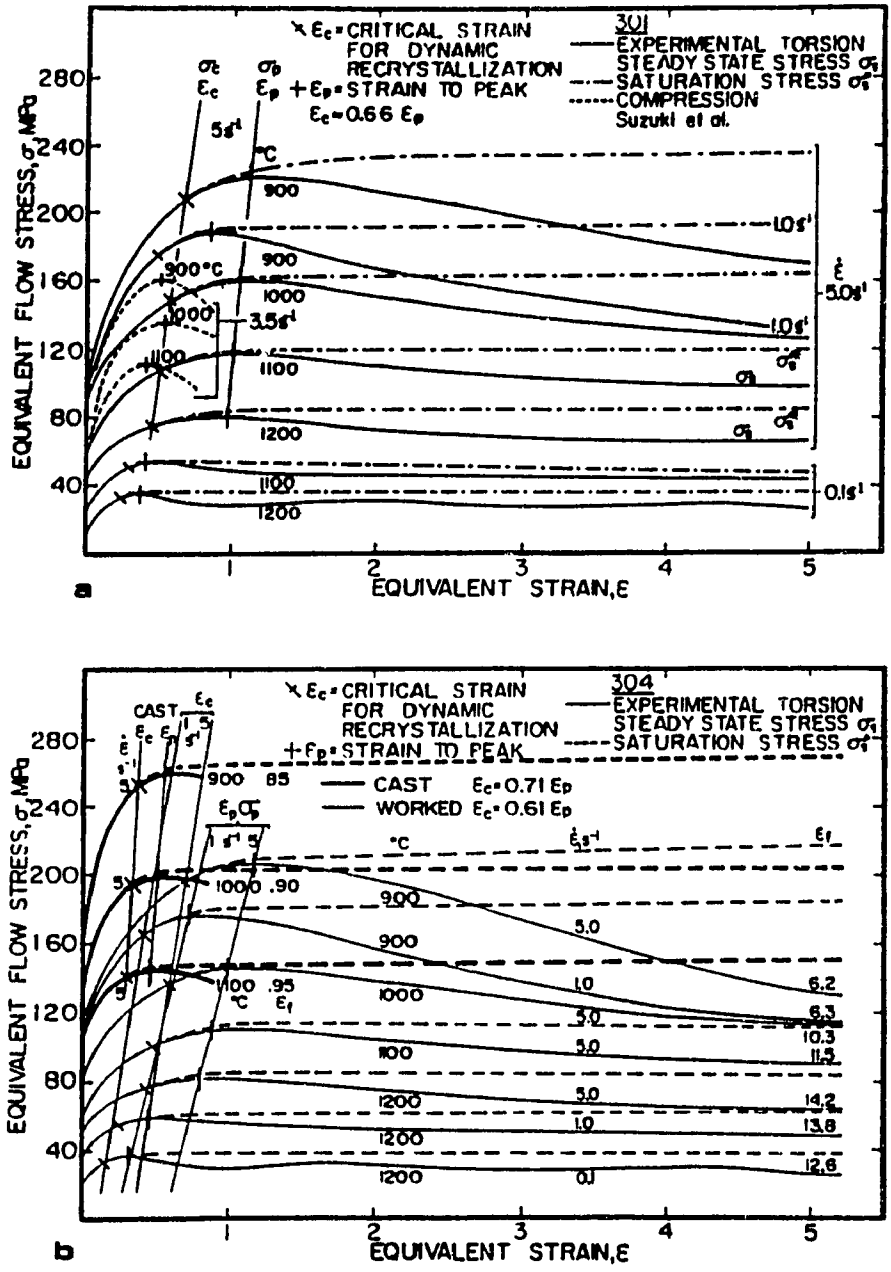

Fig. 4. Representative flow curves for a) 301W, b) 304C and 304W in the 900-1200°C temperature range at strain rates of 0.1 to 5.0 s^{-1}. Saturation stresses and strains for the initiation of DRX are indicated. Published data are included for comparison (184).

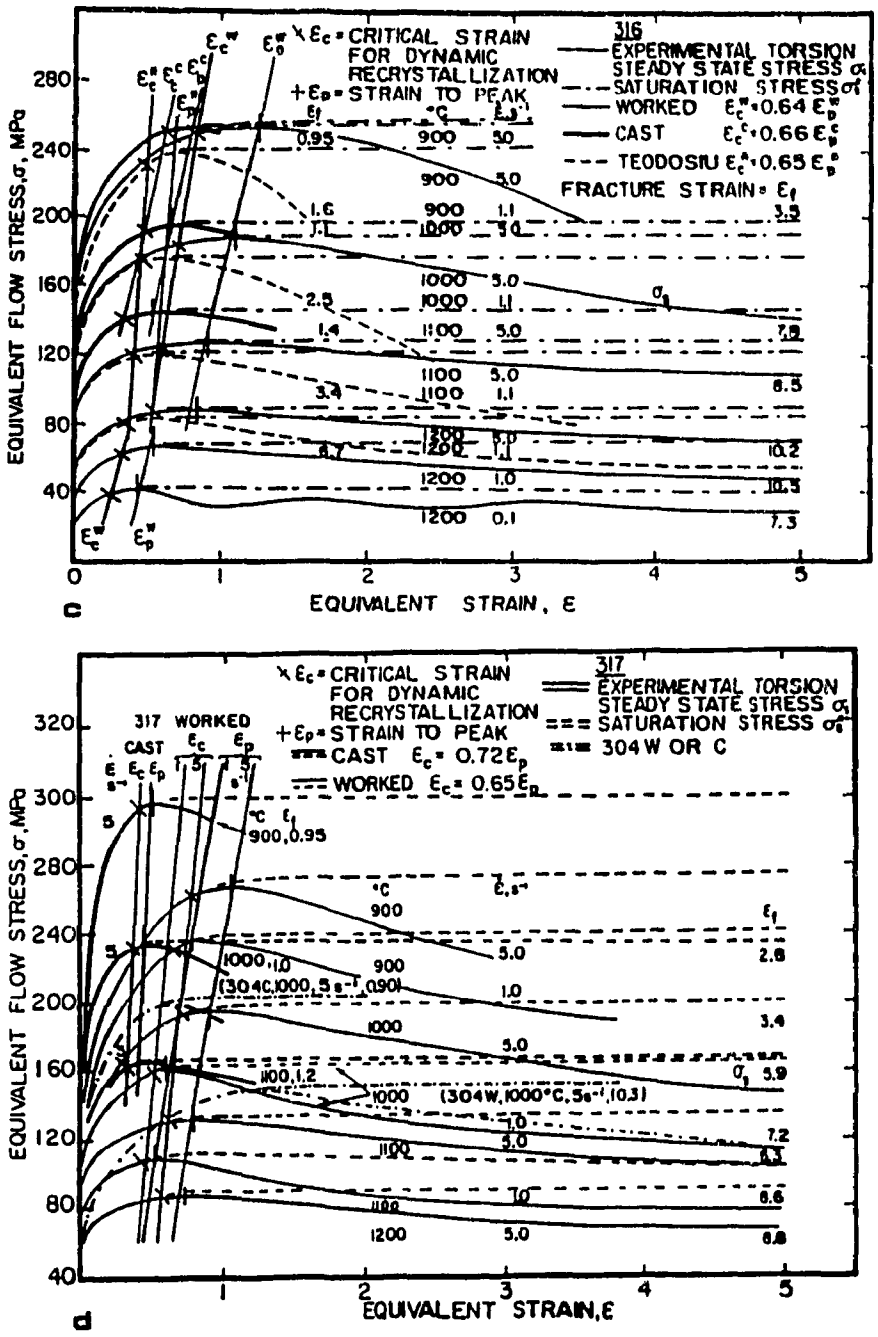

Fig. 4. Representative flow curves for c) 316C and 316W, d) 317C and 317W in the 900-1200°C temperature range at strain rates of 0.1 to 5.0 s^{-1}. Saturation stresses and strains for the initiation of DRX are indicated. Published data are included for comparison (191).

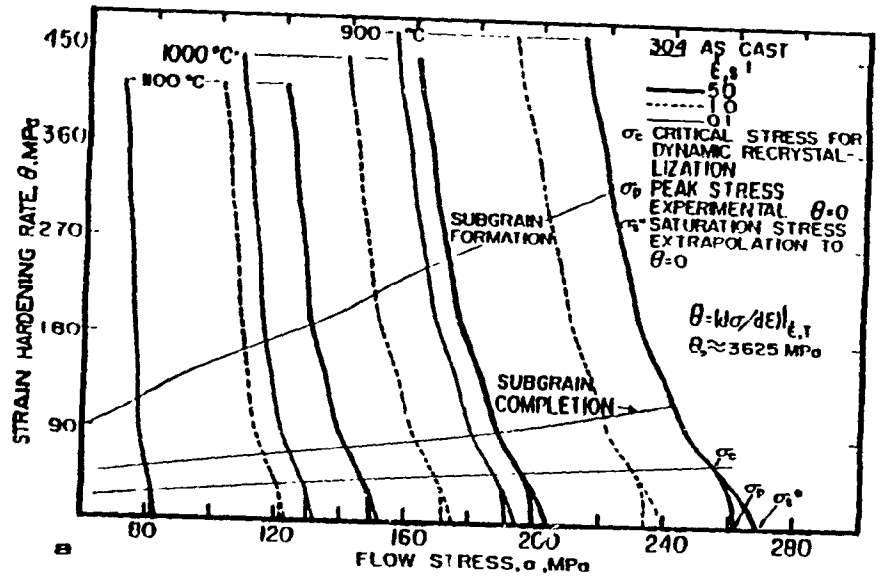

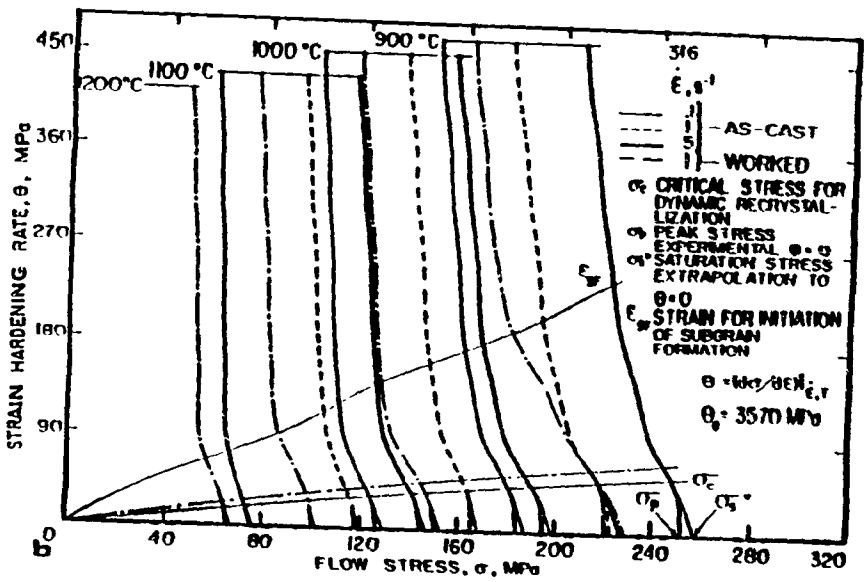

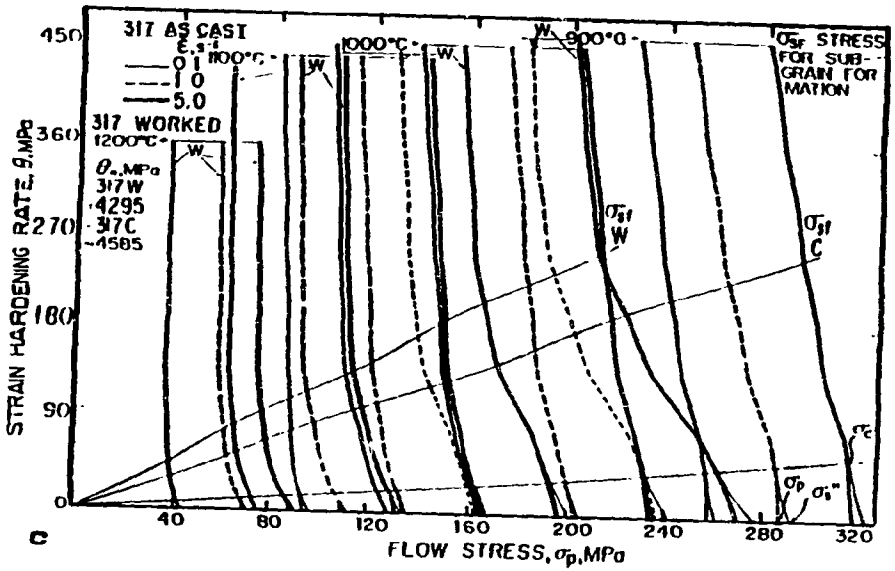

Fig. 5. Curves of the strain hardening rate θ plotted against flow stress are illustrated for a) 304C, b) 316C, and c) 317C. The lines emanating from the origin identify the points for subgrain formation and completion and for the initiation of DRX.

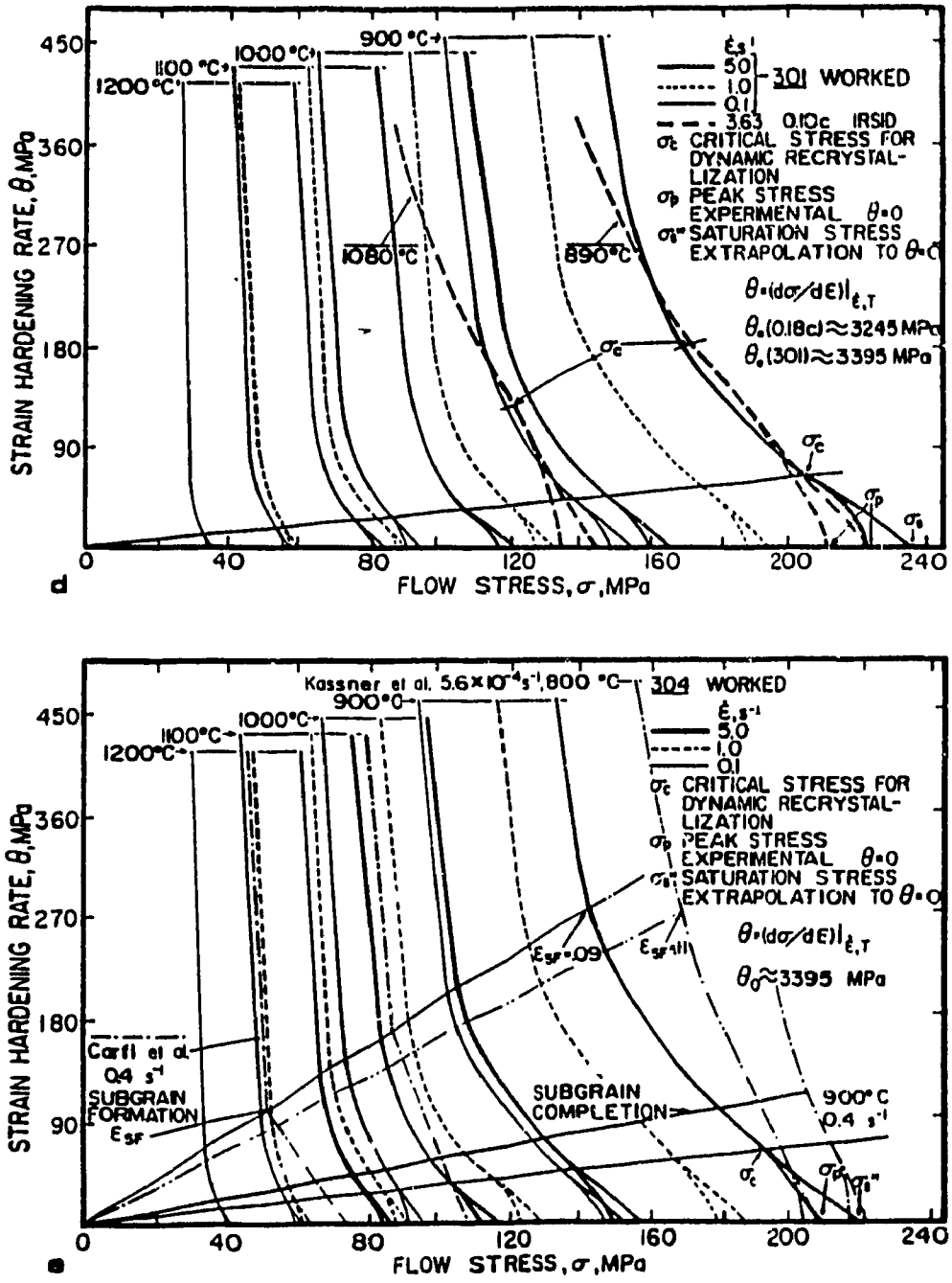

Fig. 5. Curves of the strain hardening rate θ plotted against flow stress are illustrated for d) 301W, and e) 304W. The lines emanating from the origin identify subgrain formation and completion. Published data are included for comparison (119, 123, 260).

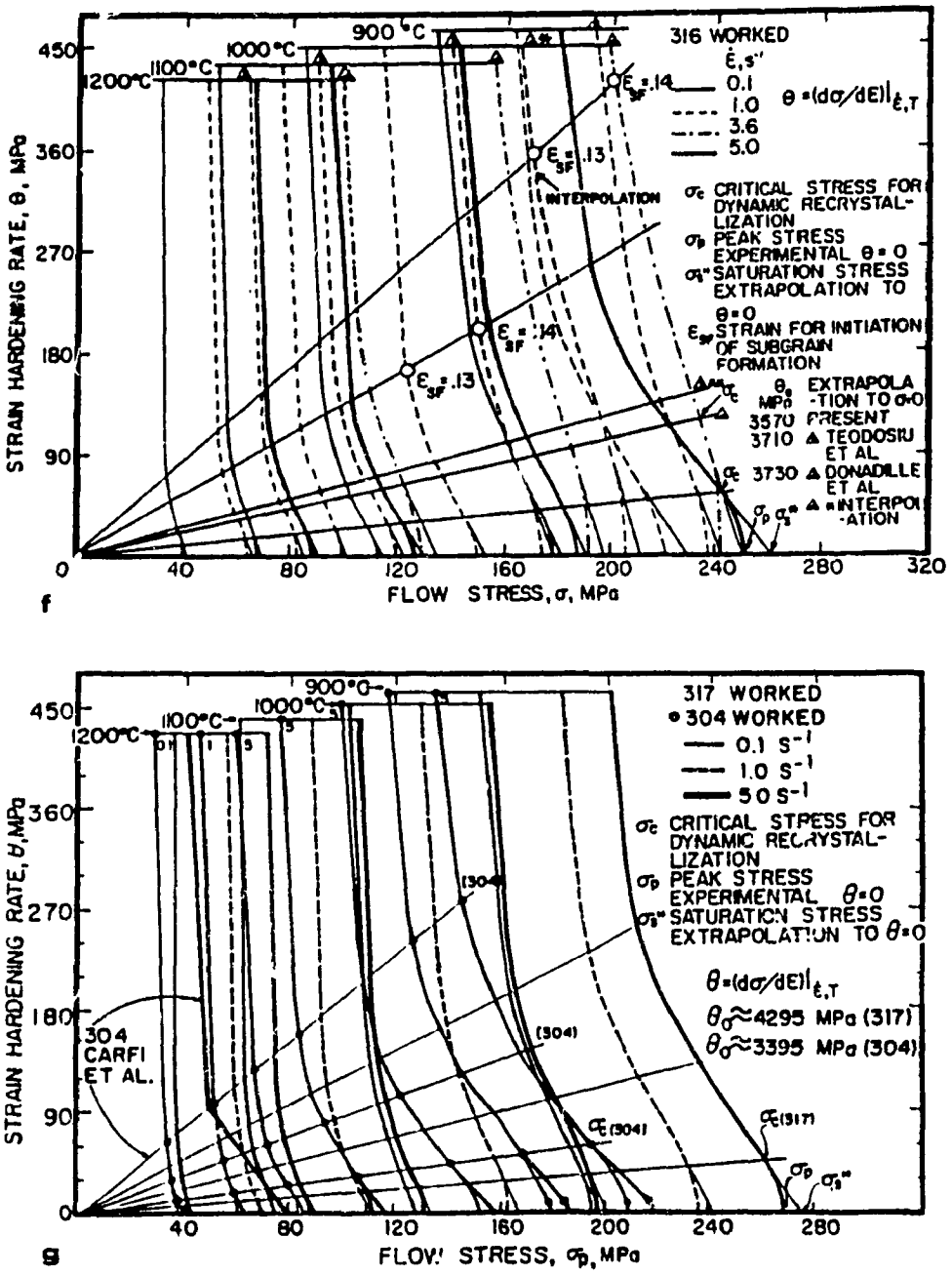

Fig. 5. Curves of the strain hardening rate θ plotted against flow stress are illustrated for f) 316W, and g) 317W. The lines emanating from the origin identify subgrain formation and completion. Published data are included for comparison (126, 191).

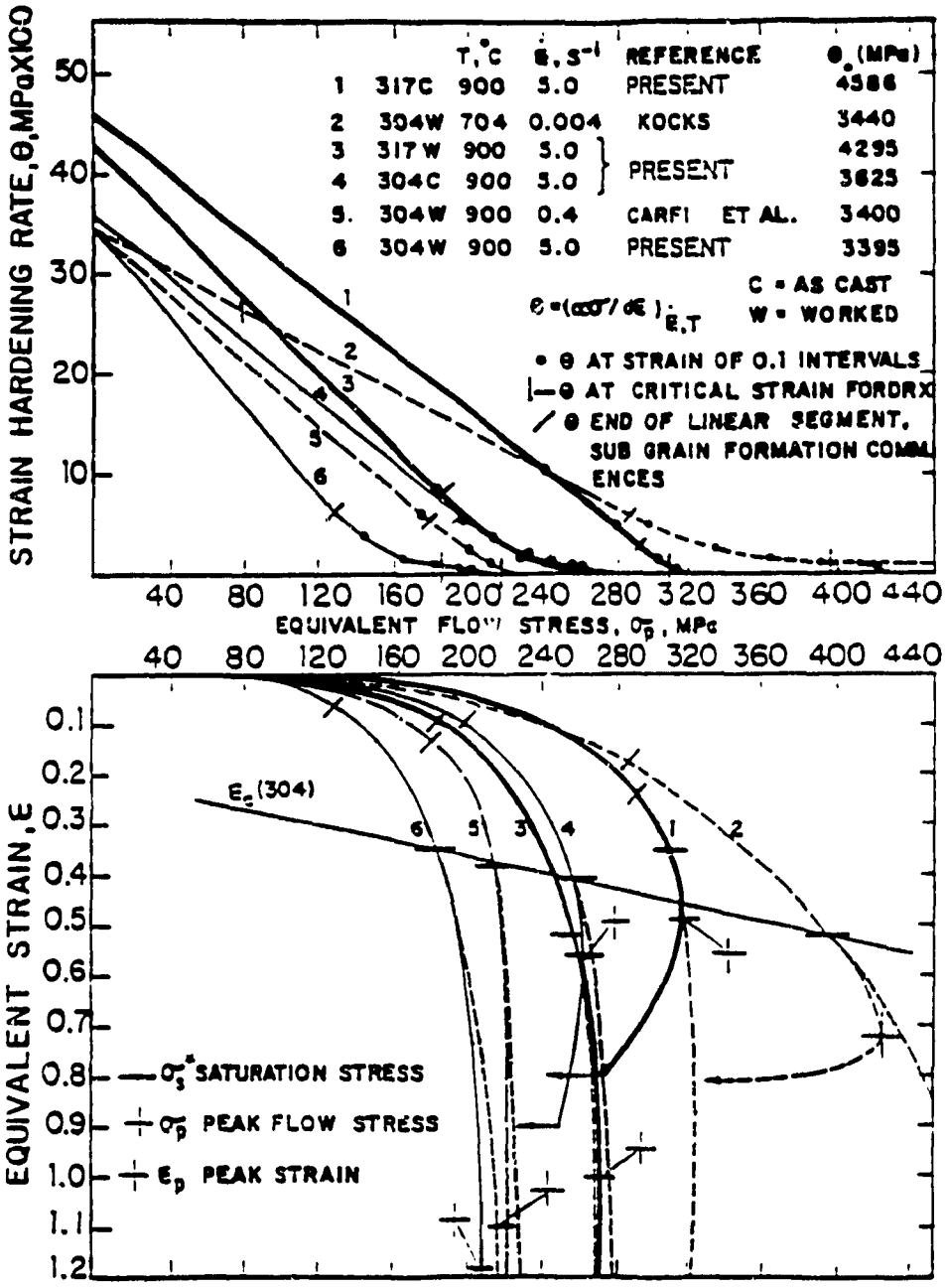

Fig. 5h. Correlation of θ-σ plots for several γ stainless steel alloys from published data with 304 and 317 in both the as-cast and worked condition at different T and $\dot{\varepsilon}$ (113, 119).

at σ=0, designated as θ_0. Each curve consists primarily of two distinct segments. Firstly, θ decreases linearly with the flow stress (Sec. 2.2.4) over a significant σ range of the σ-ε curve from θ_0 to where subgrain formation begins. Secondly, the θ-σ curve gradually changes to a lower slope, linear segment. Finally, the curve drops towards θ = 0 (at σ_p) from where the inflection at σ_c indicates that DRX has become operative (Secs. 2.3.2, 2.3.3). An extrapolation of the second linear portion to θ = 0 determines the value of σ_s^* Since the flow curves for the as-cast alloys rise to higher σ_p at lower ε_p than those for the worked, the values of θ_0 are correspondingly higher, being 3625, 3905, and 4586 MPa for the as-cast 304, 316, and 317, respectively compared to 3395, 3572, and 4295 MPa for the worked. Both 301W and 304W have the same value. A comparison of θ-σ plots for 304 and 317 in both the as-cast and worked condition with that of other work (113, 119) at 900°C shows the locations of σ_c followed by full points indicating intervals of ε = 0.1 in Fig. 5h. The end of the first linear segment where subgrain formation commences is also noted.

4.1.3 KOCKS-MECKING ANALYSIS

In a plot of log σ_s^* as a function of T, Fig. 6a,b (113, 126, 183, 191, 261) (Sec. 2.2.5), the σ_s^* values for each strain rate extrapolate to a common saturation stress σ_{so}^* for each alloy, these being 14.1 x 10^3, 7.5 x 10^3, 16.8 x 10^3, and 28.2 x 10^3 MPa for 301, 304, 316 and 317, respectively.

Figure 7 (119) is a demonstration of the dependence of the saturation stress on T and $\dot{\varepsilon}$ according to the Kocks-Mecking analysis (Sec. 2.4.3):

$$\dot{\varepsilon}_s/\dot{\varepsilon}_o = \exp\left(-\Gamma \ln\left[\sigma_{so}^* / \sigma_s^*\right] / RT\right) = \left(\sigma_s^* / \sigma_{so}^*\right)^{\Gamma/RT} \qquad (21)$$

$$\Delta H(\sigma) = \Gamma \ln\left(\sigma_{so}^* / \sigma_s^*\right) \qquad (22)$$

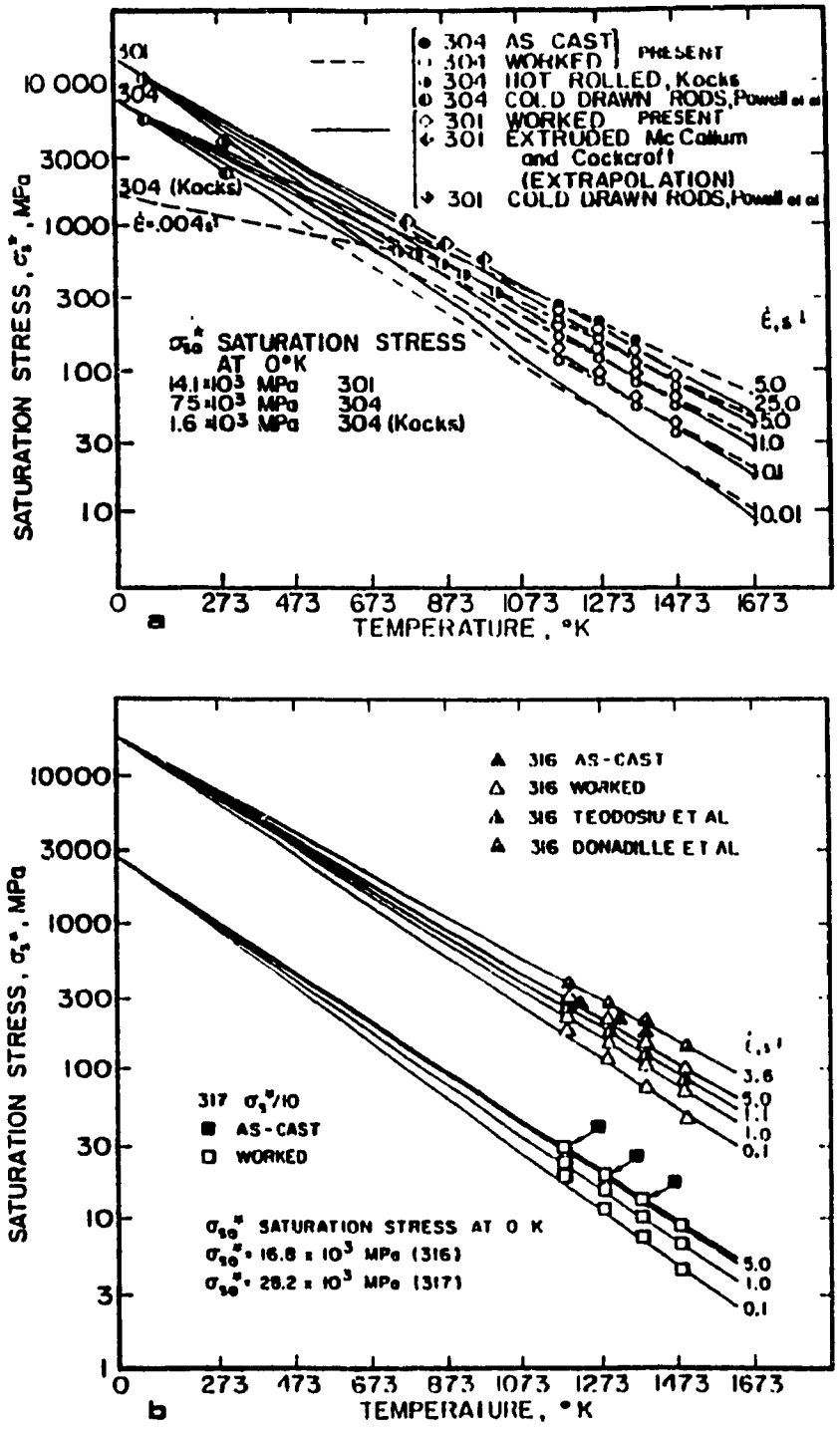

Fig. 6. Comparative log σ_s^* versus T plots of a) 301 and 304 and b) 316 and 317 exhibit straight lines for each $\dot{e}$, converging to a vertical axis at σ_{s0}^* which is somewhat higher for the former than the latter. Published data are included as confirmation of the analysis (113, 126, 183, 191, 261).

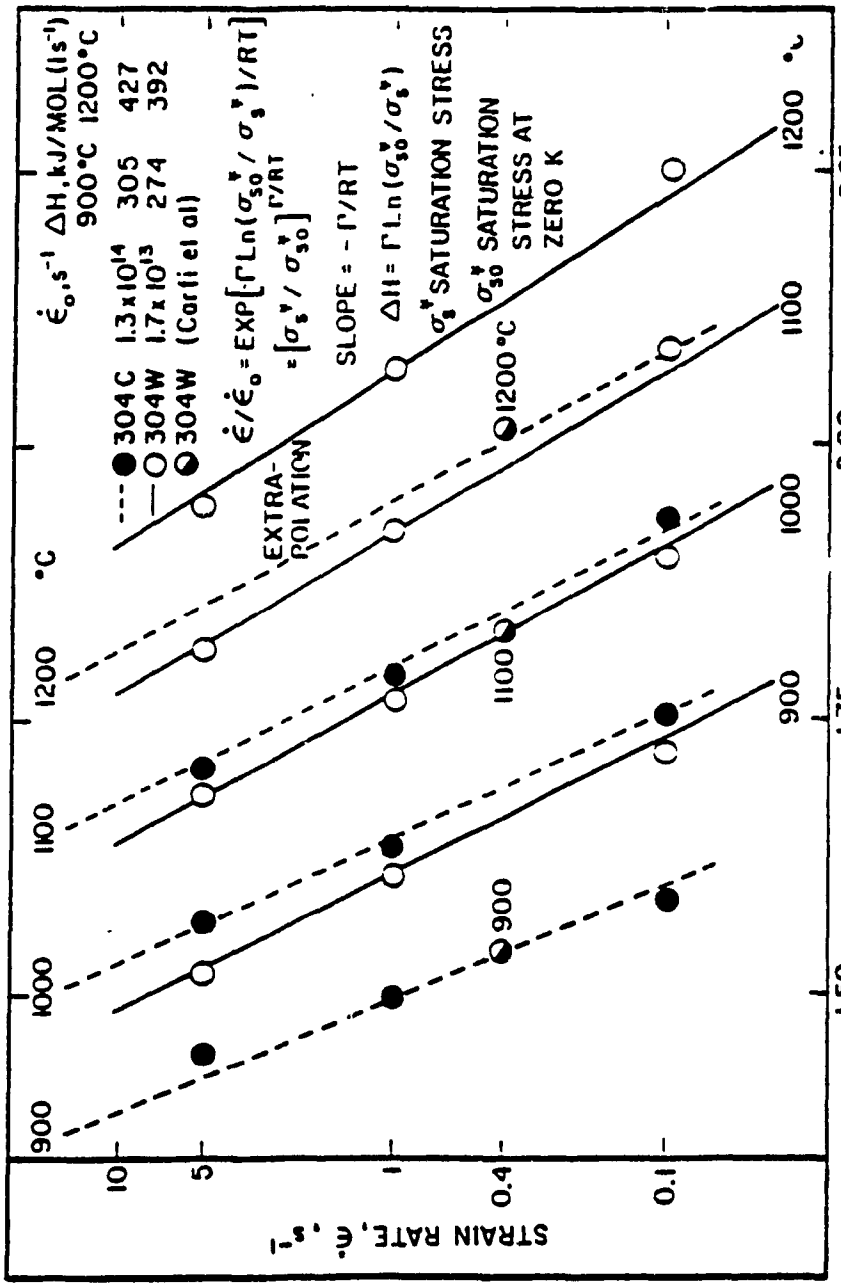

Fig. 7. The plot of log $\dot{\epsilon}$ versus log σ_{so}^*/σ_s^* produces straight lines for both 304C and 304W which converge at different unique points $\dot{\epsilon}_o$ in confirmation of Eqn. 21. Published data are included for comparison (119).

where Γ is a material SFE parameter, σ^{*}_{so} is the saturation stress at 0 K and $\dot{\varepsilon}_0$ and R are constants. The $\dot{\varepsilon}_0$ values for 304W, 316W and 317W are 1.7 x 10^{13}, 2.9 x 10^{15}, and 7.9 x 10^{17} s^{-1}, with 1.3 x 10^{14} s^{-1} as the 304C value. For the worked materials, ΔH values decrease over the same rising Z range from 393 to 274, 451 to 369, 489 to 408 for 304W, 316W, and 317W with 304C decreasing from 427 to 407 as T falls (Fig. 7). In addition, the term Γ/RT equals the inverse of the strain rate sensitivity of Fig. 3 and the n'' exponent of the power law in creep.

The plots of the respective stresses σ^{*}_{s} against log $\dot{\varepsilon}$ (Fig 8a-c) which are linear for each temperature indicate the strain rate sensitivity, m, of each alloy when only DRV is the operative softening mechanism. Similar to the slopes in Fig. 3, those of log σ^{*}_{S} versus log $\dot{\varepsilon}$ decrease with falling T. However, while the set of m values related to Γ_e for the worked materials (Fig. 3a-d), are greater than the sets of m values related to σ^{*}_{s}, they are lower for the as-cast.

The extrapolation of these slopes (Fig. 9a-c) converge to a strain rate $\dot{\varepsilon}_m$ and corresponding σ^{*}_{sm} where apparent athermal conditions are attained. The sets of values for 301, 304, 316, and 317 are 1 x 10^4 s^{-1} and 537 MPa, 1 x 10^5 s^{-1} and 617 MPa, 3.4 x 10^5 s^{-1} and 804 MPa, and 1.4 x 10^4 s^{-1} and 521 MPa, respectively. The logarithm of σ^{*}_{s} increases linearly with falling T but rising logarithm of $\dot{\varepsilon}$.

4.2 EMPIRICAL CONSTITUTIVE EQUATIONS

4.2.1 PEAK STRESS AND PEAK STRAIN BEHAVIOR

For all alloys and conditions, ε_p and σ_p (Secs. 2.2.1-2.2.3) increase with rise in $\dot{\varepsilon}$ and fall in T (Figs. 10 and 11). The sequence of declining ε_p is 301, 316, 304 and 317 for the worked and 316, 304, and 317 for the

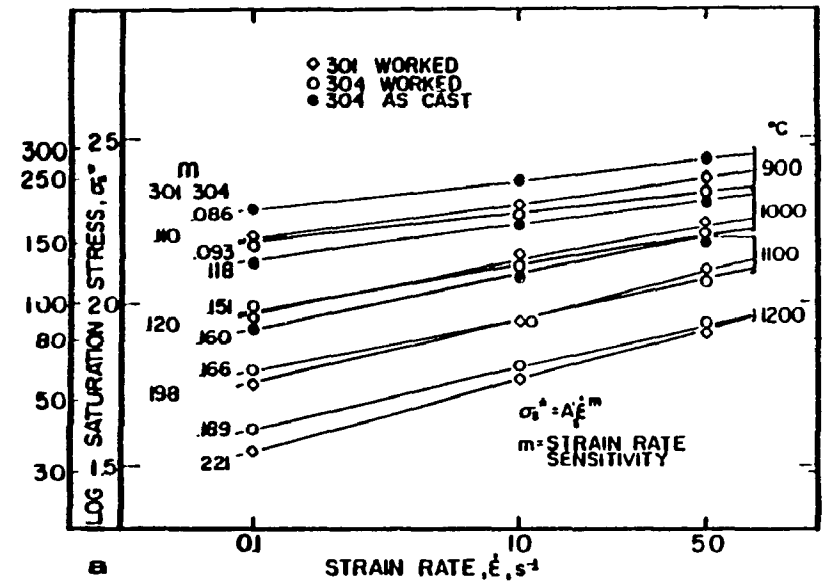

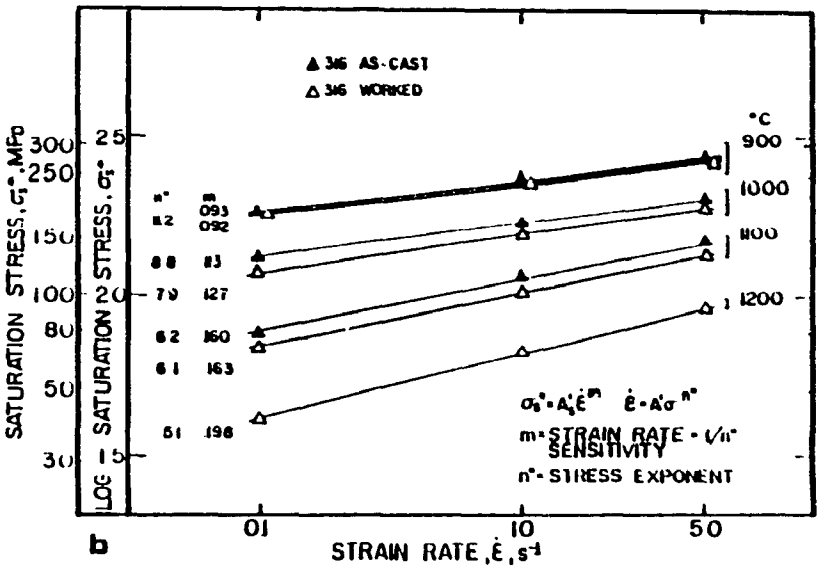

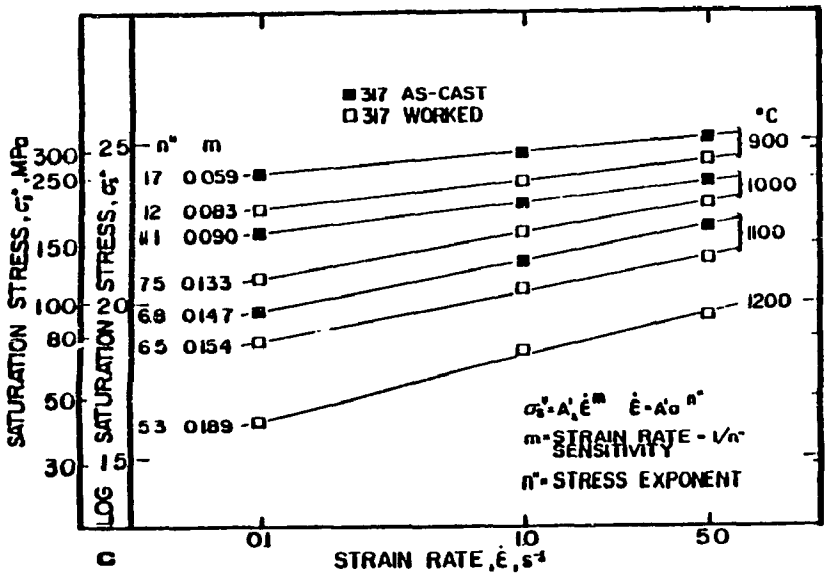

Fig. 8. Comparative plots of log σ_s^* versus log $\dot{\varepsilon}$ for a) 304C, 304W and 301W and b) 316C and 316W, c) 317C and 317W giving straight lines for each T with the slope increasing as T rises. The stress exponent n'' is the reciprocal of this strain rate sensitivity m.

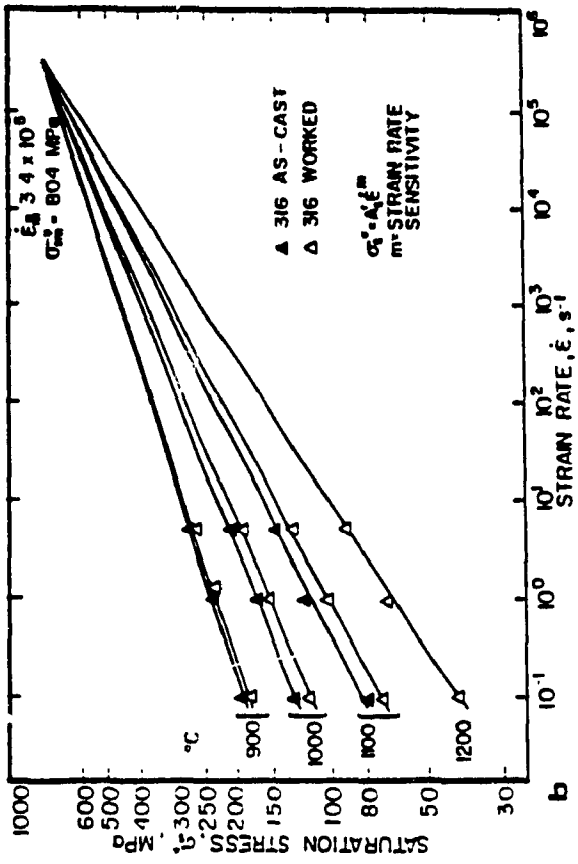

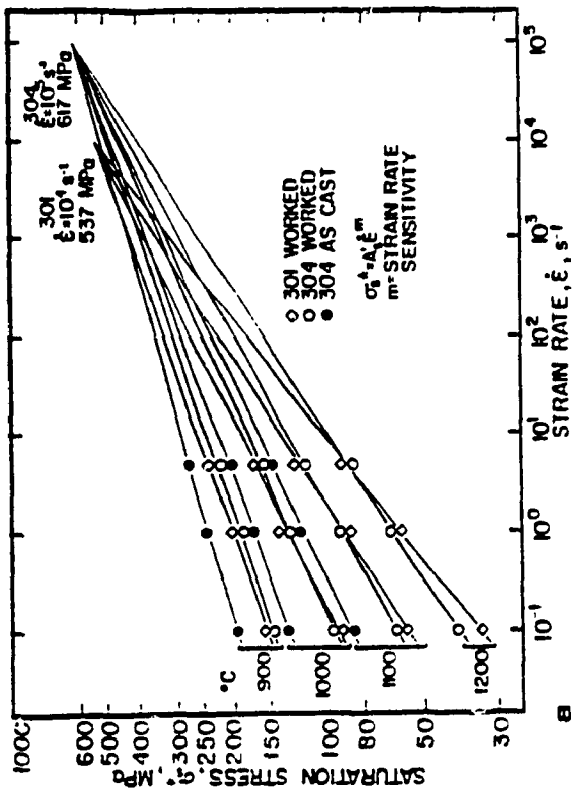

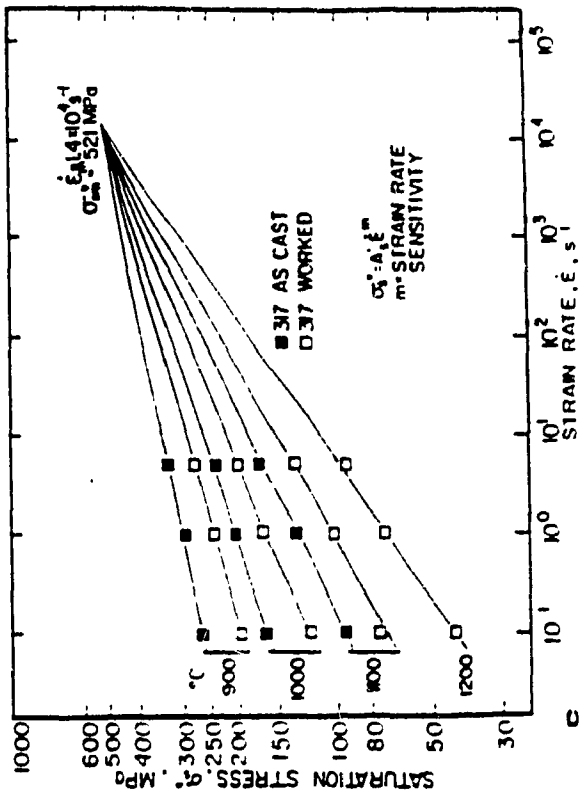

Fig. 9. The plots of log σ_s^* versus log $\dot{\epsilon}$ a) 301 and 304, b) 316C and 316W, c) 317C and 317W result in straight lines for both 301 and 304 for each T which converge at a unique σ_m where stress is independent of T.

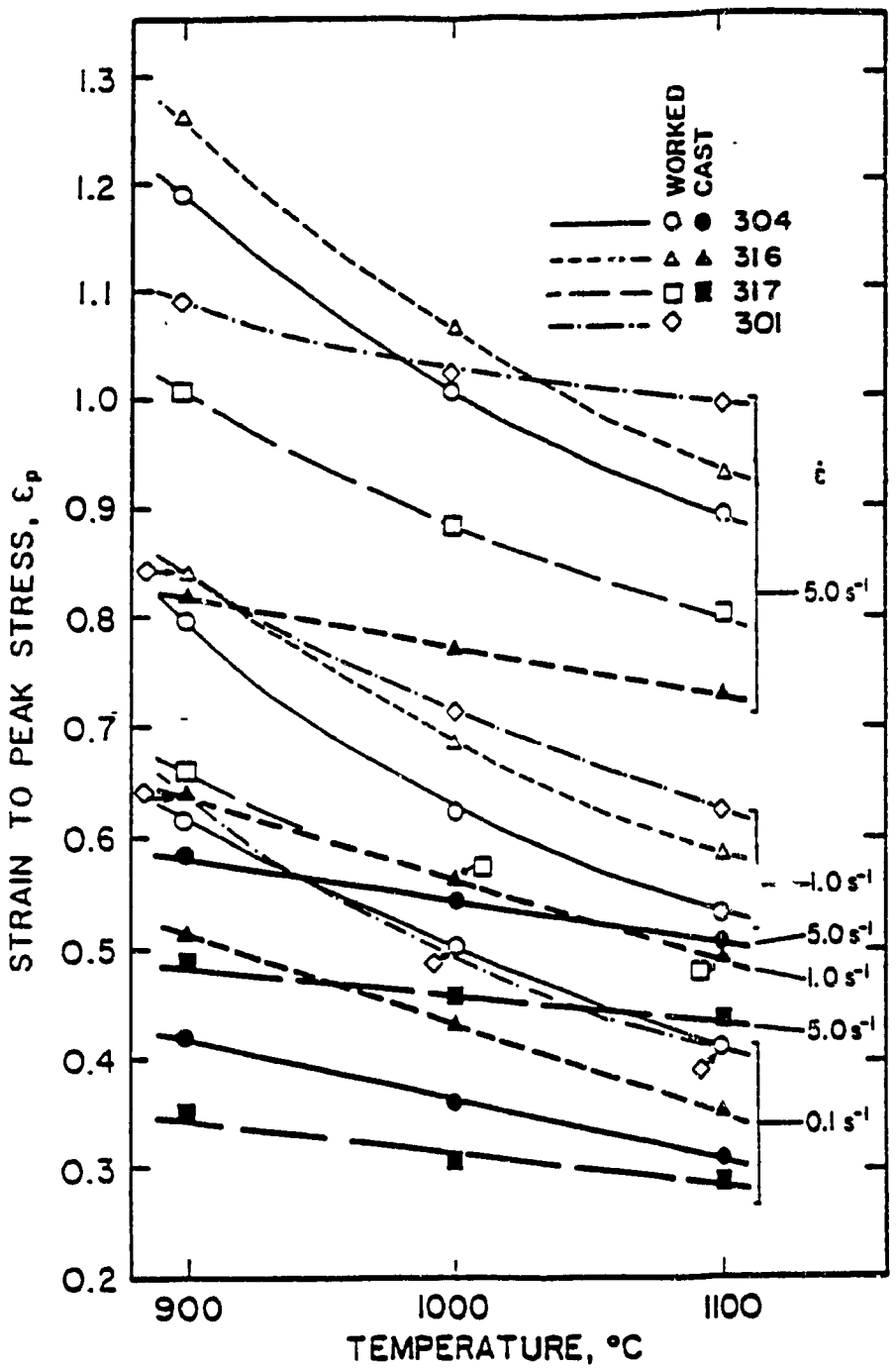

Fig. 10. The strain to peak ε_p as a function of T and $\dot{\varepsilon}$ for 301 W and 304, 316, and 317 in both the as-cast and worked condition. The as-cast steels are low because of enhanced nucleation at δ ferrite particles; 316C is highest because of the lowest δ content.

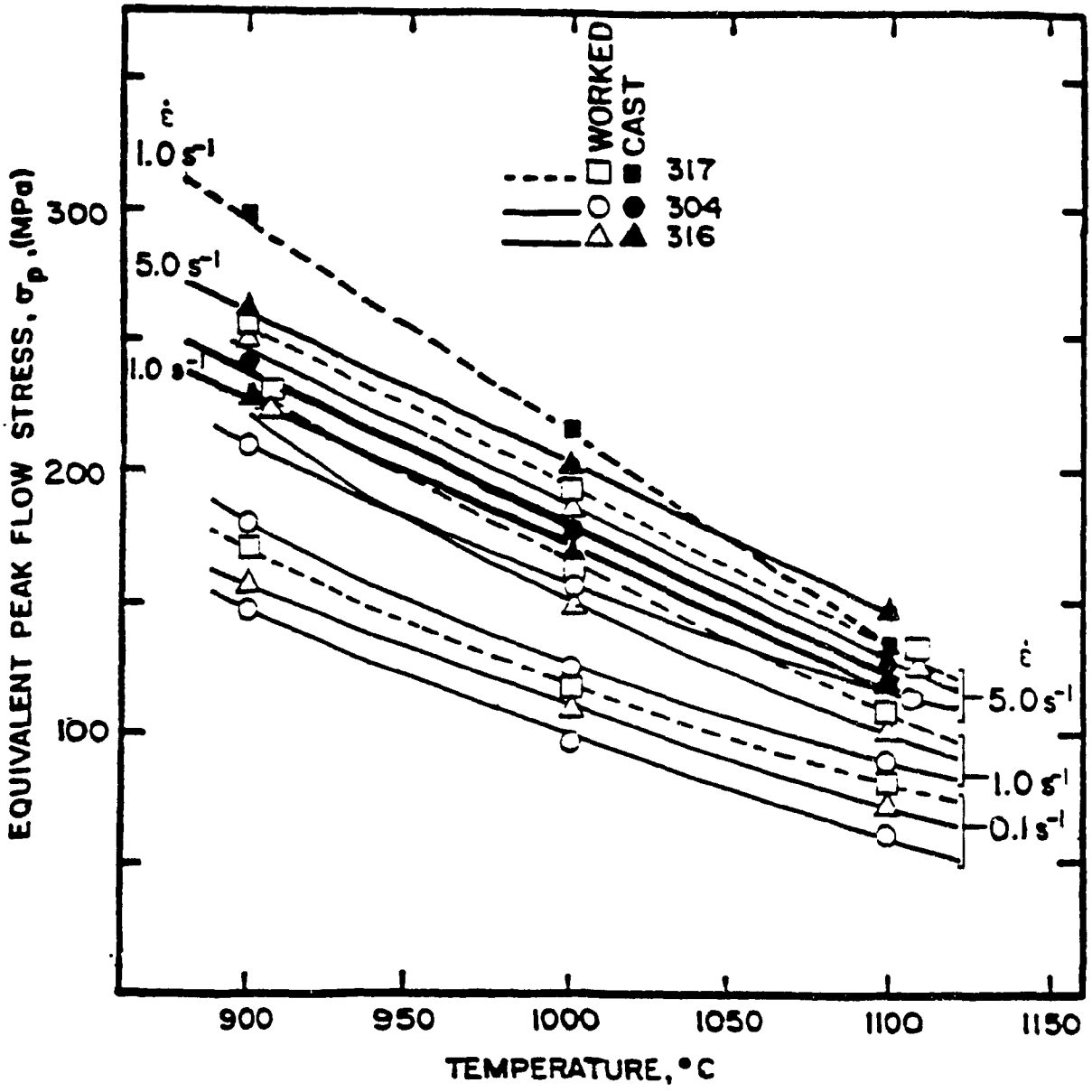

Fig. 11. The peak flow stress σ_p as a function of T and $\dot{\epsilon}$ for 301W and 304, 316, and 317 in the as-cast and worked condition. The worked steels, generally lower than the as-cast hardened by δ ferrite, rise in the order 301, 304, 316, and 317, whereas the 316C is lower than 304C because of less δ.

as-cast alloys with the last being much lower. The sequence of diminishing peak stress in the as-cast alloys is 317, 304 and 316 (by a small amount) due to the influence of δ phase (Fig. 11). In the homogeneous worked alloy, it is 317, 316, and 304, in relation to the solute content, with 301 behaving somewhat differently at low T.

4.2.2 PEAK STRESS CONSTITUTIVE EQUATION

The linear relationship between log $\dot{\varepsilon}$ and log sinh $(\alpha\sigma_p)$, Fig. 12a-d (49, 77, 163, 165, 167, 182-184, 191, 195) confirms the hyperbolic sine function (Secs. 2.4.1, 2.4.2):

$$Z = \dot{\varepsilon} \exp (+ Q_{HW}/RT) = A (\sinh (\alpha\sigma_p))^n \qquad (17)$$

where A, α, n, Q_{HW} are empirical constants and R is the universal gas constant. Fig. 12 demonstrates that $\dot{\varepsilon}$ has the same effect upon the peak flow stress at each T since the lines are parallel with slope equal to n. These values are 4.4 and 4.6 for 301W and 304W and 4.5 for 304C, 316C, 316W, 317W with a lower value of 4.0 for 317C. The increasing distance between the sets of lines illustrates the augmenting effect decreasing T has upon σ_p. All values of σ_p are greater for the as-cast alloys than those for the worked material. In confirmation of the Arrhenius function in Eqn. 17, log sinh $(\alpha\sigma_p)$ is plotted against 1/T in Fig. 13a-d (126, 163, 165, 167, 177, 182, 184, 188, 191) giving straight parallel lines of constant $\dot{\varepsilon}$ which are used to calculate the activation energy for hot working (Q_{HW}). Whereas, the derived values for the as-cast alloys are 407, 402, and 508 kJ/mol, they are 393, 454, and 496 kJ/mol for the worked 304, 316, and 317 respectively, with 301W being 399 kJ/mol.

4.2.3 PEAK STRAIN CONSTITUTIVE EQUATION

Since the value of ε_p is important in the estimation of DRX

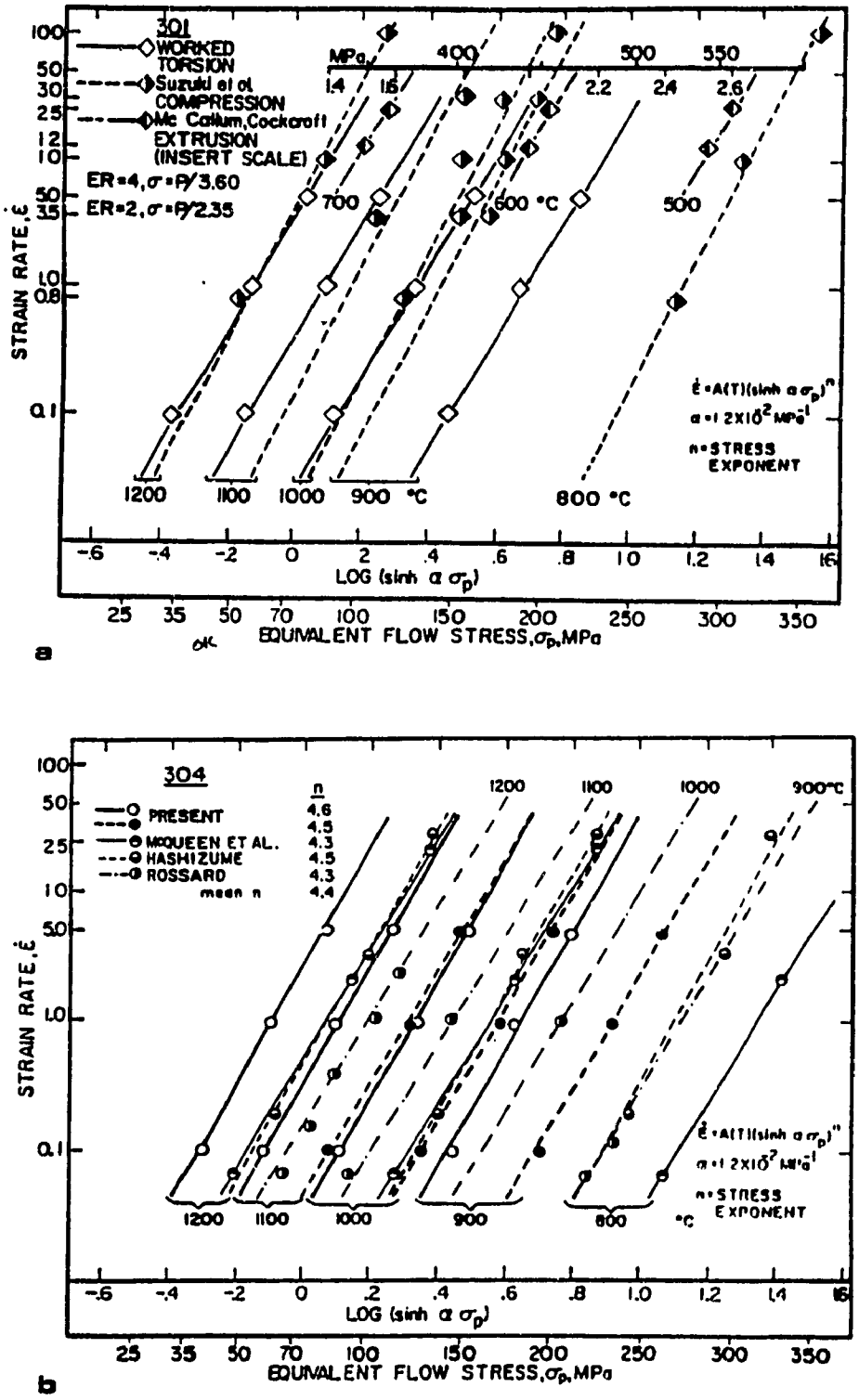

Fig. 12. Plots of log $\dot{e}$ and log sinh $\alpha\sigma$ for a) 301W and b) 304C and 304W provide straight and parallel lines for each T and confirms Eqn. 17. Published data are provided for comparison (49, 165, 167, 183, 184).

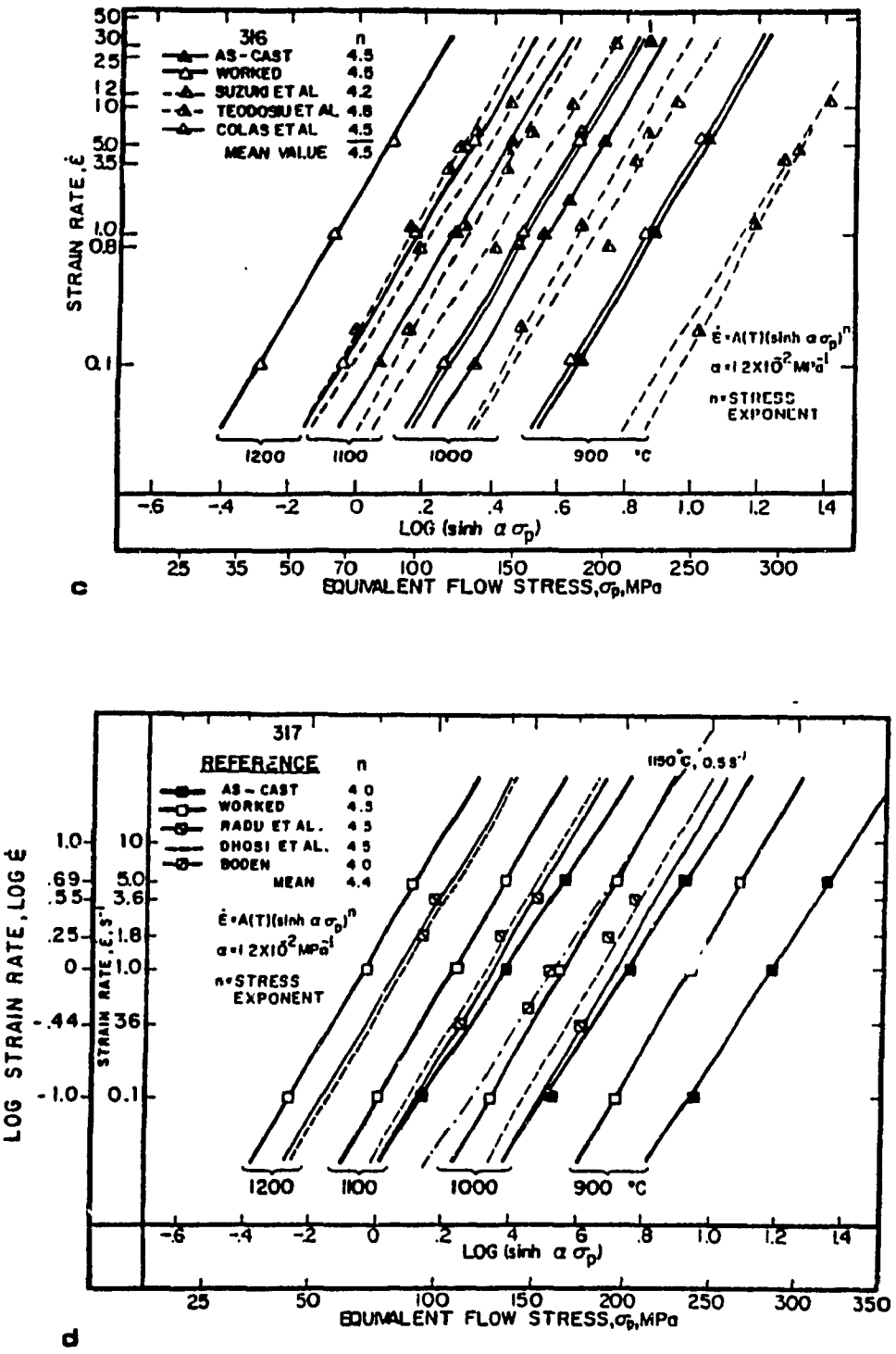

Fig. 12. Plots of log $\dot{\varepsilon}$ and log sinh $\alpha\sigma$ for c) 316C and 316W, d) 317C and 317W provide straight and parallel lines for each T and confirms Eqn. 17. Published data are included for comparison (77, 163, 182, 184, 191, 195).

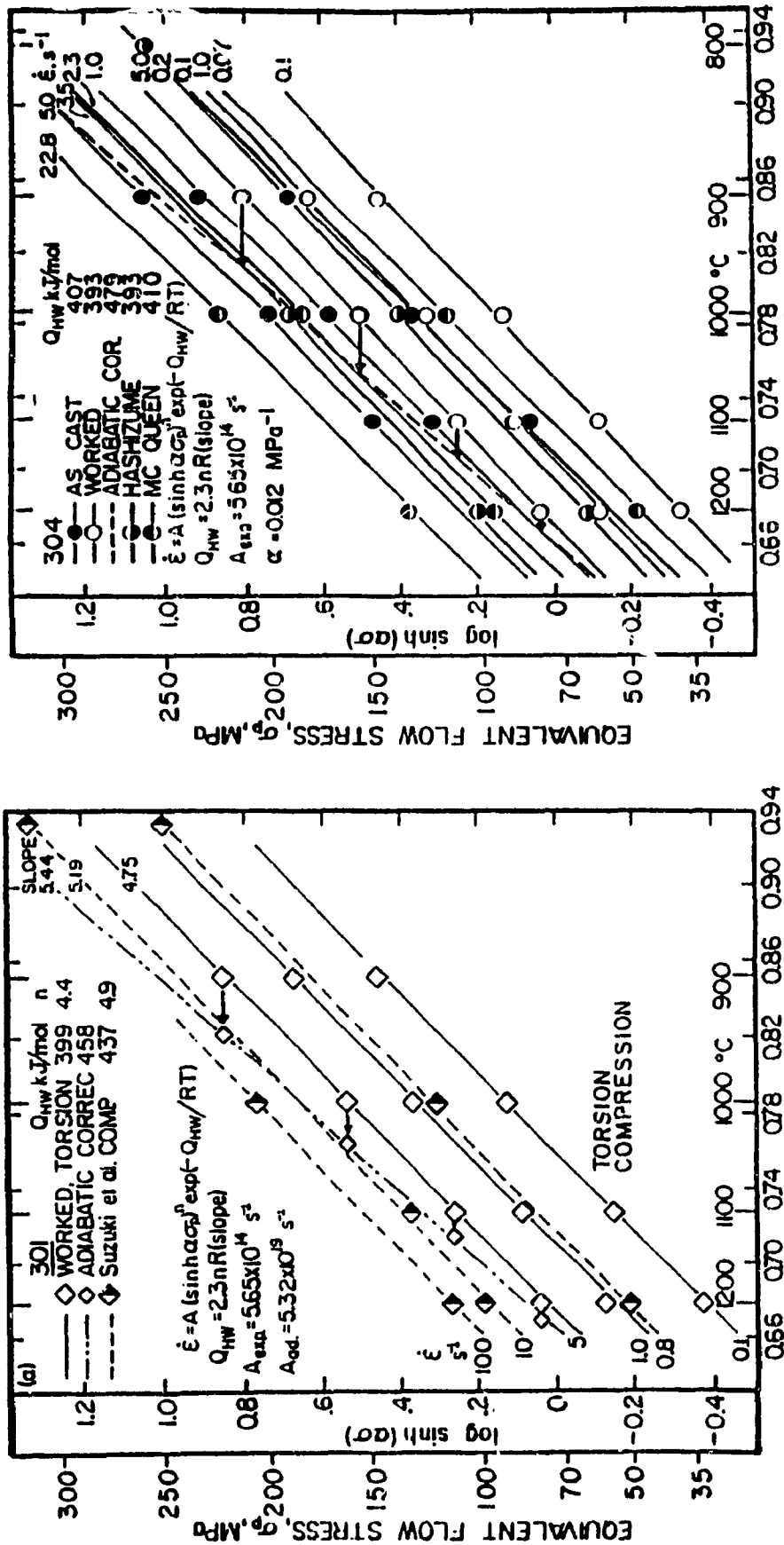

Fig. 13. Plots of log sinh $\alpha\sigma$ versus $1/T$ for a) 301W and b) 304C and 304W provide straight and parallel lines for each $\dot{\epsilon}$ and confirms Eqn. 17. Published data are included for comparison (165, 167, 184).

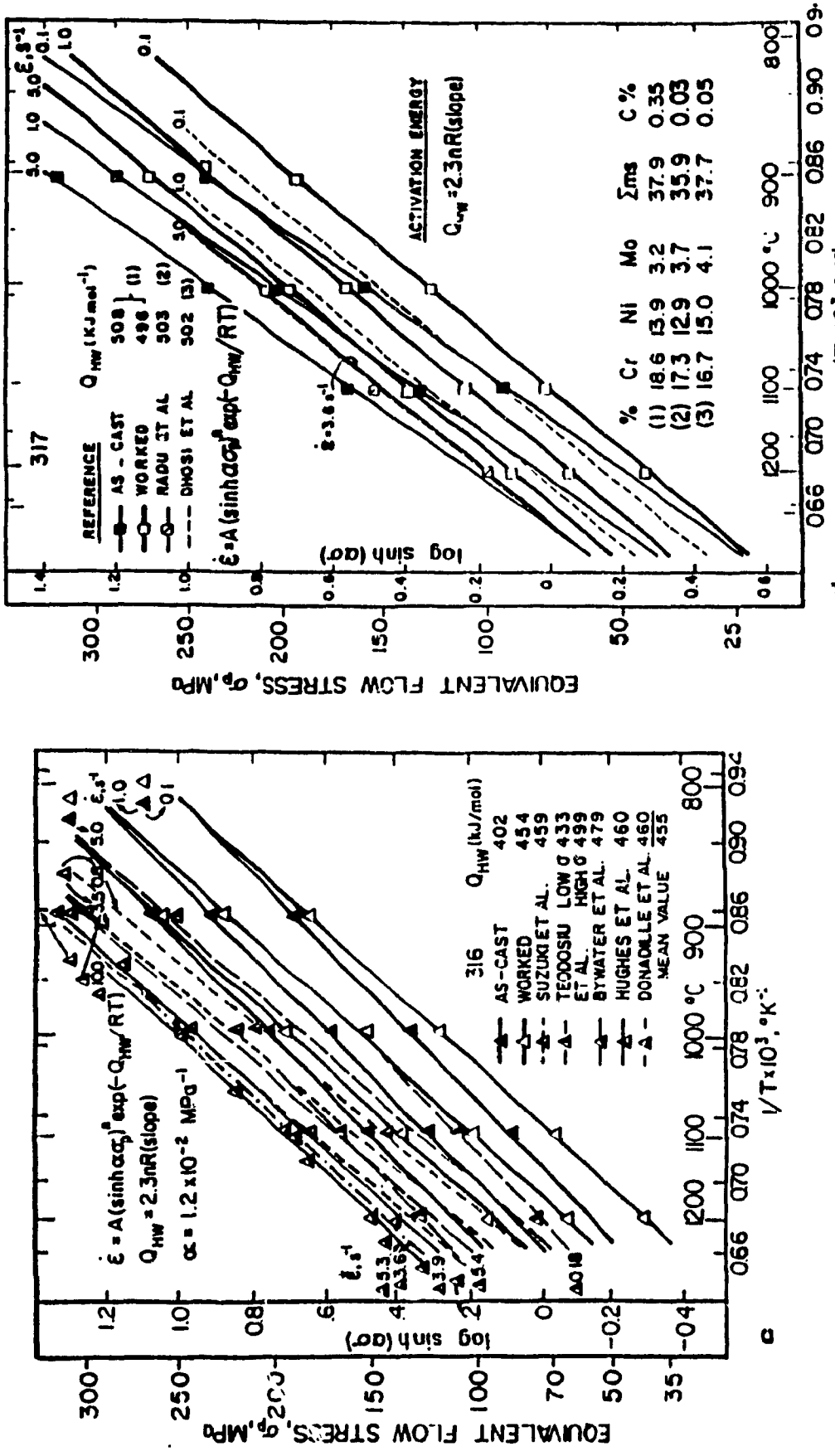

Fig. 13. Plots of log sinh $\alpha\sigma$ versus 1/T for c) 316C and 316W d) 317C and 317W provide straight and parallel lines for each $\dot{\varepsilon}$ and confirms Eqn. 17. Published data are included for comparison (126, 163, 177, 182, 184, 188, 191).

characteristics, a formula for 304W has been developed by which it can be predicted having knowledge of the deformation conditions Z and D_0. The following relationship is plotted in Fig. 14 (76, 152, 157, 167, 174, 178, 262).

$$\varepsilon_p = A_p D_0^{0.75} Z^{0.125} \qquad (44)$$

where A_p has the value $0.45mm^{-0.75}$ $s^{-0.125}$ and Q_{HW} = 400 kJ/mol. This formula accurately estimates ε_p for original grain sizes in worked material varying between 40 and 100μm. A line of slope 0.10, representative of mild steel behavior, is included to highlight the effects of the greater metallic solute in 304W with a higher slope of 0.125. Since 304W and mild steel have significantly different Z values, the curves are normalized at 900°C, 1 s^{-1}, where carbides begin to affect the behavior of 304W.

4.2.4 TEMPERATURE COMPENSATED STRAIN RATE, Z

The formation of single straight lines for the flow stresses at various conditions (Fig. 15a,b) indicates that the independent variables $\dot{\varepsilon}$ and T influence the deformation mechanisms equivalently as expressed by the Zener Hollomon Parameter Z. In Fig. 15b, the saturation stresses for as-cast and worked are plotted and found to be on straight lines. Since the alloys have different Q_{HW} values and hence differing Z values, the curves are normalized at the deformation conditions of 900°C, 1 s^{-1} to permit comparison where most significant differences in deformation characteristics occur. The strengths increase in the order 301W, 304W, 316W, and 317W, i.e. of solute content, except for the high value of 301 below 1000°C as carbides precipitate due to the high 0.11C content. Furthermore, as shown in Fig. 15b, the locus of σ_s^* values which are subject to work hardening and DRV alone have the same slope n as those values of σ_p

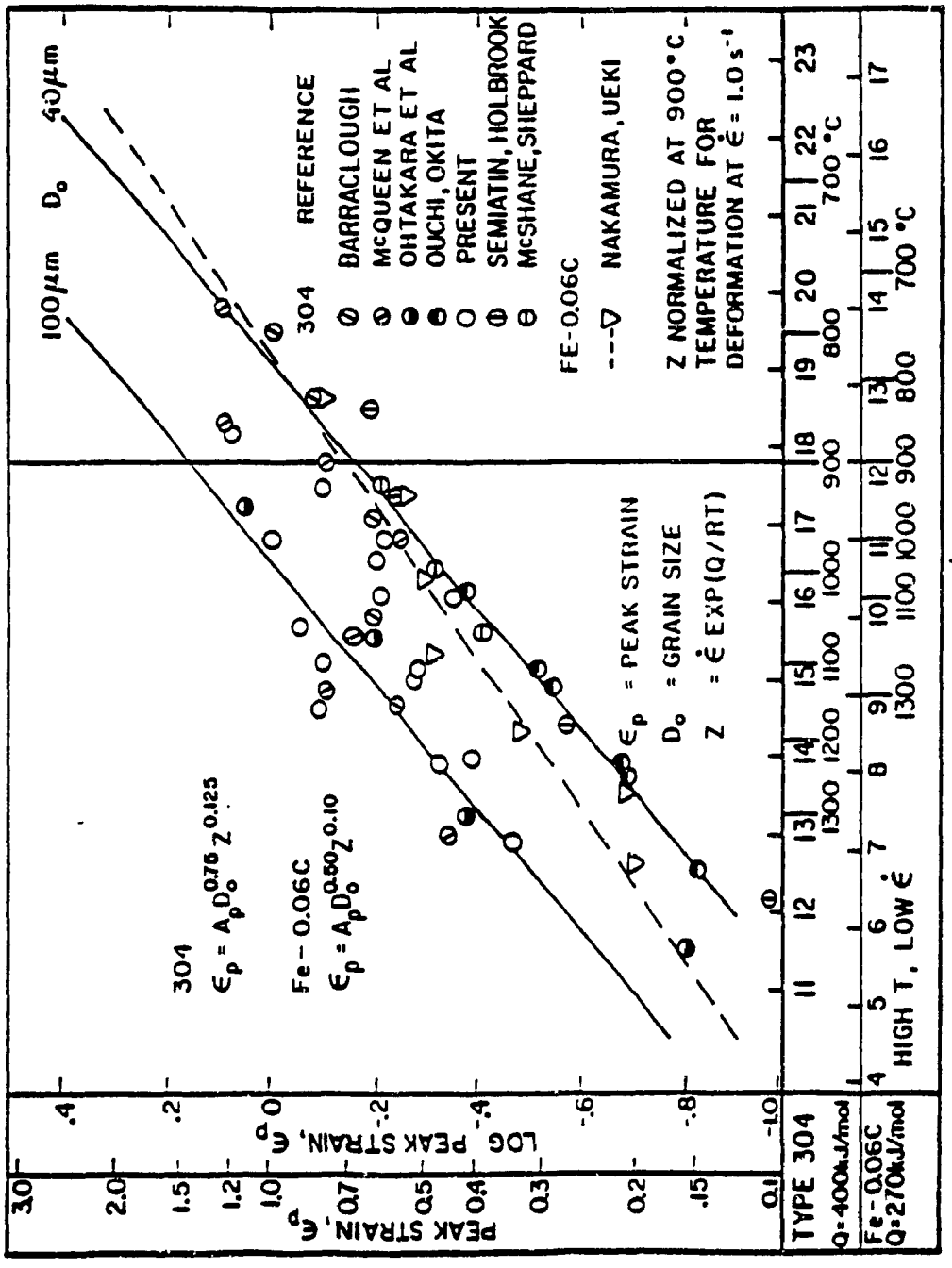

Fig. 14. With extensive results from the literature (76, 152, 157, 167, 174, 178), a logarithmic plot of ε_p versus Z (Q_{itw} = 400 kJ/mol) reveals an expression for calculation of ε_p for any given D_o and Z. Data for an Fe 0.06C alloy is presented for comparison (262).

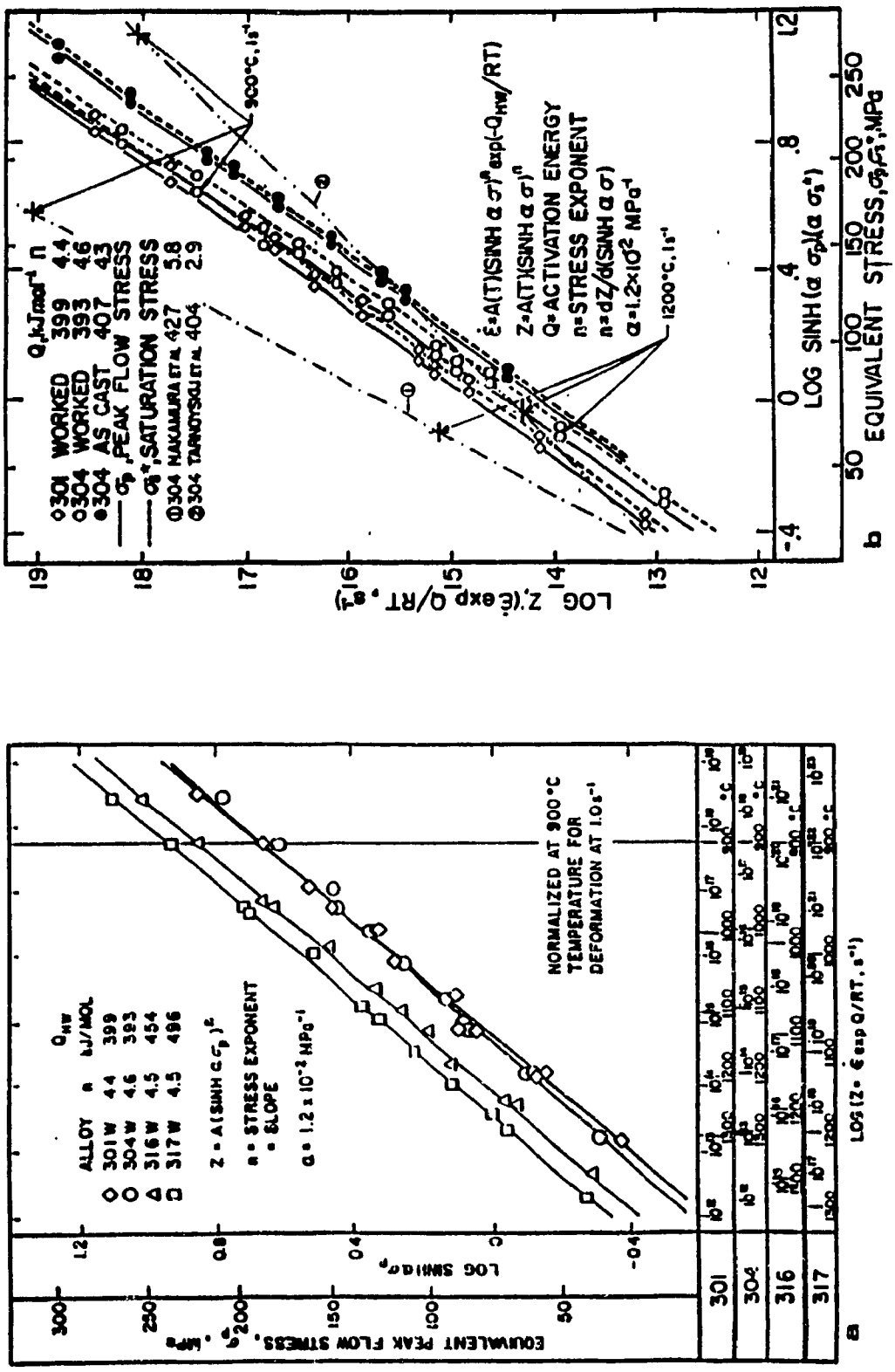

Fig. 15. A plot of log σ_p against log Z for a) 301W, 304W, 316W, and 317W, and b) 301W, 304C, and 304W, showing the variation of σ_p and σ_s^* with Z. Added from the literature are σ_p lines for 304W alloys with differing metallic solute contents (176, 179). All data for a given alloy are drawn into a single line and confirms Eqn. 17.

which are mildly affected by DRX as well as DRV. Since σ_s^* attains higher values due to the absence of DRX , the constant A (Eqn. 17) has a value higher than A for σ_p. In addition, the σ_p, σ_s^* values for the as-cast are higher than those for the worked material. Furthermore, the percentage difference between σ_s^* and σ_p for the as-cast is considerably less than that for the worked due to the higher level of stress at inception of DRX and the narrower peak as a result of its more rapid nucleation in the as-cast. Finally, the comparative results are added to Fig. 15b (176, 179) to illustrate the effects that different activation energies and stress exponents have upon the flow stress.

As shown in Fig. 16a,b both the exponential function A'' exp ($\beta\sigma_p$) and the power law A' $\sigma_p^{n''}$ are both subject to breakdown at $\sigma_p \approx 100$ MPa. This stress at which the transition takes place is approximately the inverse of the constant α. While the former is suitable for high stresses, the latter is suitable for low stresses as found in creep. This confirms the choice of the hyperbolic sine function which satisfies both high and low flow stresses found in the as-cast and worked material.

4.2.5 ACTIVATION ENERGIES AND CHARACTERISTIC TEMPERATURE

The Q_{HW} values calculated from Figs. 12 and 13 and the results of other researchers (49, 57, 63, 76, 77, 119, 126, 152, 158-195) are tabulated in Tables 1-4. The values of log Q_{HW} have been plotted against log S, solute content, Fig. 17. The data fall in a fairly narrow band of ±25 kJ/mol which is approximately ±6%. Q_{HW} increases by about 13.5 kJ/mol per 1% solute. The characteristic temperature T' (Sec. 2.4.2) is given by:

$$T' = Q_{HW} / R \ln A \qquad (19)$$

and is determined to be a constant for each alloy as illustrated in Fig. 18

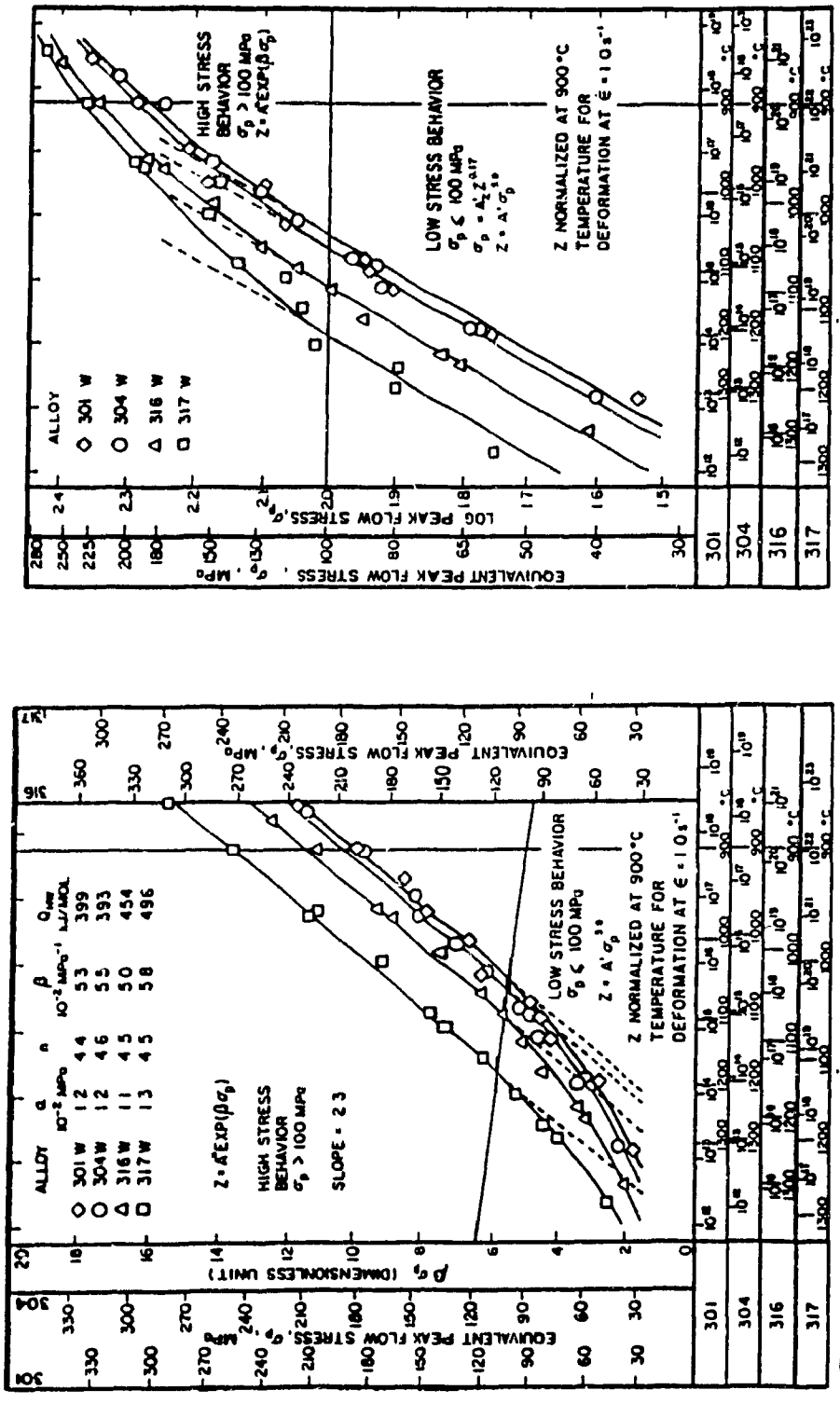

Fig. 16. A plot for 301W, 304W, 316W, and 317W showing the relationship of σ_p to Z. It is evident that a) the exponential law (Eqn. 16) breaks down below ≈ 100 MPa, and b) the power law (Eqn. 15) breaks down above ≈ 100 MPa.

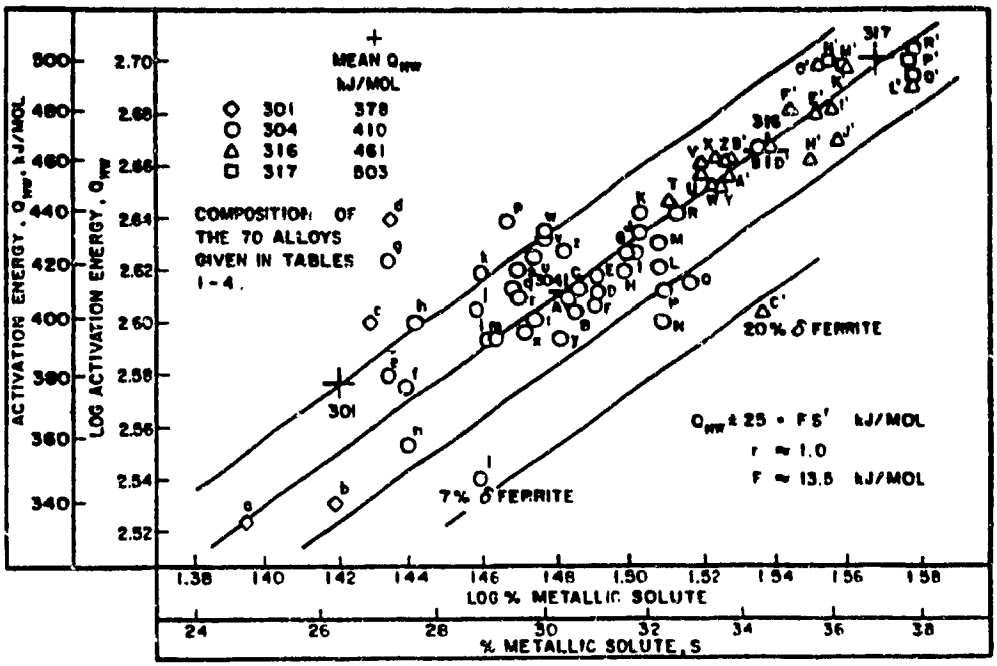

Fig. 17. The relationship of Q_{HW} to the solute concentration for 301, 304, 316, and 317. The concentrations of the 70 alloys are given in Tables 1-4 (49, 57, 63, 76, 77, 119, 126, 152, 158-195). For some segregated as-cast alloys, Q_{HW} is unusually low (present 316, 162).

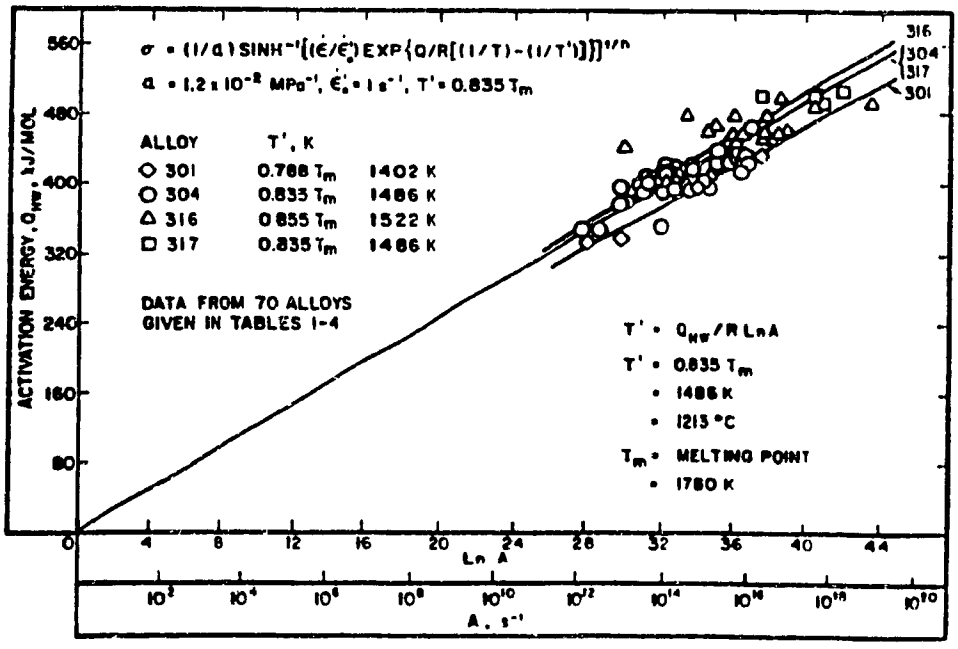

Fig. 18. This plot of the activation energy Q_{HW} against the constant A in Eqn. 17 allows derivation of the constant T' for the inverted sinh $\alpha\sigma$ function of Tanaka et al. (Eqns. 19, 20).

which is a plot of Q_{HW} versus ln A for the stainless steel alloys in Tables 1-4 including the present. The lines for each alloy pass through the origin and show that T' = 1486 K for 304W and 317W; for 316W, T' = 1522 K and for 301W, T' = 1403 K. Tanaka et al. (196) reported that T' = $0.780T_m$ which is confirmed in the present case with T'/T_m ranging from 0.788 to 0.855.

4.2.6 TRANSITION FROM ATHERMAL YIELDING

The decrease in the yield stress σ_{yo} and steady state flow stress σ_s with falling Z is shown in Fig. 19a,b (263). The lateral displacement of the graphs for the different alloys results from different values of Q_{HW} which rise with increasing Mo contents. These graphs illustrate directly the resulting effects of work hardening and restorative mechanisms of DRV and DRX. In the higher Z range, σ_{yo} is practically athermal while σ_s decreases rapidly as Z diminishes. The yield stress becomes athermal at about 825, 850, 875, and 900°C for 304W, 301W, 316W, and 317W. In the low Z range, the difference between σ_{yo} and σ_s decreases rapidly and is indicative of faster DRV and DRX. It is noted that these restorative mechanisms are more effective at reducing the differences $\sigma_s - \sigma_{yo}$ in the worked than in 304C, 316C, and 317C with 0.31, 0.20, and 0.23 δ-ferrite. As illustrated in Fig. 19b for 316W, σ_s drops much more after σ_p than in the as-cast material. This is representative of all alloys. Furthermore, the drop of σ_p with respect to σ_p^* is greater in the worked alloys than in the as-cast.

4.2.7 CORRECTION FOR DEFORMATIONAL HEATING

From Eqn. 5 in Sec. 2.1.6, the deformational heating for 301W, 304W, 316W, and 317W increases T at the peak 11 and 44°C, 12 and 52°C, 15 and 61°C, 15 and 59°C at 1200°C and 900°C, 5 s^{-1}, respectively. When correction is made for ΔT, Q_{HW} for 301W, 304W, 316W, and 317W are 454, 479, 562, 605

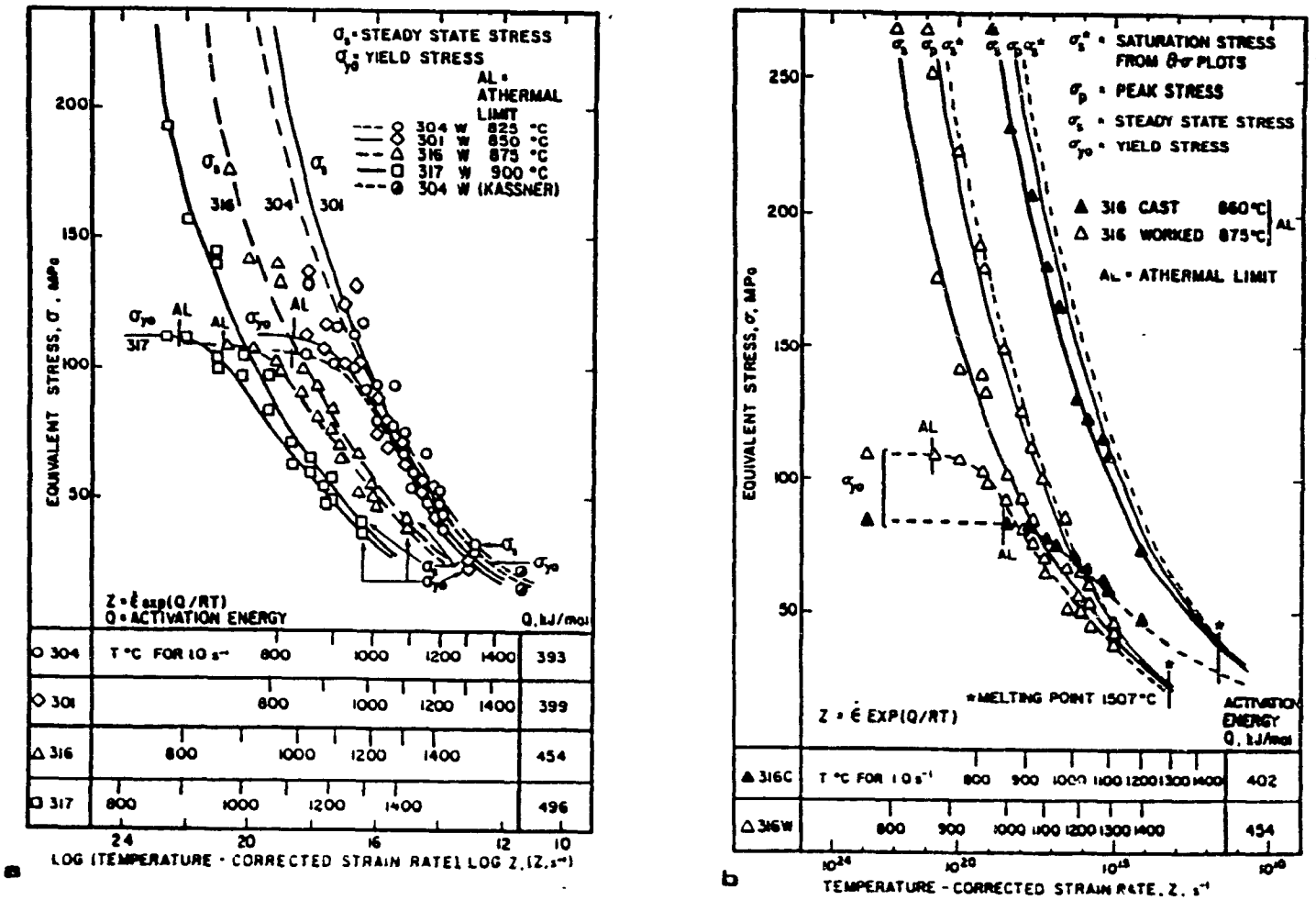

Fig. 19. Relationships between yield and steady state flow stress as a function of Z for a) 301W, 304W, 316W, and 317W are presented with additions of published data points (263), and b) the variation of σ_{yo}, σ_p, σ_s^* with T compensated $\dot{\varepsilon}$ for both 316C and 316W. At high Z, the strain hardening is high, especially in the as-cast condition but becomes low at low Z. The T scales are for 1 s^{-1}.

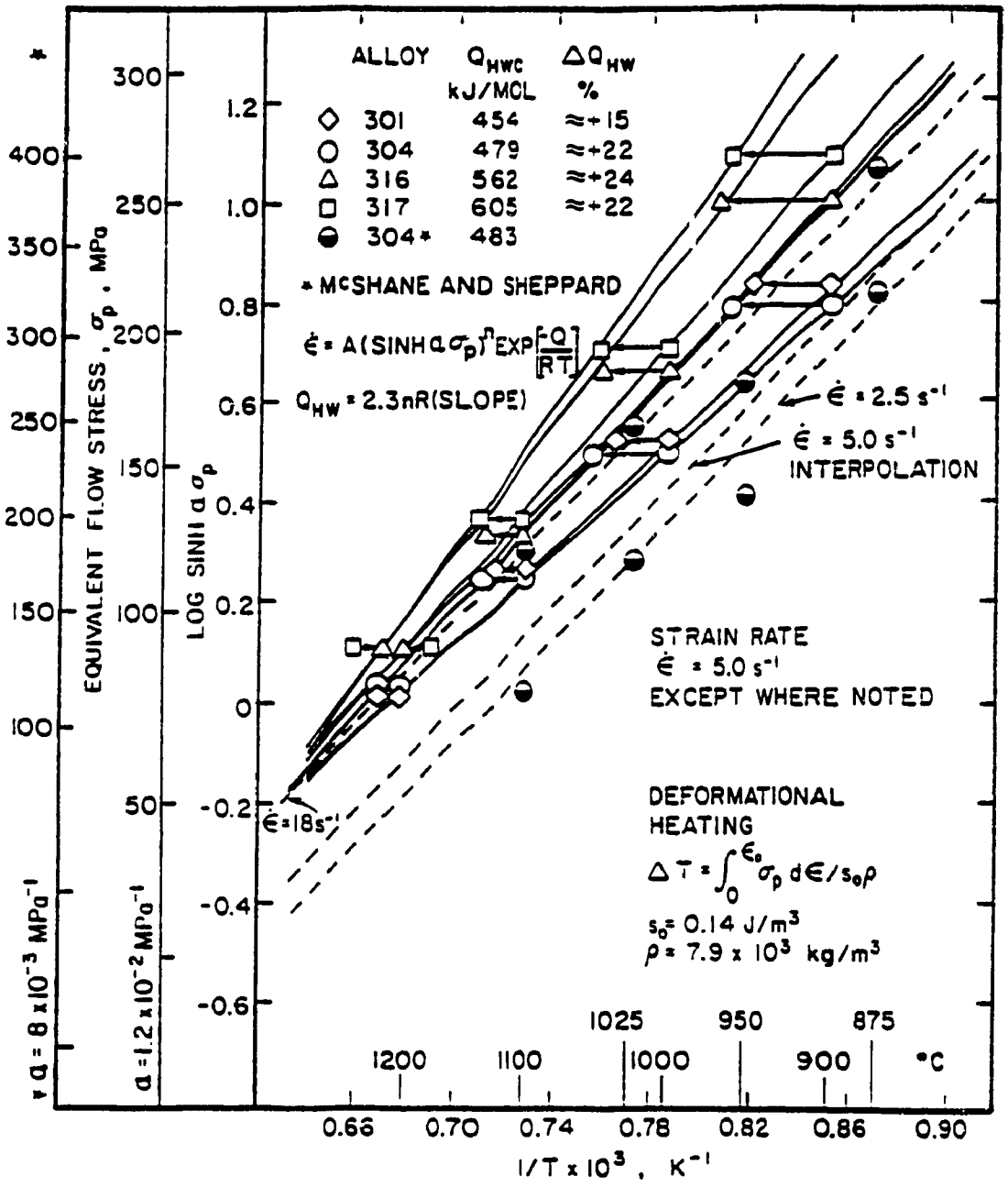

Fig. 20. Replotting of log sinh $\alpha\sigma$ versus 1/T lines, to reflect the T increase due to deformational heating calculated by Eqn. 5, leads to the derivation of Q_{HWC}. Published data are included for comparison (157).

kJ/mol which represents a 14, 22, 24, and 22% increase, Fig. 20 (157). In the case of 304W, deformation at high Z (900°C, 5 s^{-1}) produces a measured flow stress of 208 MPa which is actually for a temperature condition of 952°C as a result of deformational heating. Consequently, the correct flow stress at 900°C calculated from Eqn. 17 is somewhat higher, about 252 MPa. Consequently, 301W, 316W, and 317W have real flow stresses of 256, 307, and 322 MPa at 900°C.

4.3 KINETICS OF DYNAMIC RECRYSTALLIZATION

4.3.1 CRITICAL STRAIN; TIME FOR INITIATION

The critical stress and strain for DRX were derived from θ-σ curves in Fig. 5 (Sec. 4.1.2). The dependency of DRX initiation of all four alloys in both the as-cast and worked condition on the deformation conditions, hence the variations of ε_c with Z, is presented in Fig. 21a,b (138, 264) with 304 having some similarity to previous results. For 304, 316, and 317, at 900°C, 1 s^{-1}, ε_c is 0.33 and 0.46, 0.36 and 0.49, 0.58 and 0.54 for the as-cast and worked materials, with 301W being 0.52. As T increases to 1200°C these values decrease to 0.20 and 0.25, 0.15 and 0.29, 0.40 and 0.32, with 301W falling to 0.36. From low Z, ε_c rises slowly to 1000°C and then increases rapidly to 800°C. In order to highlight differences, the T at which DRX is initiated at a given ε_c (0.5) is indicated. These temperatures for the alloys in both the worked and as-cast conditions, in the above order, are 817 and 889, 887 and 979, 842 and 928°C, with 301W being 917°C. Figure 22 (119, 126, 168, 174, 196) shows the effect that T and $\dot{\varepsilon}$ have upon the time ($t_c = \varepsilon_c/\dot{\varepsilon}$) (Secs. 2.25, 2.3.3) for the initiation of DRX which is the critical strain divided by the strain rate. With respect to the peak strain, the relationship $\varepsilon_p = 1.5\ \varepsilon_c$ is maintained for

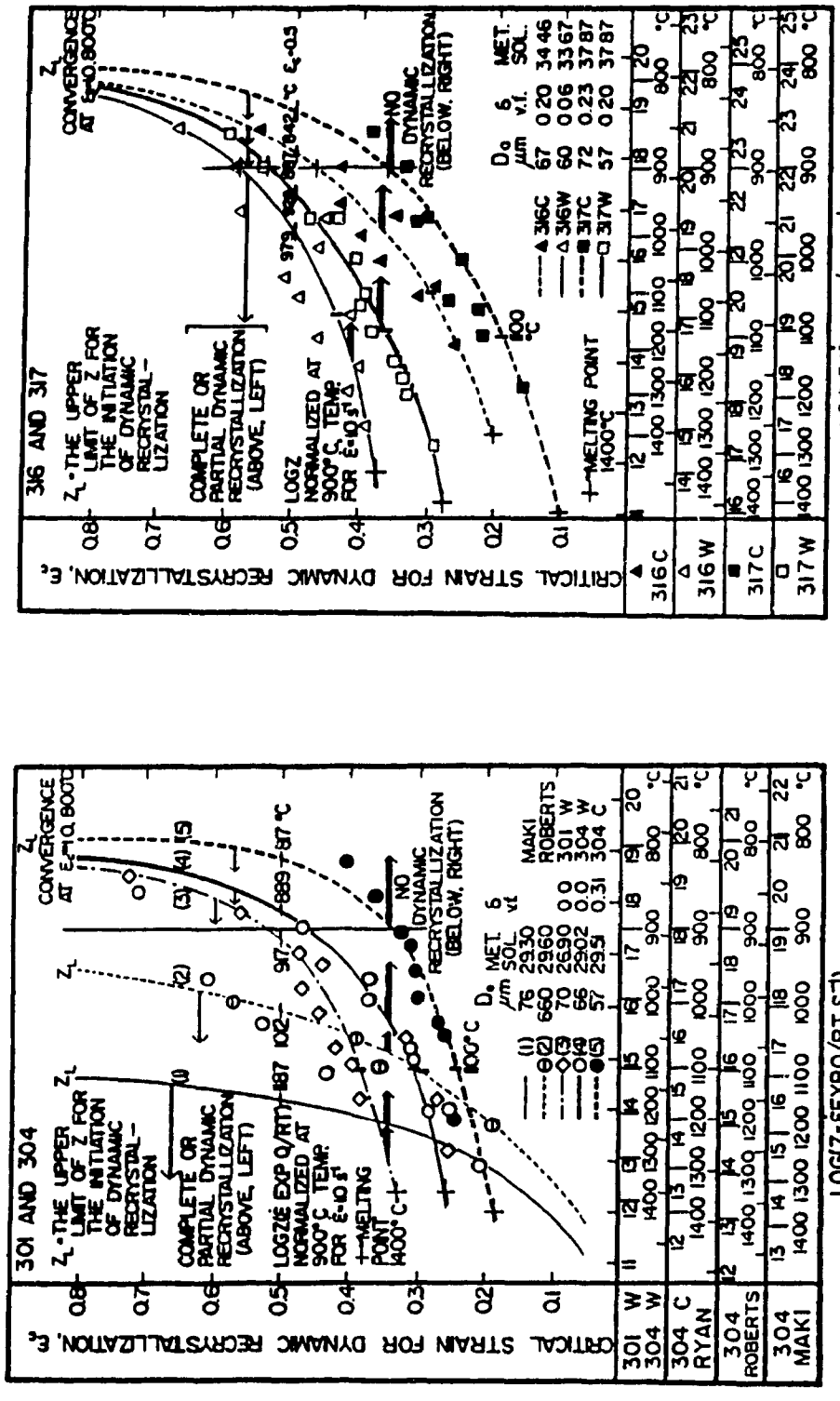

a b

Fig. 21. The critical strains for DRX (derived from θ-σ plots in Fig. 5) in both as-cast and worked a) 301W and 304, b) 316 and 317 rise with Z. Other research is included (138, 264), notably to show the effect of D_o. For a given pass ε, the curves may be interpreted as giving the limiting Z_L, above which there is no DRX and hence no refinement.

304W, 316W, and 317W as well as for those presented in the literature. The values of ($\varepsilon_c/\varepsilon_p$) range between 0.55 and 0.74.

4.3.2 PERIODIC FLOW CURVES

Periodic flow curves are observed only at 1200°C, 0.1 s^{-1}. To find how the limits of this behavior are related to other features of the curve, ε_p and ε_x are plotted against σ_p in Fig. 23 (136, 174). The crossover indicates the change in flow curve behavior according to the theory outlined in Sec. 2.3.4 . This behavior occurs at strain rates of 0.18, 0.36, 0.24, and 0.18 s^{-1} for 301W, 304W, 316W, and 317W at 1200°C. With peak strains of 0.44, 0.38, 0.49, and 0.38 respectively, it takes approximately one second to attain σ_p for 304W and two seconds for all other alloys.

4.3.3 AVRAMI KINETIC ANALYSIS

The strain for X_{DRX} = 0.5% was chosen to be at a strain of 0.01 beyond ε_c which is in agreement with other research (31, 134, 168). The time for X_{DRX} amount of DRX equals the strain minus the critical initiation strain divided by $\dot{\varepsilon}$. As stated by Elfmark (166), DRX is approximately 99% complete at the onset of steady state; this is comparable with 98% proposed by Luton and Sellars (97). The values for ε_s were determined from representative flow curves (Fig. 4a-d) and verified in Fig. 23. The times for X_{DRX} = 0.5% and for X_{DRX} = 99% as derived above are presented in Fig. 24 (168, 174, 195) which is a plot of the data according to the Avrami equation (2.3.5, Eqn. 10) expressed as:

$$\log \ln [\ 1/(1-X_{DRX})\ ] = k_{DRX} \log t + \log \beta_{DRX} \qquad (45).$$

From such a plot the slopes k_{DRX} are determined as 1.27 and 1.30 for 304W and 317W with initial grain sizes of 70 and 57μm, respectively. In this

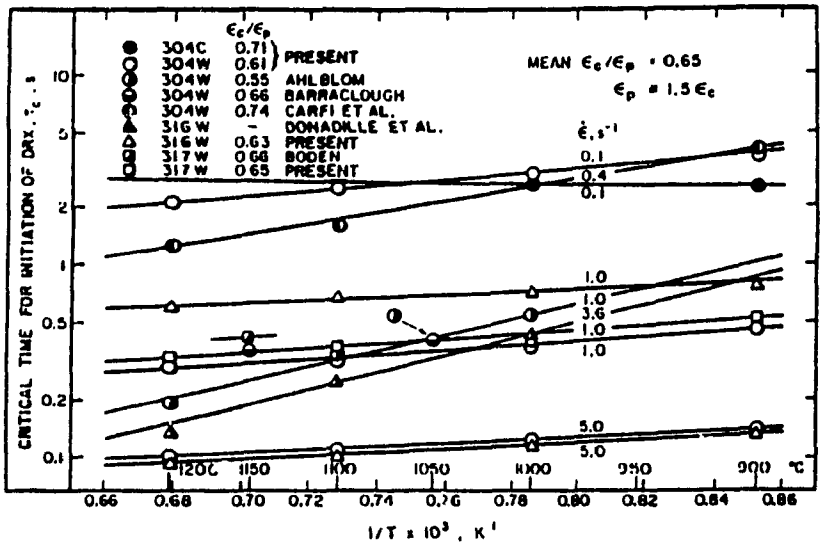

Fig. 22. The critical time for the initiation of DRX (derived from θ-σ plots of Fig. 5) for 304W rises slightly with decreasing T, whereas 304C exhibits the converse behavior. The effect of decreasing strain rate is much more marked. Curves for other alloys from the literature are included for comparison (119, 126, 168, 174, 196).

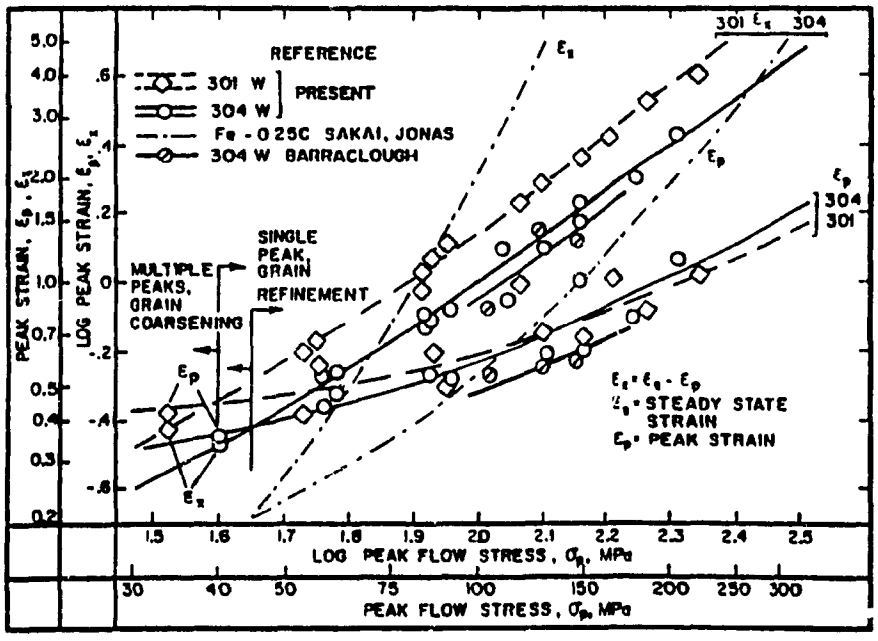

Fig. 23. The logarithmic plots of ε_p and of ε_x as a function of σ_p indicates by their intersection, the transition from periodic to single peak flow curve behavior for 301W and 304W. Published data are included for comparison (136, 174).

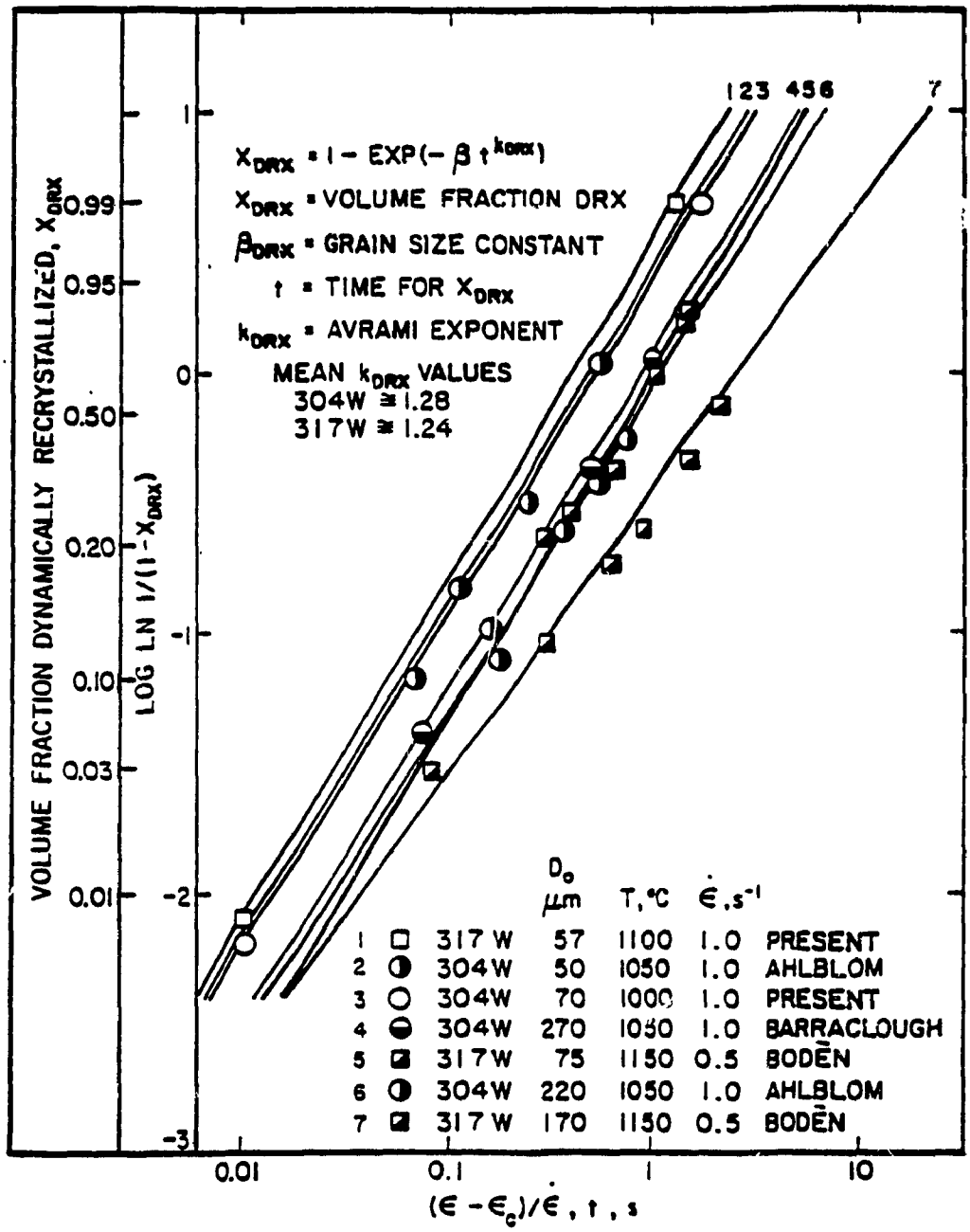

Fig. 24. The Avrami expression is fitted to the mechanical data with mean slopes of 1.28 and 1.24 for 304W and 317W. The time for DRX rises as D_0 increases. Metallographic results for other alloys are added as confirmation of the analysis (168, 174, 195).

equation β_{DRX} is the grain size constant, and slope k_{DRX} is the time constant. The slope diminishes to 1.08 for a 317W with a D_0 of 170μm tested at 0.5 s^{-1}. The mean values of the time exponent k_{DRX} for 304W and 317W, both the present and previous work (168, 174, 195), are 1.28 and 1.24 respectively. The values of β_{DRX} range between 0.4 and 3.4 for all alloys. The present mechanically derived points are confirmed by previous metallographic data.

The amounts of recrystallization as a function of strain can be derived from the lines in Fig. 24 and are plotted in Fig. 25 (168, 174, 195). In such a plot of X_{DRX} versus strain, the curves emerge from the DRX critical strains for the alloys and proceed linearly until significant fractions of X_{DRX} have been achieved. This happens at about 65% for fine grained alloys and 50% for the coarser ones. The strains at which different alloys attain a certain percentage of DRX are presented in relation to their flow curves, Fig. 26 (168, 174, 195). The points at which DRX starts (ε_c) and nears completion (ε_s) are indicated on each curve with intervening values determined from optical microscopy or calculated from mechanical metallography in Fig. 24. The time to the onset of steady state rises linearly as T decreases, Fig. 27 (168, 174). As $\dot{\varepsilon}$ decreases, t_s increases with 304W having the shortest times followed by 316W and 317W. The 301W alloy has the longest times for DRX at strain rates of 1 and 5 s^{-1}. Generally, alloys with larger D_0 require longer times for DRX, indeed the rate of DRX varies inversely with grain size D_0 for any given value of X_{DRX}, Fig. 28 (168, 174). The rate of DRX is calculated by taking the derivative of the Avrami expression. The slope decreases with rising X_{DRX} as a result of impingement of the growing grains.

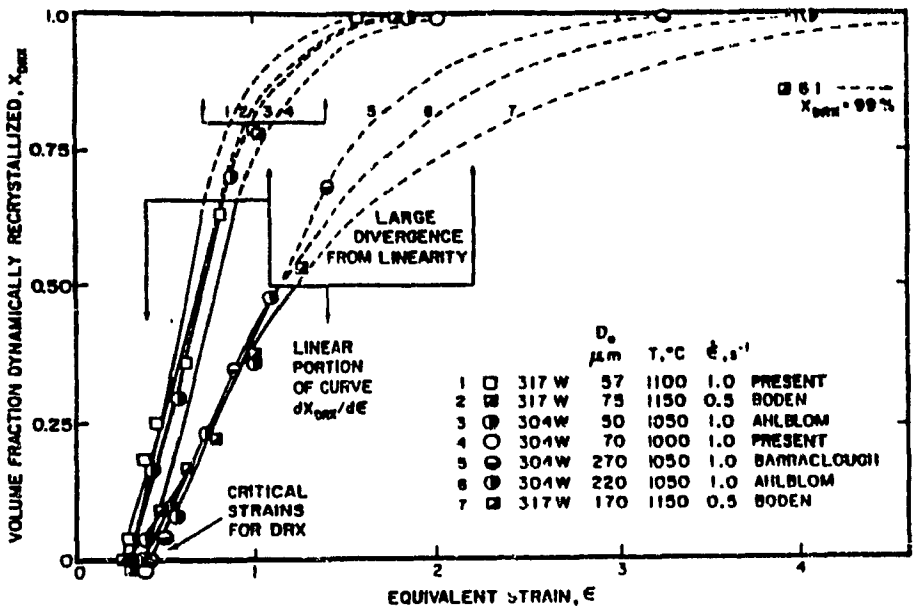

Fig. 25. Curves of the volume fraction dynamically recrystallized plotted against ε illustrate 1) the absence of incubation and the critical strain, and 2) the divergence from linearity above X_{DRX} = 70% for small D_0 and above X_{DRX} = 50% for large D_0 in 304W and 317W. Research from the literature is included for completeness (168, 174, 195).

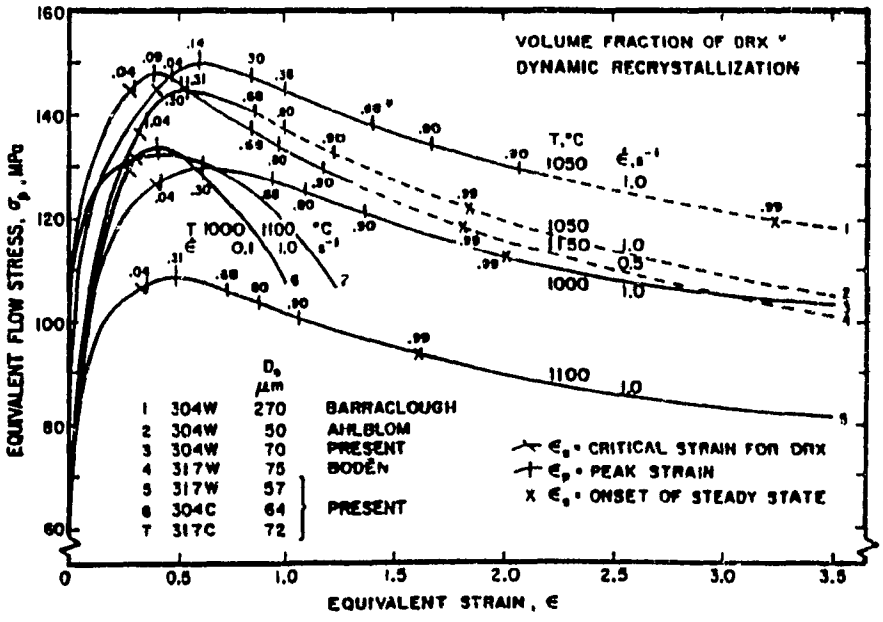

Fig. 26. Continuous flow curves for both 304W and 317W indicate the progress of DRX percentage at selected strains along the curve to 99% DRX (ε_s). ε_c and ε_p are indicated. Appropriate published results are included for comparison (168, 174, 195).

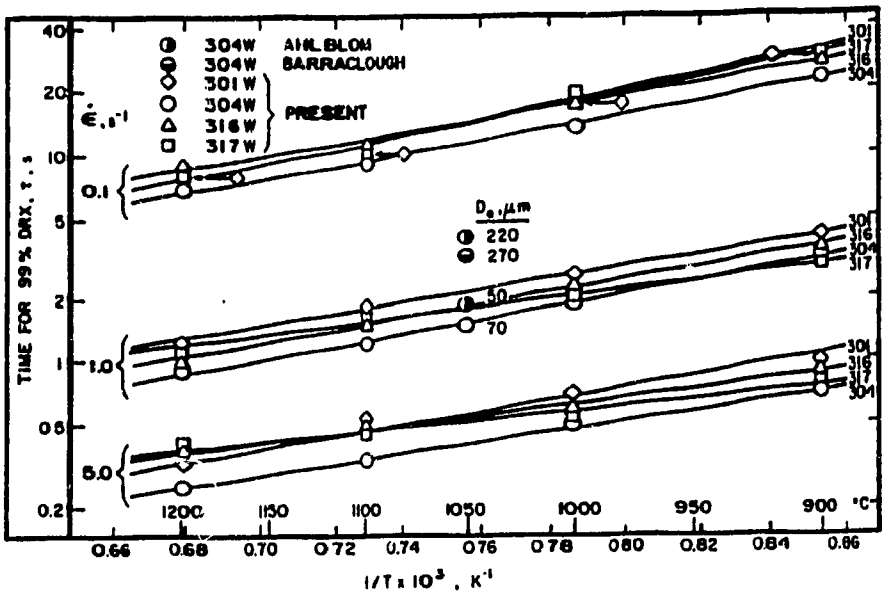

Fig. 27. Time for 99% DRX, i.e. to the onset of steady state, ε_s, t_s increases linearly as 1/T increases and rises markedly as $\dot{\varepsilon}$ decreases. The displacement of these lines to longer times as D_0 increases is supported by other research (168, 174).

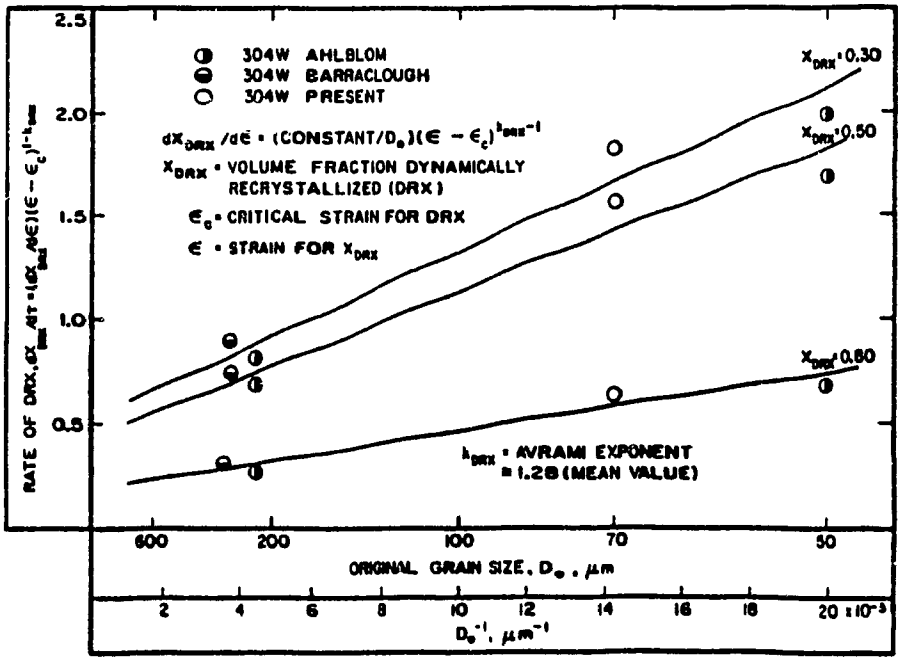

Fig. 28. The rate of DRX, which declines for 30, 50, and 80% X_{DRX}, is shown to be inversely related to D_0 by using data from several 304W alloys (168, 174).

4.3.4 COMPLETION OF FIRST WAVE OF DYNAMIC RECRYSTALLIZATION

The time for 99% DRX ($t_s = \varepsilon_s/\dot{\varepsilon}$) depends upon sinh $\alpha\sigma_s$ in accordance with the following equation (Fig. 29a,b) (Sec. 2.3.4):

$$t_s = A_{DRX} (\sinh \alpha\sigma_s)^{-n_{DRX}} \exp (Q_{DRX}/RT) \qquad (46)$$

where σ_s and Q_{DRX} are the stress and activation energy at the onset of steady state, n_{DRX} is the stress exponent, R is the gas constant, A_{DRX} is a material constant, and α equals 1.2×10^{-2} MPa. The values of n_{DRX} for 301W, 304W, 316W and 317W were determined to be 4.1, 4.3, 3.6, and 3.5. respectively. A graph of log sinh $\alpha\sigma_s$ versus 1/T (Fig. 30a,b) consists of a series of parallel lines, one for each $\dot{\varepsilon}$. The Q_{DRX} values for corresponding alloys in the above order are 306, 291, 296, and 310 kJ/mol. The 304W activation energies Q_{CRX}, Q_{HW}, and Q_{DRX} calculated at the critical, peak and steady state points along the flow curve are 351, 393, and 291 kJ/mol, respectively. From the slopes in Fig. 30b, Q_{DRX} for 301W at 306 kJ/mol is greater than that for 304W and compares to 399 kJ/mol (Q_{HW}) for the peak.

4.4 STATIC RECRYSTALLIZATION

4.4.1 MULTISTAGE STUDY OF STATIC RECRYSTALLIZATION

Static recrystallization was studied by means of mechanical metallography (Secs. 2.5.2, 2.6.3, 2.6.4). Multistage tests performed on 301W and 304W at 1100°C, 1 s^{-1} are shown in Fig. 31a,b, where after each deformation strain of 0.4, the material is unloaded and held for 50s in order to induce complete recrystallization. Between each of these large passes, the specimen is deformed to a prestrain of 0.2 and held for an interval of variable time. Upon reloading, a flow curve is produced which has a yield stress which is lower as the preceeding interval was longer.

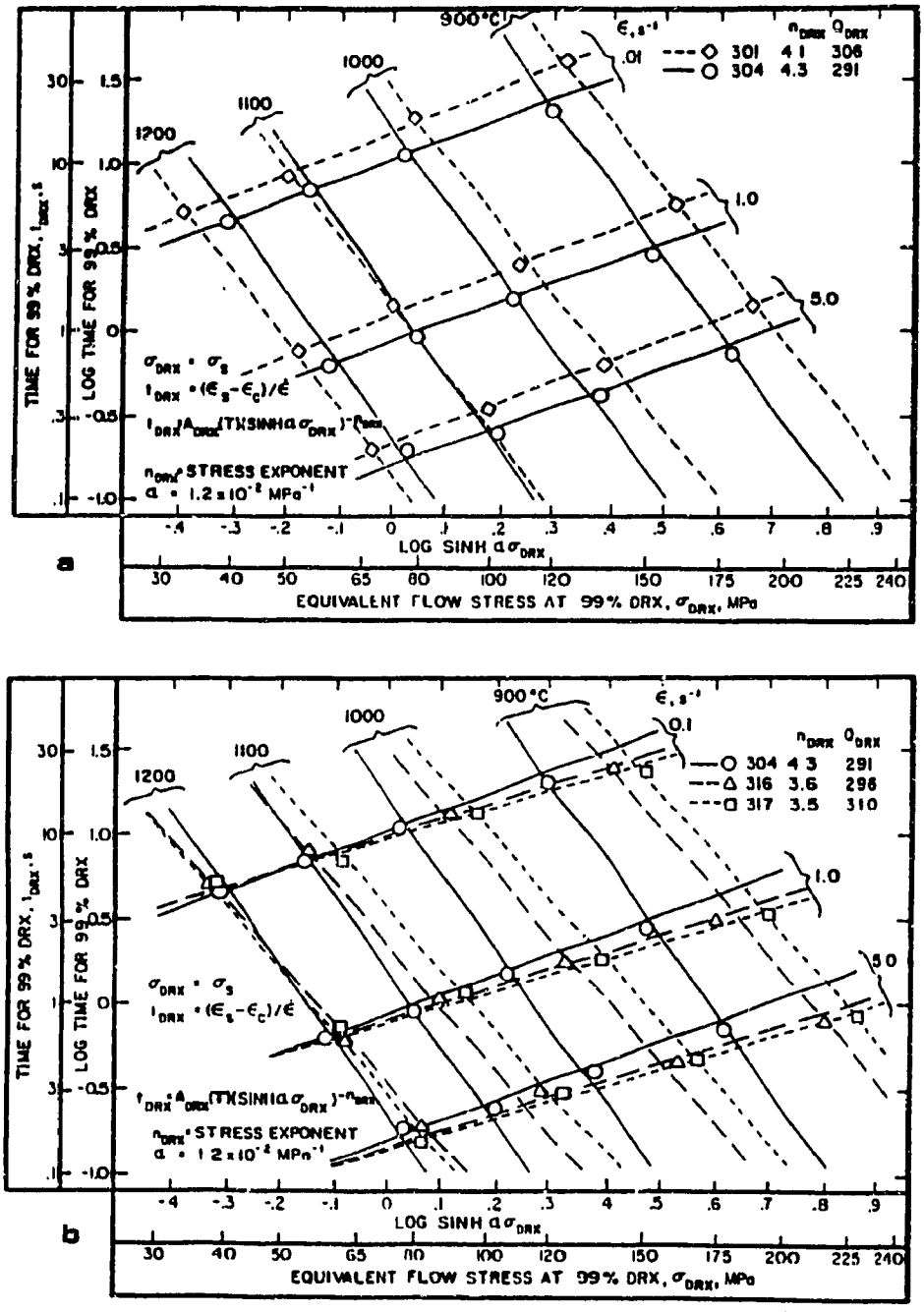

Fig. 29. In a logarithmic plot the time for 99% DRX decreases linearly with sinh $\alpha\sigma$ at constant T for a) 301W and 304W, and b) 316W, 317W plus 304W.

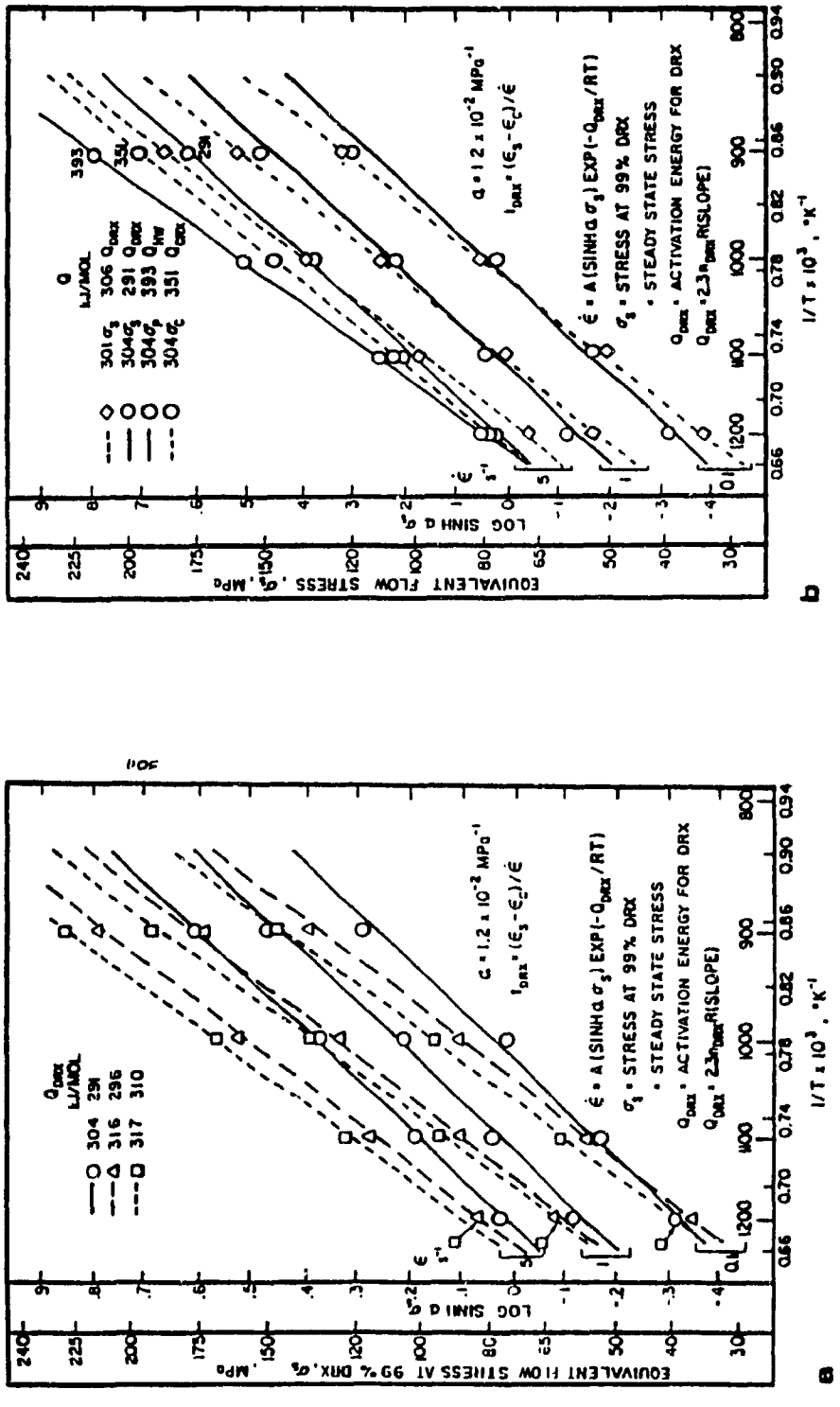

Fig. 30. Plot of log sinh $\alpha\sigma$ against 1/T shows a) the Q_{DRX} values at 99% DRX (ϵ_s, σ_s) for 304W, 316W, and 317W and b) the Q values at ϵ_c, ϵ_p, and ϵ_s along the continuous flow curve.

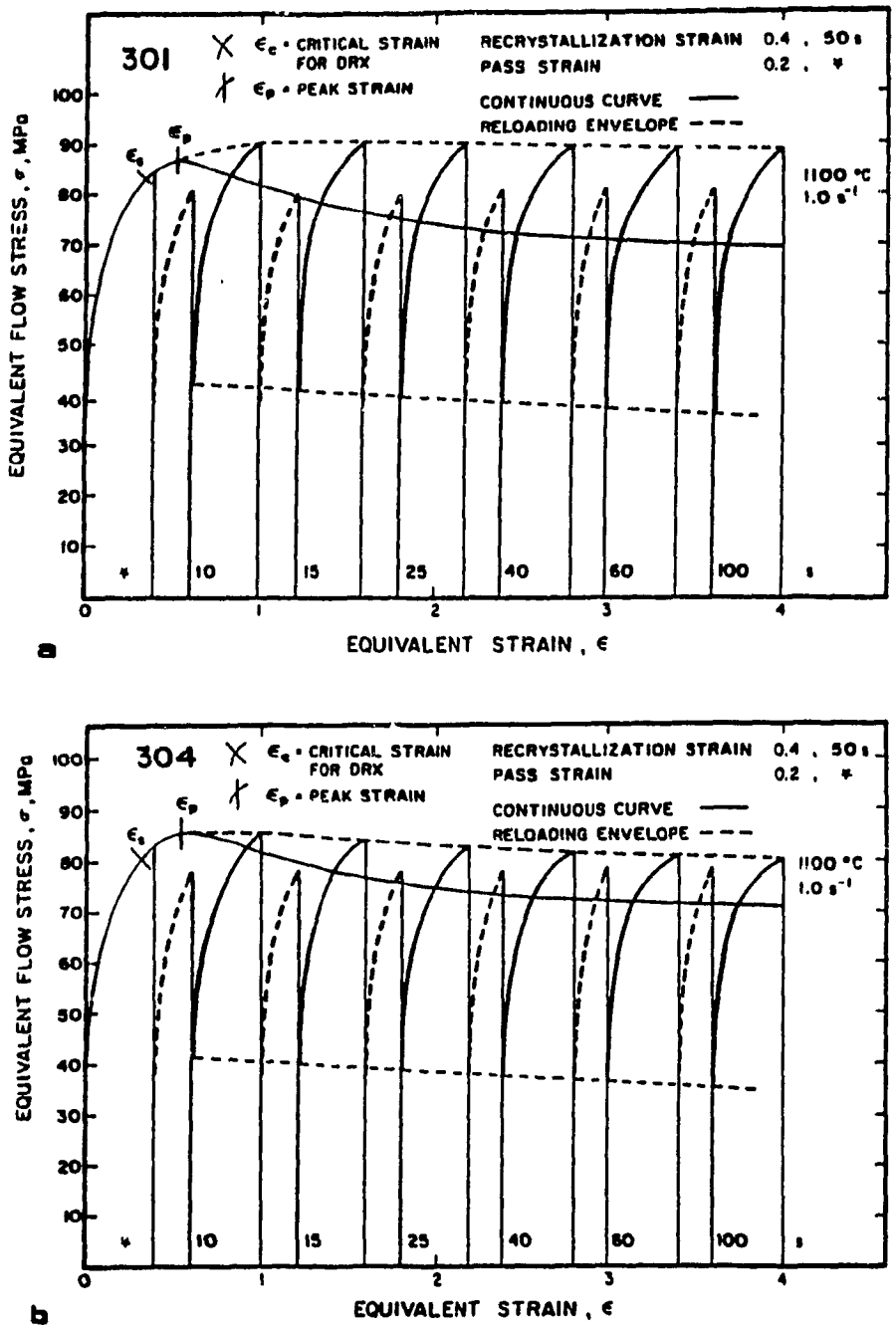

Fig. 31. Multistage flow curves for a) 301W and b) 304W showing large passes followed by long intervals to fully recrystallized material to repeatable grain size. There are also the equal prestrain passes (thick dashed) followed by consecutive intervals of increasing duration and then the reloading curves to measure the drop in stress. ε_c and ε_p are indicated on the continuous flow curve.

This measuring pass is carried to a strain of 0.4 in order to bring about complete SRX to the same grain size during the 50s before the next prestrain pass. The produced set of solid and dashed curves with a saw-toothed appearance have envelopes which are almost horizontal indicating the similarity in each (Secs. 2.6.6, 2.6.7); the dashed curves also have a constant yield stress indicative of SRX. The solid reloading curves have a declining envelope indicative of increasing SRX as the time before is raised.

4.4.2 KINETICS OF STATIC RECRYSTALLIZATION

The fractional softening determined by the multistage tests was converted to volume fraction recrystallized using the work of Barraclough and verified by Eqn. 26 (Sec. 2.6.4). The matrix of volume fraction recrystallized values is plotted against log time in Fig. 32 (174, 208, 265) and forms the predictable S curve which is indicative of the softening kinetics expressed by the Avrami equation (Eqn. 45) (Sec. 2.5.4). The value of k_{SRX} is 1.3 for both 301W and 304W with the slower recrystallizing alloys of 316W and 317W being 1.2 and 1.1 respectively. These are comparable with other work. The activation energy Q_{SRX} was determined in plots of log $t_{0.5}$ against 1/T to be 369 and 362 kJ/mol for 301W and 304W.

The dependence of the temperature-compensated time ($W_{0.5}$) on Z is illustrated in Fig. 33 where the derived slope of -0.375 is in agreement with that of other work (168, 174, 266). The A_{SRX} values for 301W and 304W are greater than that of other work due to the smaller values of Q_{SRX} arising from smaller initial grain sizes with faster SRX kinetics. A normalization of $t_{0.5}$ from both the present and a wide variety of other work performed on 304W at different strain rates and large original grain

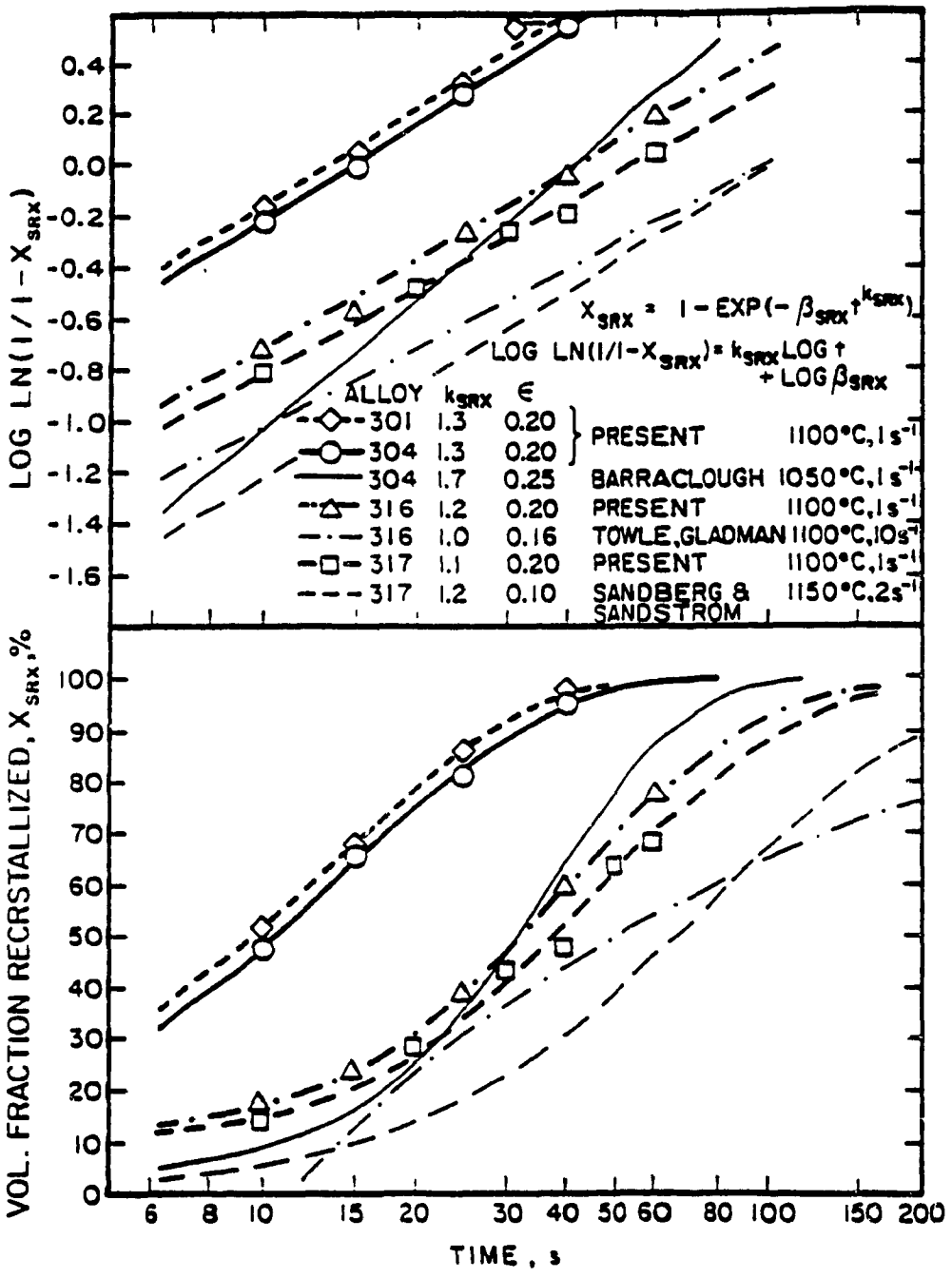

Fig. 32. A plot of the volume fraction recrystallized versus log t for 301W, 304W, 316W, and 317W, where the data form the traditional sigmoidal S curve. In addition, the time exponent k_{SRX} in an Avrami plot is shown for all alloys. The data from published papers are included for comparison (174, 208, 265).

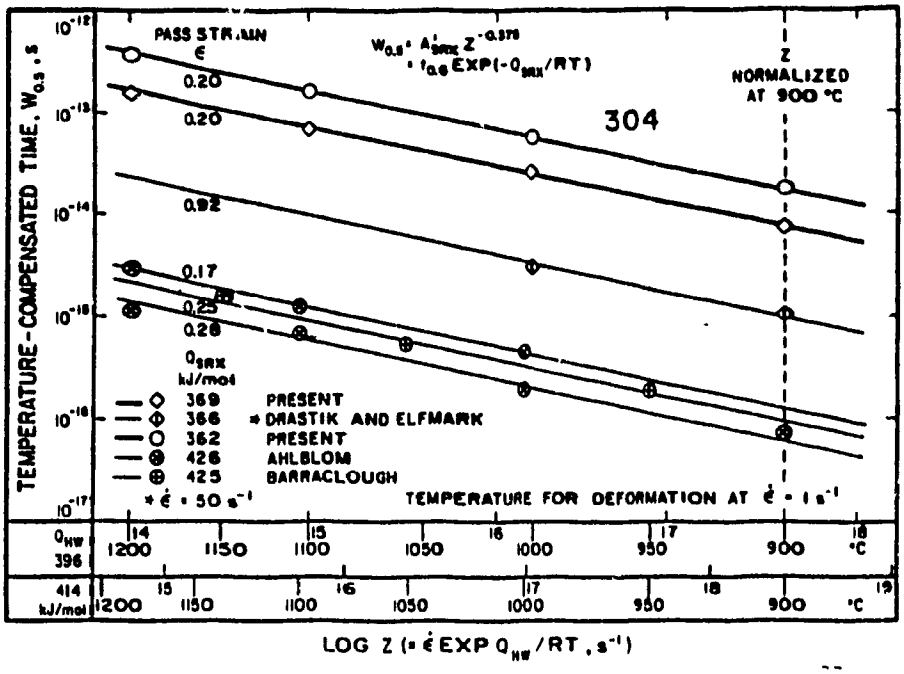

Fig. 33. A logarithmic plot of the compensated-time for DRX, $W_{0.5}$, versus log Z where all data fall along lines with the same slope at longer times for higher pass strains, confirming Eqn. 24. Published data are included for completeness (168, 174, 266).

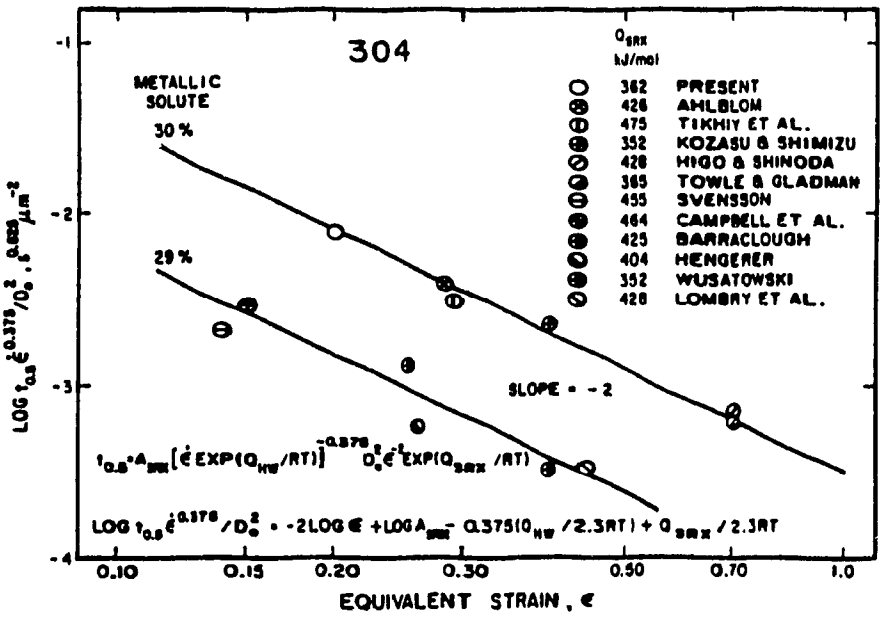

Fig. 34. An analysis of the present and extensively published data (106, 130, 168, 174, 180, 204, 213, 265, 267-269), showing the -2 power dependence of $t_{0.5}$ upon strain, confirming Eqn. 24. In addition, $t_{0.5}$ increases as metallic solute content rises.

sizes is realized in a plot of log ($t_{0.5}$ $\varepsilon^{0.375}/D_0^2$) versus strain, Fig. 34 (106, 130, 174, 180, 204, 213, 265, 267-269) with a resultant slope of -2 which validates the following equation for the determination of Q_{SRX}:

$$t_{0.5} = A_{SRX}\, D_0^2\, \varepsilon^{-2}\, [\dot{\varepsilon}\, \exp(Q_{HW}/RT)]^{-0.375}\, \exp\,(Q_{SRX}/RT) \qquad (24)$$

The present results are compared with an extensive representation of other work on 301W and 304W in Fig. 35 (106, 130, 168, 174, 180, 204, 206, 212, 213, 265, 267-270) where Q_{SRX} varies widely from 551 to 334 kJ/mol, in reference to the present 369 and 362 kJ/mol. All data are satisfied by the preceding equation.

4.4.3 ISOTHERMAL MULTISTAGE TESTS

Representative flow curves from isothermal multistage tests (Secs. 2.6.4, 2.6.6), deformed at 900-1000°C, 0.1-1.0 s^{-1} for 301W and 304W and at 1100°C, 0.1-1.0 s^{-1} for 304C illustrated in Fig. 36a-c, exhibit a peak and work softening to a steady state regime characteristic of DRX. Their pass curves progress towards a repetitive shape. Moreover, their envelope curves through the pass maxima exhibit only weak peaks before becoming horizontal near the value of the continuous steady state.

The fractional softening (Sec. 2.6.4) determined from these tests are plotted against pass strain in Fig. 37a for 301W and 304 in both the as-cast and worked conditions with the former having the lower FS. It can be seen that while there is a considerable increase in FS as $\dot{\varepsilon}$ is increased one order of magnitude at 900°C, this $\dot{\varepsilon}$ effect is much less at the higher T. Furthermore, there is a comparative FS rise as the interval time increases. Therefore, FS increases with rising T, $\dot{\varepsilon}$, and t_i. This conclusion is confirmed by the data for as-cast 304, 316, and 317 (Fig. 37b) with the latter two showing much slower softening.

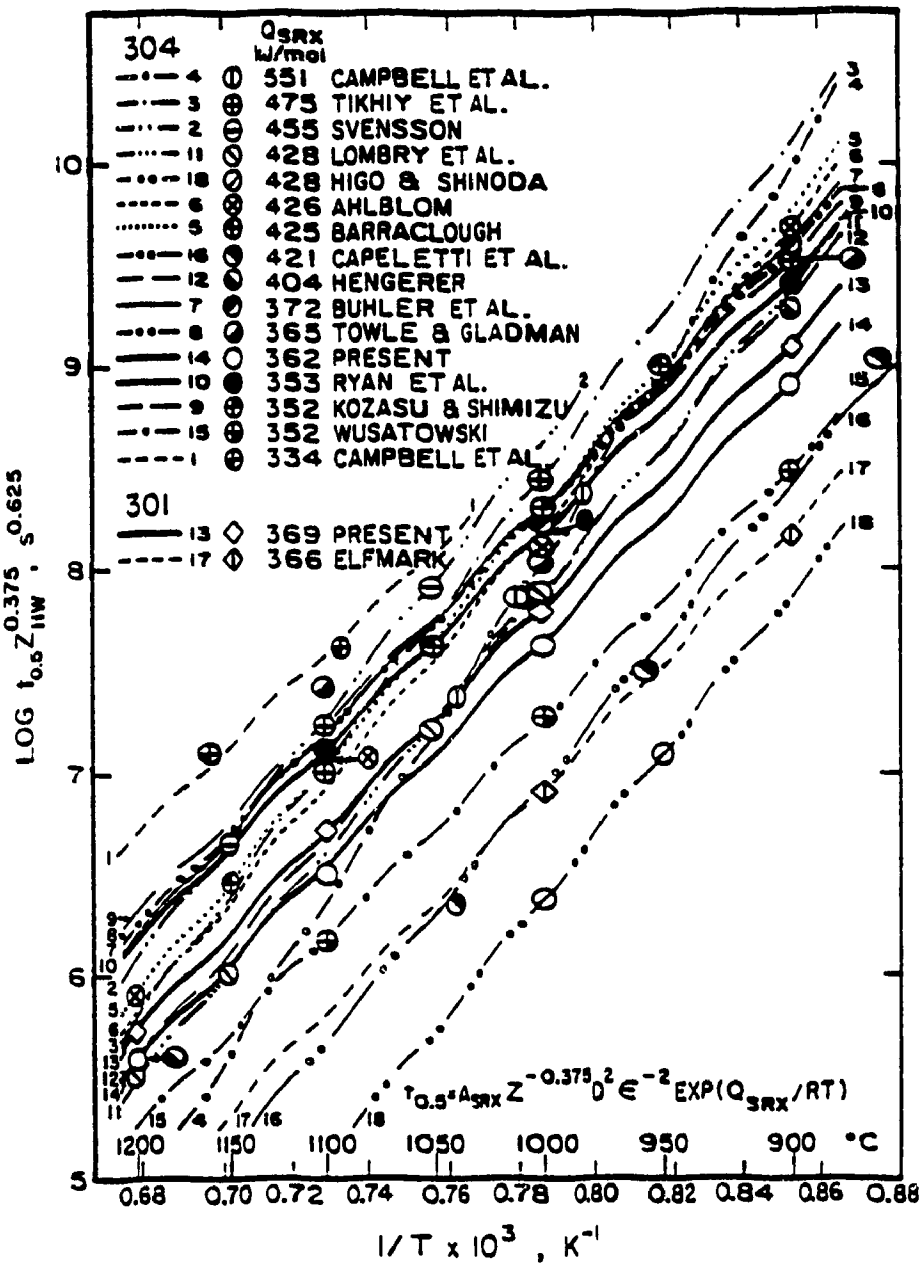

Fig. 35. A plot of the $Z^{0.375}$ corrected $t_{0.5}$ values versus 1/T for 301 and 304 as-cast and worked alloys from which the Q_{SRX} values are determined. Extensive published data are included for completeness (106, 130, 168, 174, 180, 206, 204, 213, 265, 267-269).

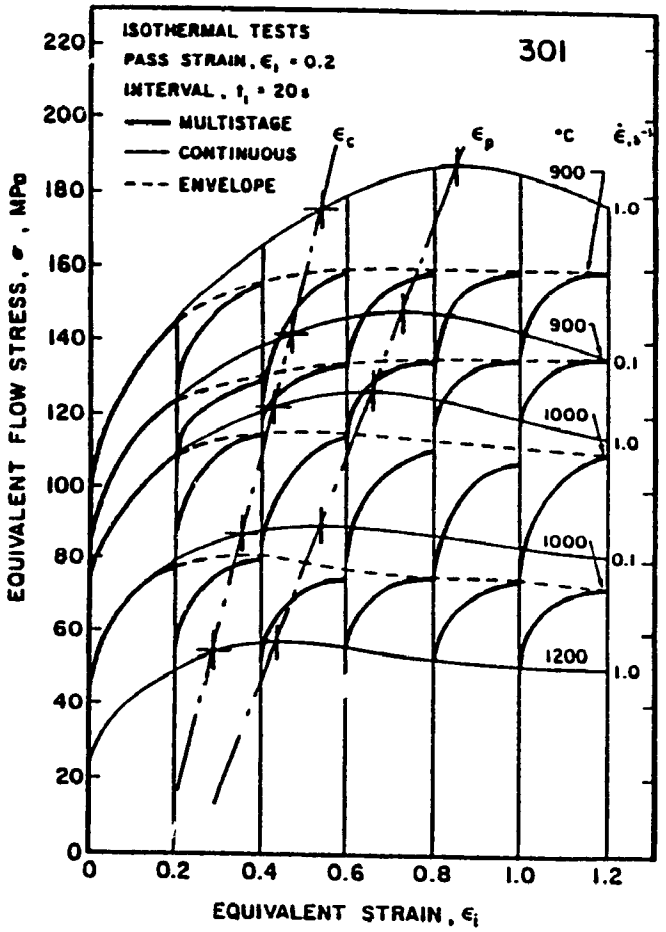

a

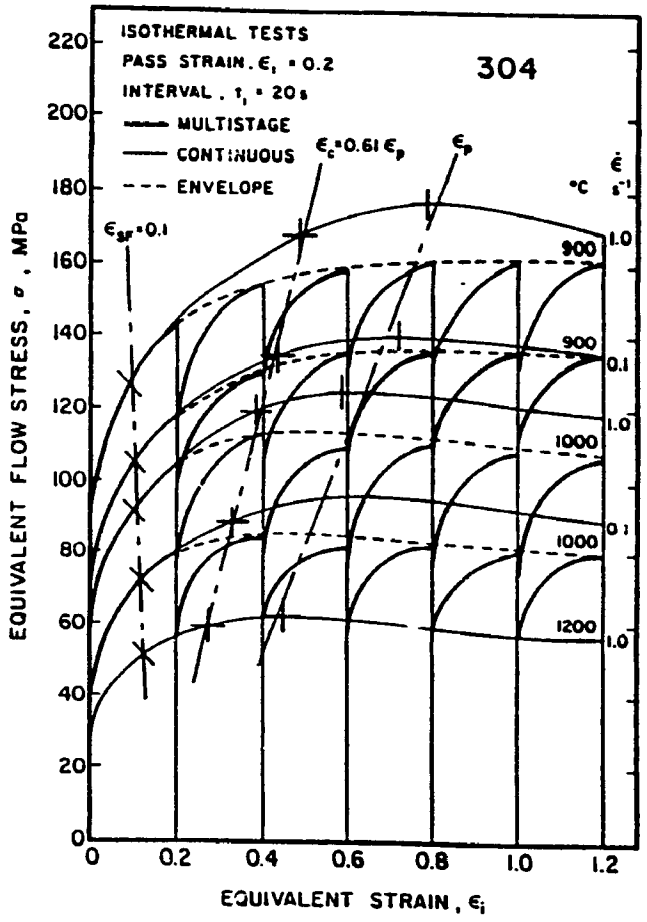

b

Fig. 36. Multistage iso-strain rate deformations with ε_i constant at 0.2 and t_i at 20s for a) 301W and b) 304W at 900 and 1000°C at both 0.1 and 1.0 s^{-1}. The dashed lines represent the envelope which encloses the successive peaks. ε_c and ε_p are indicated on the continuous flow curves.

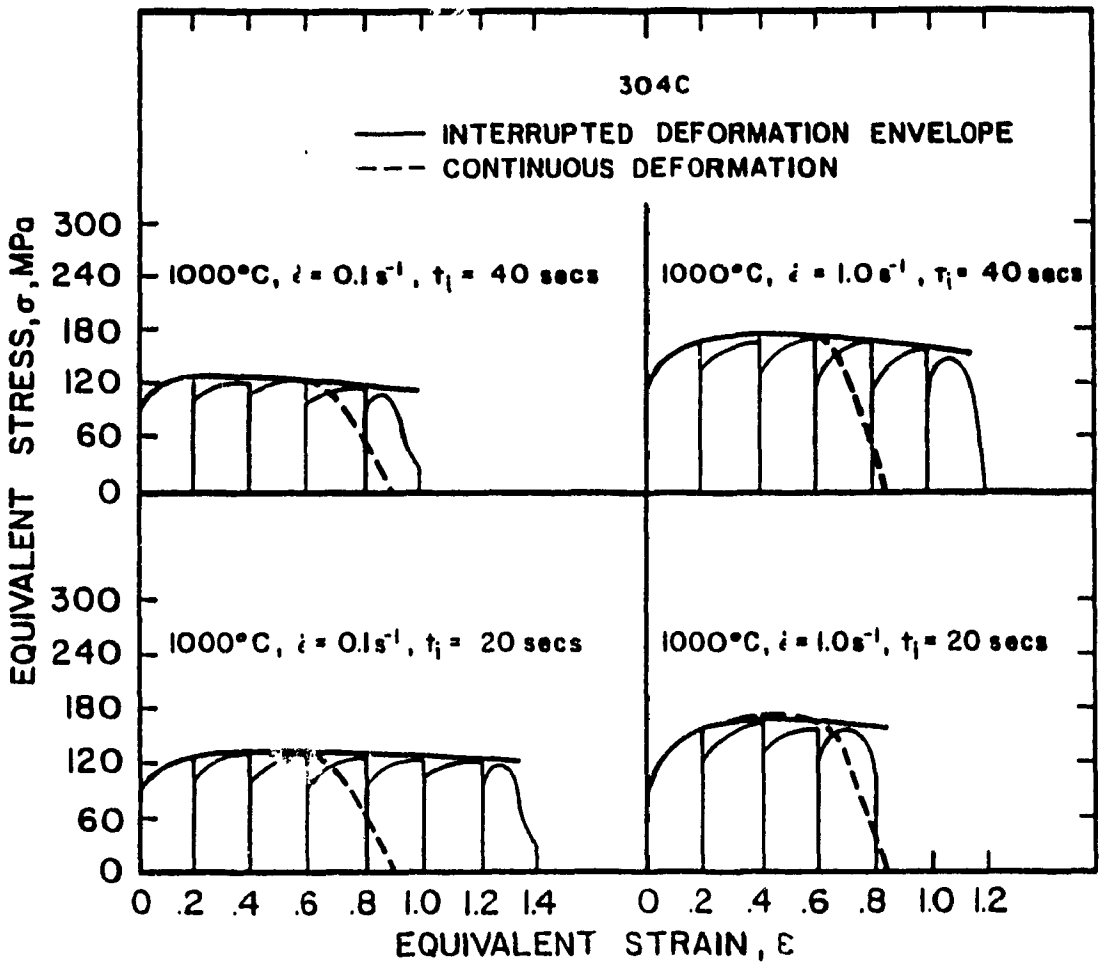

Fig. 36c. Multistage curves for 304C at 1000°C and both 0.1 and 1.0 s^{-1} with two interval times.

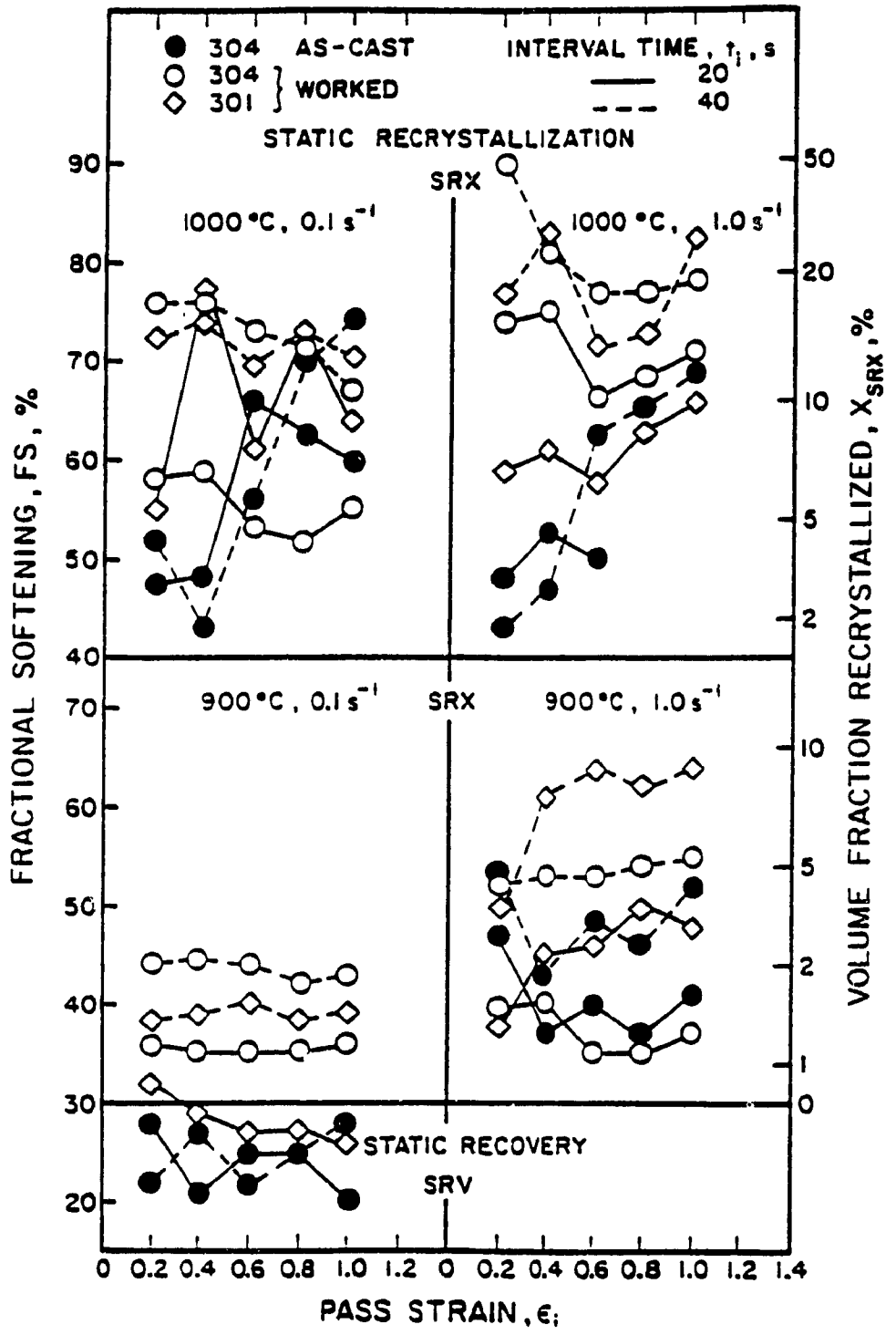

Fig. 37a. Fractional softening plotted as a function of cumulative pass strain shows the effect of increasing T, $\dot{\epsilon}$, and interval duration for 301W, 304W, and 304C. The volume fraction recrystallized is indicated on the right vertical axis which commences at 30% FS according to Barraclough (174).

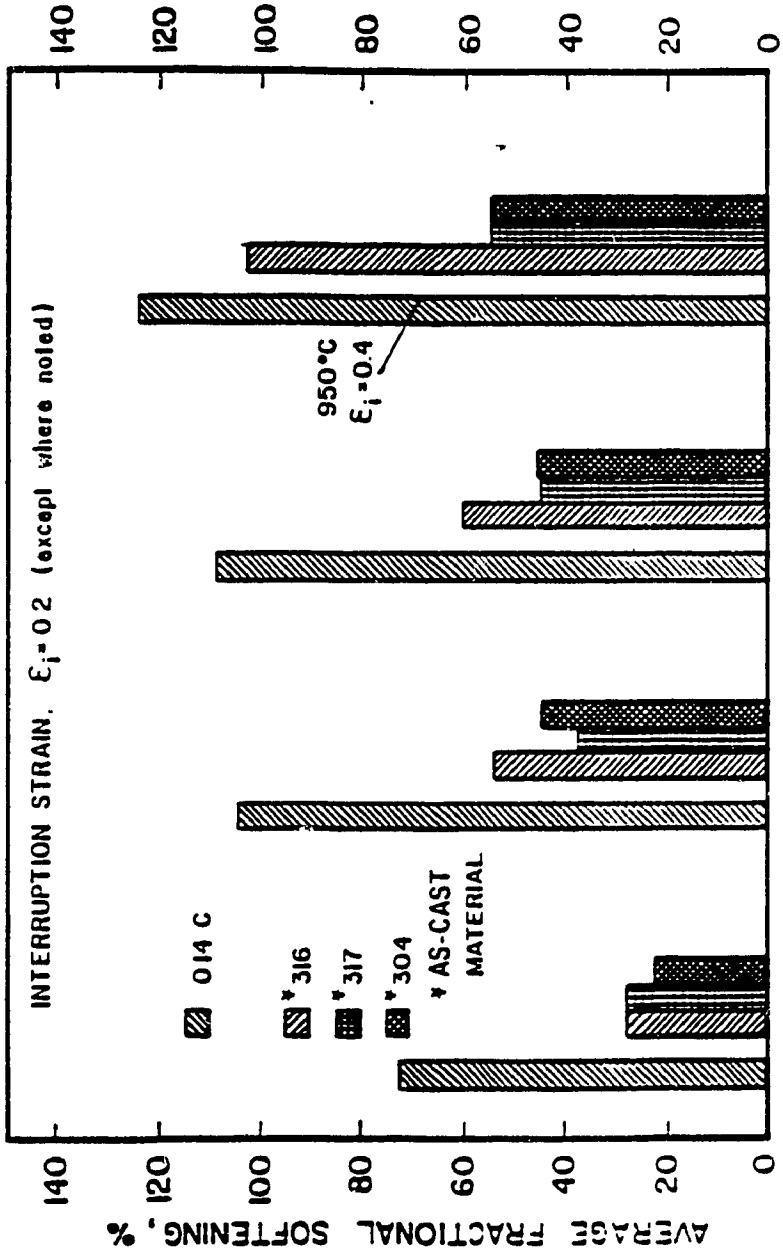

Fig. 37b. FS represented as bar graphs for 304C, 316C, and 317C for various deformation conditions. A 0.14 C steel (10, 215) is included for comparison. The FS is seen to increase as T changes from 900 to 1000°C, $\dot{\varepsilon}$ from 0.1 to 1.0 s^{-1}, and t_i from 20 to 40s.

The yield stress and flow curve in each pass, and hence the mean pass flow stress, are strongly affected by the fractional softening preceding the pass as a result of the carry-over of the worked substructure from previous passes as illustrated in Fig. 38. Therefore, in the case of rolling simulation consisting of several stands at constant $\dot{\varepsilon}$ and ε_i but falling T, the flow stress in each of the following stands is higher than in the first. When FS is low as a result of the short interval, the subsequent passes have a higher yield and resultant peak flow stress which remains reasonably constant throughout the succeeding passes. Therefore, the flow curves in stands 2, 3, and 4 have similar maxima as shown in Fig. 38 (10). The rise is higher at lower T and for 316 and 317 than 304.

4.5 HOT DUCTILITY

4.5.1 TEMPERATURE AND STRAIN RATE DEPENDENCE

Upon observation of the matrix of values of ε_f depicted in the isometric diagram of Fig. 39, it can be seen that the ductility of 304W increases with rising T and $\dot{\varepsilon}$, whereas for 304C and 317C as well as 317W, it increases with rising T but falling $\dot{\varepsilon}$. In a more detailed manner, Fig. 40a (10, 42, 167, 188, 271) presents the ductility for 304 both as-cast and worked in comparison with 301W which has a higher ε_f at 1200^{o}C, but a lower ε_f at 900^{o}C. The ductlity of 316 illustrated in Fig. 40b (191, 228) increases with rising T and falling $\dot{\varepsilon}$, with the worked being considerably higher than that of the as-cast material but lower than the 304W. As previously stated, deformational heating raises T, thereby leading to a ductility much larger than the true value at high Z. The ductility as a function of $\dot{\varepsilon}$ is presented more clearly in Fig. 41 (191, 228). The rise in 304W ductility with increasing $\dot{\varepsilon}$ is expected to eventually change from

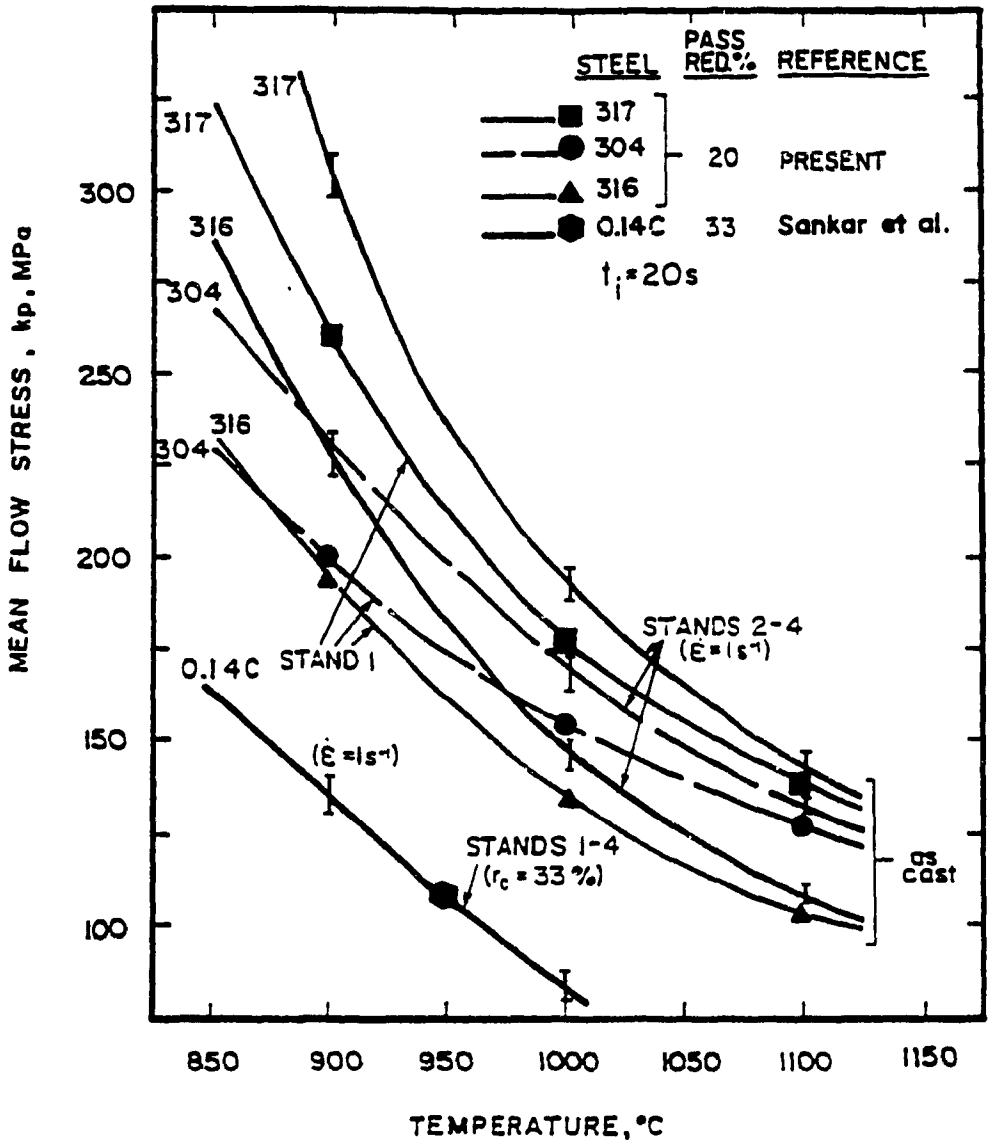

Fig. 38. The mean flow stress k_p from a 20% reduction rolling pass has been calculated from multistage tests with intervals of 20s duration at several T. Because of limited FS between passes for 304C, 316C, and 317C, k_p is higher in stands 2 to 4 than in stand 1; however, for C steel (10, 215) at 33% reduction, complete SRX keeps all stands the same.

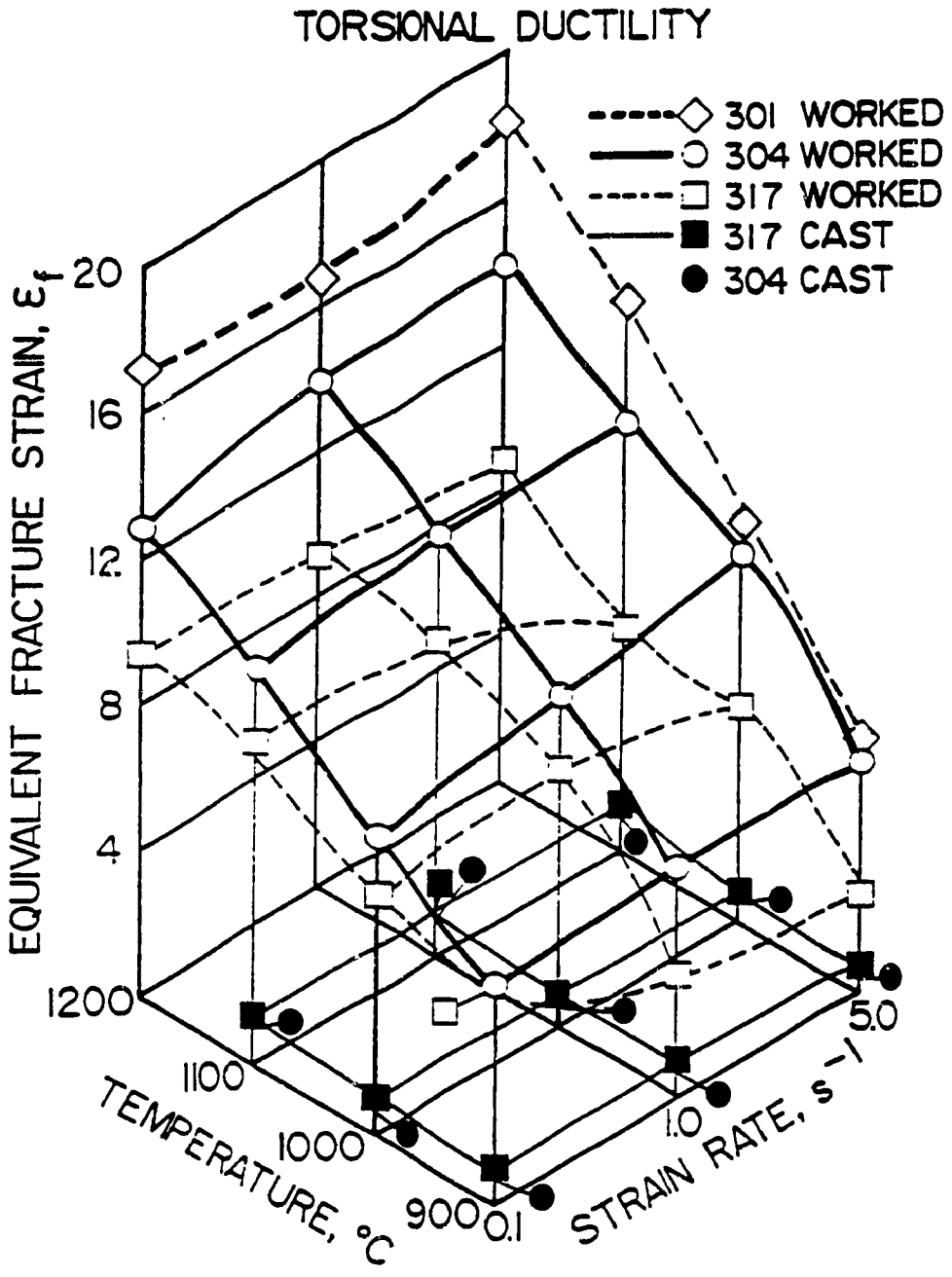

Fig. 39. The T and $\dot{\varepsilon}$ dependences of ductility, for as-cast and worked 304 and 317, in addition to 301W, are illustrated isometrically.

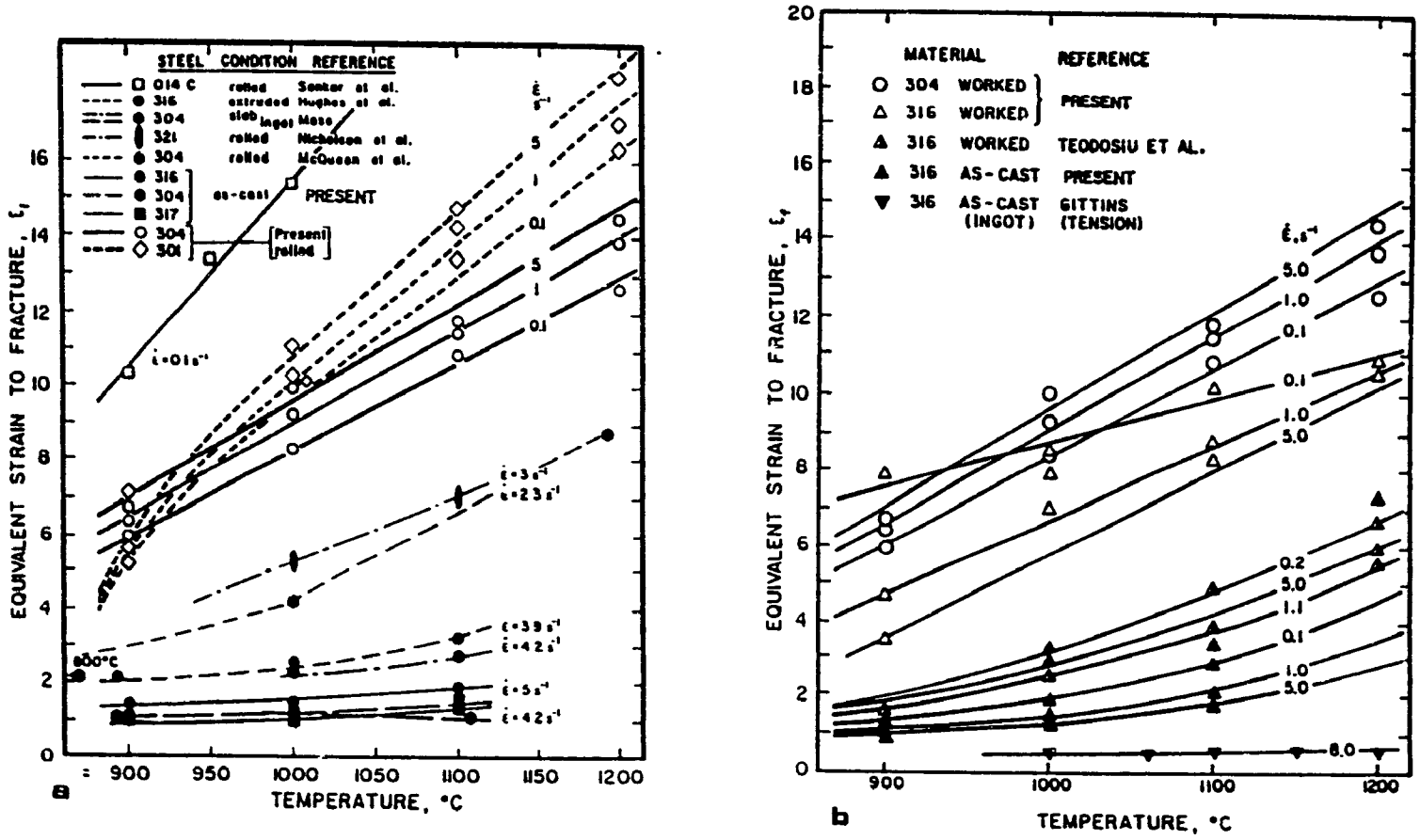

Fig. 40. The fracture strain dependence on T and $\dot{\varepsilon}$ illustrates that a) the ductility of 301W and 304W increases with rising T and with rising $\dot{\varepsilon}$, and b) the ductility of 316C and 316W increases with rising T and declining $\dot{\varepsilon}$ The ductility is considerably lower for the as-cast and for other alloys reported in the literature (10, 42, 167, 188, 191, 215, 228, 271).

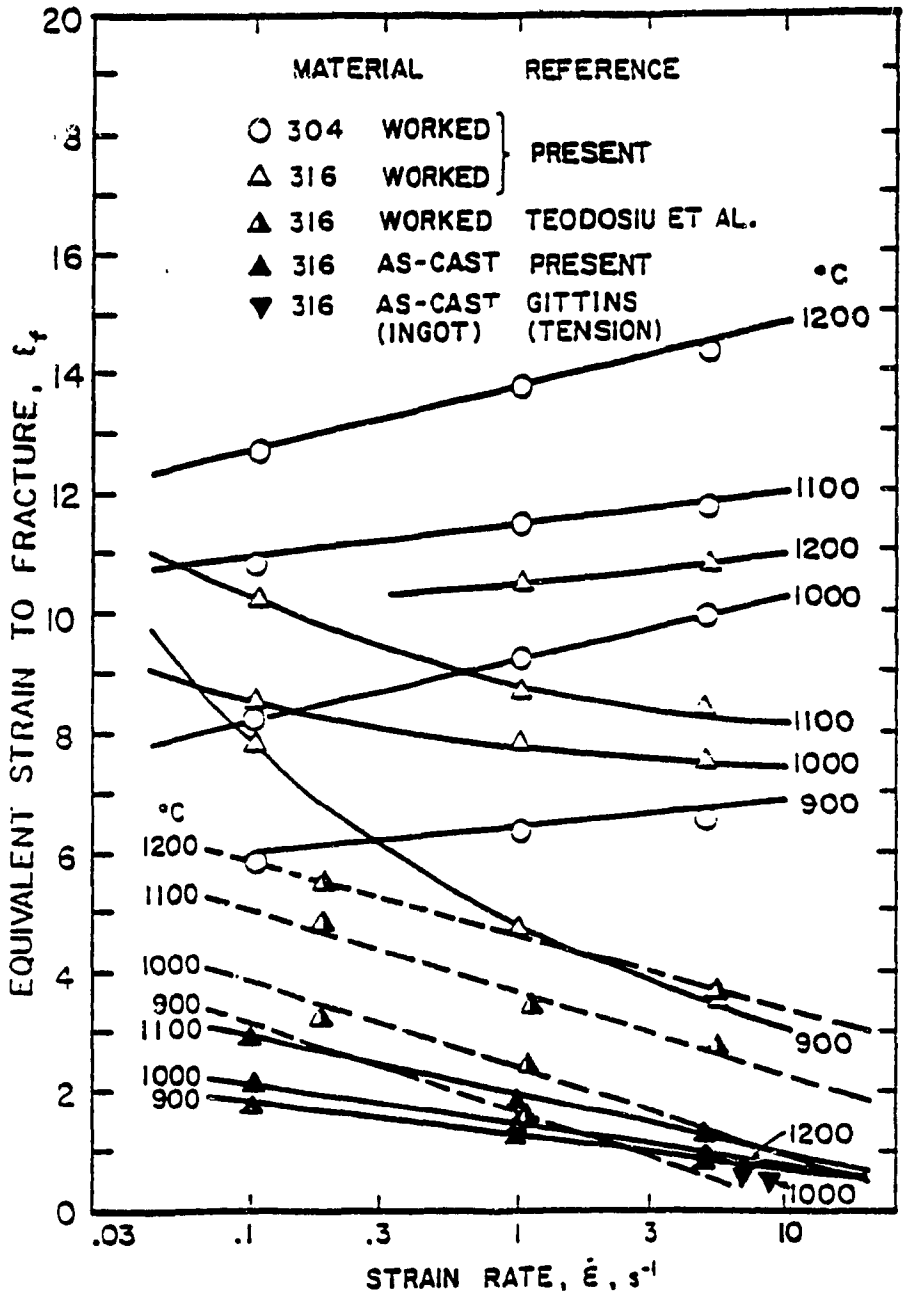

Fig. 41. The hot ductility of 316C and 316W as a function of $\dot{\varepsilon}$ for several T. Comparison is made with 304W and results in the literature (191, 228).

positive to negative, thus exhibiting the peak which is sometimes observed (Sec. 2.7.1). The fracture strain for 316W decreases as $\dot{\varepsilon}$ rises except at 1200°C where it rises slightly, having passed the ductility peak. From Figs. 39 and 40, it is evident that rising temperature has a much more positive effect.

4.5.2 FRACTURE CONSTITUTIVE EQUATION

The time-to-fracture (equaling $\varepsilon_f/\dot{\varepsilon}$) criterion, borrowed from creep analysis, is valid for all alloys with the as-cast and worked materials being fitted by the following exponential and hyperbolic sine functions respectively (Sec. 2.7.4):

$$t_f = A_f'' \exp(-\beta_f \sigma_f) \exp(Q_f/RT) \qquad (47)$$

$$t_f = A_f (\sinh \alpha\sigma_f)^{-n_f} \exp(Q_f/RT) \qquad (35)$$

Using the exponential function and Arrhenius relationships between σ, $\dot{\varepsilon}$ and T (Eqn 47), the same n_f and Q_f values for 304C and 317C were derived from both strength and fracture data, whereas the fracture values of n_f and Q_f for 316C were significantly higher as shown in Fig. 42a,b. The β_f, n_f and Q_f values for 304C, 316C, and 317C are 5.4 X 10^{-2} MPa^{-1}, 4.1 and 404 kJ/mol, 4.8 X 10^{-2} MPa^{-1}, 4.0 and 511 kJ/mol, 6.5 x 10^{-2} MPa^{-1}, 5.4 and 505 kJ/mol, respectively.

The time-to-fracture criterion expressed by Eqn. 35 is confirmed in Fig. 43. Comparing 304C with 304W which is shown in Fig. 43a,b, (191) the stress exponents (n and n_f) change from 4.3 to 4.1 for 304C and from 4.6 to 5.2 for 304W, while Q_f values change respectively from 407 to 404 kJ/mol and from 393 to 377 kJ/mol. The data for 316W agree closely with those for 304W at 0.1 s^{-1}. Both 304W and 316W fracture at a similar strain ε_f of approximately 12.5 at 1200°C, 5 s^{-1} where the high T has put carbides into

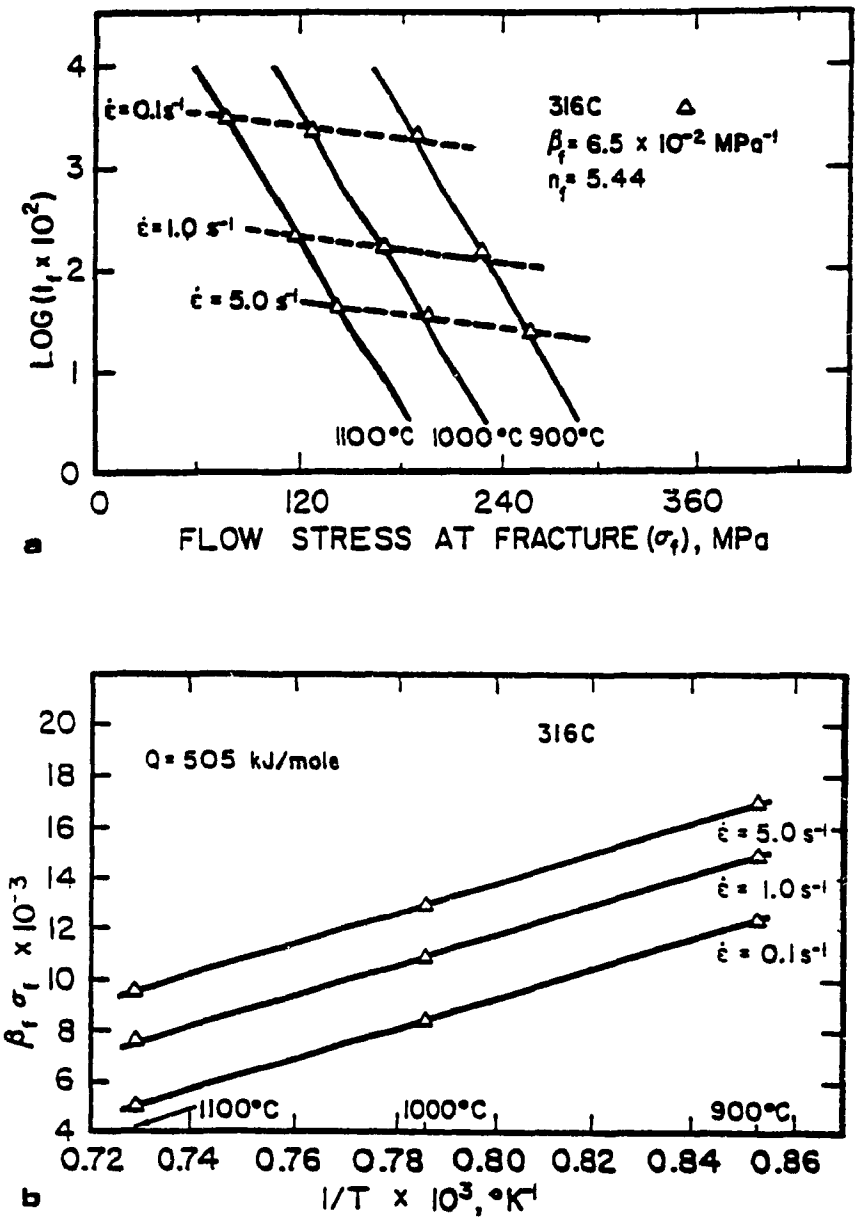

Fig. 42. Fracture times derived from hot torsion tests on 304C demonstrate a) an exponential relationship with rupture stress, there being straight lines for each T, and b) the fracture stress depends on T according to an Arrhenius relationship, there being a straight line for each $\dot{e}$.

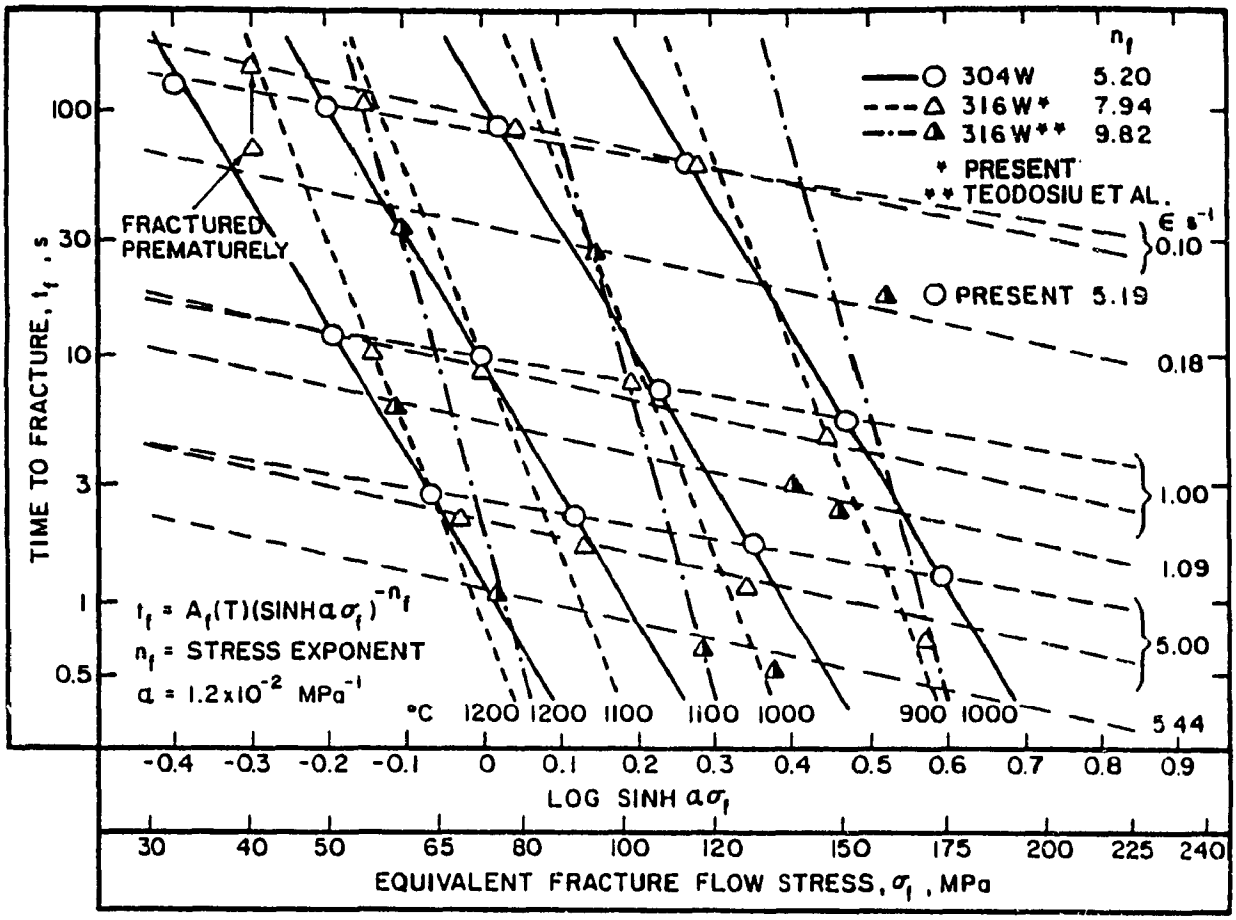

Fig. 43a. Torsion fracture times derived for 304W and 316W demonstrate the hyperbolic sine relationship with fracture stress, there being a straight line for each T. Published data are included for completeness (191).

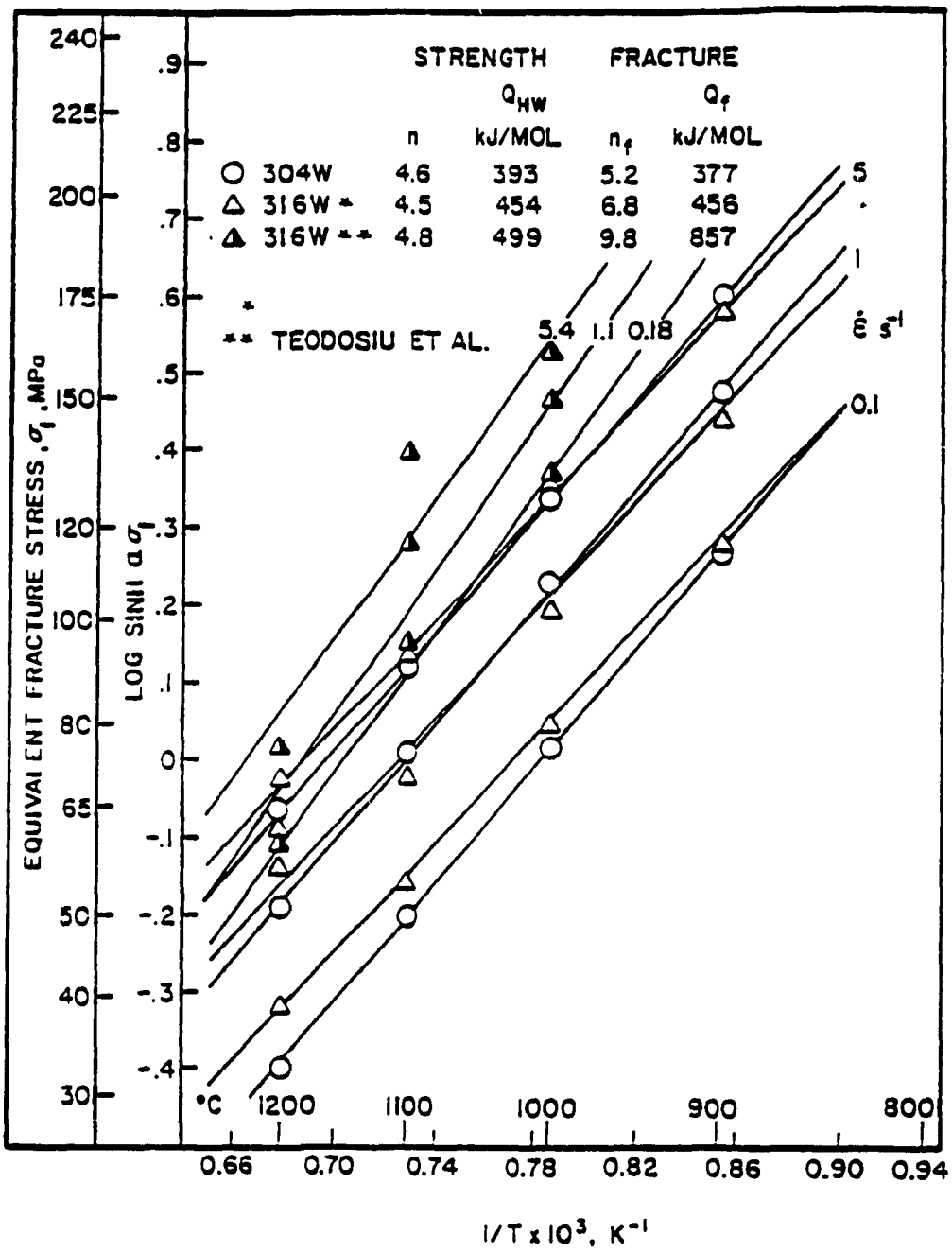

Fig. 43b. The sinh $\alpha\sigma_f$ relationship for 304W and 316W depends on T according to an Arrhenius relationship, giving a straight line for each $\dot{\varepsilon}$. Published data are included for completeness (191).

solution for the Mo bearing 316W. As T decreases and $\dot{\varepsilon}$ remains at 5 s^{-1}, their ductilities begin to diverge, being 6.3 for 304W and 4.6 for 316W at 900°C. The 316W differs markedly from the 304W in that the ductility decreases as $\dot{\varepsilon}$ rises; this appears in Fig. 43a only as a divergence downwards of the 316 points at 1 and 5 s^{-1}. The 317W alloy behaves similarly to 316W.

4.5.3 ELFMARK DUCTILITY ANALYSIS

According to Elfmark (251, 252) (Sec. 2.7.6), the temperature compensated time for DRX, W_{DRX}, is given by the following expression:

$$W_{DRX} = t_{DRX} \exp(-Q_{DRX}/RT) \qquad (40)$$

and is plotted against Z_{DRX} on a log-log scale in Fig. 44a. This function draws the data for all conditions into a single line in the same manner as the line of sinh $\alpha\sigma$ versus Z (Fig. 15). The following function satisfies 301W, 304W, 316W, and 317W:

$$W_{DRX} = 0.08\ Z_{DRX}^{-0.88} \qquad (48)$$

which compares with a power of 0.90 found by Elfmark (251) for γ stainless and a wide variety of carbon steels. The W_{DRX} function is the inverse of the stress one, hence high ductility is associated with high W_{DRX} values but with low σ values. The ductility for 316W is finally related to W_{DRX} in Fig. 44b where the resulting straight line indicates a unique relationship:

$$\varepsilon_f\ Z_{DRX}^{-1} = 7 \times 10^4\ W_{DRX}^{1.37} \qquad (49)$$

The slope of 1.37 agrees with 1.33 determined by Elfmark (251).

4.5.4 DUCTILITY IMPROVEMENT FROM MULTISTAGE SRX

In multistage tests, the ductility of an alloy augments considerably (Sec. 2.7.6). Figure 45 illustrates an increase of 50% for the present 304C and that of another author (180) for 304W; this increase is also seen in

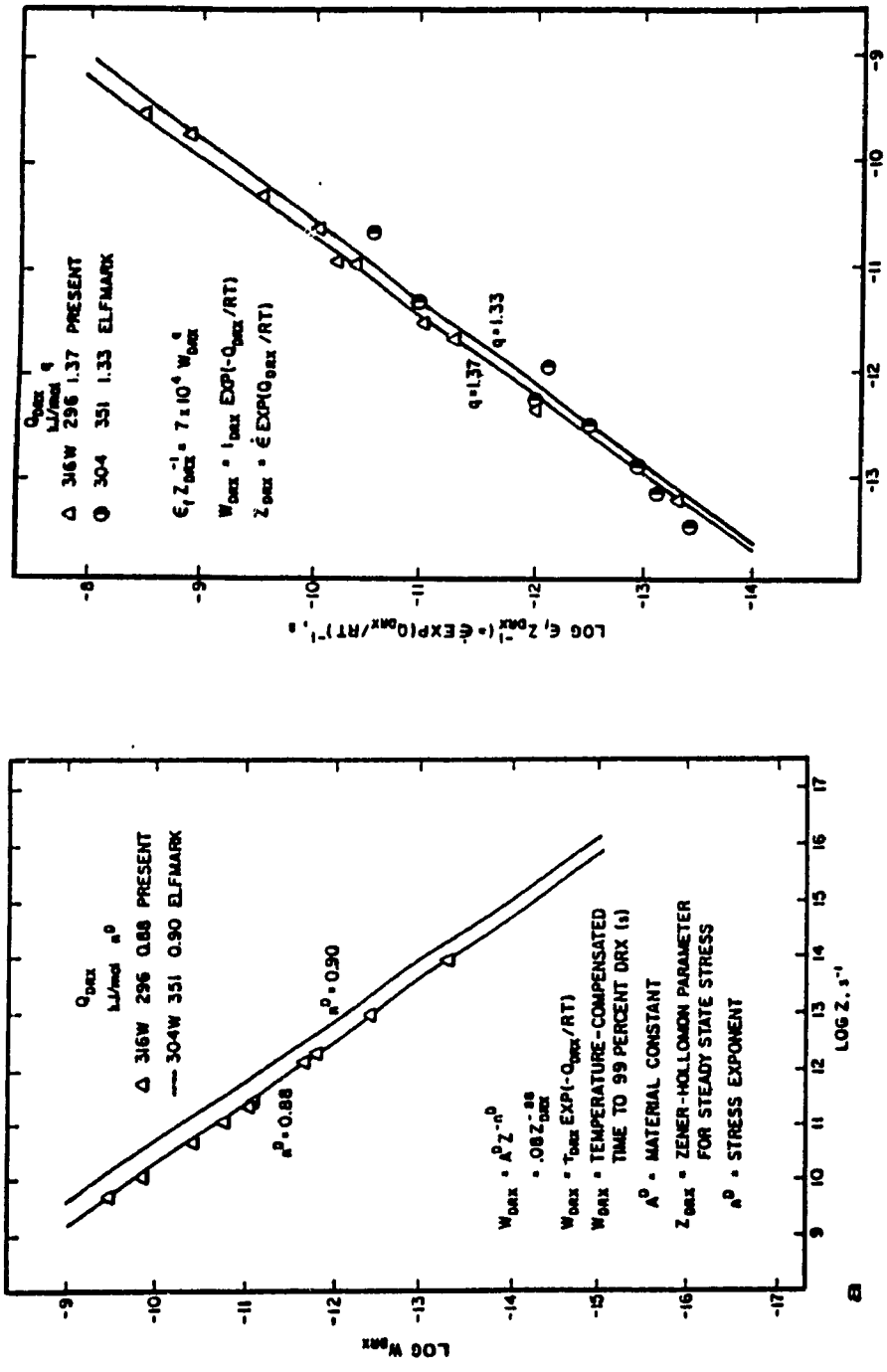

Fig. 44. a) The temperature compensated time for DRX, W_{DRX}, plotted against Z_{DRX} illustrates how the T compensated $\dot{\varepsilon}$ draws the data into a single line, and b) the dependence of ductility (ε_f Z_{DRX}^{-1}) on W_{DRX} is a single line for all deformation conditions, being in agreement with the 304W data of Elfmark (251, 252).

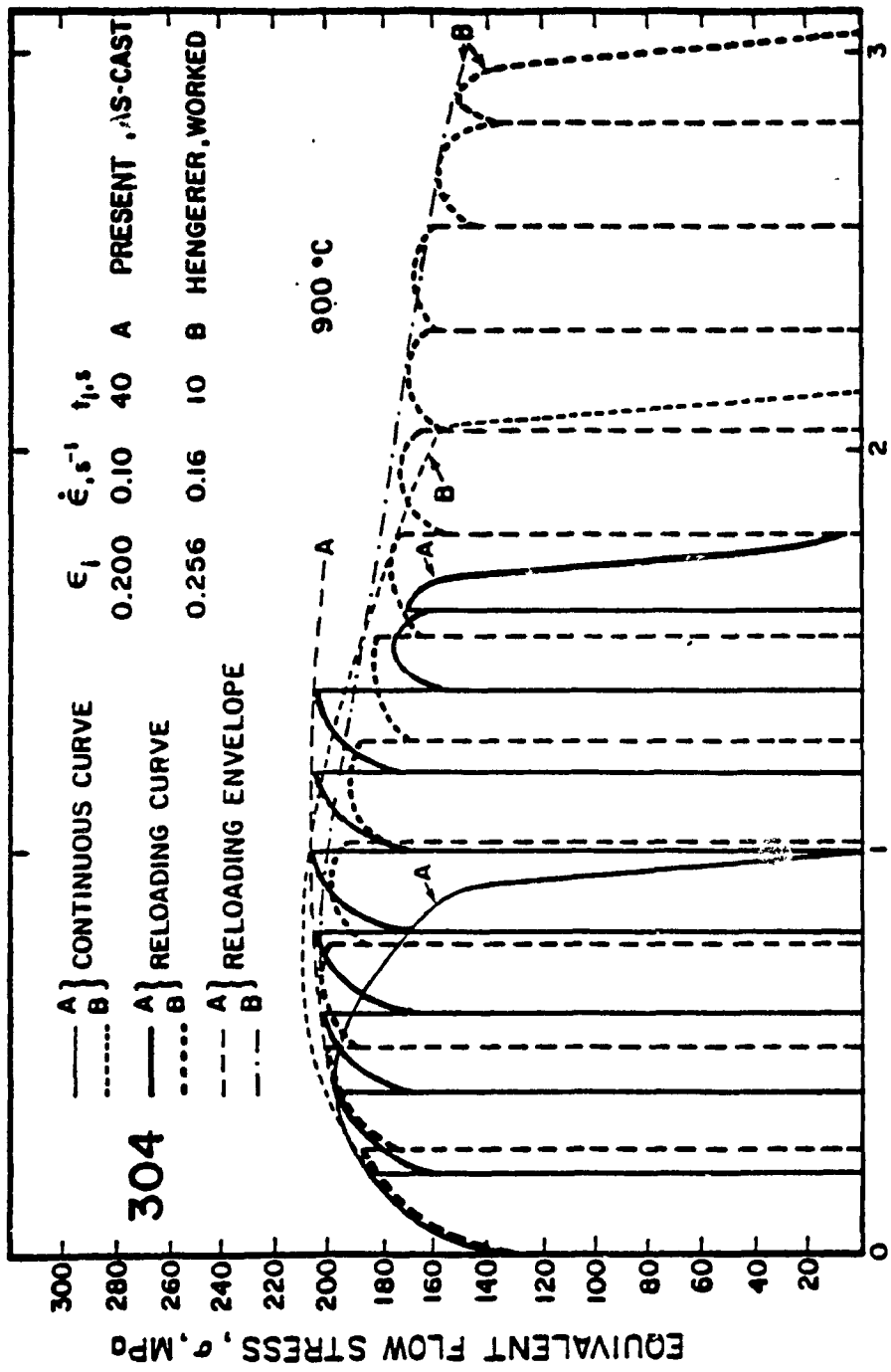

Fig. 45. Multistage flow curves of 304C deformed at 900°C, 0.1 s^{-1} show the ameliorating effects of SRX on ductility compared to continuous straining. Published 304W data under similar deformation conditions are included for comparison (180).

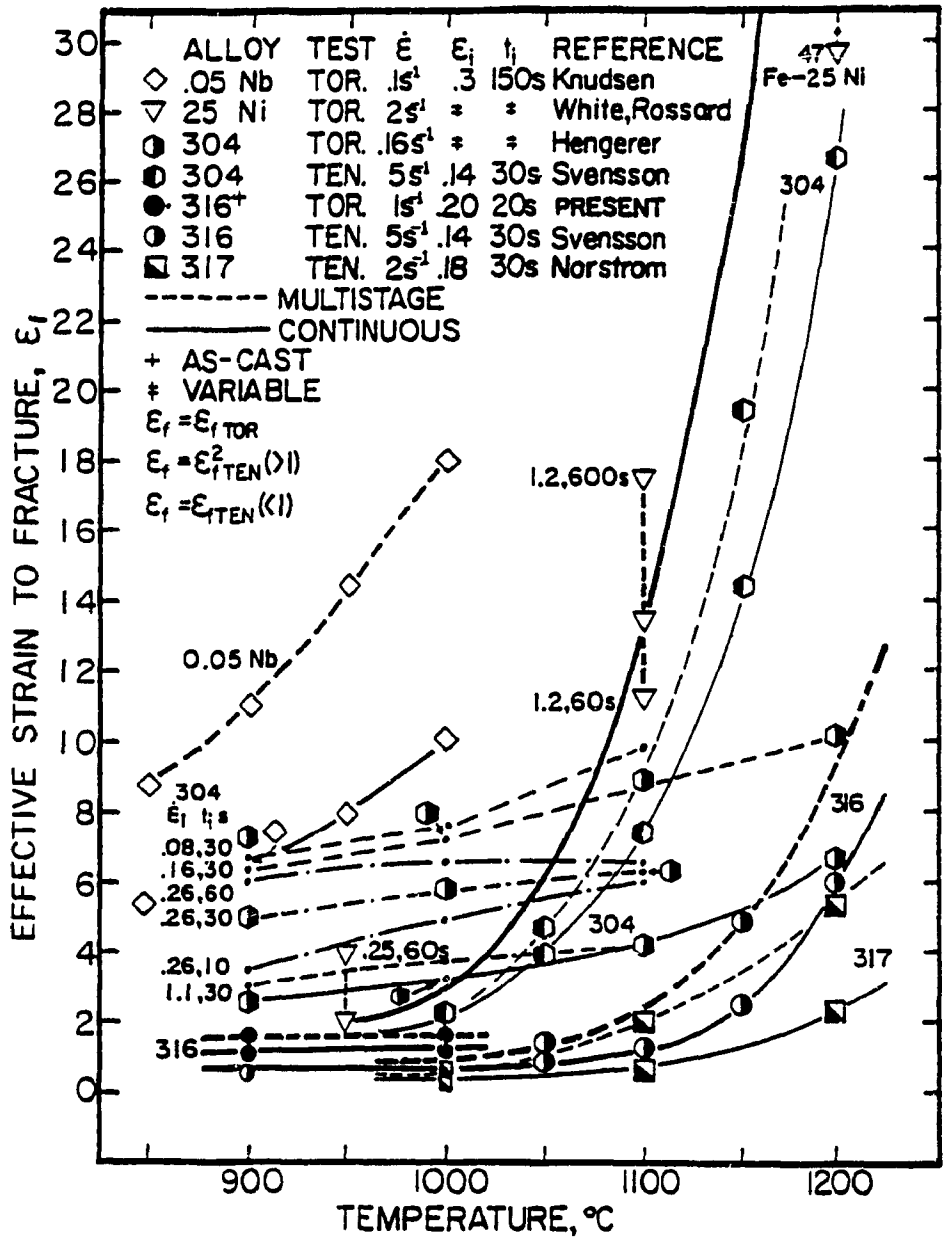

Fig. 46. A plot of fracture strain versus T illustrates the generally ameliorating, but sometimes deleterious (at short times) effects of interval for SRX upon ductility. 316C is compared with extensive published data (12, 106, 180, 229, 230, 233). Tensile strains have been converted to torsion according to Eqn. 43.

Fig. 36c. Ductility rises with increases in pass strain and interval. The surveyed results (12, 106, 180, 230, 233) in Fig. 46 further show that, compared to continuous straining, ductility is higher in isothermal multistage tests where individual passes do not initiate cracking and time intervals are sufficient to cause substantial SRX.

4.5.5 MICROSTRUCTURAL EVIDENCE FOR FRACTURE MECHANISMS

Figure 47 shows concentration of pores below surface grooves in 304W (900^{o}C, 5 s^{-1}). Broad surface cracks in 301W deformed at 1100^{o}C, 5 s^{-1} are shown in Fig. 48. In Fig. 49, a strip of longitudinal section extending inwards from the surface illustrates diminishing pore density with decrease in ε and $\dot{\varepsilon}$. In the 316W alloy, discrete pores and fissures are observed in Fig. 50. In 317W with the lowest ductility at 1100^{o}C, 1 s^{-1}, Fig. 51a shows fairly large discrete pores on the grain boundaries. Also, for 317W deformed at 900^{o}C, 1 s^{-1}, stringers of retained δ ferrite containing fissures are easily observable in Fig. 51b.

4.5.6 AS-CAST DUCTILITY (SUUTALA ANALYSIS)

The ductility of the as-cast alloys compared in Fig. 52 are in agreement with the results of Myllykoski and Suutala (109), with 317C solidifying in the γ mode and 304C and 316C solidifying in the δ mode. The ductility peak occurs when the $Cr_{eq.}/Ni_{eq.}$ ratio (109) is slightly higher than 1.5. Therefore, 316C being closest to the transition has the greatest ductility because the δ occurs in the smallest volume fraction at the dendrite cores where it is less likely to induce interphase cracking, being away from the impurities segregated at the γ grain boundaries.

In these as-cast specimens, it can be seen that fissures are associated with δ ferrite. The δ ferrite which formed between the dendrites

Fig. 47. An optical micrograph of a longitudinal section of a 304W specimen deformed at 900°C, 5 s^{-1} illustrates a high density of pores forming beneath a groove. X 135.

Fig. 48. An optical micrograph of a tangential section of a 301W specimen deformed at 1100°C, 5 s^{-1}shows broad surface cracks which are most marked at opposite edges where the section is closest to the surface and almost disappear in the middle except for their deepest tips. X 150.

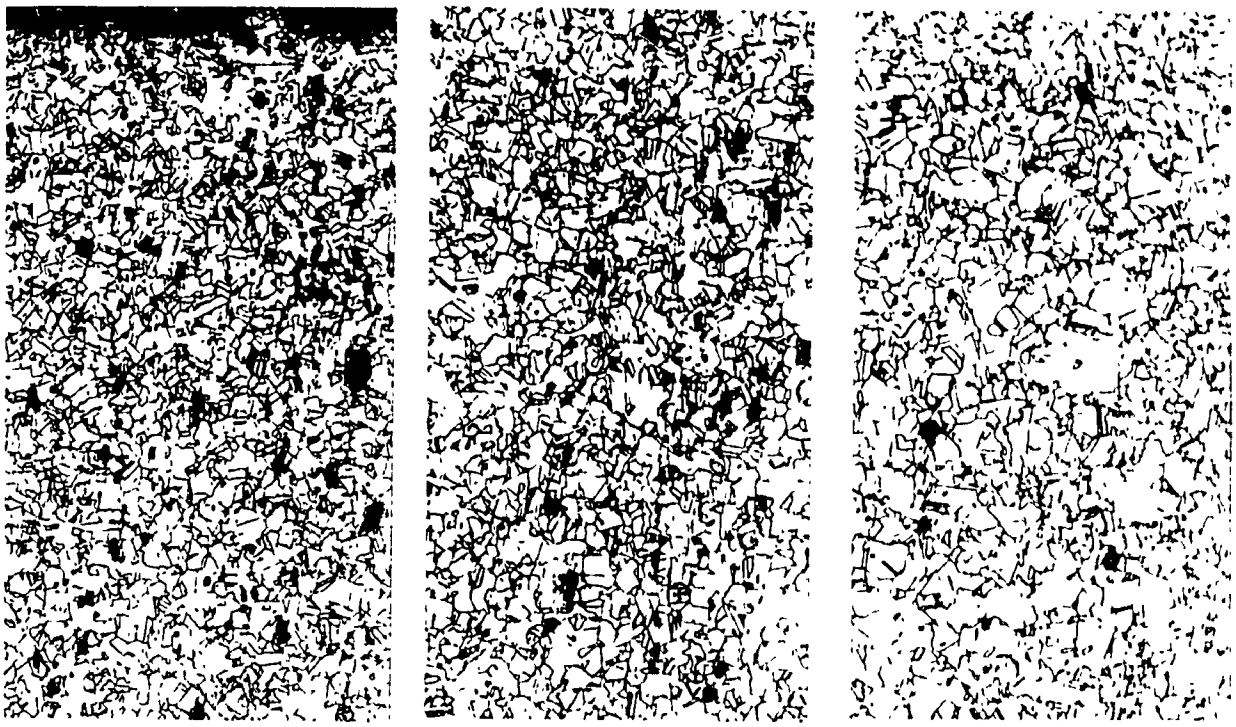

Fig. 49. Optical micrographs of a 301W specimen deformed at 1000°C, 1 s^{-1} depicts a narrow strip extending inwards from the surface in sequence (a,b,c); the pore density decreases as a result of the strain gradient. X 75.

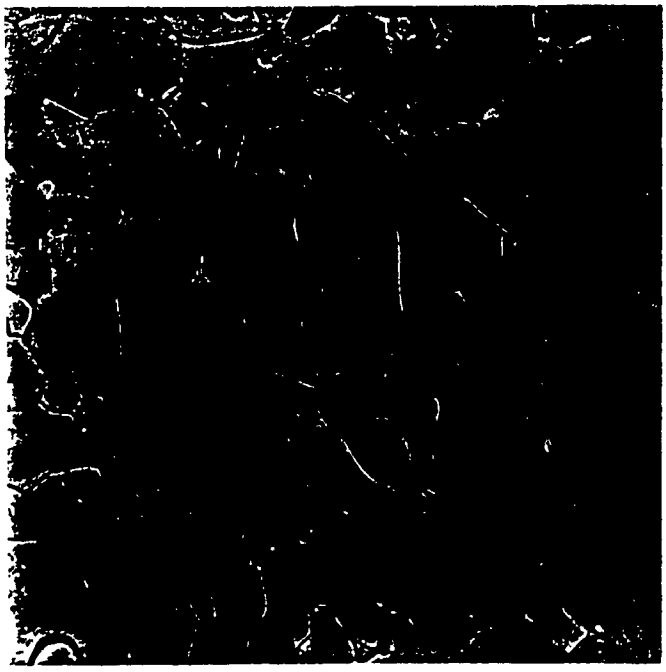

Fig. 50. An optical micrograph of a 316W specimen deformed at 1200°C, 5 s^{-1} illustrates widely spaced pores at high T. X 150.

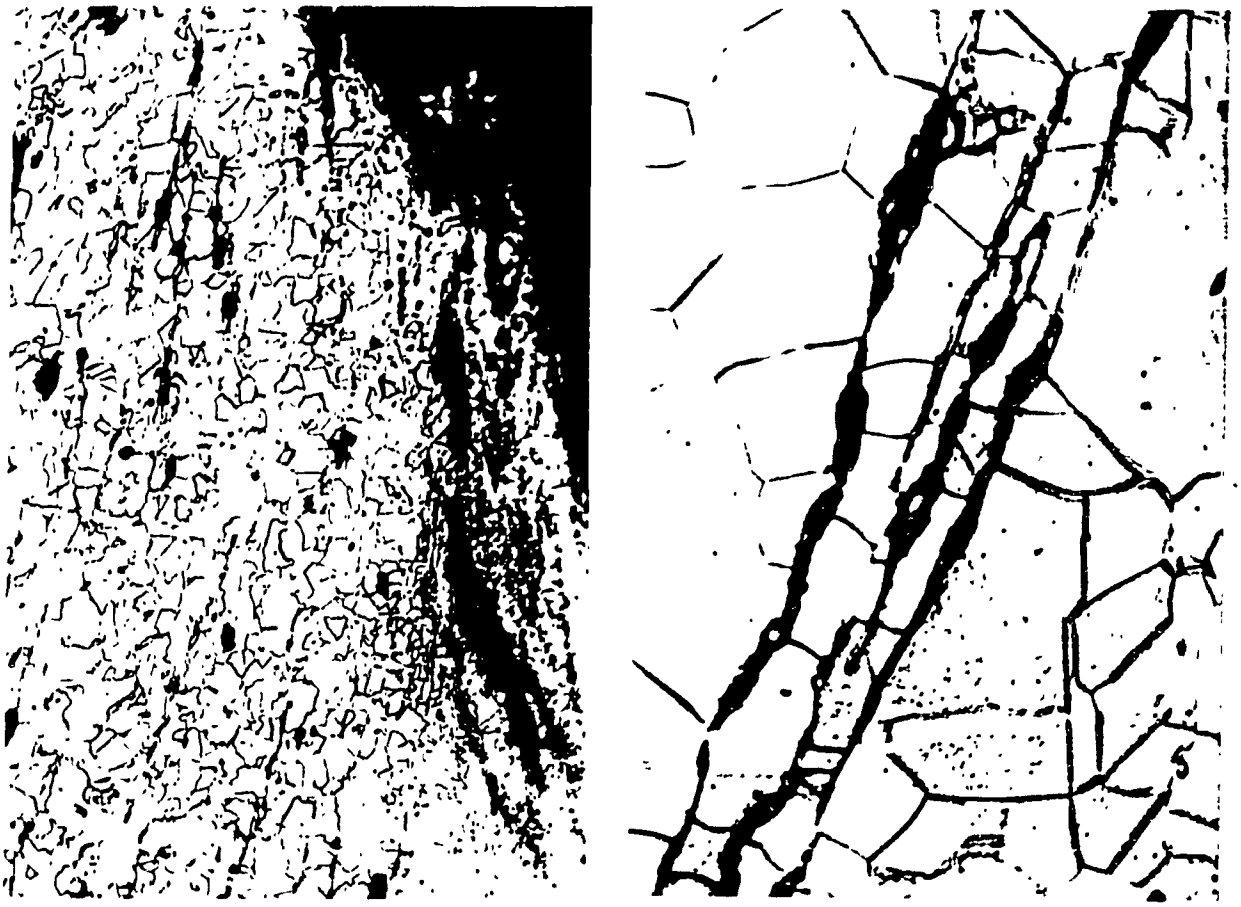

Fig. 51. Optical micrographs of a 317W specimen deformed at 900°C, 1.0 s^{-1} taken from a) a tangential section showing auxiliary cracks, fissures, and pores about to link up. X 100, and b) a longitudinal section near the failure zone exhibiting stringers of δ phase which contains fissures. X 600.

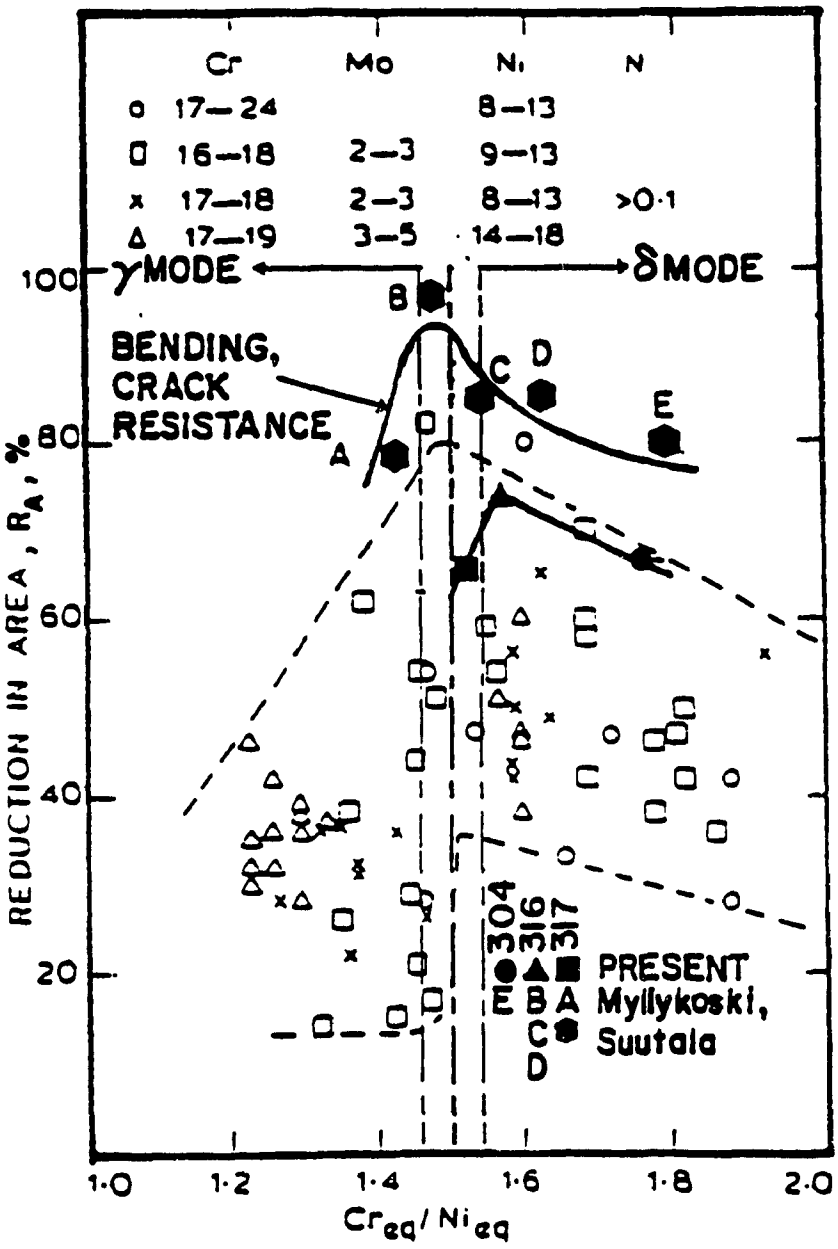

Fig. 52. The ductility of the 304, 316, and 317 as-cast alloys is plotted against the ratio Cr_{eq}/Ni_{eq} on a graph of published results collected by Myllykoski and Suutala (109). The increase in ductility as the ratio decreases from 2.0 to 1.5 is related to a diminishing δ phase content with δ mode solidification. Below 1.5, the drop in ductility is associated with the combined segregation of δ and impurities in γ mode solidification. The present results are in agreement if the change in solidification mode occurs at a ratio of 1.5 ± 0.05.

Fig. 53. Optical micrograph of a) a longitudinal section of 317C deformed at 1000°C, 0.1 s^{-1} showing cracks parallel to the stringers of δ phase. X 200, and b) a tangential section of 316C specimen deformed at 1000°C, 5 s^{-1} showing δ stringers in elongated form connected by pores and leading to surface grooves. X 200.

during solidification, becomes elongated and oriented normal to the axis of the specimen. In 317C (Fig. 53a), branching cracks are observed parallel to the elongated δ ferrite with many pores lying along the δ stringers. In 316C, the δ dendrites are at the cores of the γ grains and deform into distorted shapes which are associated with pores or large cracks as shown in Fig. 53b.

4.6 MICROSTRUCTURES

4.6.1 OPTICAL MICROSTRUCTURES

While Fig. 54a shows the δ ferrite along the cores of the original dendrites of a longitudinal section of 304C, Fig. 54b illustrates interdendritic ferrite in a transverse section of 317C (both before hot torsion). The three optical micrographs in Fig. 55a-c show segregated δ ferrite in undeformed 317C, and DRX grains and elongated δ ferrite in 317C deformed at 1000°C, 0.1 s^{-1}, and at 1000°C, 1 s^{-1}. Specimens tested to beyond the onset of steady state exhibited uniform equiaxed DRX grain structures which are finer than the original grain size for all alloys. It can be seen that 301W DRX grain sizes (Fig. 56a,b) of 13μm and 24μm, arising from deformation at 900 and 1100°C at 5 s^{-1}, are finer than the original grain size of 66μm. The long marks are spiral grooves from oxidation during twisting.

As shown in Fig. 57a-d, refinement of the 304W original grain size from 70μm to 12 and 45μm occurred for deformation conditions of 900°C, 5 s^{-1} and 1100°C, at 5 s^{-1}. An exception to this occurred at low Z (1200°C, 0.1 s^{-1}), where the original grains coarsened to 78μm (Fig. 57d) in association with a periodic flow curve. When the quenching was slow, the nuclei produced during deformation grew metadynamically (Sec. 2.5.3) from

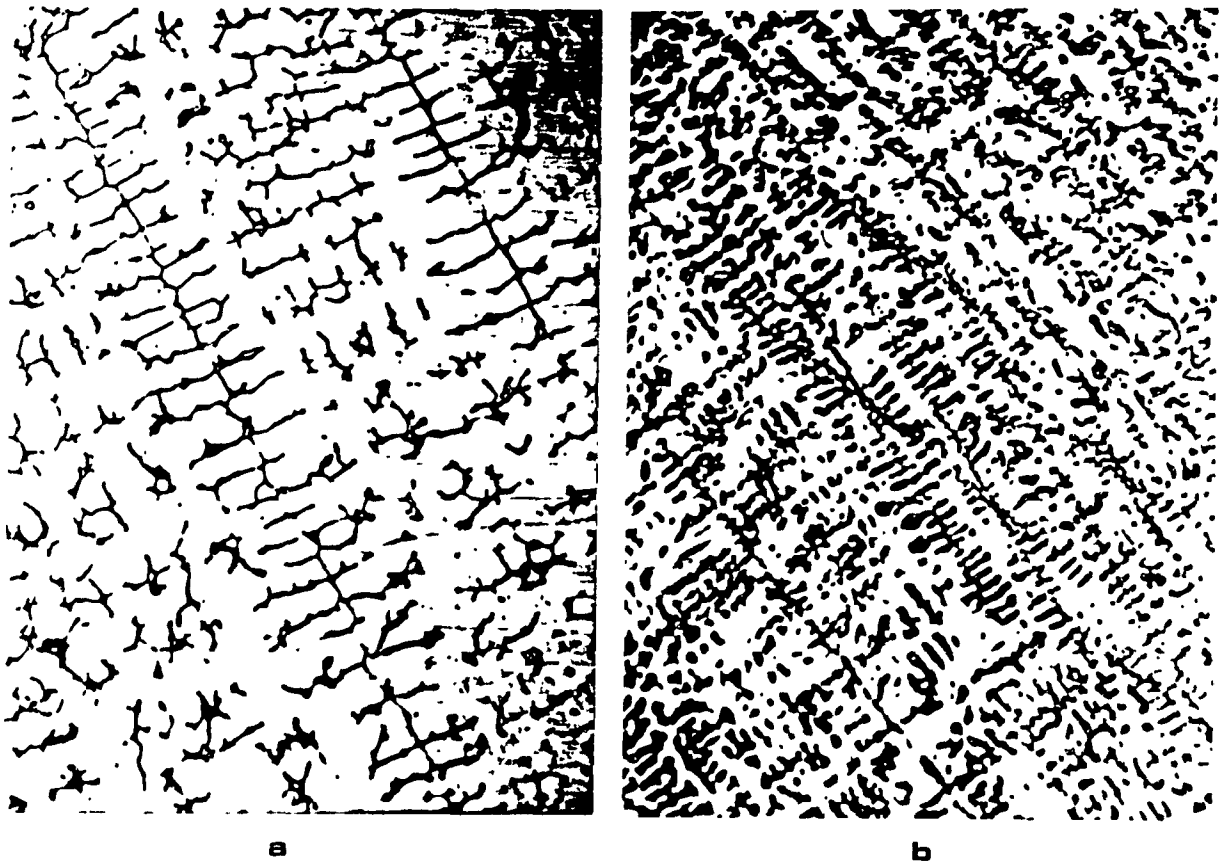

Fig. 54. An optical micrograph of an undeformed longitudinal section of a) 304C specimen revealing δ ferrite along the cores of the original dendrites. X 40, and b) 317C specimen revealing interdendritic δ ferrite. X 40.

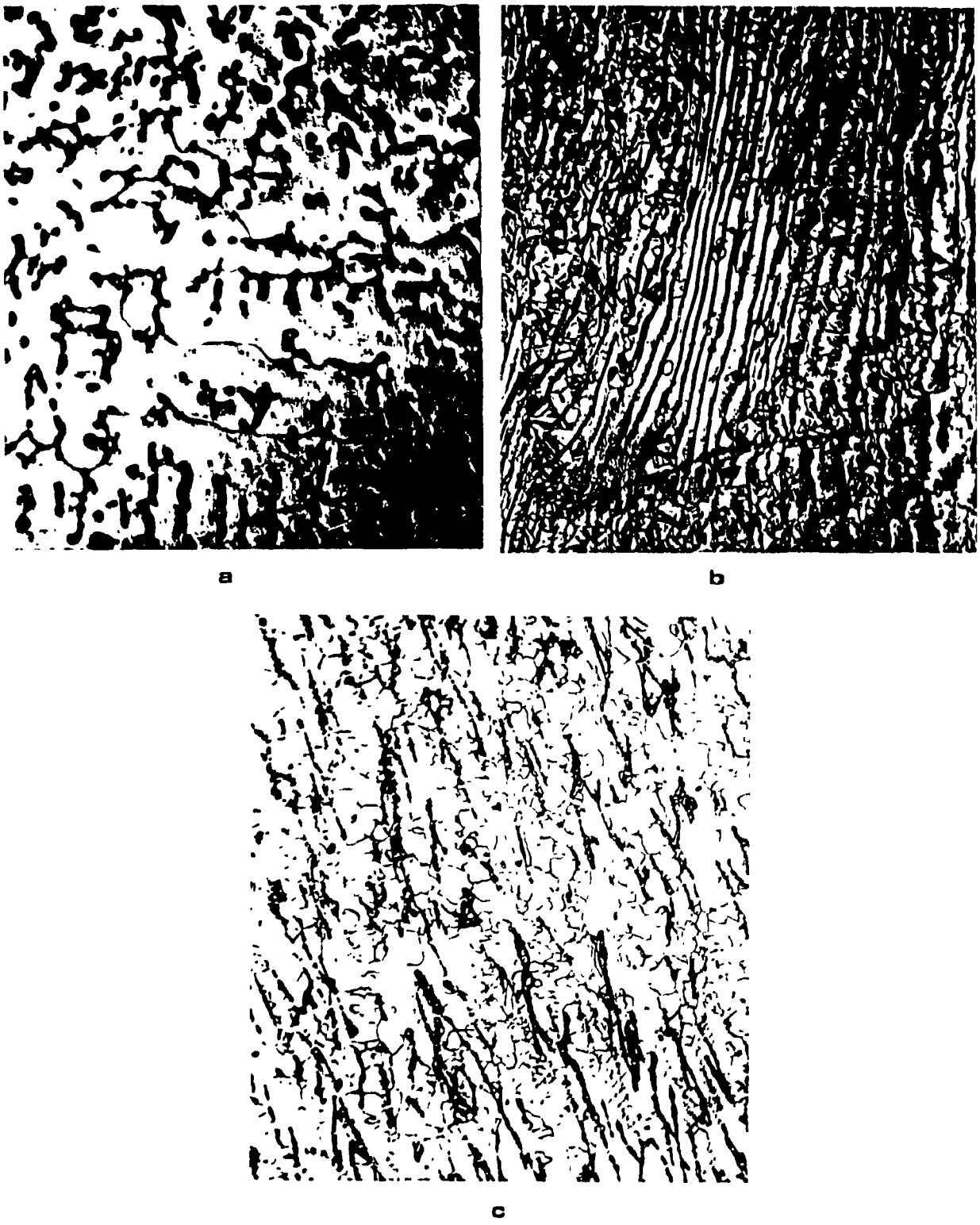

Fig. 55. Optical micrographs of tangential sections of 317C specimens a) recrystallized grain with δ ferrite. X 100, b) deformed at 1000°C, 0.1 s^{-1} the DRX grains with δ ferrite. X 100, and c) deformed at 1000°C, 1.0 s^{-1} DRX grains with δ ferrite.X 300.

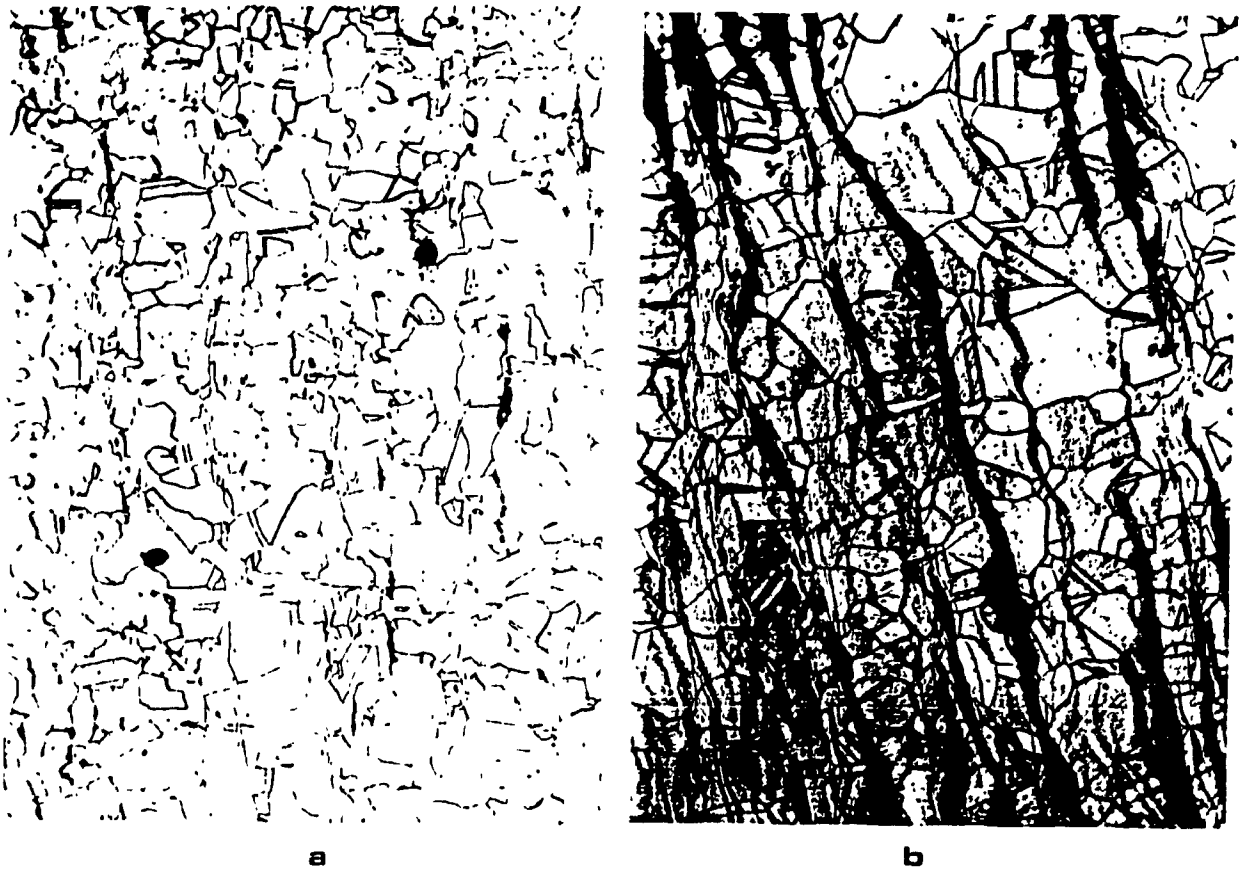

Fig. 56. Optical micrographs of tangential sections of 301W a) deformed at 900°C, 5 s^{-1} illustrates the small slightly elongated DRX grains. X 300, and b) deformed at 1100°C, 5 s^{-1} shows large equiaxed DRX grains. X 150.

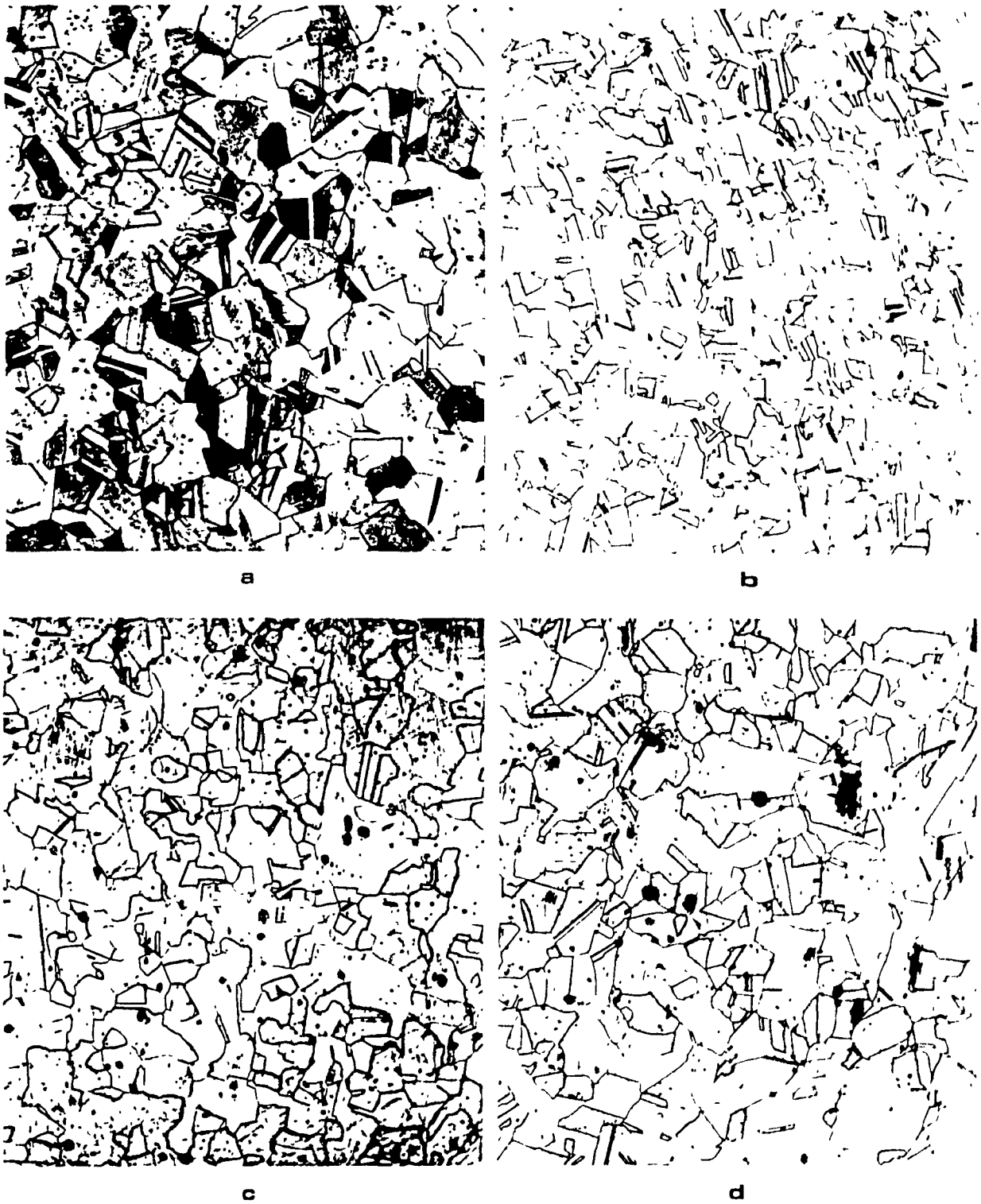

Fig. 57. Tangential section of 304W a) prior to hot torsion, showing original homogenized grains, b) deformed at 900°C, 5 s^{-1}, refined DRX grains. X 300, c) deformed at 1100°C, 5 s^{-1} medium equiaxed DRX grains. X 150, and d) deformed at 1200°C, 0.1 s^{-1}, coarse DRX grains. X 75.

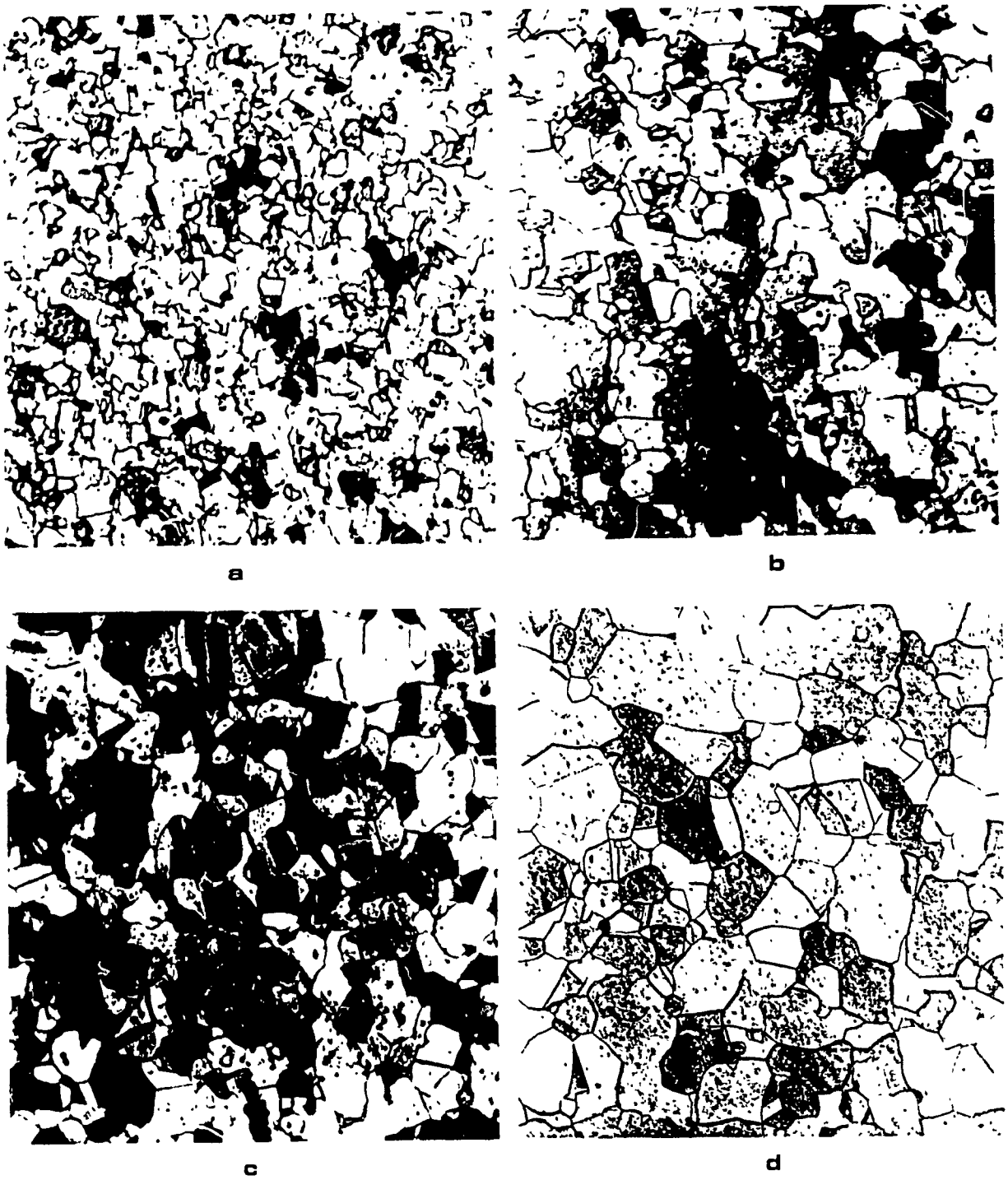

Fig. 58. Microstructures on tangential sections of 316W a) deformed at 900°C, 0.1 s^{-1}, very fine DRX grains. X 400, b) deformed at 1000°C, 0.1 s^{-1}, refined DRX grains. X 300, c) deformed at 1100°C, 0.1 s^{-1} medium DRX grains. X 200, and d) deformed at 1200°C, 5 s^{-1}, large equiaxed grains. X 150. These four micrographs illustrate that DRX grains enlarge markedly with rising T.

25 to 45μm as can be seen in Fig. 57b. The microstructures of 316W deformed at 900, 1000, 1100°C at 0.1 s^{-1} and at 1200°C, 5 s^{-1} (Fig. 58a-d) are equiaxed and enlarge markedly with rising T. The following micrographs (Fig. 59a-c) illustrate the increase in D_s in 317W as T increases from 900 to 1200°C at 5 s^{-1}. The overall microscopic evidence is that refinement takes place under all these deformation conditions in agreement with Fig. 23, and as explained later, with the theory of Sakai and Jonas (133, 136, 137), i.e. for the initial grain size, Z always exceeds the critical value (Sec. 4.6.3). Moreover, since all alloys deformed to a given pass strain of 5 produced DRX grains, Z also lies below the limiting Z value as illustrated in Fig. 21.

4.6.2 STATICALLY RECRYSTALLIZED MICROSTRUCTURES

Due to complete SRX after the first pass of multistage deformation depicted in Fig. 31, the new grain sizes of 301W and 304W are smaller at 36 and 40μm (Fig. 60a,b) than their respective original grain sizes of 66 and 70μm. The 304W grain size is refined from 70 to 10μm (Fig. 61) after seventeen passes with T declining from 1200 to 900°C at 1 s^{-1} (Sec. 4.7.1). This compares with a DRX grain size of 14μm produced by an isothermal continuous test conducted at 900°C, 1 s^{-1} as presented below (Fig. 62).

4.6.3 GRAIN SIZE DEPENDENCE ON Z PARAMETER AND STEADY STATE STRESS

The log-log plot of Z against D_s, solid lines Fig. 62 (133) is approximately linear for all steels (Sec. 2.3.4). In addition, the graph contains the points showing the critical Z_c for grain refinement against the initial grain size D_0 on a scale which is half that of D_s. The observed critical change-over points from Fig. 23 are marked by crosses on the symbols and dashed lines are drawn through them parallel to the D_s lines.

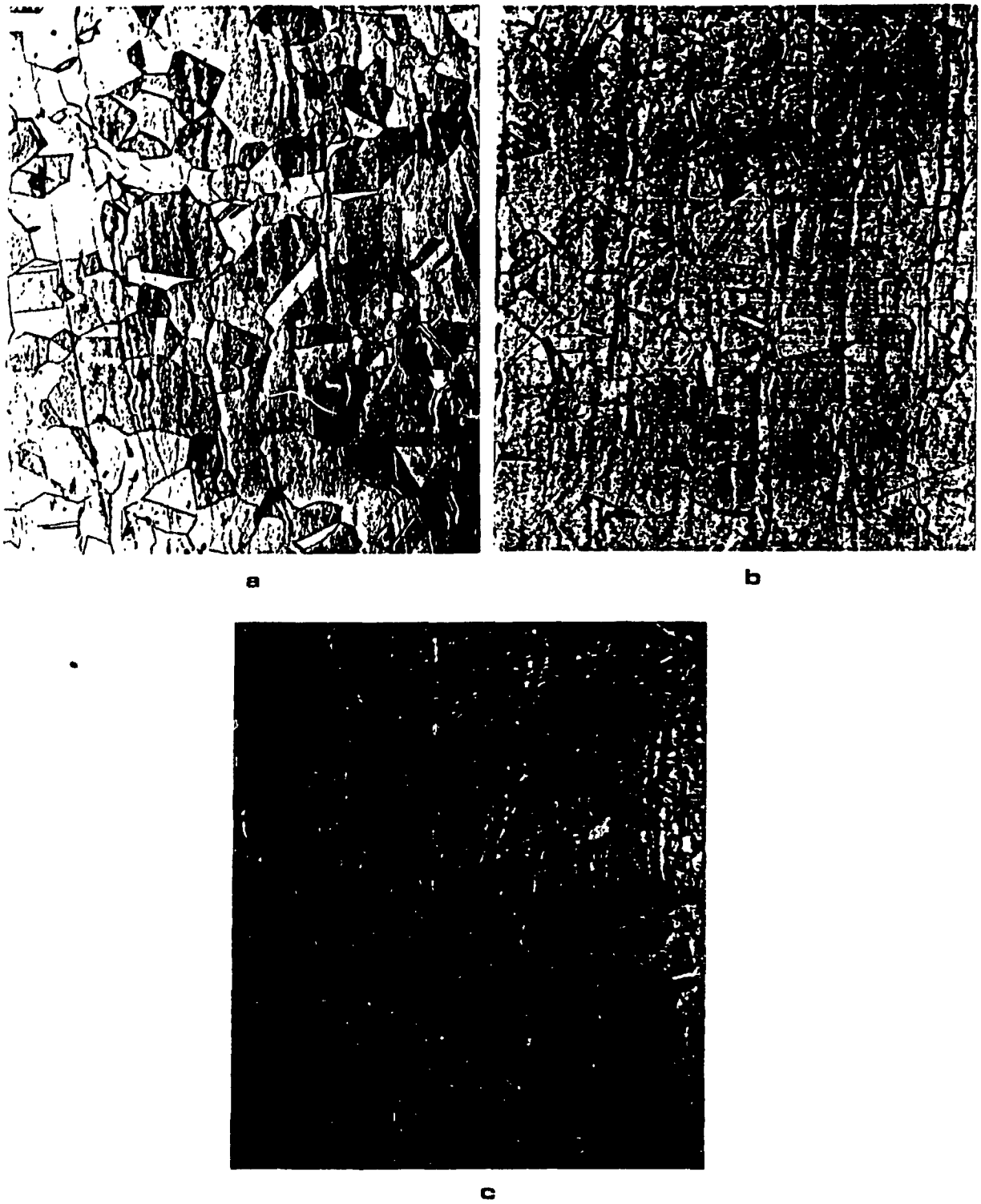

Fig. 59. An optical micrograph of tangential sections of 317W deformed at 5 s^{-1}, a) at 900°C, refined grains. X 600, b) at 1000°C, medium equiaxed DRX grains. X300, and c) at 1100°C, coarse equiaxed DRX grains. X 200.

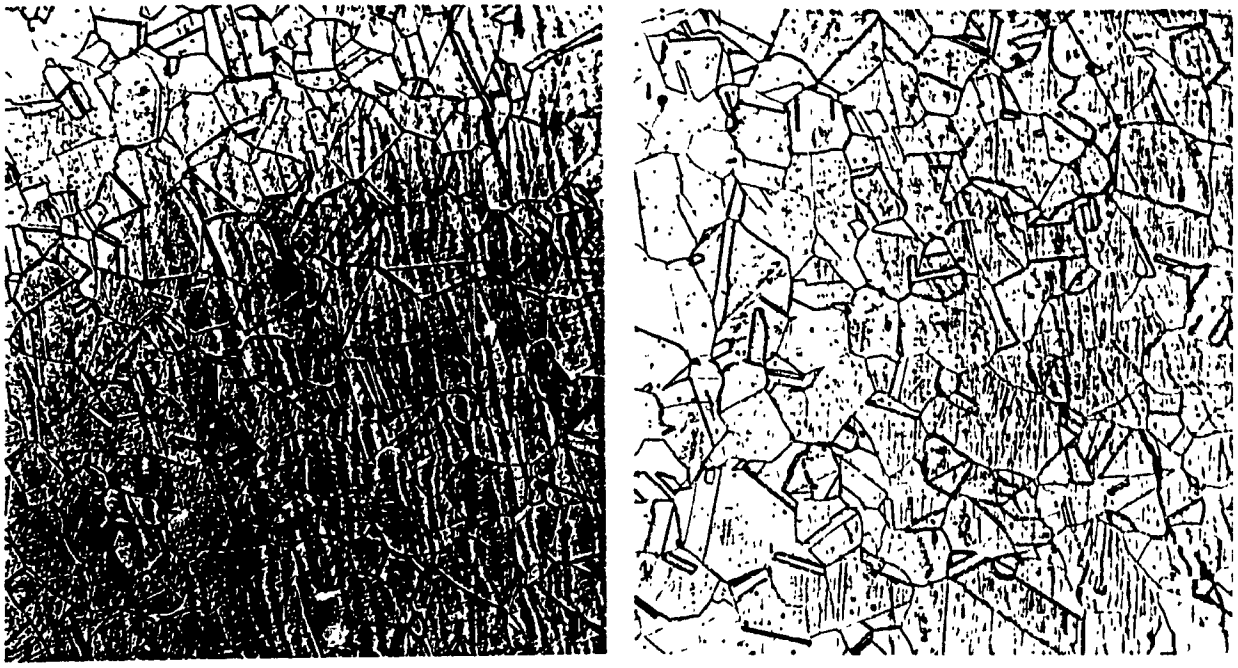

a b

Fig. 60. Optical micrographs of tangential sections of a) a 301W specimen, X 150, and b) a 304W specimen, X 150, subjected to multistage deformation at 1100°C, 1 s^{-1} with 60s interval duration, leading to a complete SRX microstructure. X 150.

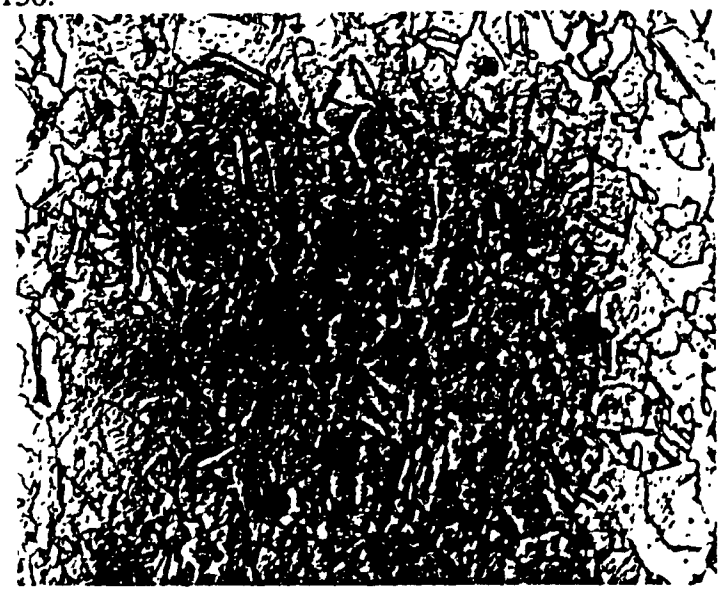

c

Fig. 61. Tangential section of a 304W specimen subjected to a schedule where T has decreased from 1200-900°C, 1 s^{-1} at 0.9°C/s. X 400. The original grain diameter of 70μm has been refined to 10μm.

These two lines (Z versus D_s and Z_c versus D_0) coincide for 304W. In agreement with theory of Sakai and Jonas (133, 136, 137), the congruence occurs at Z versus approximately 1.7 D_s for 301W, 316W, and 317W which is similar to the 1.8 reported for the 0.16C alloy (133). Since all alloys have different Z values due to differing Q_{HW} values, the slopes are normalized at 900°C, 1 s^{-1} where solute interactions cause the widest variations in DRX behavior. Therefore, for a combination of D_0 and Z lying to the left of the dashed line, grain coarsening takes place. Conversely, for a point with coordinates D_0 and Z lying to the right of the dashed line, grain refinement takes place. At 900°C, 1 s^{-1}, the initial grain size which is the lower limit for refinement increases from about 8 to 14μm in the sequence 317W, 316W and 301W. For the same sequence of steels with 50μm starting diameter, the Z for refinement increases as indicated by the vertical line in Fig. 62. Z_c rises in the sequence, 304W, 316W, and 317W, so that for $\dot{\varepsilon}$ = 1 s^{-1}, the upper limits for refinement are 1130 (0.16C), 1190 (301W), 1180 (304W), 1210 (316W), and 1240°C (317W). In order to reduce D_s from 50 to 10μm, T has to be decreased from the above temperature to 830, 840, 850, 900, and 930°C in the same sequence.

Figure 63 is a a log-log plot of D_s versus the steady state flow stress (σ_s). While there is some scatter of the data for the present and other work (138, 168, 174, 195), a straight line is drawn through the points with a slope of -1.23. Those specimens which were quenched sometime after deformation had metadynamically recrystallized and gave larger grain sizes (D_{MRX}) than the DRX ones. These data lie above those of DRX having a slope of -1.31. These behaviors are expressed by the following formulae:

$$D_s = B\ \sigma_s^{-k_s} = 6.8\ \sigma_s^{-1.23} \qquad (50)$$

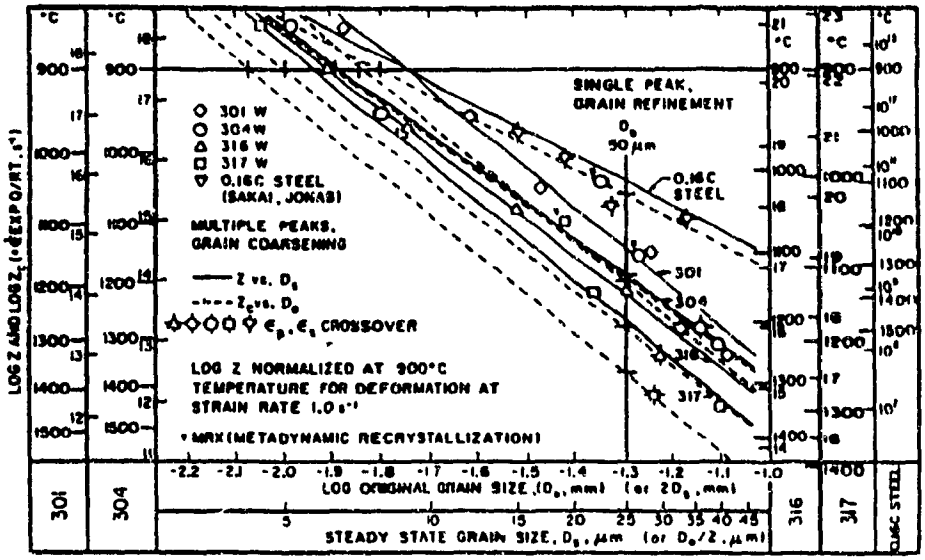

Fig. 62. Logarithmic plot of Z_c versus D_o (points with crosses) and Z versus D_s with scale twice D_o (open points). For comparison purposes, the values of Z_c for alloys 301W, 304W, 316W, and 317W and 0.16C (133) with an ideal original grain diameter of 50 μm are indicated.

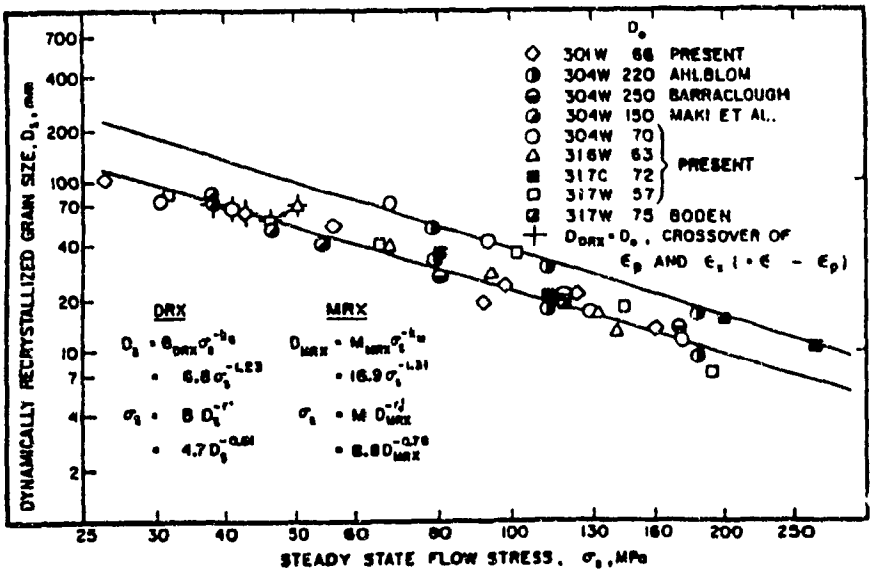

Fig. 63. A logarithmic plot of D_s versus σ_s demonstrating negative slopes of 1.23 and 1.31 for DRX and MRX, respectively. Crossover points for 301W, 304W, 316W, and 317W determined from plots such as Fig. 23 are shown. Published data are included for completeness (138, 168, 174, 195).

$$D_{MRX} = M\ \sigma_s^{-k_M} = 16.9\ \dot{\sigma}^{1.31} \qquad (51)$$

4.6.4 TRANSMISSION ELECTRON MICROGRAPHS

Examination of specimens of 304W, 316W, 317W and 317C by TEM reveals subgrains which range from elongated at high Z to equiaxed at low Z. It should be noted that all the specimens have undergone recrystallization as confirmed by optical metallography; thus the substructure confirms that it is DRX. Moreover, the variations in both D_s and d_s with Z indicate the close connection between the two and that they both play an important role in defining the flow curve.

The 304W set of micrographs shown in Fig. 64a-d show elongated substructures formed by DRV at high Z (900°C, 5 s^{-1}). Of particular interest is the DRV colony surrounded by SRX grains depicted in Fig. 64c. At low Z (1200°C, 0.1 s^{-1}, Fig. 64d), the subgrains become equiaxed. These micrographs illustrate much larger subgrains, 6.7μm at low Z compared to 1.5μm at high Z (Fig. 64a) Both micrographs of 316W, depicted in Fig. 65a,b illustrate DRV substructures at both 1100° and 1200°C at 5 s^{-1}.

In 317W, Fig. 66a,b illustrates the increase in subgrain size and decrease in aspect ratio as Z decreases through the range 1000°C at 1 s^{-1} to 1100°C at 5 s^{-1}. Within each specimen, there is a variation in subgrain shape and orientation. As with the other alloys, the elongated subgrains are more frequent and regularly spaced at high Z (Fig. 66a). Figure 67a-d reveals: a) DRX grains distinguished by variations in the substructure, b) the appearance of a DRX nuclei, c) SRX grains with twins growing statically into the substructure leaving few dislocations. Figure 67d depicts a region of SRX grains nucleated around δ stringers which contain a DRV substructure. Finally, a set of TEM micrographs (Fig. 68a-d) of 317C

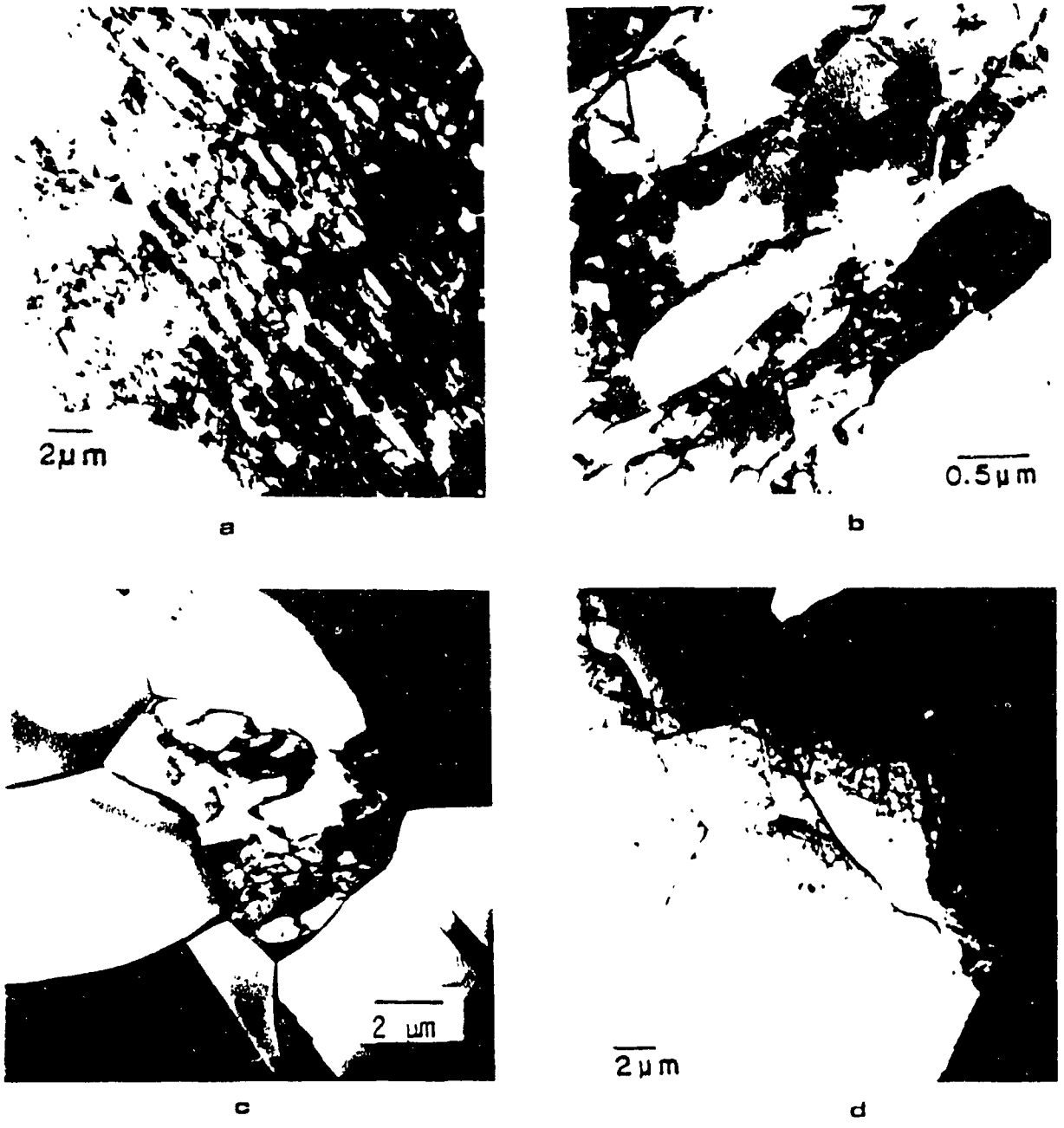

Fig. 64. TEM micrographs of tangential sections of 304W a;b) deformed at 900°C, 5 s^{-1}, elongated subgrains, c) deformed at 900°C, 5 s^{-1}, a DRV colony of subgrains surrounded by SRX grains.and d) deformed at 1200°C, 0.1 s^{-1}, large equiaxed subgrains which grow markedly with increasing T.

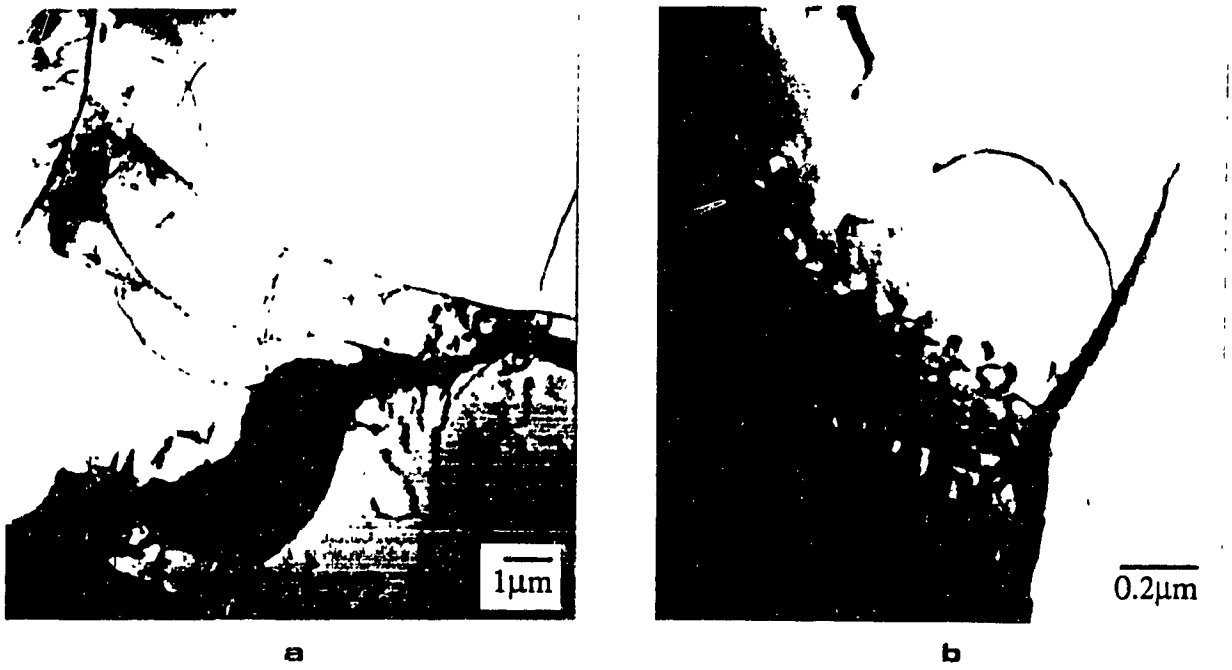

Fig. 65. TEM micrographs of tangential sections of a 316W a) deformed at 1100°C, 5 s^{-1} the DRV substructure with DRX grains, and b) deformed at 1200°C, 5^{-1} the markedly large subgrains from increased T.

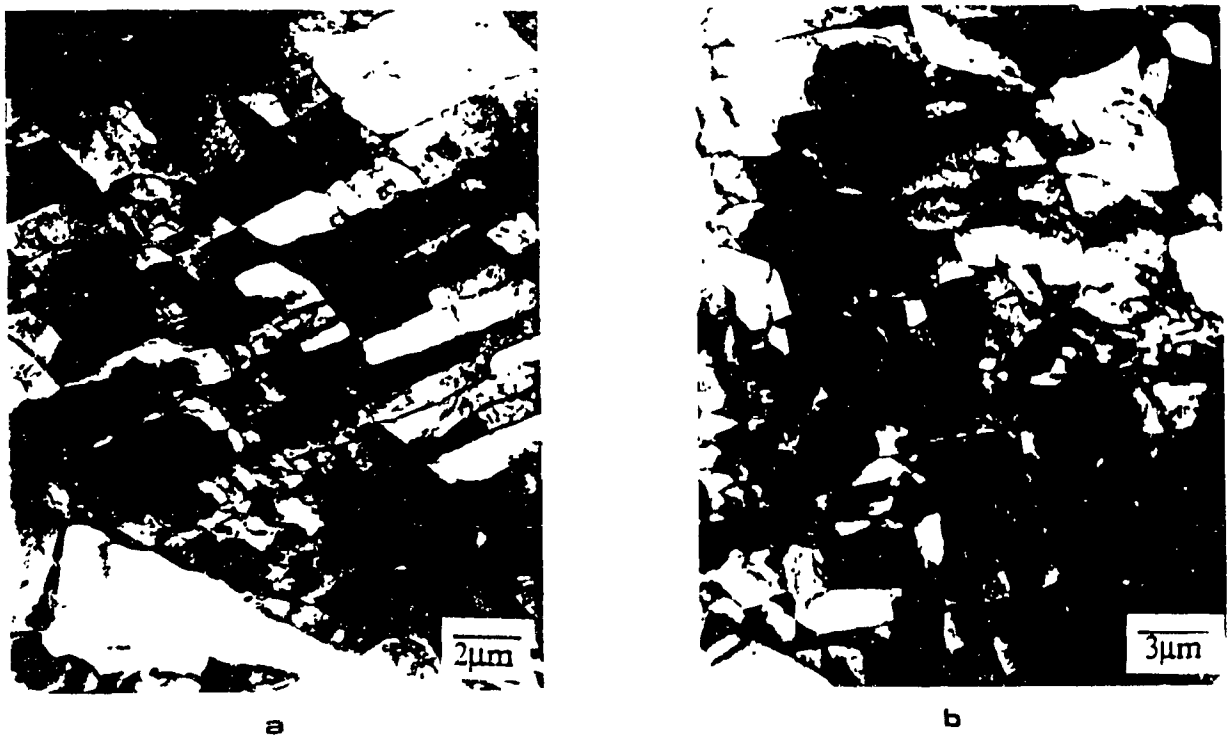

Fig. 66. TEM micrographs of tangential sections of 317W a) deformed at 1100°C, 5 s^{-1} illustrating large equiaxed substructure, and b) deformed at 1000°C, 5 s^{-1} illustrating decreased subgrain dimensions.

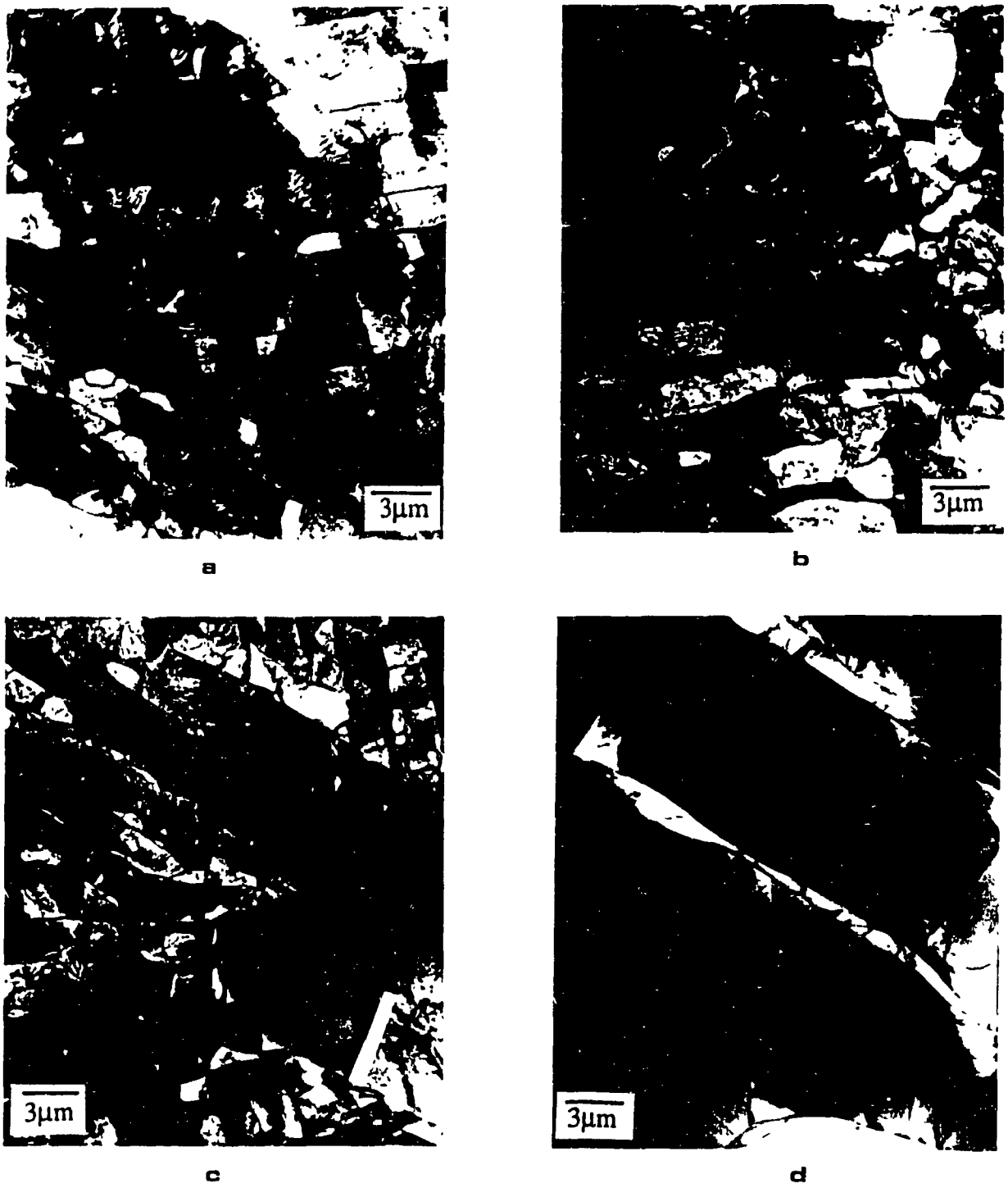

Fig. 67. TEM micrographs of tangential sections of 317W deformed at 1000^{o}, 1 s^{-1} a) illustrating a DRX grain distinguished by variations in substructure, b) illustrating a DRX nucleus, c) grains, containing twins, growing statically into the substructure, and d) a region of SRX grains nucleated around δ stringers.

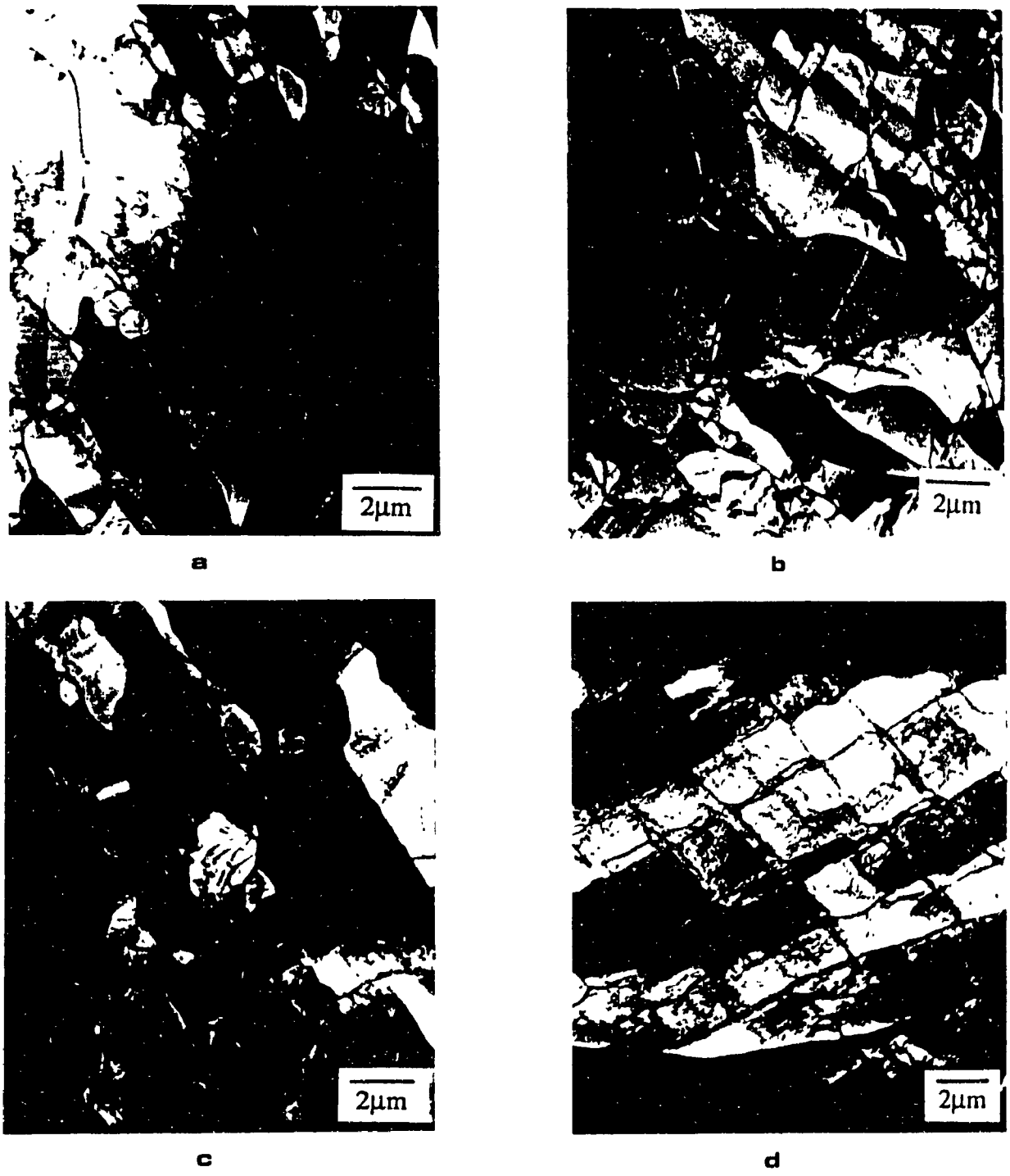

Fig. 68. TEM micrographs of tangential sections of 317C deformed at 1100°C a) at 0.1 s^{-1} showing equiaxed subgrains within DRX grains, b) at 1 s^{-1} showing medium equiaxed subgrains, c) at 5 s^{-1}; diameter decreasing with rising $\dot{\varepsilon}$, and d) deformed at 1000°, 1 s^{-1} illustrating the increase in aspect ratio as T declines.

specimens tested at 1100°C at 0.1, 1, 5 s^{-1} and 1000°C at 1 s^{-1} exhibit very similar behavior as 317W under the same deformation conditions. As T rises and $\dot{\epsilon}$ declines, the subgrains are larger and more highly polygonized. At high Z, the subgrain walls are thick having a high dislocation density, while at low Z the walls are regular and narrow with much decreased dislocation density.

4.6.5 SUBGRAIN SIZE DEPENDENCE ON Z AND ON σ_s

The log of the subgrain size (d_s) is plotted against the log of the steady state flow stress for 317C in Fig. 69a. The slope is about -1 in agreement with previous results (87, 140, 272) (Sec. 2.3.6). In addition, the reciprocal of the subgrain size (Fig. 69b) is proportional to log Z (87, 140, 157, 260) and the present work is represented by the equation:

$$d_s^{-1} = -1.82 + 0.15 \log Z \qquad (52)$$

Normalization at 900°C, 1 s^{-1} reveals that under these deformation conditions d_s is 1.11μm and 1.39μm for 317C and 317W respectively, with d_s equalling 1.21μm for 304C from other work (87, 140, 157, 260). The relationship for 317W is lower with a y-intercept of -2.55. An extensive analysis of cells and subgrains for 304 and 316 from the literature (87, 140, 145-148, 260, 272-278) is illustrated in Fig. 70a,b, respectively. The logarithm of both cell and subgrain diameters are linearly related to the log of the steady state flow stress with slopes of -2 and -1, respectively.

4.6.6 PROPERTIES OF RETAINED SUBSTRUCTURE

The Vickers hardness (H_v) of 304C, 316C, and 317C subjected to hot torsion were measured after quenching. Their respective hardness values are plotted against Z in Fig. 71 where they rise with decreasing T and rising $\dot{\epsilon}$. The value of H_v is proportional to Z (Sec. 2.3.7) raised to the power

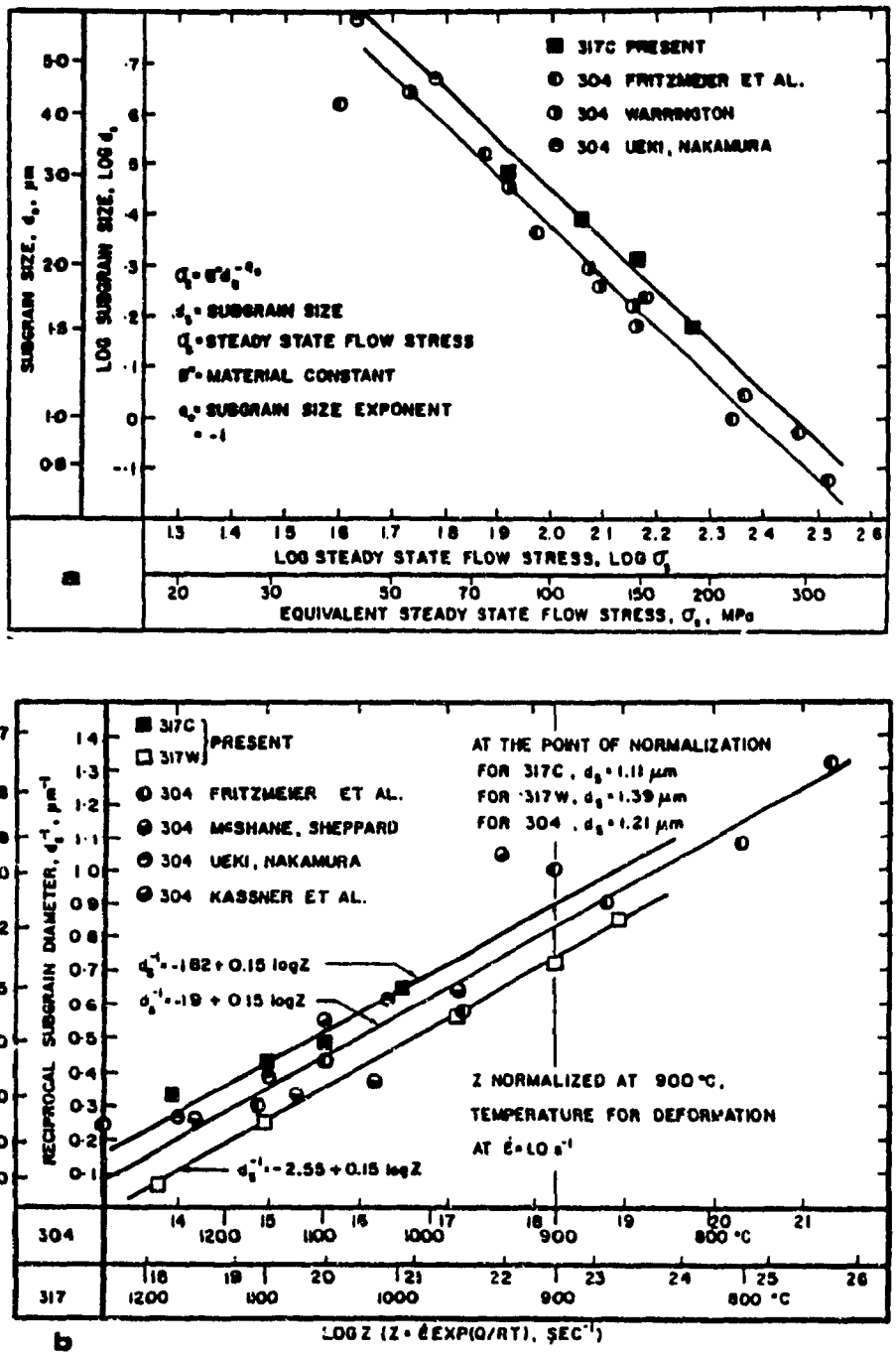

Fig. 69. a) Plot of log subgrain size against log flow stress for 317C, exhibiting a slope of -1. Published 304W data are included for comparison (87, 140, 272); and b) Plot of the reciprocal subgrain diameter against log Z, exhibiting a linear fit. Due to δ ferrite particles, the subgrains in 317C are smaller than those in 317W and published data on 304W (87, 140, 157, 260). The Z scales are normalized to bring the condition 900°C, 1 s^{-1} into coincidence.

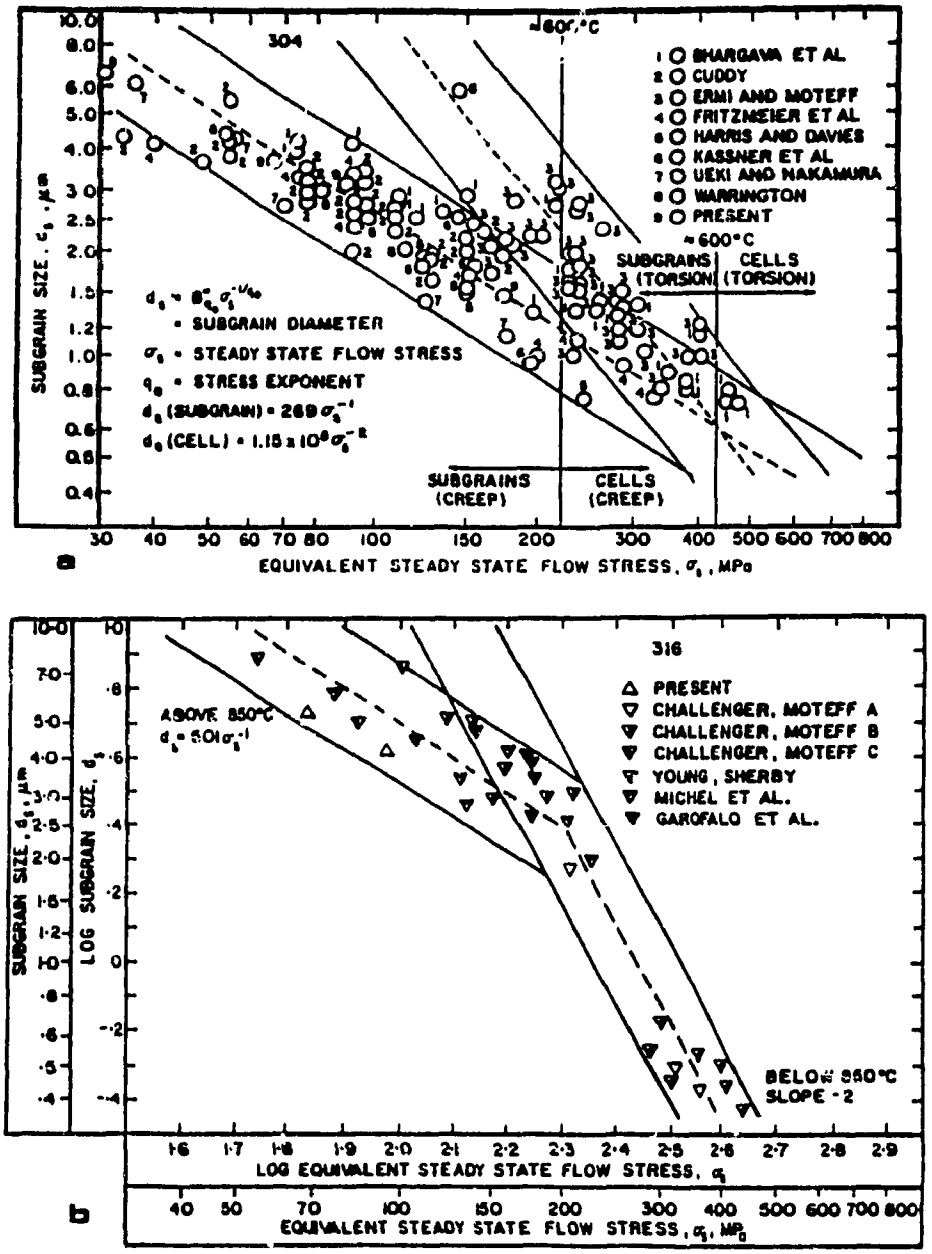

Fig. 70. Plot of log subgrain and cell sizes versus log of steady state flow stress illustrating a -1 slope for a) 304W determined from extensive research data (87, 140, 145-148, 260, 272) which falls into a narrow band; and b) 316W as a function of stress for both creep and hot torsion are compared with extensive data from the literature (273-278). The transitions from subgrains to cells with a slope of -2 are indicated for both alloys; in 304, the large cells arise from creep-fatigue (148).

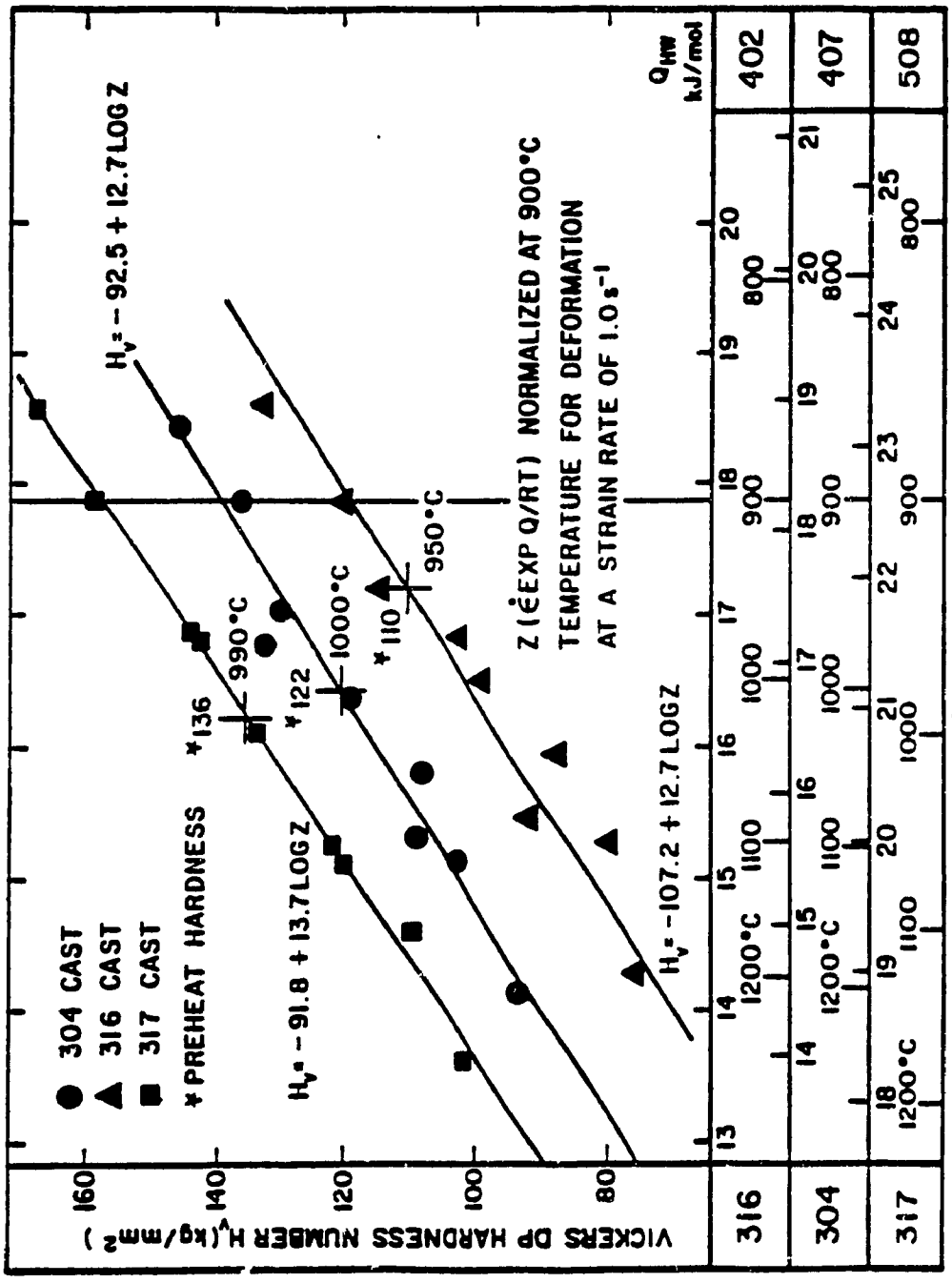

Fig. 71. Hardness for 304C, 316C, and 317C is uniquely dependent on Z as a result of changing subgrain size and is also strongly affected by the volume fraction of δ particles.

12.7 for 304 and 316, with 317 being 13.7. The hardness of the alloys rises with δ-ferrite and solute content in the order 316, 304, and 317.

4.7. SIMULATION OF INDUSTRIAL PROCESSES

4.7.1 MULTISTAGE SIMULATION

In multistage tests with declining temperature (Sec. 2.6.7), the 301W flow curves exhibit a saw-toothed shape for seventeen passes on a cumulative strain graph (Fig. 72). The decline in T with increasing pass number is shown and averages 0.9°C/s. The sets of curves are representative of iso-strain-rate (AA , DD) and rising strain rate (CC) conditions with equal interval times of two values. An envelope curve through the maxima of each pass for each set can be approximated by two linear segments; the second one with considerably higher slope begins at about the eighth pass as T falls below 1050°C.

The plot in Fig. 73 is in accordance with the sinh constitutive equation (Eqn. 17). Lines are drawn through the points for the same T or pass number. Their slope is 3.9 which is lower than 4.4 determined for peak stresses in continuous tests (FF') as illustrated by the data points and dashed lines at 1000 and 900°C. The dependence of σ on T results in straight lines (Fig. 74). The slope for declining T (Q_{HW} = 352 kJ/mol, AA,DD) is lower than that for continuous isothermal tests (Q_{HW} = 399 kJ/mol, FF'). The data from multistage isothermal tests provide a series of parallel lines with a still lower slope (Q_{HW} = 307 kJ/mol, EE'). In a logarithmic plot of sinh ασ versus Z (Fig. 75), the isothermal continuous data (FF') for a variety of T and $\dot{\varepsilon}$ conditions are collected into a single line, likewise the isothermal multistage (EE)'. The data for the three declining T tests (ABC) are drawn into a narrow band approximately parallel

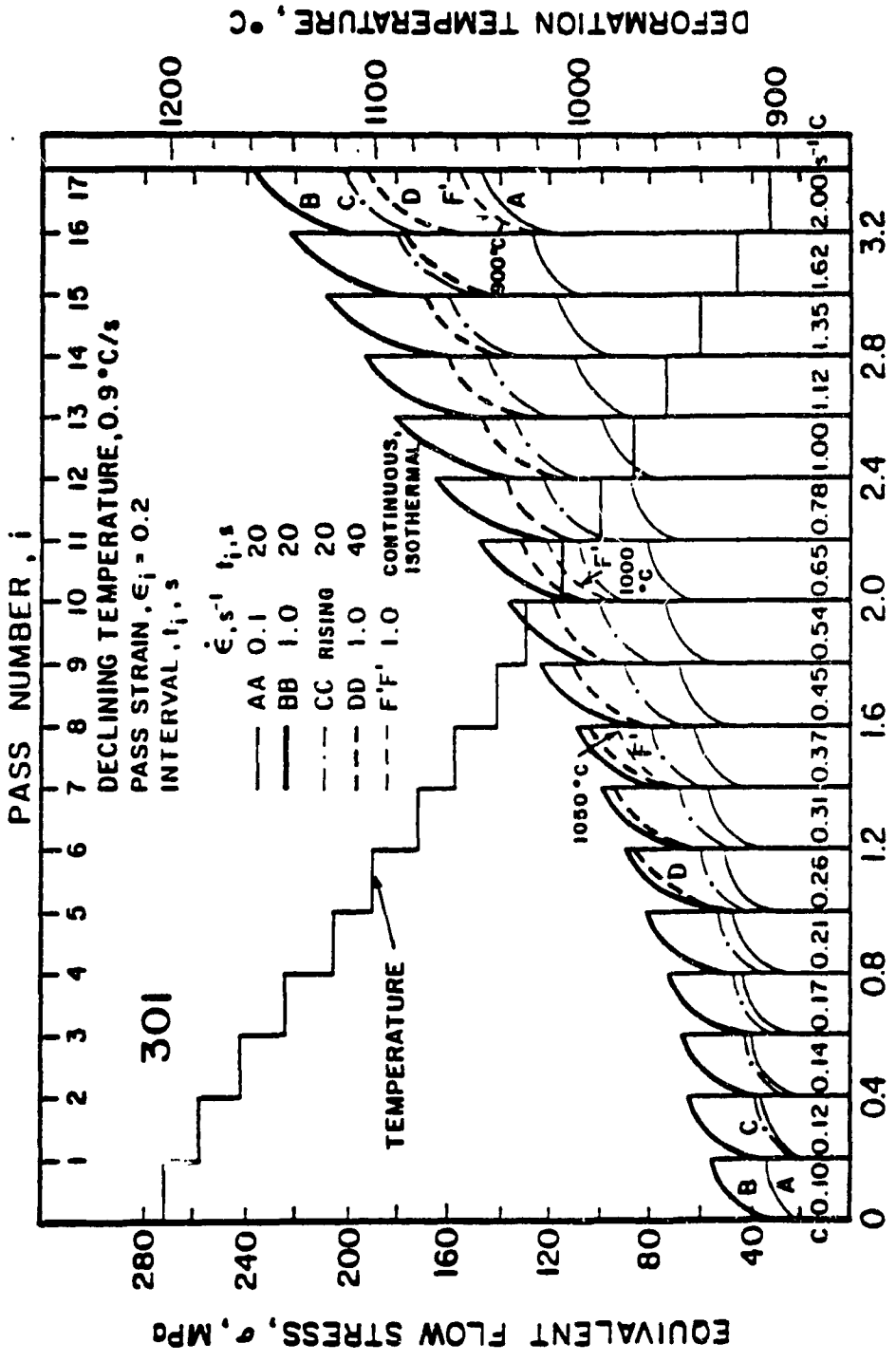

Fig. 72. Multistage torsional stress strain curves for 301W with a stage strain of 0.2 plotted cumulatively. For a declining T of 0.9°C/s (1200-900°C), the strain rate is constant at either 0.1 (AA) or 1.0 s^{-1} (BB) or rises gradually from 0.1 to 2.0 s^{-1} (CC).

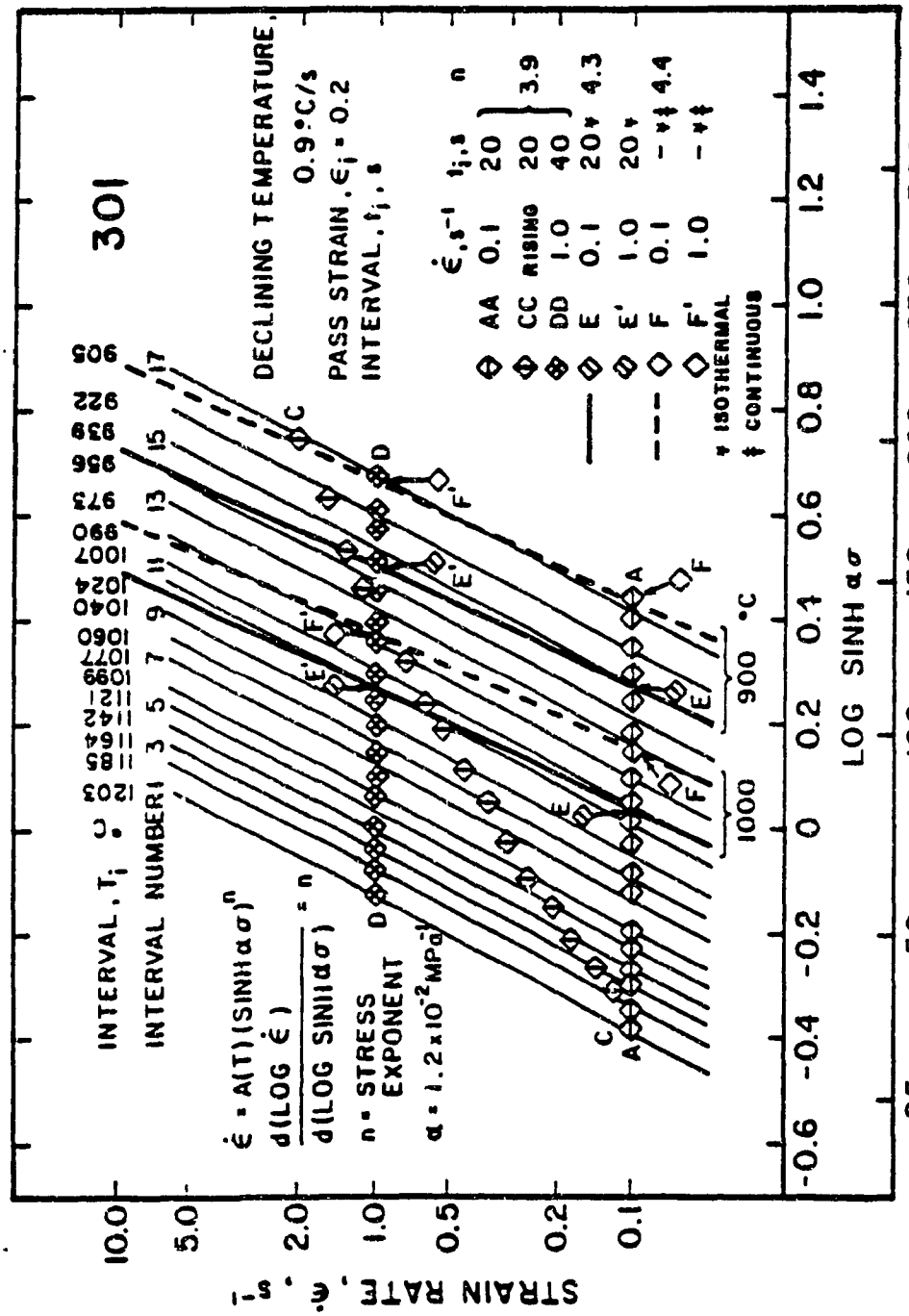

Fig. 73. Logarithmic plot of $\dot{\epsilon}$ versus sinh $\alpha\sigma$ according to Eqn. 17 for four sets of multistage tests on 301W: isothermal E and E' at 1000 and 900°C and dropping T (1200-900°) for 0.1 s^{-1} (AA), 1.0 s^{-1} (DD) and rising $\dot{\epsilon}$ (0.1-2.0 s^{-1}) (CC). Isothermal continuous data (FF') are included for comparison.

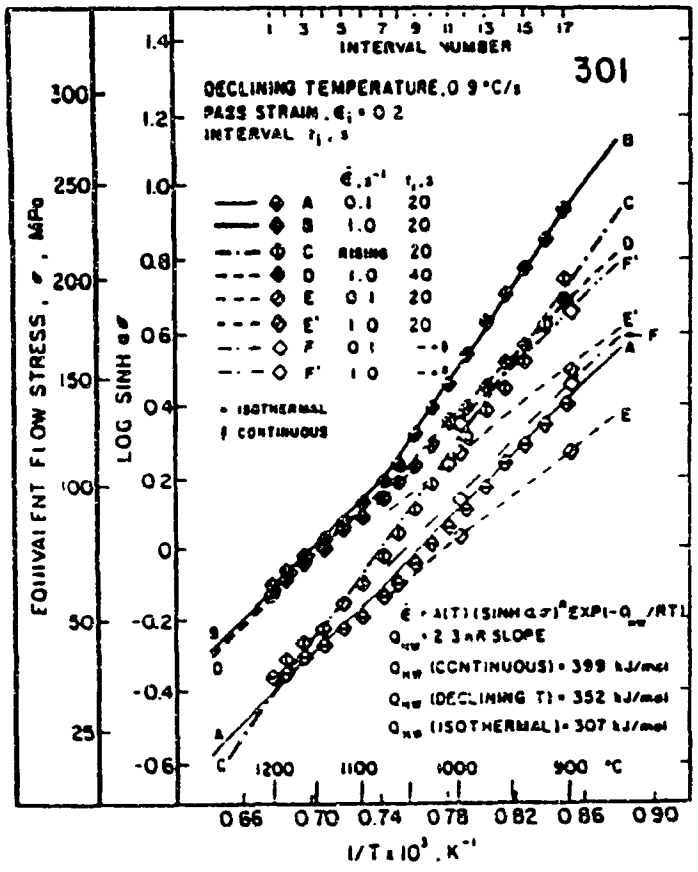

Fig. 74. Plot of sinh $\alpha\sigma$ against 1/T according to Eqn. 17 for the same tests on 301W as in Fig. 72: isothermal continuous (F and F') and multistage (E and E') and declining T, 0.1 s^{-1} (AA), rising $\dot{\varepsilon}$ (CC), 1.0 s^{-1} (BB), (DD). While the interval duration was 20s in the first three, and 40s in the last.

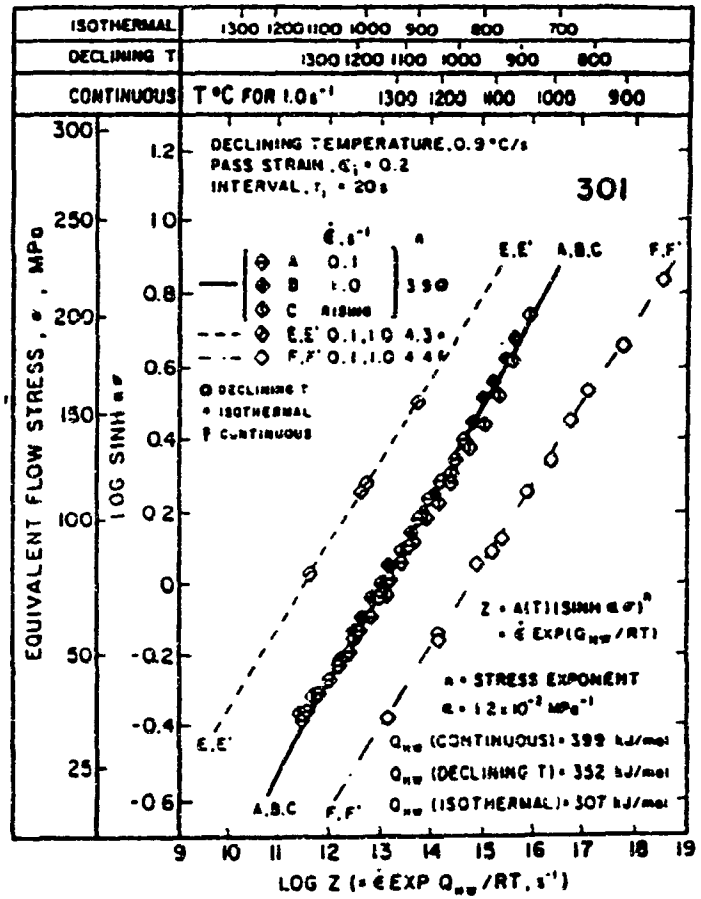

Fig. 75. Plots of log sinh $\alpha\sigma$ versus Z for 301W draw data from declining T but different $\dot{\varepsilon}$ conditions into a narrow band which is roughly parallel to the lines for isothermal conditions and multistage deformation. In all cases, t_i = 20s.

to the isothermal lines but at a stress level about 20% higher than the multistage and a little lower than σ_p for the continuous tests.

The flow stresses, such as yield σ_{yo}, mean pass stress k_p, and the maximum σ_m in each pass are plotted against the pass number (Fig. 76). The data for each condition do not fall in a straight line but can be approximated by two linear segments. In each, a low slope is followed by a high slope; the change, being more marked at high $\dot{\varepsilon}$, takes place at about 1050°C in similarity to the envelope in Fig. 72. The fractional softening during the i'th interval following the i'th pass (Sec. 2.6.7) is presented in Fig. 77. The values determined are seen to decline as T falls and as $\dot{\varepsilon}$ and interval time decrease. Isothermal data for the first and fifth intervals (EE') are provided. The relationship of FS to X_{SRX} from metallography is included for comparison; SRV is strong even at the lowest T, but SRX is less than 5%.

The flow stress is rising not only because deformation T is falling but also because FS is declining with the result that more worked regions are being carried over from one pass to another. The state of strain, ε_{yi}, at the start of a pass is determined through the shape of the flow curve and the following equation (25, 26):

$$n' = d\ln\sigma/d\ln\varepsilon = \varepsilon/\sigma\ (d\sigma/d\varepsilon) = (\varepsilon_{yi}/\sigma_{yi})\ [(\sigma_{mi} - \sigma_{yi})/\varepsilon_i] \quad (53)$$

The strain hardening coefficient n' was determined from isothermal curves across the range studied and a value of 0.15 was found suitable. Therefore, ε_{yi} was calculated for every pass after the first, and was plotted in Fig. 78. As expected, ε_{yi} rises as T and FS fall as the number of passes increase.

The times for 50% SRX, $t_{0.5}$, are evaluated at $X_{SRX} = 0.5$ from the

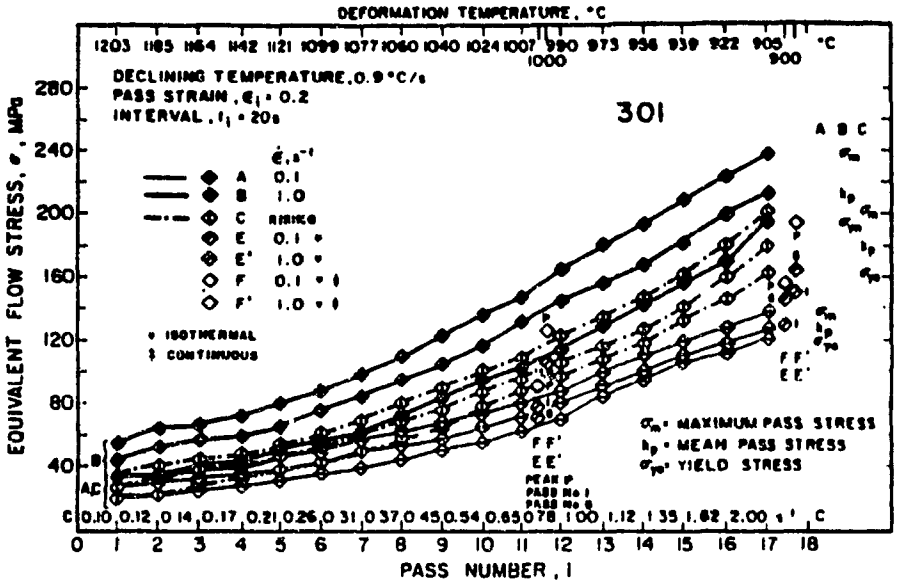

Fig. 76. For 301W, the yield stress σ_{yo}, the maximum stress σ_m and the mean pass stress k_p are plotted against pass number for declining T (top scale) at 0.1 s^{-1} (A), 1.0 s^{-1} (B) and rising $\dot{e}$ (C, bottom scale).

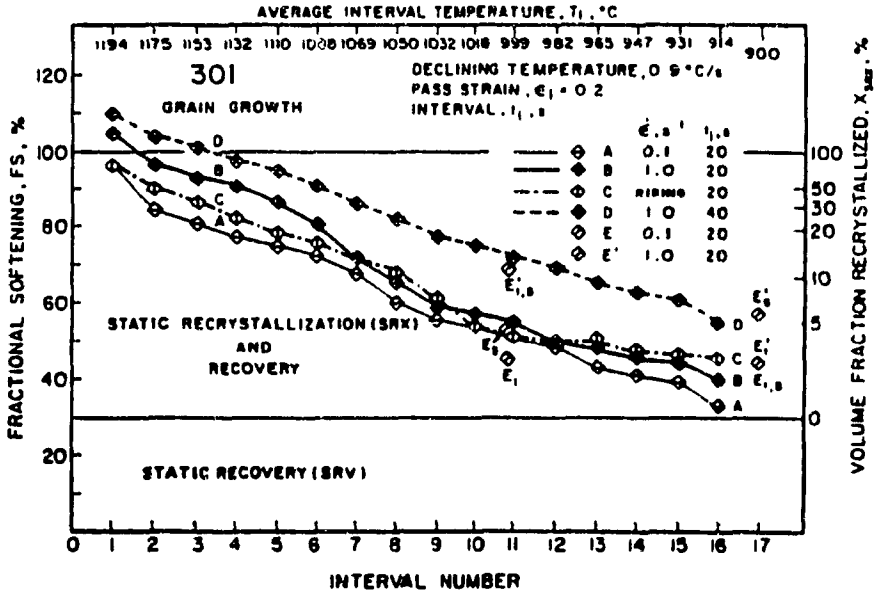

Fig. 77. Fractional softening for 301W during intervals of 20s (A,B,C) or 40s (D) in multistage tests with declining T at 0.9°C/s at 0.1 s^{-1} (A), 1.0 s^{-1} (B,D) or rising $\dot{e}$ (C). FS for isothermal multistage tests are indicated for comparison. Some isothermal data for the first and fifth intervals are provided. The relationship of FS to X_{SRX} from metallography (174, 208).

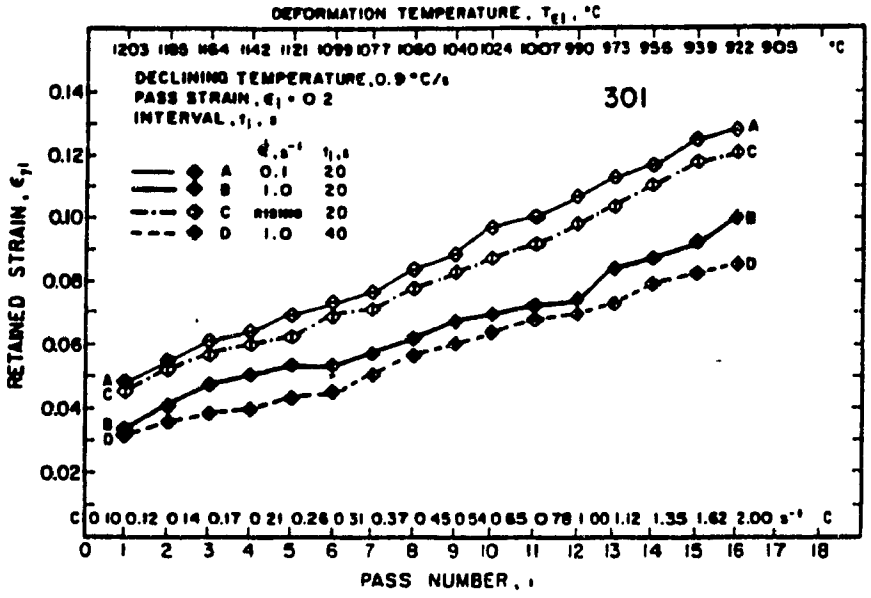

Fig. 78. The initial strain state in 301W at the start of each pass estimated by Eqn. 53. This is also proportional to the unrecrystallized volume (Fig. 77) carried over from one pass to the next in multistage tests with declining T at 0.9°C/s at 0.1 s^{-1} (A), 1.0 s^{-1} (B,D) and rising $\dot{\varepsilon}$ (C); T_i = 20s (A,B,C).

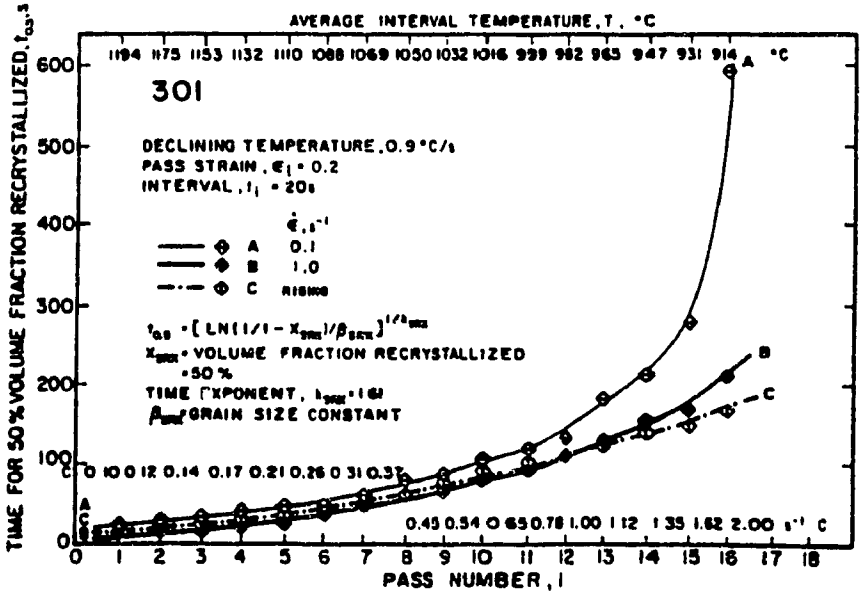

Fig. 79. The time for 50% volume fraction recrystallized derived by Eqn. 24 from the FS data during each interval of multistage tests at declining T for $\dot{\varepsilon}$ of 0.1 (A) and 1.0 s^{-1} (B) and rising $\dot{\varepsilon}$ (C).

Avrami analysis (Secs. 2.5.4, 4.4.2) and are presented in Fig. 79. There it can be seen that the rate of SRX decreases as T_i declines and becomes markedly slow after the final three passes. In Fig. 80 (266), the plot of log ($t_{0.5}$ $Z^{0.375}$) versus 1/T gives a straight line confirming the validity of the present case. From the slope and that of isothermal data added for comparison, values of Q_{SRX} (T declining) and Q_{SRX} (isothermal) were determined to be 290 and 369 kJ/mol respectively. The effect of $\dot{\epsilon}$ on the rate of SRX is illustrated in Fig. 81. A rise in $\dot{\epsilon}$ by a factor of ten increases the rate by about 1.7 times.

4.7.2 PLANETARY HOT ROLLING MILL

An analysis of the planetary mill used for the hot rolling of continuously cast γ stainless steels 301, 304 and 316 at Atlas Steels, Tracy is depicted in Fig. 82(a-d) for the purpose of determining the power requirements of this process from torsional strength data. Fig. 82a (279) is a schematic sketch of the mill layout showing the position of planetary work rolls deforming material as they revolve around the rotating backup rolls. The feed rolls push the slab forward between successive planetary rolls; Fig 82b shows the arcs of contact before and after the passage of one roll, the difference in which is defined as the draft. The distribution of this draft is calculated from 30 sections across the bite and is illustrated in Fig. 82b. At the point of mean strain rate, the draft has attained its maximum.

The slab speeds increase as it proceeds through the bite from entry to exit. Figure 82c permits calculation of the cumulative time during reduction. The strain rate distribution throughout the bite (Fig. 82d) is determined to vary continually between 16 and 132 s^{-1} which is employed in

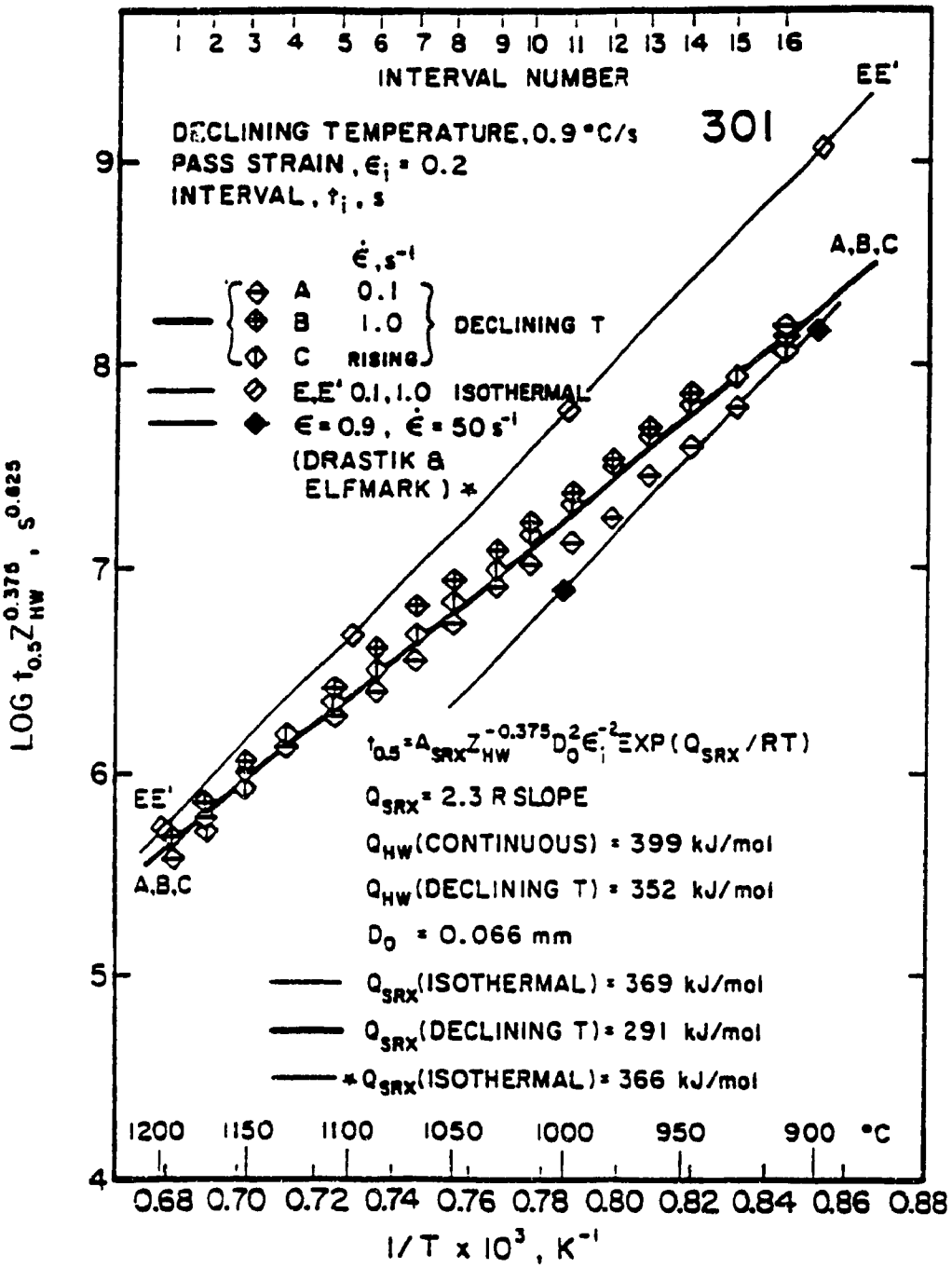

Fig. 80. The kinetics of SRX according to the Arrhenius relationship for multistage tests on 301W for both isothermal and declining T tests. The latter has a lower Q_{SRX} since the strain energy rises as T declines; this is partially compensated by the $Z^{0.375}$. The $t_{0.5}$ for Drastik and Elfmark (266) is much reduced since the strain energy is higher due to $\dot{\epsilon} = 50\ s^{-1}$.

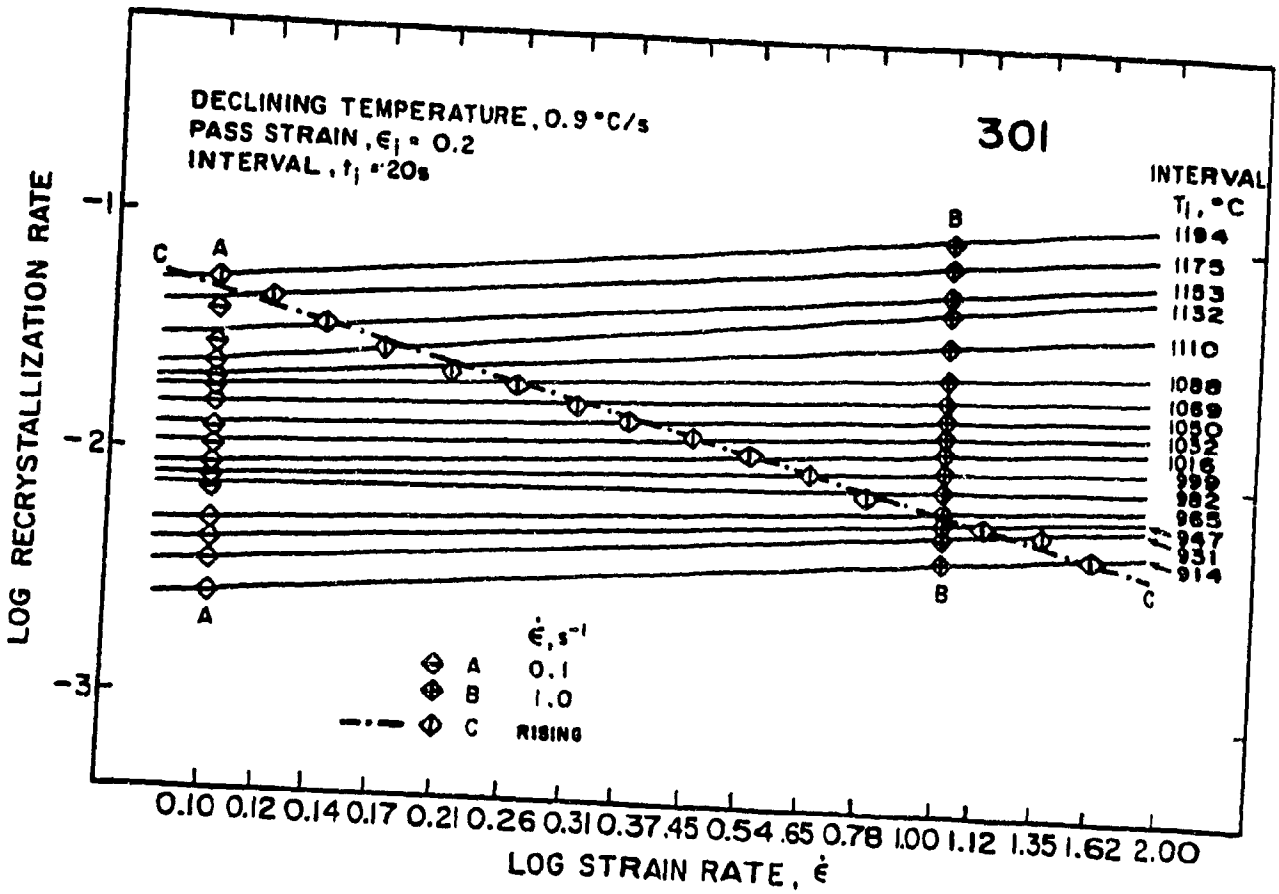

Fig. 81. A logarithmic plot illustrating the effect of $\dot{\epsilon}$ on recrystallization rate (the inverse of $t_{0.5}$) for multistage tests with declining T at 0.1 s^{-1} (A), 1.0 s^{-1} (B), and rising $\dot{\epsilon}$ (C).

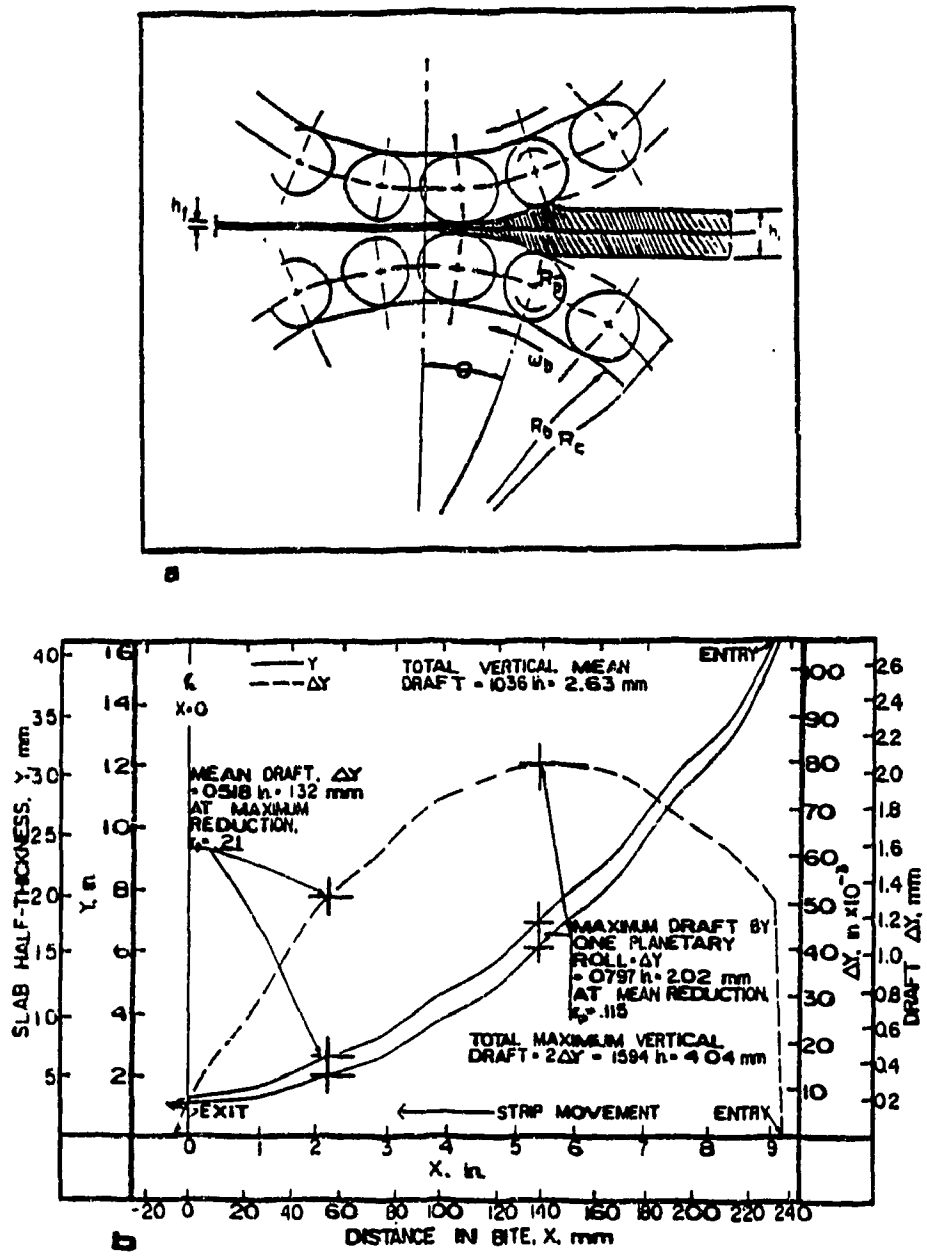

Fig. 82. Two drawings of the planetary mill mechanism showing: a) the positions of the planetary work rolls deforming material as they revolve around the rotating backup rolls (279), and b) loci of points on the material before and after deformation by one pair of planetary work rolls and the distribution of draft along the bite (280).

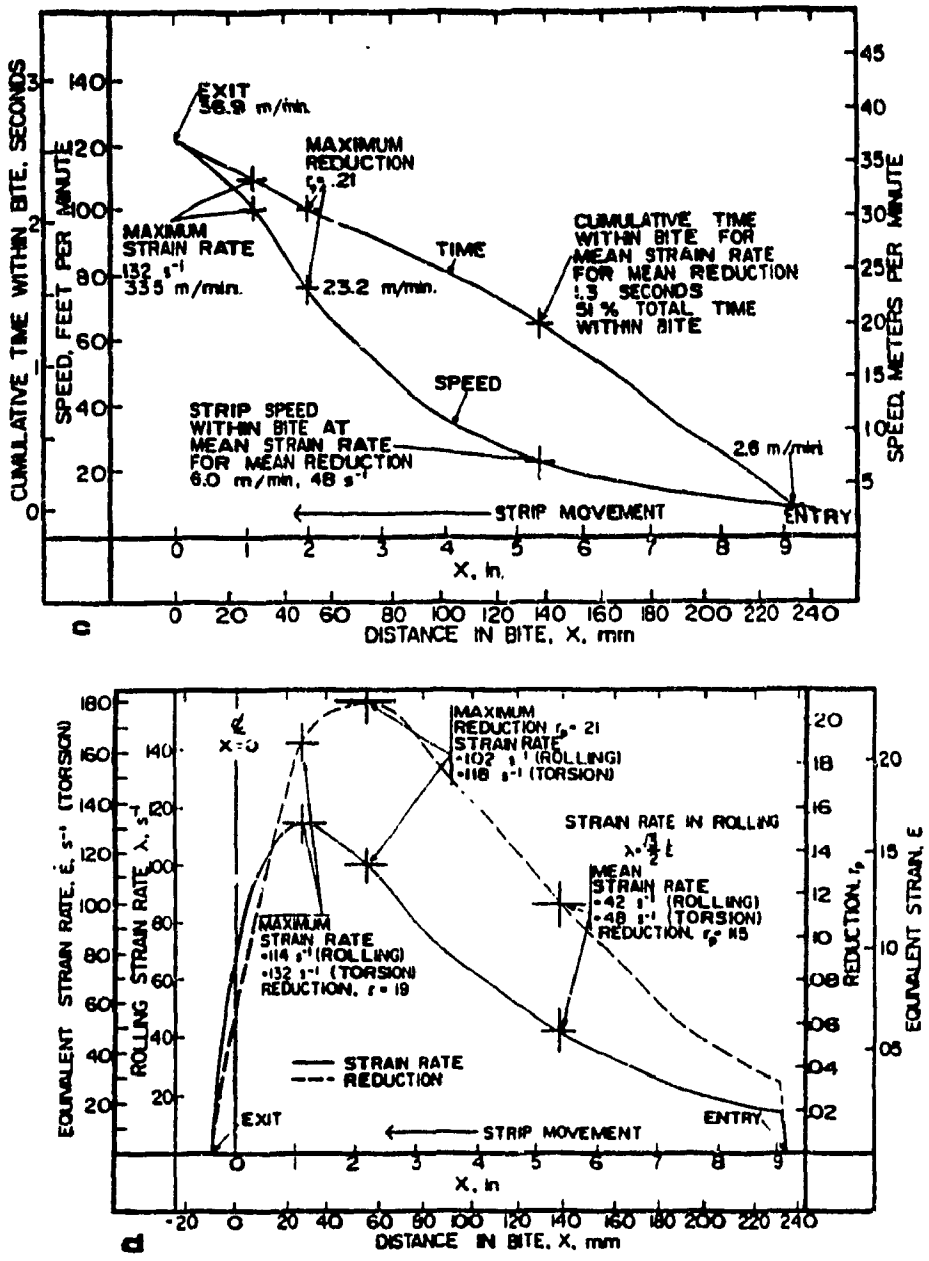

Fig. 82. Two drawings of the planetary mill mechanism showing: c) distribution of the slab to strip speeds as the material proceeds through the bite from entry to exit, and d) distribution of reduction and mean strain rate due to one pair of planetary work rolls (280).

the calculation of the roll separating force at the mean strain rate. Since the average time between successive deformations by the rotating planetary rolls is about 0.03 seconds, no static restoration is assumed to occur (1, 22, 38, 39). Henceforth, the process can be considered continuous and can be simulated by a continuous torsion test under similar deformation conditions.

The following formula has been developed in order to calculate the mean flow stress for each planetary roll from the torsion test:

$$k_{P_i} = 1 / \varepsilon_1 \int_{\sum\varepsilon=i-1}^{\sum\varepsilon=i} \sigma (\dot{\varepsilon}, T) \, d\varepsilon \qquad (54)$$

Consecutive representative flow curves (Fig. 83a,b), rising with increasing strain rate at a mean constant temperature of 1307^{o}C with account taken of deformational heating, exhibit rapid strain hardening followed by gradual softening as DRV and DRX proceed. With the peak stress for each separate condition related to the peak strain defined by Eqn. 44, it can be seen that σ rises slowly to a maximum at the highest $\dot{\varepsilon}$ (132 s^{-1}) where it falls rapidly to zero at the completion of deformation. It is noted that the mean flow stress of 77MPa for 304W is almost equal to the stress developed at the mean $\dot{\varepsilon}$ of 48 s^{-1}. As a result of this approximate equality, representative flow curves for all alloys were developed for the mean strain rate condition and plotted in Fig. 83b . These k'_p values are 76, 78, 85, and 92 MPa for 301W, 304W, 316W, and 317W, respectively.

The roll separating forces for 301W, 304W, 316W, and 317W are respectively determined to be 1159, 1188, 1307 and 1403 newtons per mm width (Fig. 84). The instantaneous power requirement for the planetary assembly is given by the formula (280):

$$\text{Power} = [\{2(P_T \sin \alpha_1 + G_T/R_p) R_b\}/(1 + \cos \theta_1) + \{(G_T R_b)/R_p\}] \omega_b \qquad (55).$$

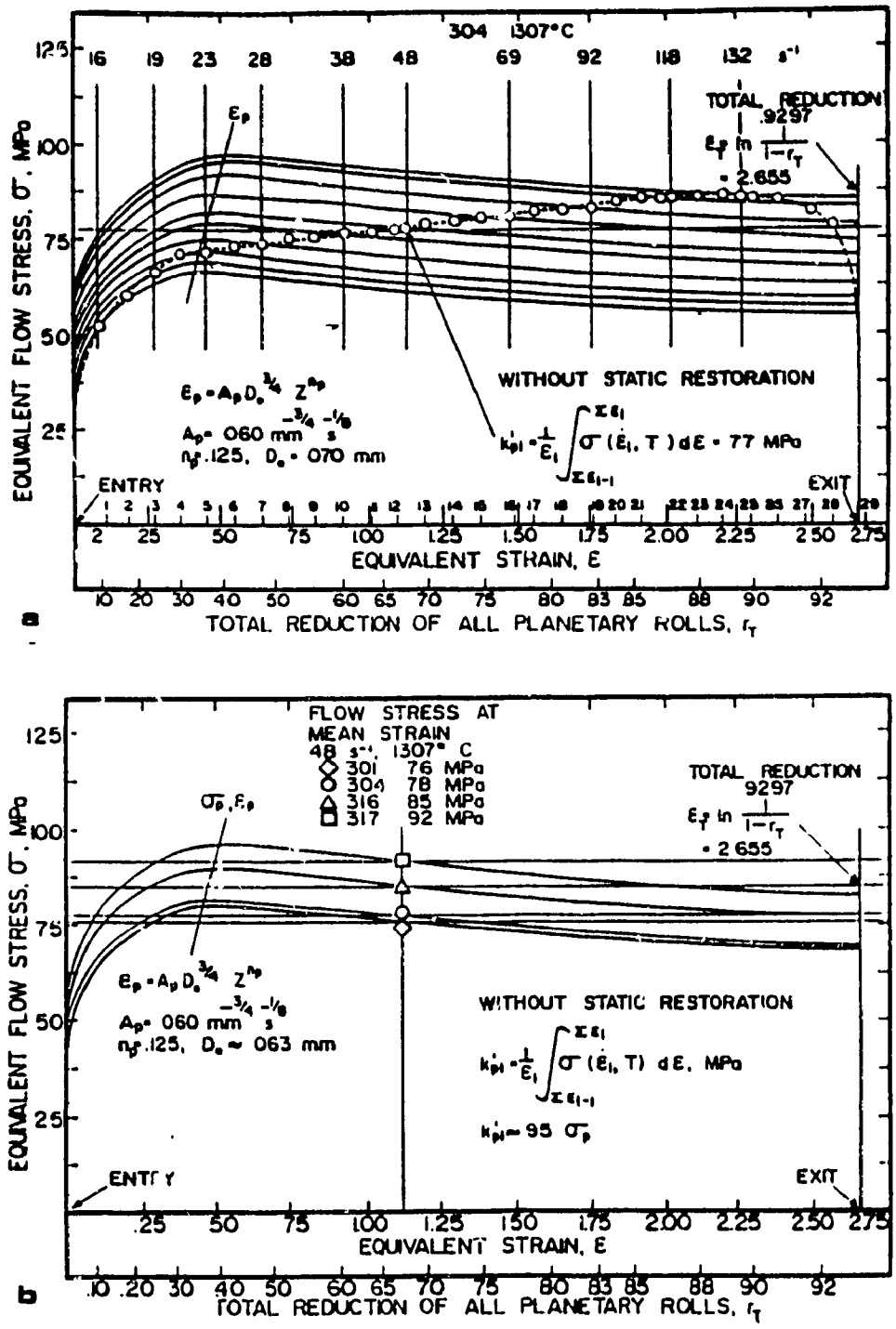

Fig. 83. a) Series of continuous flow curves at different strain rates up to the maximum attained in the planetary rolling mill and the curve related to the series of flow stresses attained at different points across the bite as different planetary rolls impose the strain rates indicated, and b) representative σ-ε curves of 301W, 304W, 316W, and 317W and the derivation of upper mean flow stresses at the mean strain rate of 48 s^{-1}.

P_T is the total roll separating force, α_1 is the subtended angle at the point of mean strain rate, G_T is the total torque, R_p is the planetary work roll radius, The angle of bite θ_1 at the point of mean strain rate is approximately 10 degrees. R_b is the radius of the backup roll, and ω_b is the angular velocity of the backup rolls. Calculations considering a 1321 mm wide slat gives the instantaneous power requirements as 4810, 4880, 5500 and 5780 kW for the alloys in the preceding order. As shown in Fig. 85 (33, 281-283), the roll separating force, and hence the instantaneous horsepower requirement, are functions of the metallic solute content.

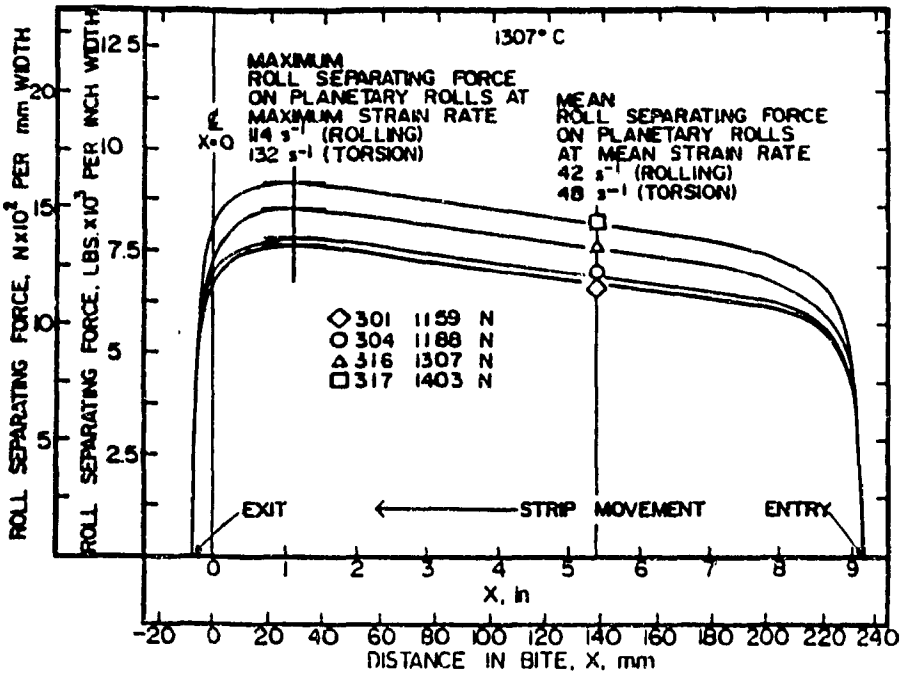

Fig. 84. Curves showing the steady increase in planetary roll separating forces as the material is increasingly deformed. These curves, rising in the order 301W, 304W, 316W, and 317W, proceed through a mean strain rate condition to a peak where they quickly fall to zero. These are similar to the derived curve in Fig. 83a.

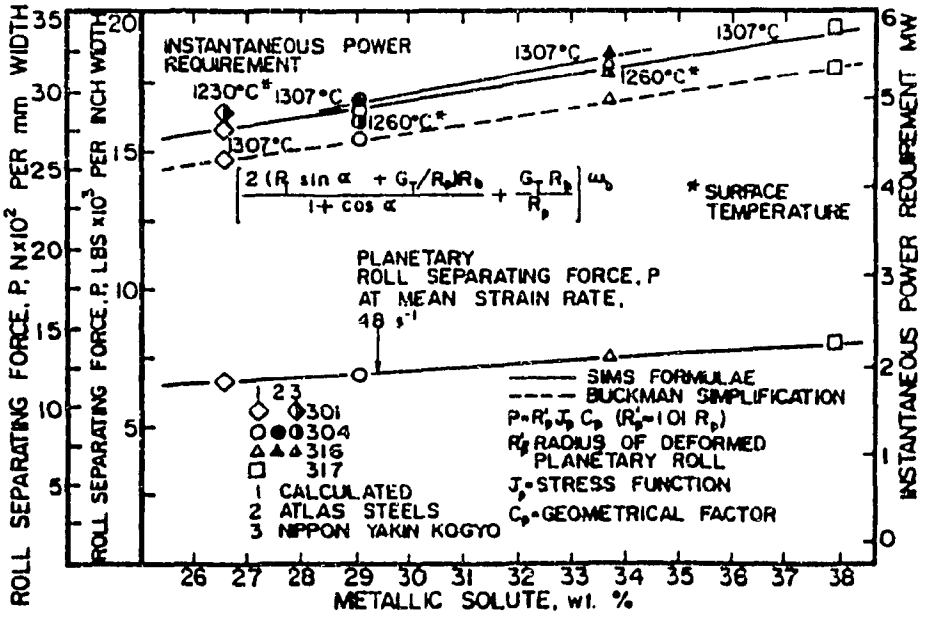

Fig. 85. A graph of planetary roll separating force per unit width and instantaneous power requirements versus metallic solute using the formulae of Buckman, Sparling, and Sims (33, 280, 281). Calculated values are in good agreement with those measured at Atlas Steel (282) and Nippon Yakin Kogyo (283).

CHAPTER 5

DISCUSSION

5.1 WORK HARDENING - RESTORATION - FLOW STRESS

5.1.1 FLOW CURVE CHARACTERISTICS

The experimentally derived torque values plotted in Fig. 3a-d indicate that the slope which represents the strain rate sensitivity rises to higher values as T increases as a result of rising DRV (49, 182, 184). The values for the as-cast are slightly higher than those for the worked material at low T and the converse at high T. In addition, for all deformation conditions torques are higher in the former than in the latter. This is primarily due to the presence of δ ferrite in the former which raises the dislocation density, particularly at low T and high $\dot{\varepsilon}$. Furthermore, m rises as the solute content increases at low T (22, 86, 89, 90, 101) under circumstances where torques are higher than for 304W.

The representative σ-ε curves of both as-cast and worked material plotted in Fig. 4a-d (184, 191) are analyzed in conjunction with the θ-σ plots in Fig. 5a-g (Secs. 4.1.1, 4.1.2). At low Z (1100°C, 0.1 s^{-1}), $\sigma_{y_o} \approx 0.68\ \sigma_p$ and at high Z (900°C, 5 s^{-1}), σ_{y_o} is $\approx 0.39\ \sigma_p$ for all materials. Nevertheless, σ_{y_o} and σ_p are higher for the as-cast than the worked material due to the effects of δ particles; being > 0.6 μm, they create a fine substructure in the matrix around themselves and considerably raise θ (the slope of σ-ε curve). In the initial rise of the flow curve, θ is linearly decreasing to a strain of about ten percent (113, 119, 123, 125, 126, 191, 260). Then the rate of decline of θ slows down as a result of the formation of subgrains (SF in Fig. 5a-h) (90, 119, 124-126).

The concurrent hardening and polygonization continue up to ε_c (82, 84, 86, 88, 89, 99, 101, 132-137) at approximately 0.64 ε_p and 0.70 ε_p in the worked and as-cast materials respectively where DRX is initiated, thereby reducing θ significantly and leading shortly to the peak. As DRV and DRX override the effects of work hardening, the 304C curve ($1000^{o}C$, 5 s^{-1}) drops sharply to fracture at $\sigma_f \approx 0.94\ \sigma_p$, whereas the 304W curve drops less quickly to the onset of a steady state regime in which concurrent straining, DRV and DRX continue until fracture intervenes at a lower $\sigma_f \approx 0.81\ \sigma_p$ but at a much higher ε_f. Similar behavior is exhibited by the other alloys. For the worked materials, the curves drop ≈ 77 MPa to steady state at high Z ($900^{o}C$, 5 s^{-1}), whereas they drop ≈ 7 MPa at low Z ($1200^{o}C$, 0.1 s^{-1}) (34, 89, 90, 99, 101, 168, 174).

5.1.2 INFLUENCE OF DYNAMICALLY RECOVERED SUBSTRUCTURE

DRV is revealed by the flow curves and strain hardening rates (Secs. 2.3.1, 2.4.3, 4.1.1, 4.1.2). Inspection of the curves in Fig. 4a-d shows that the rate of initial work hardening and the maximum level of the flow stress decreases as T increases and $\dot{\varepsilon}$ decreases. This is evident in the peak stress, the steady state flow stress, and the saturation stress. Although DRX is responsible for the characteristic shape of the flow curves (Secs 2.3.2-2.3.4), it contributes only a small amount to the overall softening when differences $\sigma_s^*(T) - \sigma_s(T)$ in Fig. 4a-d and $\sigma_s^*(20^{o}C) - \sigma_s^*(T)$ in Fig. 6a-c are considered.

Consequently, the DRV substructure essentially determines the flow stress as depicted in Fig. 69a,b. The micrographs further confirm that the characteristic shape of the flow curves (Figs. 64-68) is due to the softening effects of DRV and DRX (Sec. 4.6). As seen in Fig. 68a-c,

deformation at high $\dot{\varepsilon}$ and low T results in a more rapid generation and slower annihilation of dislocations, respectively. Therefore, the steady state balance is reached at a smaller subgrain size and higher flow stress (34, 84, 86, 88, 89, 90, 99, 134).

5.1.3 PEAK STRESS AND STRAIN, EFFECTS OF SOLUTE AND δ FERRITE

The values of ε_p and σ_p are plotted as functions of T and $\dot{\varepsilon}$ in Figs. 10 and 11. The peak strain is a result of the increasing influence of DRX which starts at ε_c (0.61-0.72 ε_p) (34, 84, 86, 89,90, 99, 101, 136, 195). This strain is diminished by structural features which aid the substructure to build up sufficient density and configuration for nucleation of DRX but is augmented by features which retard growth by migration of boundaries (84, 86, 88, 89, 99). The peak flow stress reflects the averaged dislocation density, whereas nucleation reflects localized regions of high density; large particles may decrease ε_c faster than they raise σ_p. Whatever retards growth will allow dislocation density to rise in some regions so σ_p rises as ε_p rises, but not proportionally.

Metallic solute additions (34, 84, 86, 89, 90, 101, 131) in the order 301, 304, 316, and 317 clearly raise σ_p and also ε_p because solute also retards grain boundary migration and is responsible for the order of 301W, 304W and 316W. However, the large particles (>0.6μm) of δ ferrite, which require additional adjacent matrix flow and hence strain hardening, raise the as-cast σ_p, but also enhance nucleation (90), thereby reducing ε_p. The presence of about 5% δ ferrite is responsible for the lower 317W ε_p in spite of greater solute content. Solute may simply raise the flow stress without affecting the dislocation density (90). If it reduces DRV, then it could decrease ε_c.

5.1.4 STRAIN HARDENING RATE VERSUS FLOW STRESS CURVES

In the θ-σ plots (Secs. 2.2.4, 4.1.2) the initial slopes for the as-cast materials (Fig. 5a-c) are slightly lower than those for the worked (Fig. 5d-g), but because of the higher stress levels extrapolate to a higher θ_o at $\sigma = 0$ (90, 113, 114, 121-123). The average value of θ_o for the worked is 3660 MPa which is ≈ 9 percent lower than the 4040 MPa derived for the δ bearing as-cast materials. Due to greater solute, θ_o for 316 and 317 is about 14 percent greater than that derived for 301 and 304. At 900°C, 5 s^{-1}, the first segment of the as-cast curve is higher and with a slope of ≈ -15 decends more slowly than that of the worked with a slope of -20, thus indicating greater work hardening due to δ particles.

5.1.5 INFLUENCE OF DYNAMIC RECOVERY ON θ

As shown in Fig. 5h, the rate of decrease in θ through stage III from stage II is suddenly slowed with this change appearing fairly late in the θ-σ curve but occuring fairly early in the σ-ε curve. This change in slope signals a change in mechanism and microstructure (90, 114-120). Throughout the straight low σ or ε segment (high θ), the substructure consists solely of dislocation tangles which increase in density as σ and $\dot{\varepsilon}$ increase (90, 119, 126). At ε and σ near the change in slope, subgrains begin to form near the grain boundaries and then spread towards the center of the grains (119). With continuing strain these subgrains become smaller and sharper, with misorientations not changing appreciably. The initiation of this subgrain formation is marked on the θ-σ plots by the lowering in the slope as indicated by a diagonal line SF through the origin (Fig. 5a-g) (90, 119, 121-123). It is thought that the completion of the polygonization is marked by the start of the second linear segment.

Upon initiation of subgrain formation, the as-cast material does not show as great a change in the slope because of a higher more inhomogeneous dislocation density and less uniform polygonization (90). As $\dot{\varepsilon}$ decreases from 5 to 1 s^{-1}at 900°C (Fig. 5a,e) in the region of subgrain formation, θ for 304C decreases from 330 to 104 MPa (σ = 220 MPa) in comparison with 278 to 135 MPa (σ = 149 MPa) for 304W. All other alloys exhibit similar behavior. This greater decrease in θ indicates greater increase in DRV in the as-cast which is a result of its much lower initial level of recovery (90). Finally, the curve arrives at a point of inflection, indicating the initiation of DRX (90, 121).

5.1.6 EFFECTS OF DYNAMIC RECRYSTALLIZATION ON θ - CURVES

As T rises for all alloys, the slopes of the second linear segment increase, thereby graphically showing that as T augments DRV, subgrain size increases as has been confirmed by TEM (Figs. 56a,b, 65a-d, 66a,b, 67a,b, Sec. 4.6.4, 4.6.5). Again, the as-cast material with higher dislocation densities, because of the presence of δ particles (90), has progressively lower slopes in the first linear segment than the worked as T drops (260). In addition, the results of Kassner et al. (125, 260), although at a much lower T and $\dot{\varepsilon}$, agree fairly well confirming that the bend is related to formation of subgrains. The curves of Carfi et al. (119) (Fig. 5e) agree in general with the present curves but have much higher stresses particularly at 900°C because of much higher solute concentration. Due to greater dislocation accumulation in the above alloys, DRX is initiated closer to the peak strain than in the present alloys. The substructural changes in the second linear region also lead to higher misorientation cells which lead to formation of DRX nuclei (90, 119, 126). Since DRX in the as-cast is

enhanced in the region of δ particles which has been verified metallographically (90), the curve drops more quickly from the second linear segment than it does for the worked alloys.

5.1.7 TEMPERATURE-STRAIN RATE DEPENDENCE OF SATURATION BEHAVIOR

The saturation stresses σ_s^* from Fig. 5a-g give rise to a fan-shaped series of constant $\dot{\epsilon}$ lines in a logarithmic plot against T, which, in agreement with other work (113, 126, 183, 191, 261), converge at 0 K. This unique saturation stress equals 7.5 X 10^3 MPa for 304 and is much lower than the value of 14.1 x 10^3 MPa for 301 due an increasing volume of cardides as T decreases. Due to increased solute in 316 and 317, this stress rises to 16.8 x 10^3, and 28.2 x 10^3 MPa, respectively. σ_s^* can be considered to represent the condition when thermal activation is absent and strain can occur by dislocation glide alone (82, 83, 88). While the work of Donadille (126) (Fig. 6b) is in agreement, the extrapolation of Kocks (113) (Fig. 6a) appears incorrect due to inadequate data.

The pattern of strain rate sensitivity in Fig. 8a-c is similar to that in Fig. 3a-d. Due to the high stresses, this matrix of values are indicative of power law breakdown since the stress exponent n''(=1/m) varies from 5 to 11 (34, 86, 90, 96, 101, 131, 134, 154, 175). The convergence of the constant-temperature lines in an expanded log σ-log $\dot{\epsilon}$ plot illustrated in Fig. 9a-c indicates that, at some high $\dot{\epsilon}$, stress is independent of temperature. This totally athermal situation is symmetrical with the $\dot{\epsilon}$-independent condition at zero K. The critical strain rates, varying about two orders of magnitude beyond 1 x 10^4 s^{-1}, could be associated with the elastic wave velocity for steel of 5.1 x 10^5 cm s^{-1}, which represents the upper limit of dislocation velocity (65). Alternately,

the condition could be related to the character of the current high T obstacles which become entirely stress activated. In comparison to the base alloy 304, the higher carbide forming 301 and 317 have lower values of σ_m and $\dot{\epsilon}_m$.

5.2 CONSTITUTIVE EQUATIONS

5.2.1 INFLUENCE OF ALLOYING ON SINH AND POWER LAWS

The hyperbolic sine function (Secs. 2.4.1, 2.4.2, 4.2.1) suitably demonstrates the dependence of the peak flow stress on $\dot{\epsilon}$. The sets of parallel lines, one for each T of the matrix of experimental points in Fig. 12a-d show the greater effects of T on the as-cast as compared with the worked material. The as-cast material has greater peak strength than the worked for the 304 and 317 but the difference for 316 is less, since it has the lowest volume fraction of δ phase, 0.20, compared to 0.31 and 0.23, respectively. The difference in σ_p is less at lower T possibly because the γ matrix could be becoming much stronger relative to the δ phase (90). Moreover, the two phases could have similar slip characteristics, thereby facilitating slip transfer. Furthermore, it could be due to the location of the δ at the dendrite cores. The stress exponents for all alloys are in close agreement with the mean of 4.3 derived from seventy published reports listed in Tables 1-4 (49, 57, 63, 76, 77, 119, 126, 152, 158-195).

While the divergence from the power law starts at 100 MPa in Fig. 16b, it commences at 1080°C for 304W much lower than 1150°C for 317W. Since 301W and 316W curves bend over at 1050 and 1110°C respectively, the order of increasing T corresponds to that of rising metallic solute. Moreover, the rate of divergence from linearity is less for 301W and 304W than it is for 316W and 317W. Whereas, the values for β are 5.3, 5.5, 5.0, and 5.8 for

301W, 304W, 316W, and 317W respectively, the value of the power law n'' is 5.9 (90, 101, 131) for all alloys which yields a commom β (= αn), where α is a constant. The power law exponent, 5.9, is rather high compared to 4.5 determined by sinh analysis (90, 101).

5.2.2 ACTIVATION ENERGY - SOLUTE EFFECTS

The excellent fit in Fig. 13a-d shows that the calculated Q_{HW} applies across the entire deformation range throughout which there is the same mechanism for all alloys (Secs. 2.4.1, 4.2.2-4.2.5). When account is taken of the differing solute contents, the values of Q_{HW} for all alloys are in agreement with the mean values reported in Tables 1-4. Through the extensive search of other work, it was found that Q_{HW} is directly related to the total metallic solute of γ stainless steel (49, 57,63, 76, 77, 119, 126, 138, 152, 158-195). As a result, Q_{HW} can be simply calculated by the following equation derived from Fig. 17:

$$Q_{HW} = F\ S^r\ (\pm\ 25)\ \text{kJ/mol}, \qquad (56)$$

where F equals 13.5 kJ/mol, S is the percentage of metallic solute and r is a constant which is approximately equal to 1. Comparative flow stresses were calculated by the Tanaka (196) equation where the characterizing T' of 1486 K derived for 304W in Fig. 18 was used. Since the mean stress exponent is 4.3, the flow stresses for the mean 304W alloy under deformation conditions of low Z (1200^{o}C, 1 s^{-1}) and high Z (900^{o}C, 1 s^{-1}) are predicted to be 73 and 224 MPa, respectively. Flow stresses of 60 and 185 MPa for the present 304W under the same conditions are in agreement with this mean alloy (Tables 1-4) when differences in metallic solute are considered (34, 42, 86, 89, 101-104).

The log-log linear correlation for all alloys between Z, specifying

the working conditions and the peak stresses in the log-log plot of Fig. 15a, facilitates interpolation for any working condition to find the stress for use in rolling formulae. However, it should be realized that it does not take into account the effects of increasing peak strain and deformational heating with rising Z which is considered later. Similar behavior in Fig. 15b for σ_s^* is not entirely unexpected since it is quite close to σ_p, although it does increase more rapidly with Z as seen in Fig. 5a-h.

Lines have been added to Fig. 15b showing the behavior of a 304W alloy (S+7+Ti) with a 7 percent increase in metallic solute containing 0.7 Ti (176) and another 304W alloy (S-11) with a 11 percent solute increase, without significant carbide forming elements (179). Both these alloys and the present one have similar flow stresses at low Z since most elements are in solution (34, 86, 89, 90, 131). The Q_{HW} values increase with metallic solute content. The present alloy exhibits 60 MPa at 1200°C (1 s^{-1}) , S+11 at 1210°C and S+7+Ti at 1220°C. This behavior confirms the strengthening effectiveness of Ti even at high T. While the present 304W alloy with 0.06C when cooled to 900°C climbs to a flow stress of 185 MPa, the S+11 alloy with low 0.03C needs cooling to 875°C and S+7+Ti, with a high 0.11C needs only 1000°C.

5.2.3 DEPENDENCE OF PEAK STRAIN ON Z AND D_o

The effects of the deformation condition Z upon the ε_p for a variety of 304W alloys with varying grain sizes are depicted in Fig. 14 (76, 152, 157, 167, 174, 178, 262) (Sec. 4.2.2). The relation between ε_p and Z arises because increasing solute which retards DRX raising ε_p, also raises Q_{HW} thereby augmenting Z. The ε_p for small D_0 are lower than those with a

larger D_0 due to faster DRX (84, 89, 90, 99, 134). Moreover, the peak strain for mild steel (262) is near the lower limit for those of 304W alloys. It decreases less rapidly as Z decreases relative to 304W, but more rapidly as T increases because of the lower Q_{HW}. Furthermore, the grain size exponent is smaller for the mild steel.

5.2.4 KOCKS-MECKING ANALYSIS OF THE SATURATION STRESS

In the Kocks-Mecking analysis (113-115, 198), the activation energy is not a constant but varies with stress because of associated changes in the recovery mechanism as T and $\dot{\varepsilon}$ change. For each deformation condition, Fig. 7 is used to determine the stage III activation enthalpy ΔH (= Γ ln $[\sigma^*_{s0}/\sigma^*_s]$) which is strongly stress dependent. From the derived slopes $-\Gamma/RT$, the value of Γ can be determined which is subsequently used in Eqn. 22 (113, 114). The value of Γ is constant for a given T but decreases as T increases and is determined to be 78 and 93 MPa at 900°C and 77 and 89 MPa at 1200°C for worked and as-cast 304, respectively. As T decreases and $\dot{\varepsilon}$ increases, the stress ratio decreases, thus the value of ΔH decreases.

The values of ΔH agree with those determined by sinh analysis only at the higher temperatures where the activation entropy gives a constant free energy (113-118). This arises because the sinh-Arrhenius analysis assumes the same mechanism across the entire range as is traditionally assumed in creep (20, 34, 101, 156, 168). The ΔH cannot be used in the traditional Z parameter, instead Eqn. 21 should be used with the constants Γ, σ^*_{s0}, $\dot{\varepsilon}_o$. The upward extrapolation of the matrix of data points in Fig. 7 converge at a unique $\dot{\varepsilon}_o$ (113, 119) which is higher for the as-cast materials since they go to higher stresses and are less strain rate sensitive. The data from another worked alloy falls on lines for the as-cast material because it has

a higher metallic solute content (119). The ΔH values range from 392 and 427 for low Z to 274 and 304 kJ/mol for high Z (304W and 304C respectively) as the mechanism shifts from dislocation climb to cross slip (90, 113, 198). The fact that all alloys can be described by stage III theory is clear evidence of the significance of dynamic recovery mechanisms during hot working (113-123).

5.2.5 YIELD STRESS-ATHERMAL BEHAVIOR

The gap between σ_s and σ_{yo} in Fig. 19a,b is indicative of DRV with a lesser contribution from DRX (86, 90) (Sec. 4.2.5). At 850°C, $\Delta(\sigma_s - \sigma_{yo})$ for 304W is 49 MPa, whereas it is 175 MPa for 304C. This significant difference is the effect of the large quantity of elongated δ ferrite particles in the latter. As T increases to 1200°C, these differences decrease to 5 and 44 MPa respectively. In comparison, at low T the 317 has greater differences, these being 254 and 125 MPa for as-cast and worked. As T rises, the $\Delta(\sigma_s - \sigma_{yo})$ for 317 (W, 6MPa; C, 36 MPa) become similar to those of the 304 since carbides have dissolved and solute interactions have diminished considerably (34, 84, 86, 89, 90, 131, 134, 168, 176, 179).

Across the deformation conditions, the range of σ_{yo} is 75 MPA for both 304W and 317W, while it is 32 MPa for both as-cast. The narrower range for as-cast is primarily due to the dendritic distribution of δ ferrite which gives less decrease in strength as T rises in comparison to the more homogeneous equiaxed structure. Consequently, the cast is more sensitive to both T and $\dot{\varepsilon}$ for σ_p and σ_s but not for σ_{yo}. Due to its lower metallic solute content, the athermal behavior of σ_{yo} occurs below about 825°C in 304W, and below 900°C in the Mo bearing 317W. Between these alloys, 301W and 316W exhibit similar behavior with the thermally activated release of

dislocations commencing above 850 and 875°C. Note that at high T where the curves become parallel, the yielding mechanism and flow-recovery mechanism become similar (86). Data from other work on 304W (263) fall on the present curve.

A detailed analysis of the differing behavior of as-cast and worked 316 materials is demonstrated in Fig. 19b. The peak, saturation and steady state flow stress are graphically compared with the yield stress. Contrary to the other alloys, where the as-cast material is higher than the worked at all T due to the strengthening effect of δ ferrite (34, 86, 89, 101-104), 316 exhibits similar stresses at low T with 316C being stronger than 316W at high T. Due to its equiaxed homogeneous microstructure, 316W passes the athermal limit at a higher stress and temperature (875°C) than for 316C (860°C). In this low T domain there is a high degree of work hardening to the peak which is slightly higher for the as-cast material. The difference between σ_{yo} and σ_p declines to very low values by 1200°C, but are always higher for the as-cast alloy because of additional hardening around δ particles. The drop due to work softening after the peak (σ_p to σ_s) is large at high Z but small at low Z. The drop is much less for the as-cast material because the value is an estimate as a result of intervening failure. As expected from the θ-σ curves (Fig. 5b,f), σ_s^* is slightly higher than σ_p by the ratio 1.03.

5.2.6 DEFORMATIONAL HEATING: TEMPERATURE RISE AT HIGH Z

Deformational heating has significant effects upon the flow characteristics (46, 63-78) of all alloys tested (Secs. 2.1.6, 4.2.6). It increases in importance as flow stress rises with Z, particularly in high flow stress alloys such as 317W at low T because the rise in temperature

decreases the effectiveness of carbides. At 1200°C, 0.1 s^{-1} (low Z), heat production is low and the surface T remains nearly constant, since the temperature controlling system compensates (73). Thus, the calculations of ΔT are approximately 47°C per unit strain at 900°C, 10 s^{-1} and 18°C per unit strain at 1200°C, 10 s^{-1} and are in close agreement with values of 57°C and 25°C from other work for these conditions when differences in solute content are considered (70, 73, 76, 78). At high Z, the deformation moves closer to adiabatic; consequently, T rises quickly with $\dot{\varepsilon}$ causing the torque to decrease. This augments the amount of DRX work softening which is naturally steeper with increasing $\dot{\varepsilon}$ and decreasing T due to the greater difference in strength between matrix and DRX grains (84, 86, 89, 90).

5.2.7 ACTIVATION ENERGY CORRECTION

When the lines on Fig. 20 are shifted by the calculated rise in T, the corrected value Q_{HWC} for 304W is 479 kJ/mol and agrees with 483 kJ/mol found for a similar alloy through research using slightly different methods (157). Since the corrections in Fig. 20 cause an angular shift in the log sinh $\alpha\sigma$ versus 1/T lines, it can be applied by estimation to uncorrected published data. Considering the calculation of Q_{HW} for 304W by the metallic solute content method, it is observed that the 22 percent rise over Q_{HW} gives a Q_{HWC} equalling 16.5 kJ/mol for each percent of metallic solute. Consequently, for the 304W alloy with a greater metallic solute content, tested in compression by Semiatin and Holbrook (76), a Q_{HWC} of 540 kJ/mol is calculated by this method. This value agrees with Q_{HWC} of 542 kJ/mol determined, conventionally, from ΔT in Eqn. 44 at 10 s^{-1}. Since both 316W and 317W experience approximately the same percentage increase as 304W when corrected, their respective Q_{HWC} values can also be calculated as 16.5

kJ/mol times the percent of solute.

5.2.8 INDUSTRIAL APPLICATION IN MODELLING

Since deformation is taking place at high strain rate in planetary rolling (1, 38, 279, 280, 282, 283) (Sec. 4.7.2), the thermal condition in the deformation zone is considered adiabatic. Therefore, the effects of deformational heating was considered in estimating the average T as 1307 compared to a preheat of 1250°C (Fig. 83a,b). Whenever high strain rates occur in rolling mills, deformational heating should be seriously considered when conducting modelling exercises. In industrial processing at a certain nominal T and $\dot{\varepsilon}$, the work heating is expected to be greater than in torsion tests because of the redundant work associated with more complex shape changes. Furthermore, the actual temperature change is affected by friction with and by dissipation to cold tooling (8, 33, 43, 65). Nevertheless, the accurate estimation of the temperature with the use of corrected stress values is superior to the use of uncorrected stress values with the assumption that the net process heating is similar to the test heating for the same nominal conditions (22, 157). The validity of the force calculations then depends upon the ability to determine the real temperature in each pass. Deformational heating generated in the torsional simulation of a seventeen pass cross country mill (Sec. 4.7.1) where the pass strain and $\dot{\varepsilon}$ are constant at 0.2 and 1 s^{-1} varies from from a negligible 2°C at 1200°C to only about 10° at 900°C. Since the temperature effect upon flow stress is minimal, no correction was deemed necessary (21-27, 29, 30).

5.3 DYNAMIC RECRYSTALLIZATION

5.3.1 NUCLEATION

A comparison of Figs. 21a,b (138, 264) and 22 (119, 126, 168, 174, 196) reveals that a decrease in T from 1200°C to 900°C at 1 s^{-1} lengthens the initiation of DRX from about 0.25 to 0.45 seconds; the former appears large in Fig. 21a,b because of the mechanical magnification, whereas the latter is small in Fig. 22, partly because of the log scale. Although t_c varies slightly with rising T, which lowers the driving force while raising the activation level, it decreases markedly with rising $\dot{\varepsilon}$ even though ε_c rises as a result of concurrent straining slowing DRX initiation. The variation with T reduces as $\dot{\varepsilon}$ rises because of the above changes (Fig. 22). Furthermore, t_c of the as-cast material is reduced more than the worked by rising T possibly because of the decrease in the strain concentration at particles as DRV increases.

The times determined from the work of Barraclough (174) are consistent with the present work, being a little greater due to slightly higher solute content (30.7) and larger D_0. The alloy torsion tested by Carfi et al. (119) exhibits a higher slope, rising to that of the present work at 900°C, 0.1 s^{-1}; this increase in t_c is due to a higher solute (31.6). At 1 s^{-1}, the present alloys exhibit increasing t_c in the order 304W, 317W, and 316W. The considerable retardation in the present 316W alloy across the entire range is primarily due to its high solute and low carbon (0.01) content. However, for the 316W with high 35.5% solute tested in torsion by Donadille et al. (126), t_c increases significantly as T drops because solute interactions augment rapidly. In spite of its greater solute than 316W, 317W experiences shorter t_c because of the presence of 5% δ ferrite. The

317W of Boden (195), although it has a lower $\dot{\varepsilon}$ ($\approx$ 0.1 s^{-1}), approximates the present 317W at 1 s^{-1}.

In conjunction with the significant dependence of ε_c on Z in Fig 21a,b, the dependence on T at 1 s^{-1} is also evident. The behavior of 304W, 304C and 301W behave similarly to other work (119, 126, 168, 174). At low Z, ε_c is much higher for 316 because of the additional solute, but is only slightly higher for 317 because of the enhancing effects of δ ferrite. The temperature below which DRX ceases when an alloy is deformed to a strain of 0.5 at 1 s^{-1}, illustrated in Fig. 21a, are 817, 889, and 917°C for 304C, 304W, and 301W. Subjected to similar deformation conditions, these temperature limits are 842, 887, 928, and 979°C for 317C, 316C, 317W, and 316W (Fig. 21b). The values of ε_c for the as-cast materials, as well as 317W, are lower due to DRX enhancement by 31, 23, 20, and 5 percent δ ferrite for 304C, 317C, 316C, and 317W, respectively.

Due to low solute, the 301W alloy at high T (1200°C) takes a higher ε_c (0.36) to accumulate a high enough dislocation density for the initiation of DRX (Fig. 21a). On the other hand, lower solute should increase mobility thus lowering ε_c (31, 34, 84, 86, 89, 90, 99, 101, 134); one must assume that this effect is relatively less than that on density. This slowed DRX for 301W also appears in Fig. 21a (138, 264). This situation is diminished as T drops and carbides are formed so that 301W and 304W converge at 800°C. For the alloy of Maki et al. (138), tested in tension at low strain rates (1.7 x 10^{-3} s^{-1}), the lowest T for possible DRX is about 1150°C at 1 s^{-1}, which is coincident in Z value with the condition 950°C, 1.7 x 10^{-3} s^{-1}. The low reported values at low Z arise partly because these tests were conducted in tension. When consideration is being given to grain refinement

by DRX during a pass, Fig. 21a,b can be viewed as defining the limiting Z for DRX for the given pass strain. For Z conditions lying to the upper left of the curves, the specimen is either partially or completely recrystallized, whereas for those lying to the lower right, the Z is beyond the limit where DRX can occur (90, 138, 264).

5.3.2 OSCILLATORY FLOW CURVES AND SAKAI-JONAS ANALYSIS

The changeover from single peak to oscillatory behavior in the flow curves (Fig. 4a-d) is associated with ε_p (a rough measure of ε_c) becoming larger than the strain ($\varepsilon_x = \varepsilon_s - \varepsilon_p$) for the completion of DRX as illustrated in Fig. 23 (136, 174) (Secs. 2.3.4, 4.3.2). When $\varepsilon_p > \varepsilon_x$ there is no overlapping of the waves of DRX because one wave is completed at ε_x before the first grains of that wave are ready for DRX at ε_p from the first peak (34, 85, 86, 97, 133, 136-138). The crossover for 301W occurs at a lower σ_p (40 MPa) at a higher strain (0.44) compared to 304W with a σ_p (45 MPa) at a strain of 0.38. This is consistant with the lower σ and slower DRX in 301W (Fig. 23) than 304W; hence the curve for 301W is considerably higher than that of 304W. The crossover for 317W occurs at a similar σ_p (46 MPa) and strain (0.38) as 304W due to DRX enhancement by 5% δ ferrite. 316W with solute close to 317W, but no δ ferrite, has the highest crossover conditions occuring at a strain of 0.50 with a σ_p of 49 MPa. In comparison with Fe-0.25C (136) which attains σ_p = 44 MPa at a low strain of 0.2, the γ stainless alloys exhibit slower DRX kinetics due to higher metallic solute contents. The values of ε_x for deformational conditions, 1000°C, 1 s^{-1}, are 2.67, 2.04, 2.37, and 2.42 for 301W, 304W, 316W, and 317W, respectively. These values indicate that, in 304W, DRX is complete at a lower ε_s than the Mo bearing alloys; with 301W having the highest due to the retarding

effects of the larger volume of carbides. For another 304W alloy (174) with greater D_0 and high solute, the crossover by extrapolation occurs at 1305°C, 0.1 s^{-1} (equivalent to 0.01 s^{-1} at 1200°C).

The general shape of the flow curves is strongly dependent on D_0 and Z as summarized by Fig. 62 (133). The single peak curve is obtained when D_s decreases with DRX ($D_s<D_0$), and the oscillating curve is obtained when D_s increases with DRX ($D_s>D_0$); for each D_0 there is a critical Z_c above which the former behavior occurs (138). The crossover Z values from Fig. 23 and the measured D_0 are plotted in Fig. 62; they obey the predicted relationship. Moreover, there is only one point for each alloy with a larger D_s which is that having the periodic curve at lowest Z. As an example, for a Z_c at 900°C, 1 s^{-1}, the grain sizes at which transition in the curve type is possible are 16μm for the 0.16C (133) steel and 14, 13, 10, and 8μm for the alloys 301W, 304W, 316W, and 317W, respectively, confirming that DRX is strongly affected by metallic solute content. Thus at this relatively low temperature grain refinement will occur for all grain sizes larger than those above.

5.3.3 AVRAMI KINETIC ANALYSIS

In the Avrami plot (23, 70, 106, 139, 141, 204, 205, 209, 211, 212) (Secs. 2.3.5, 4.3.3), the data for 304W determined by mechanical metallography has a slope of 1.28 (Fig. 24) which is in good agreement with slopes between 1.3 and 1.4 for the experimental data from other hot deformation research determined by optical metallography (126, 168, 174, 195). The series of straight lines displace to longer times as D_0 increases. The slope is similar for the several alloys at the same $\dot{\varepsilon}$, but falls as $\dot{\varepsilon}$ decreases. The slope of 1.3 for 317W compared to 1.27 for 304W

is consistent with its slightly shorter times for DRX due to enhancement by 5% δ ferrite. β_{DRX} which is the y intercept in the transformed Avrami expression varies from 2.7 to 2.4 for 304W with small D_0 and from 1.2 to 0.9 for 304W with large D_0. The value of β for 317W alloys ranges from 3.4 for small D_0 to 0.36 for a large D_0 at a strain rate of 0.5 s^{-1}. Consequently, β_{DRX} is sensitive to D_0 while k_{DRX} is not (31, 134, 168).

The plot of X_{DRX} against strain (Fig. 25) (Sec. 4.3.3) (31, 134, 168, 174, 195) can be transformed into the conventional S-shaped curve of X_{DRX} versus log t by dividing ε by $\dot{\varepsilon}$ (31, 138). Moreover, the present graph differs from the S curve insofar as DRX proceeds rapidly as soon as it is nucleated (31, 34, 84, 86, 89, 90, 99, 101, 138); thus many sites, being developed by the dislocation accumulation, become operative simultaneouly near ε_c. This rapid advance compared to SRX is consistant with ε_c for DRX being much larger than ε_c for SRX (22, 84, 86, 143, 168, 203). X_{DRX} increases in direct proportion to strain until considerable DRX has been attained and then the curves bend over reaching much higher strains as DRX nears completion in consistency with the shape of the flow curves (Fig 4a-d). The doubling of the strain for completion from 2 to 4 as D_0 quadruples (138) is primarily due to the lower grain boundary area per unit volume for preferential nucleation (89, 90, 99). The GB is more important in DRX than in SRX with the new grains forming necklaces along the old GB or along the interface of new and old grains (84, 86, 90, 97, 99, 132, 142, 144).

In accordance with the data illustrated in Fig. 28, the rate of DRX is inversely related to D_0 (168, 174). While there is scatter at X_{DRX} equalling 0.30, it becomes much less as X_{DRX} goes to 0.80. Manipulation of

the Avrami expression (Eqn. 10), in which β_{DRX} is replaced by K/D_0 (K being a constant), the time derivative is taken and results in the following expression for the rate of DRX (134, 195):

$$dX_{DRX}/dt = k_{DRX}\, K/D_0\, t^{k_{DRX}-1}\, (1-X_{DRX}) \qquad (57)$$

Replacing t with $(\varepsilon-\varepsilon_c/\dot{\varepsilon})$ the following equation is obtained:

$$dX_{DRX}/d\varepsilon = (C_{DRX}) \,/\, D_0\, (\varepsilon-\varepsilon_c/\dot{\varepsilon})^{\,k_{DRX}-1} \qquad (58)$$

where the constant C_{DRX} equals $k_{DRX}K(1-X_{DRX})$. From Fig. 28, at X_{DRX} equaling 0.80, the value of C_{DRX} is 0.04 for the present 304W compared to the mean of 0.05 from a high value at large D_0 (174) and low one at small D_0 (168).

5.3.4 DRX DISTRIBUTION ALONG FLOW CURVE

From the flow curves in Fig. 26 (168, 174, 195), the onset of steady state, which is a function of T, $\dot{\varepsilon}$, and D_0, is about three times ε_p. The present 304W with a solute content of 29.0 and a Z value of 1.3×10^{16} s^{-1} has a flow stress which is lower than the 304W of Ahlblom (168) with a solute of 29.6 as well as a slightly higher Z value of 3×10^{16} s^{-1}. The higher stress curve is also attributable to the approximately 7% higher flow stresses obtained in tension and compression testing due to texture and Taylor factor differences (40, 53). Both of these curves are lower than that of Barraclough (174) due to 30.7 metallic solute content and a larger D_0. Due to 1% greater Mo content and greater N content, the 317W of Boden (195) has a considerably higher σ_p than the present 317W.

Indicated along each curve are the percentages of DRX attained since its initiation at ε_c. Alloys having similar metallic solute and grain size, attain 31% DRX at ε_p (134). Due to larger D_0, hence slower DRX kinetics, the 304W of Barraclough (174) has considerably less about 14%. Boden's

(195) 317W with a 4.3 Mo content which retards DRX achieves only 9% at ε_p. As demonstrated in Figs. 22 and 25, 304W and 317W have similar DRX characteristics in spite of their obvious differences. Moreover, they attain the same DRX percentage at the peak (31%); 317W exhibiting such a low strain due to the favorable effects of 5% δ ferrite.

As shown in Fig. 25 (168, 174, 195), the alloys experience initiation of DRX at different ε_c, which cluster around a mean value of 0.33. However, the progress is strongly dependent upon D_0; ε_s for all alloys with a small D_0 ranges between 1.6 and 2.0, but for large D_0, it is about 3.2. For about the same D_0, ε_s increases approximately linearly with rising σ_p. After 90%, DRX slows down to the extent that it takes approximately one third of the total strain to advance to completion. The T dependence for 99% DRX (Fig. 27) is moderate for 301W, 304W, and 316W, but for 317W it is much lower indicating the retarding effect of δ ferrite. While 304W has the highest DRX kinetics at all T, 301W has the lowest at low T. This is consistent with Fig. 23, where ε_x is much higher for 301W than for 304W which is related to extended overlapping of DRX waves (84, 86, 88, 89, 90, 97, 99, 101, 133-137), and is consistent with the high ε_c. DRX times for 316W with high Mo content lie between 301W and 304W. The time for 304W of Ahlblom (168) is greater than that for the present 304W due to greater solute content in spite of the faster kinetics generally experienced in compression and the smaller D_0. The completion of DRX for large D_0 are displaced to greater times due to reduced area of grain boundary or interface between the new grain necklaces and old grains (84, 86, 99, 142, 144).

5.3.5 ACTIVATION ENERGY FOR DRX

The $\dot{\varepsilon}$ dependence of time for 99% (Fig. 29a,b) (Sec. 4.3.4) are comparable to the constitutive plots of $\dot{\varepsilon}$ versus sinh $\alpha\sigma_p$ (Fig. 12a-d) where the constant T lines slope upwards to the right because of the reversal of the vertical axis ($t = \varepsilon/\dot{\varepsilon}$). The slopes of the parallel lines for 301W and 304W are 4.1 and 4.3 respectively compared with 4.4 and 4.6 derived from peak flow stresses, in consistency with the lower strain rate sensitivity of σ_s. From Fig. 30a (comparable to Fig. 13) the Q_{DRX} for 301W is slightly higher than that for 304W (similar to Q_{HW}), again due to carbides at low T. As a result of the inclusion of lines for σ_c and σ_p in Fig. 30b, the manner in which the activation energy varies along the flow curve from the initiation of DRX (Q_{CRX}) through the peak (Q_{HW}) to the onset of steady state (Q_{DRX}) is noted (101). From the critical stresses which are the upper limits of DRV alone, a Q_{CRX} of 351 kJ/mol is found which compares favorably with the value of 314 kJ/mol for creep (34, 84, 86, 101, 156, 168). A similar value of 380 kJ/mol was determined by Ahlblom (168) at a constant strain of 0.3 which is within the region of DRV. At the peak of the curve, where the DRX has lowered the strain hardening rate to zero (θ-σ plots, Fig. 5a-h), Q_{HW} has a value of 393 kJ/mol in comparison to 418 kJ/mol determined by Ahlblom (168). Finally, calculated for data at the onset of steady state Q_{DRX} is 291 kJ/mol which is less than the Q_{HW} as discussed in Secs. 2.4.1. Similar behavior is exhibited by 316W and 317W in Fig. 30a where the slopes rise to lower values due to solute which increases σ_p, and consequently σ_{DRX}. Since this higher solute retards the completion of DRX (31, 84, 86, 89, 90, 99, 101), it raises their values of Q_{DRX}. While all alloys have similar DRX kinetics at high T (Fig. 30a), this

behavior begins to rapidly diverge as T falls. Nevertheless, their Q_{DRX} values vary marginally when compared with their Q_{HW} values. This comes about because the work softening after the peak is quite large at low T and high $\dot{\varepsilon}$, where DRX eliminates a rather high density of dislocations (31, 84, 86, 89, 168).

5.4 STATIC RECRYSTALLIZATION

5.4.1 FRACTIONAL SOFTENING

Determination of the degree of static recrystallization by metallographic means is tedious and fails to measure softening from SRV. In this report, the method of mechanical metallography (10, 12, 21-26, 199, 201, 202, 203, 215-219) (Eqn. 26) is employed because the drop in flow stress is simple to measure the softening due to SRV, SRX, and grain growth which results in a FS greater than 100 percent (10, 22, 30, 84, 86, 89, 199, 208) (Secs. 2.6.3, 2.6.4, 3.3.3, 4.4.1-4.4.3).

Due to the incubation time for the commencement of SRX (22, 201-203), the first 30% FS is due to DRV (174, 199, 208). In Fig. 37a, FS is plotted against accumulated pass strain with a horizontal line drawn through 30% in the lower portion of the graph indicating where SRX starts (Sec. 4.4.3). Under all conditions, the as-cast has lower values of FS due to δ ferrite. The static softening behavior of the as-cast alloys is performed through an analysis of Fig. 37b where the average FS for each deformation condition is indicated. The 316C has the largest FS despite the fact that it has the lowest flow stress and hence stored strain energy. Both occur due to the alloy having the lowest concentration of δ ferrite. The 304C, having a much higher fraction of δ ferrite, has about 3% greater flow stress but 10-40% less softening for equivalent conditions. The 317C with less δ than the

304C has 20% greater flow stress and about the same FS.

The FS rose for all alloys as the interval increased from 20 to 40 s. Furthermore, an increase in temperature had a more pronounced effect in raising FS than did $\dot{\varepsilon}$. While there is a 26% increase in FS at 900^{o}C compared with 14% at 1000^{o}C when the strain rate rises from 0.1 to 1 s^{-1}, FS increases 71% at 0.1 s^{-1} and 54% at 1 s^{-1} when T increases from 900^{o}C to 1000^{0}C. Whereas, the increase in the former is primarily due to greater stored energy from higher flow stresses, increases in SRV and SRX through thermal activation is more effective in raising FS (31, 84, 86, 89, 99). Volume fraction recrystallized increases from about 5% to 15% when the T rises at the highest $\dot{\varepsilon}$.

5.4.2 SRX KINETICS

The testing method illustrated in Fig. 31a,b (Secs. 2.6.4, 4.4.1, 4.4.2) allows the determination of FS for different interval times. The envelope curve exhibits weak peaks for both 301W and 304W with the latter dropping more rapidly due to greater FS. The work of Barraclough (174) is used for conversion of FS to X_{SRX} defined by Eqn. 28, which is verified by the formula developed by Sandberg and Sandstrom (208) (Eqn. 27) where the characterizing value t_o for 304W equals 0.37 for deformation conditions 1100^{o}C at 1 s^{-1}. Figure 32 shows the slope of the Avrami expression and the traditional sigmoidal S curve. The behaviors of 301W and 304W are similar to that of 304W of Barraclough (174) displaced to longer times. This divergence is primarily due to a lower test T of 1050^{o}C and larger D_0. These differences generate the same k_{SRX} value of 1.3 for the present work with a corresponding higher value of 1.7 for the other work (174). The low k_{SRX} values of 1.2 and 1.1 for 316W and 317W are due to high solute

inhibiting the growth of SRX grains (22, 89, 99, 134, 139, 208). As with DRX kinetics β_{SRX} is a strong function of the original grain size. Due to the larger grain volume, it takes longer time for the growing grains to consume the old grains. The slopes for both 316W and 317W are displaced to the right due to high Mo contents.

In agreement with other recent work (106, 130, 168, 174, 180, 204, 213, 265, 267-269), $t_{0.5}$ is a strong function of the pass strain and the power of -2 differs from -4 found for C-Mn steel (203) (Sec. 4.4.2). The present work is plotted in Fig. 34 with extensive other work which has been normalized with respect to $\dot{\epsilon}$ and D_0. While there is some scatter, the results form two lines which are representative of the alloys' metallic solute content. In order to observe the pass strain rate effect upon $t_{0.5}$, the temperature compensated time $W_{0.5}$ is plotted against log Z (Fig. 33) (Sec. 4.4.1). Here it can be seen that $t_{0.5}$ is proportional to Z to the power -0.375 as previously observed (168, 174, 266); thus it decreases as $\dot{\epsilon}$ increases. The lines for the present 301W and 304W are displaced higher due to a much finer D_0. Furthermore, the work of Drastik and Elfmark (266) approximates the present 301W because it was deformed at a much higher pass strain and $\dot{\epsilon}$. The displacement is also due to the higher Q_{SRX} resulting from a greater solute content. Q_{SRX} values for 301W and 304W were calculated from Fig. 35, which shows the temperature dependence of $t_{0.5}$, normalized for strain energy. Other work is included for comparison (106, 130, 168, 174, 180, 204, 206, 212, 213, 265, 267-270). While these values are similar to Q_{HW}, they do not indicate complete similarity in mechanism but rather the similar influences of alloying upon both mechanisms.

5.4.3 ISOTHERMAL MULTISTAGE DEFORMATION AND INDUSTRIAL SIGNIFIANCE

The representative multistage flow curves, of 301W and 304W (Fig. 36a,b) illustrate the effects of SRV and SRX between passes. Since the first pass represents the first segment of the regular continuous curve, subgrain formation occurs at about a strain of 0.1 (24, 25). Furthermore, only DRV is operative during any pass because the strain is less than ε_c (> 0.3). The multistage curves fall below the continuous curve for all conditions. Nevertheless, during intervals at high T they drop more deeply due to increased softening and less accumulated strain. Furthermore, the envelope curves for 900°C become horizontal and are well below the continuous curve (10, 12, 19, 22, 30, 86, 180, 215). Those for 1000°C exhibit weak peaks before becoming horizontal slightly below the continuous initially and later becoming slightly above the steady state regime of the continuous curve. The difference arises because the softening at 900°C causes more stress reduction even though at 1000°C the fraction is higher.

As shown in Fig. 36a,b the succeeding passes of this isothermal multistage schedule are considerably higher due to incomplete softening during preceding intervals. The envelope of curves 2 to 6 form broad flat peaks because the pass curves have similar maxima and similar yield stresses due to similar softening in the intervals. In application of this data to the simulation of a 4 stand mill, Fig. 38 illustrates the increase in the mean flow stress at different T of stands 2-4 over stand 1 (5, 6, 10, 15, 215). These mean flow stresses required for force calculations determined from this type of test more closely represent the real situation in passes after the first than those calculated from tests on recrystallized starting material. They are only an approximate simulation

because in real schedules the temperature of deformation is usually decreasing; a more realistic physical modelling with declining T were performed and will be discussed later (16, 19, 20-27, 30, 35, 36).

5.5 HOT DUCTILITY

5.5.1 MECHANISMS; DEPENDENCE ON T AND $\dot{\varepsilon}$

The ductilities of all as-cast and worked alloys increase with rise in T as accelerated DRX more effectively retards the propagation of intergranular cracks (12, 22, 34, 89, 99, 106, 180, 226-230, 233) (Secs. 2.7.1, 2.7.2, 4.5.5). The cracks arise from intergranular sliding which commences at about 600°C. The sliding on boundaries, alligned parallel to the shear plane, induces stress concentration in boundaries lying $\pm$ 45° to it; this gives rise to triple junction wedge cracks (22, 34, 86, 89, 101, 226-230). The nucleation of the cracks is delayed as T rises and $\dot{\varepsilon}$ falls by the increased DRV which permits increased lattice flow to accomodate the sliding, thereby relieving the stress concentration. When DRX occurs, it moves the grain boundaries away from the cracks, thereby halting their propagation and permitting them to be blunted (22, 34, 84, 86, 89, 101, 226, 229, 230). Nevertheless, the fissuration gradually increases with strain as additional cracks form on new boundaries or old ones propagate upon recapturing migrating boundaries (Fig. 50a).

With rising T and $\dot{\varepsilon}$, the former providing more thermal activation and the latter more driving force (86, 101, 226), DRX occurs more rapidly and in more frequently repeated waves as indicated by the decrease in ε_c and ε_p (Fig. 4a-d). The positive effects of enhanced DRX are clearly illustrated for 301W and 304W where ε_f increases as both T and $\dot{\varepsilon}$ increase (10, 42, 86, 89, 90, 162, 167, 168, 188, 191, 215, 235, 271) (Figs. 39, 40a) (Sec.

4.5.1). Rising T greatly increases GB migration, thereby reducing the time that a fissure may capture a boundary and grow. While the T dependence for both 316W (Fig. 40b) and 317W is the same as above, their ductilities decrease as $\dot{\varepsilon}$ rises (22, 34, 73, 191, 226-228).

Increasing $\dot{\varepsilon}$ may have the following effects: a) enhancing DRX through increased driving force, b) decreasing the relative proportion of GB sliding and hence cracking, and c) increasing σ and hence stress concentration at cracks, thereby speeding up their propagation (91, 92). While the first two mechanisms prevail, as in 301W and 304W, the ductility, mounts towards a maximum as $\dot{\varepsilon}$ rises. Due to solute-increased flow stress, this increasing propagation of cracks is already occurring in 316W and 317W at a lower $\dot{\varepsilon}$. Therefore, these two are on the declining side (Figs. 39, 40b, 41) of the maximum at the strain rates studied, whereas simple alloys such as 301W and 304W (Figs. 39, 40a, 41) are on the rising branch.

5.5.2 EFFECTS OF SOLUTES AND SEGREGATES

When compared with carbon steel, all alloys have a considerable lower ductility, decreasing with increasing solute content. Since rising solute lowers SFE (127-130) reduces DRV (82, 84, 86, 88) and increases lattice strength, it reduces the ability of the grains to accomodate differential GB sliding, thus increasing the stress concentrations at the triple junctions and the rate of cracking (34, 42, 86, 89, 101, 106, 107, 236-233). Moreover, rising solute, by diminishing GB mobility, reduces the ability of DRX to isolate, blunt, and halt cracks, resulting in the decreased ductility of 316W and 317W.

Figures 39 and 40 illustrate the effects of both $\dot{\varepsilon}$ and T on the comparative torsional ductilities of 301W, 304W, 317W, 317C, and 304C. The

301W has a higher ε_f at 1200°C than 304 W due to lower solute but drops to below the latter as T decreases below 925°C due to the precipitation of carbides in the former. Both 301W and 304W have much better torsional ductility than 316W and 317W because of their Mo content, which may form carbo-nitrides at the bottom of the working range. The ductility was lowest in 317W because the 5% δ ferrite slows DRX, thus raising the frequency of GB capture by fissures. The 304 material is superior in ductility to a wide variety of alloys depicted in Figs. 40, 41 (10, 42, 167, 188, 191, 215, 228, 271) and notably to an alloy tested in the slab, ingot, or as-cast condition (271). While the present 304W is higher than other variations due to lower metallic solute content, its ε_f is lower than 0.14 carbon steel (10, 215).

With 31% δ ferrite compared with 23% for 317C, the 304C has the lowest ductility due to the rapid propagation of cracks between large δ particles (240-245). The alloys 304C and 316C solidify with ferritic dendrite cores (Fig. 51a) which are separated from the segregated impurities at the grain boundaries (109-112) (Secs. 2.7.3, 4.5.6). Thus, their as-cast ductility is not adversely affected by combinations of these two factors as is 317C, solidifying with δ at the γ boundaries (109-112) (Fig. 52). While 316C has a greater alloy content than 304C, it has a higher ε_f due to a lesser δ content. The poor ductility of 304C arises from cracking at the γ-δ interfaces and partly from the δ phase limiting grain boundary migration which normally retards GB cracking (109-112) even though it inhances nucleation. At high Z, the fracture occurs before DRX makes significant progress.

5.5.3 GITTINS-SELLARS FAILURE CONSTITUTIVE RELATIONSHIP

A time-to-fracture criterion, derived for creep (34, 131, 249, 250) has been proven valid for torsion data of both 304 and 316 in both the as-cast and worked conditions (Secs. 2.7.3, 4.5.2). Use of the exponential function for 316C (Fig. 42a,b) provides values of β, n, and Q_{HW} for fracture data differing from those for strength; this arises from the strain rate dependence of ε_f. 304C and 317C are alike in having similar fracture and strength coefficients which are related to the strain rate having a negligible effect upon ductility (34, 226). Fig. 43a,b reveals a similar valid relationship for the present 316W and that of Teodosiu et al. (191), but with application of the hyperbolic sinh function. The time to fracture decreases with rising $\dot{\varepsilon}$ even though ε_f decreases. As with the as-cast material, 316W has values of n_f and Q_{HW} which are substantially larger than the equivalent values for hot strength data.

This analysis considers the formation, growth and linking up of voids as retarded by DRX (22, 34, 86, 89, 91, 92, 101, 131, 226-230). For the high Z case ($900^{o}C$, 5 s^{-1}) where D_s was measured to be 12 μm and with estimation that the surface energy of the fractured material (γ) = 100 N/M (250), the shear modulus (μ) = 42.7 ($900^{o}C$) and 34.8 ($1200^{o}C$) GPa (146, 178, 284, 285), and Poisson's ratio (ν) = 0.31 (284), then the predicted value $t_f \exp(-Q/RT) = 3.6 \times 10^{-20}$s as compared with the experimental value of 4.5×10^{-18}s. For the low Z conditions ($1200^{o}C$, 5 s^{-1}) where D_s equals 75 μm, the calculated value is 2.8×10^{-17}s as compared with 6.5×10^{-15}s for the experimentally measured one. Therefore, theory predicts temperature-compensated fracture times which are two orders of magnitude lower than those found experimentally. The failure of the theory to

accurately predict fracture times is probably due to the retardation of crack growth by the migrating boundaries during DRX (229, 230, 249, 250). In addition, it is impossible to estimate how often waves of DRX pass during steady state prior to fracture.

5.5.4 ELFMARK FAILURE CONSTITUTIVE RELATIONSHIP

The hot ductility in continuous tests is finally examined by means of a plasticity parameter derived by Elfmark (251, 252) (Secs. 2.7.5, 4.5.3). The mechanism of failure is related to grain boundary sliding and to the nucleation, growth and linking up of fissures. DRX inhibits this process by moving the grain boundaries away from the fissures, thus halting their propagation until they once again capture a boundary (34, 86, 89, 91, 92, 101, 131, 226-230). Because of the significance of this inhibiting effect, the important index is the time (t_{DRX}) for 99% DRX which is considered to be coincident with the beginning of the steady state regime (97, 266). The T and $\dot{\varepsilon}$ dependence of σ_s is determined from sinh and Arrenhius plots (Figs. 29a,b and 30a,b). The value of Q_{DRX} derived is 296 kJ/mol which is less than Q_{HW} as discussed in Sec. 2.4.1. Elfmark (251, 252) introduced a temperature-compensated time W_{DRX} which draws the data for all conditions into a single line. The ductility is related to this W_{DRX} in Fig. 44b. Although the fundamental fracture criterion is tied to the propagation of fissures, the final time to failure is dependent only on parameters derived from the flow curves without microstructural measurement.

5.5.5 EFFECTS OF MULTISTAGE DEFORMATION

Ductility can be greatly improved by intervals of short time between stages of deformation (7, 22, 34, 86, 101, 106, 180, 193, 226, 229, 230) (Secs. 2.7.4, 4.5.4). SRV and particulary SRX help the action of the

dynamic mechanisms in impeding nucleation and growth of cracks. For optimum results, the strain in each pass should be small enough to limit the fissuration but large enough to induce SRX (22, 86, 101, 229, 230). The critical strain for SRX is considerably lower than that required for the initiation of DRX (22, 84, 86, 143, 200). In as-cast alloys, the intervals also allow for improved homogenization by solution of δ particles which reduces their deleterious effects already described. Figure 45 clearly illustrates the increase in ductility for both 304C and 304W due to pauses of short interval time. Whereas, the ductility is less for the as-cast because of the presence of δ particles than the worked, multistage deformation extends the ductility 50 percent (180) in both cases.

The results in Fig. 46 largely show that in comparison to similar continuous tests, ductility is higher in isothermal multistage tests (12, 106, 180, 229, 230, 233). While each test has repeated equal passes separated by equal intervals, ductility enhancement is also attained when these parameters are varied. For 304W, the hot ductility rises with augmented intervals at low T, whereas at high T it declines at longer times, because of grain growth and the recapture of boundaries by fissures. The improvement is large where the continuous ductility is low and small where it is high, because the static mechanisms do not contribute much additional change to the microstructure developed dynamically. The effectiveness of pauses diminishes as the pass strain increases because the cracks have a prolonged opportunity to propagate in each pass since the SRX during the interval does not prevent their nucleation but can only blunt and not heal those already formed (22, 106, 229, 230). Improvements in ductility from multistage tests vary greatly with the alloying additions,

since different solutes and precipitates may cause different degrees of fissuration and of retardation of static restoration (34, 86, 101, 225-241).

5.6 MICROSTRUCTURE

5.6.1 DRX GRAIN STRUCTURE

The initial microstructure of 304W which consisted of equiaxed grains with annealing twins are replaced with equiaxed, substructure-containing DRX grains (Secs. 2.3.2, 2.3.4). The DRX grains at 900^{o}C, 5 s^{-1} which are only 12 μm, nucleate as a result of bulging of, or high misorientation cells occurring, at the grain boundaries, forming in successive layers until the old grains are consumed (34, 84, 86, 89, 90, 101, 117). Concurrent deformation has two complimentary effects: i) the new grains are inhibited from growing by the formation of substructure within them, and ii) high angle deformation bands in the old grains near the interface with the new ones lead to a second round of nucleation. The latter effect is more pronounced at high Z.

5.6.2 GRAIN SIZE DEPENDENCE ON σ AND Z

The microstructures observed in the worked alloys at the beginning of steady state consisted of equiaxed DRX grains (Figs. 56a,b, 57a-d, 58a-d, 59a-c) which are quite different from the elongated original grains, if only DRV had occurred (84, 86, 168). These grains are confirmed to be the result of DRX because a substructure is present (31, 84, 86, 87, 89, 90, 99, 132, 136, 168). All alloys are dynamically recrystallized, having undergone more than one wave of DRX in the steady state regime (97-101, 133-137). At low T, the grain boundaries contain some carbide particles which at high T have gone into solution (103, 104), thereby facilitating

migration. While D_s is independent of D_0 and strain in the steady state region, it is strongly dependent upon stress which is a function of T and $\dot{\varepsilon}$ (Secs. 2.3.4, 4.6.3). The flow stress as a function of D_s conforms to the following equation:

$$\sigma_s = 4.7\ D_s^{-0.81} \qquad (59)$$

where the power is within the range 0.7-0.8 found in the literature (31, 84, 86, 89, 90, 99,101, 131, 136).

The stress calculated from the crossover condition ($D_0 = D_s$) in Fig. 23 fall along the line for D_s in Fig. 63, thereby attesting to the validity of the testing methods and metallography. The results also confirm the relative grain size model (133, 136, 137) illustrated in Fig. 62. As the stress increases D_s decreases with a power of -1.23, whereas D_{MRX} declines with -1.31 (Fig. 63). Due to the usual difficulties of quenching-in the DRX microstructure (42, 43, 55, 168) some specimens experienced MRX. Thus, as the flow stress decreased tenfold, D_s increased by a factor of 17, whereas D_{MRX} increased by a factor of 21. Consequently, while the grain size increased 70% from 7 (D_s) to 12 μm (D_{MRX}) at a high stress of 250 MPa, it increased 90% from 129 μm to a value of 248 μm at a lower stress of 25 MPa. In the dynamically recrystallized microstructures found in some 304W (Fig. 57b) and 317C, the D_{MRX} values are in full agreement with those derived by Ahlblom (168) who observed specimens with dynamic, metadynamic, and static recrystallized microstructures.

The variation in DRX grain size with log Z for 301W, and 304W are shown in Fig. 62. All data have been normalized at 900°C, 1 s^{-1}. While grain refinement of the original grain size (66 and 70μm respectively) occurs between 1100 to 900°C (5 s^{-1}), grain coarsening, consistent with

cyclic DRX as indicated by the σ-ε curves in Fig. 4a,b, occurs at 1200°C, 0.1 s^{-1}. Since the current measurements are mainly for 5 s^{-1}, the data also show that log D_s declines linearly as (1/T) increases. This linear logarithmic plot further indicates that D_s is related to σ by a negative power (138, 168, 174, 195) (Fig. 63).

While rapid cooling after deformation should have prevented SRX in these high solute alloys, some specimens had very large SRX grains. An additional observable difference between the SRX and DRX grains is that the former contains annealing twins in greater concentrations and with undeformed boundaries (132, 168) (Fig. 68c). The as-cast alloys, which exhibit dendritic structures with segregated δ phase, also contain equiaxed γ grains between elongated δ stringers after straining to fracture (Fig. 58b,c). Both DRX and SRX grains are dependent upon the density of nucleation which is a strong function of T and $\dot{\varepsilon}$. While the SRX grains arise from the same substructure, they grow larger since they are not inhibited by concurrent deformation inducing internal substructure (22, 86, 99, 101, 203) (Fig. 63a,b).

5.6.3 DRV SUBSTRUCTURES

As shown from Fig. 5a-h, rapid work hardening takes place during hot deformation up to a strain which varies between 0.08 and 0.15, beyond which the formation of the cellular substructure is established by a medium level of DRV (124-126) (Secs. 2.3.1, 4.6.4, 4.6.5). As the strain increases, the number of subgrains per unit volume also increases up to the steady state condition where a stable equiaxed polygonized substructure is maintained (2, 4, 20, 75, 82-84, 86, 88, 90, 95). As the new grains grow, eliminating the existing substructure, new tangles and subboundaries form in them

reestablishing the polygonized substructure which ultimately leads to another round of nucleation. Subgrains are formed with boundaries of well defined arrays of dislocations at T > 600°C (82, 83), while the formation of cells with boundaries of diffuse dislocations takes place at T < 600°C (146) (Fig. 56a,b). From Figs. 53 and 56a,b, it can be seen that the DRX grains are larger than the DRV subgrains by an order of magnitude (168) and vary more slowly with stress.

Recent TEM observations (Figs. 65-68) have shown that subgrains first form along grain boundaries indicating a higher density and stress level there. The subgrains are then observed to spread inwards as polygonization takes place close to the center of the grains (84, 86, 89, 90, 99, 119, 126, 136, 168). It has also been noted that GB bands form, that is regions of higher misorientation near the boundary. These are likely the source of the dynamic nuclei that form first along the boundary (86, 90, 99).

While the presence of a substructure confirms that the almost equiaxed grains result from DRX (84, 86, 89, 99, 132, 136), the observation of similar polygonized substructures in both the as-cast and worked alloys as before the peak verifies the existence of DRV concurrent with DRX. Such substructures existing in the DRX grains explain the reason why the latter undergoes SRX when held at high T after hot working (22, 34, 84, 86, 89, 90, 203) (Fig. 65c). As T rises and $\dot{\varepsilon}$ declines, the subgrains change from elongated to equiaxed, becoming larger and more polygonized (Figs. 65a-c, 66a,b, 67a,b, 68a-d, 69a-d). Consequently, they contain fewer dislocations within them with neater arrays in the walls.

5.6.4 SUBGRAIN SIZE DEPENDENCE ON σ AND Z

As seen in Fig. 70a,b, the size of cells and subgrains is a strong

function of steady state flow stress (Secs. 2.3.1, 2.3.6, 4.6.5). As T increases, the subgrains become more equiaxed with reduced dislocation density. An extensive compilation of data from the literature (87, 140, 145-148, 260, 272-278) confirms that subgrain diameter is related to the flow stress by the following equation for 304W and 316W respectively:

$$d_s = 269\ \sigma_s^{-1} \qquad (60)$$

$$d_s = 501\ \sigma_s^{-1} \qquad (61)$$

The cell diameter below 600°C for the former is related by the equation which follows:

$$d_s = 1.15 \times 10^5\ \sigma_s^{-2} \qquad (62)$$

The subgrain diameters of the present work are in good agreement with those found in the literature and confirm the equation developed by Raj and Pharr (286) through an extensive analysis of creep data.

In comparison with subgrain diameters reported presently and in other work on 304W (87, 140, 157, 260, 272), the present 317C values are slightly smaller but have the same dependence on Z. From Fig. 69a, it is seen that for a given subgrain diameter the flow stress for 317C is greater than that for 304W. Thus, it appears that the strengthening arises in part from the direct action of the solutes and precipitates and in part through the fact that they alter the substructure to be smaller at a given deformation condition. Thus, at 900°C, 1 s^{-1}, the subgrain diameters of 317C and 304W (Fig. 69b) are 1.11μm and 1.21μm, which gives strengths of 275 and 195 MPa, respectively. These subgrain diameters are about one magnitude smaller than the corresponding DRX grains of 16 and 13μm. Nuclei may arise directly from the subgrains at high $\dot{\varepsilon}$ or from interactions between subgrains and existing boundaries at low $\dot{\varepsilon}$ (84, 86, 87, 99, 117, 132). When 317W is compared with

317C (Fig. 69b), the subgrains for the latter are smaller partly due to the higher strain energies resulting from 23% δ ferrite in comparison with 5% retained in the worked. Due to the inhibiting effects of Mo, especially at high Z (900°C, 1 s^{-1}), the subgrain size for 317W at 1.39μm is smaller than a subgrain size of 1.51μm for 304W (Figs. 69b, 70a).

5.7 PRODUCT QUALITY

5.7.1 PRODUCT MICROSTRUCTURES

In the previous section a variety of microstructural features were described as those evolving during either the deformation alone or multistage processing. They have been analyzed in association with the mechanical measurements in order to clarify the mechanisms which are able to explain the flow curve shape, the net strain hardening rate, the constitutive equations and constants, the ductility and static restoration. However, it is possible to regard these microstructures as those of the product at room temperature. If the material is cooled rapidly after deformation, the DRX substructure is retained to strengthen the product (22, 86, 90, 95, 149-152) as discussed in the next section. The grains would be elongated if before the peak or refined and equiaxed after the peak to improve the mechanical properties. If the cooling is slow, the recrystallized grains are more refined if the previous pass had higher ε or $\dot{\varepsilon}$ or lower T (22, 24, 34, 36, 86, 99, 203).

5.7.2 PRODUCT STRENGTH

The hardness values of 304C, 316C, and 317C have been measured after hot torsion (Fig. 71) (Secs. 2.3.7, 4.6.6) In these alloys which have undergone partial DRX due to early fracture but no SRX, the hardness rises with Z as a result of the increasingly finer subgrain diameters (22, 152,

203). The hardness is highest for the 317C because of its high solute and strengthening by 23% δ ferrite. The 304C follows because of 31% volume fraction of δ particles. The 316C is lowest because it has only 20% δ. The hardness of these alloys in the preheated condition is higher than after hot working as a result or redistribution and dissolution of the δ phase (102-104). It is only after deformation conditions of 990, 1000, and 950°C at 1 s^{-1} for 317C, 304C and 316C that the hardness becomes superior to the as-cast hardness. Furthermore, it is only after such deformation that the alloys properties depend on subgrain strengthening across the entire range (Fig. 71) (132, 149, 150, 152). This is evidence of the evolution of microstructure during straining which has a profound effect on hot flow stress, ductility and room temperature strength (22, 34, 86, 149, 152). Analysis reveals that such hardness is inversely proportional to the subgrain size as has been found through other work (22, 34, 84, 86, 88, 89, 150).

5.8 SIMULATION OF BAR MILL

5.8.1 FLOW CURVE BEHAVIOR

Since the deformation behavior of the alloys was similar in many ways, the simulation of 301W (Sec. 4.7.1) is described here in detail with differences for 304W and 316W noted. The flow curves rise as T declines (Figs. 72, 76), but only partially as a result of the dependence of σ on T. A considerable contribution arises from the carryover of strained material (Secs. 4.4.3, 4.7.1) from one pass to the next as can be seen from the decline in FS presented in Fig. 77, where the more important scale is that of X_{SRX} (Secs. 2.6.4, 2.6.7). When SRX falls below 20% (≈ 80% FS), the more marked hardening is noticeable in the increase in slope of the envelope

joining the maxima (25-28) in Fig. 72 which is illustrated in Fig 76. While 304W exhibits similar behavior, it occurs earlier for 316W at 1100°C where carbides have started to precipitate, thereby significantly raising the mean flow stress (25, 26). The inherent influence of T and $\dot{\varepsilon}$ on the deformation mechanism can be seen in the increase in the distance between the σ_{yo} and σ_m curves (Fig. 76) which is related to the strain hardening rate θ (= $d\sigma/d\varepsilon$) (Sec. 2.2.4). During isothermal continuous deformations, θ mounts in a regular manner as T falls and $\dot{\varepsilon}$ rises. The influence of $\dot{\varepsilon}$ on σ can be seen in Figs. 72 and 76 by much higher pass flow curves and σ_m envelope curves respectively. Moreover, the tests at rising $\dot{\varepsilon}$ (CC) gradually rise from the set at 0.1 s^{-1} (AA) to that at DD or BB (Figs. 72, 76). Figures 73 and 74 also clearly show this effect. Due to the carbide and solute retarding effects on softening during the pass interval (10, 12, 22, 24, 25, 26, 30, 34, 36, 89, 101, 201-203, 215), the flow stresses at the termination of rolling are 238, 204, and 238 MPa, for 301W, 304W, and 317W respectively. Whereas, the flow stress of 301W is higher than 304W due to a greater volume of carbides, 317W is higher because of the multiple effects of carbides, solute, and δ ferrite (25, 26). Furthermore, these flow stresses decrease as the interval duration increases (Figs. 72, 76) (19, 21, 22, 24-26, 30).

5.8.2 ACTIVATION ENERGIES

The combined effect of Z-dependence (84, 86, 89, 90, 101) and carryover of worked material (10, 12, 21, 22, 25, 26, 36, 199) can be examined through the constitutive relationship. In the sinh analysis of 301W (Fig. 73), the slope is 3.9 in comparison with 4.4 for the continuous curves evaluated at the higher peak strain, ranging from 0.4 to 1.0 (Fig.

12a). Multistage isothermal tests give a still different result n = 4.3 (Fig. 36a) (Secs. 4.4.3, 5.4.3). The T dependence analysis in Fig. 74 shows that there are two separate values of Q_{HW} : a) isothermal multistage, 307 and; b) declining T, 352 kJ/mol. These values are both less than 399 kJ/mol for continuous isothermal tests (Fig. 13a). Whereas, the behavior for 304 is similar for all T, 316W experiences a sudden change in slope at about 1100°C due to strengthening by carbides (22, 24-27). Consequently, 316W has a Q_{HW} (declining) of 384 changing abruptly to 402 kJ/mol at lower T. While its Q_{HW} (continuous isothermal) is 454, a mean Q_{HW} value of 393 kJ/mol is determined. It is noted that none of these Q_{HW} are determined under constant structure conditions since D_{SRX} and the fraction recrystallized change after each pass (Figs. 61, 77).

5.8.5 ACCUMULATED STRAIN

The retained strain ε_{yi} (Secs. 2.6.6, 4.7.1) (Fig. 78) at the start of a pass is estimated from the average slope of the pass flow curve relative to the flow curve for recrystallized material at that temperature. It is a strain term corresponding to the increased strength (σ_{yi} - σ'_{yi}) but it is not dependent on just the reloading stress but the shape of the flow curve. As expected it can be considered as the opposite of FS. Comparison with Fig. 77 shows that ε_{yi} rises more uniformly with the pass number especially in the last 4 passes where FS_i is falling. The order of these test conditions in Fig. 78 are inverted from those in Fig. 77. The low $\dot{\varepsilon}$ data (A) are the highest followed by the rising $\dot{\varepsilon}$ curve (C); the high $\dot{\varepsilon}$ curves B and D are much lower.

When compared to the accumulated strain, which equals 0.2(i-1), ε_{yi} is only in the range 0.10-0.15ε_i after 6 passes (0.1 s^{-1}, 20 s). Even after 16

passes where the accumulated strain is 3.2, ε_{y16} is only 0.1. The isothermal results (Fig. 36a) show that, even in the continuous test, the strain energy accumulates only to the peak at 0.6-0.8 and then drops to become constant in the steady state regime. In the case of isothermal multistage (900°C, 1 s^{-1}, 20 s), ε_{yi} increases up to the third pass and then becomes constant at 0.1. Due to carbides and high solute 316W followed by 301W have much greater retained strain than 304W.

5.8.4 STATIC SOFTENING

Static softening between stages (Sec. 2.6.7) is apparent in the saw toothed appearance of the flow curves in Fig. 72. As the interval is lengthened, the set of flow curves decrease (Fig. 72) and the FS rises markedly (Fig. 77). As shown in Fig 77, the level of FS decreases with declining T but rises with increasing $\dot{\varepsilon}$. The latter is seen in comparison of 0.1 and 1 s^{-1} and in the gradual shift of the rising $\dot{\varepsilon}$ tests (CC). The effect of $\dot{\varepsilon}$ arises from the increase in strain energy, i.e., the driving force for SRX. Augmentation of the strain energy by raising the pass strain has a similar effect. Raising T decreases the density of dislocations and hence reduces the driving force for SRX (22, 24, 30, 34, 86, 89, 199, 203); however, it is evident that its contrasting effect of accelerating the rearrangements involved in nucleation and migration of grain boundaries predominates. The influence of strain energy is normalized by introducing the term $Z^{0.375}$ into the analysis of the T dependence in Fig. 80 and can be compared with other work (106, 130, 168, 174, 180, 204, 213, 265-269) in Fig. 35 (Sec. 2.5.4). However, SRX up to 100% is found only in the first few passes at very high T and has fallen below 50% by the fourth pass (1130°C) for t_i = 20 s and the seventh pass (1070°C) for 40 s at 1 s^{-1}. For

the short interval, SRX is less than 5% after the eleventh pass at T below 1000°C; however, softening by recovery is of the order of 40%. For 316W SRX is about 2% for the same conditions.

Since the degree of SRX is so low for many of the conditions, the progress of SRX can only be estimated by assuming the kinetics of SRX are the same after the first few passes as after isothermal testing. This is done by determining the Avrami constants β_{SRX} and k_{SRX} where possible and applying them to other conditions to calculate $t_{0.5}$ from the data for each condition. The plot in Fig. 80 can thus be derived with some scatter of the points so that there is only one line for all the declining T data. The Q_{SRX} (declining) is only 290 kJ/mol compared to 369 kJ/mol from isothermal interrupted tests (25, 26) (Fig. 35). In the latter the level of strain energy is limited to that from a single pass (0.2) on recrystallized material. The values for 316W are considerably higher at 364 and 418 kJ/mol due to greater solute which slows SRX kinetics. During deformation, considerable strain energy has accumulated as confirmed by both Figs. 77, 78. The effect of strain energy induced in the immediate pass is illustrated by decrease in $t_{0.5}$ as Z rises (Fig. 80) and increase in rate as $\dot{\varepsilon}$ rises (Fig. 81). The latter effect is quite small as previously observed. The $t_{0.5}$ presented in Fig. 79 provides a clearer picture of the effect of interval temperature. The sharp rise at low T about 930°C for 1 s^{-1}, indicates the potential for preserving the hot worked substructure for room temperature strengthening (22, 34, 87, 89, 101, 132, 168, 203). These results are confirmed by the analyses of 304W and 316 W results. The flow curves for all alloys exhibit the same characteristic shape for deformation under declining T conditions. The low T behavior for 301W and 316W were

similar due to the strengthening effect of carbides resulting from high C in the former and Mo in the latter. Consequently, the softening kinetics of 304 were superior to the other two.

5.8.5 MICROSTRUCTURAL EVOLUTION

Although the grain structure was not studied after each pass, it can be inferred on the basis of other work that slight grain coarsening occurred after the first or second pass (25, 26). After later passes, the SRX is expected to give grains much finer than the original (22, 25, 26) and this is indeed what was observed by metallography for 304W, 316W, and 317W where the original grain sizes of 70, 60, and 57μm were finally refined to 10, 9, and 8μm respectively (Fig. 61).

5.9 PLANETARY ROLLING MILL SIMULATION

5.9.1 ROLL SEPARATING FORCE

From observation of the roll separating force distribution (Fig. 84), it can be seen that the force slowly increases through the common point of mean strain rate, mean flow stress, and mean reduction to a peak and then drops rapidly to zero (39, 280). The lower force than that used in conventional rolling is related to the small radius and hence contact arc of the planetary rolls. However, the force is raised because many small rolls are in contact simultaneously. The effect of roll flattening is negligible since it only increases the effective roll radius one percent. Furthermore, since complete reduction takes place in 2.54 seconds with the passage of approximately 80 planetary work rolls (279, 280), only 94 percent of the heat due to the work of deformation is dissipated with the material having a slightly higher surface T at exit than that which it had upon entry (282, 283). The temperature is consistent with that measured in

a similar mill at the Nippon Yakin Kogyo Company in Japan (283).

5.9.2 INSTANTANEOUS POWER REQUIREMENT

According to Figure 85, the analysis for 301W (Sec. 4.7.2) predicts a power requirement which is lower than that measured industrially. This is due to the lower T used at Nippon Yakin Kogyo (283). The two industrially measured values for 304W (282, 283) differ because the surface temperature is quoted. When the mean true T is determined, the T used by the Japanese is higher than that used here by Atlas (282); therefore, this results in a lower power requirement. The 316W alloy exhibits similar behavior. Consequently, the current analysis slightly understimates the power requirements for all alloys (35, 281). In addition, the measured results from both companies lie on parallel lines indicating consistency of the behavior of the similar mills and deviate only slightly from the slope of the experimentally determined lines. Evidently, both roll separating force and instantaneous power requirement are functions of metallic solute.

5.9.3 METALLIC SOLUTE DEPENDENCE

It is interesting to note that while the activation energies for these alloys increase 2, 16, and 26 percent over the 393 kJ/mol for 304W, the instantaneous power requirements are 2 percent lower for 301W and 10 and 18 percent greater for 316W and 317W respectively compared with 304W. In the case of 301W in which the carbon content is significantly greater than 304W, most carbides are in solution at the rolling temperature, thereby lowering the effective flow stress. This is contrary to the condition for cross country rolling where the greater volume of carbides at 900^{o}C significantly raises the flow stress. With respect to 316W and 317W, the activation energy is calculated from conditions existing in the 900-1200^{o}C temperature range, while power requirements are determined at 1307^{o}C where the metallic solute content is much less effective than at 900^{o}C.

CHAPTER 6

CONCLUSIONS

Hot torsion tests in the range 900-1200^{o}C, 0.1-5 s^{-1} were carried out on 301, 304, 316, and 317 steels in the as-cast and worked homogenized conditions. The schedules employed included isothermal continuous, isothermal multistage, and declining temperature multistage. All alloys were examined through flow curve characteristics, constitutive equations, and optical and electron microscopy. From the results and comparisons with previous research and theories, the following conclusions were reached.

1. While the flow curves for the as-cast alloys rise to a peak and decline and fracture shortly thereafter, those for the worked have full dynamically recrystallized characteristics where after the peak, the flow stress declines to a steady state regime in which fracture intervenes at some high fracture strain.

2. The peak stress declines with rising temperature, decreasing strain rate, and declining solute. Likewise, the peak strain is lowered by decreasing Z, original grain diameter, and solute. The segregated δ in the as-cast alloys raises the peak stress, but reduces the peak strain in reference to the worked material.

3. Due to dynamic recovery, the strain hardening rate θ falls rapidly as the flow stress and strain increase; the rate of decline increasing as temperature is raised or strain rate reduced. θ-σ curves accurately identify the formation of subgrains and the dynamic recovery saturation stress.

4. The critical strain for the initiation of dynamic recrystallization can be derived from θ-σ curves. The critical time for the initiation of dynamic recrystallization rises with decreasing temperature with the mean of the critical strain for dynamic recrystallization to peak strain ratio constant at about 0.70 and 0.64 for as-cast and worked alloys, respectively. As T decreases, the upper limiting condition beyond which no dynamic recrystallization can occur is established at $800^{o}C$, 1 s^{-1}.

5. The logarithm of the saturation stress increases linearly with log strain rate and with declining temperature to attain the saturation stress at zero Kelvin which increases as solute rises (stacking fault energy decreases). As a result the enthalpy increases as Z declines and agrees at high temperature with the activation energy for deformation determined by Arrhenius analysis.

6. The yield stress becomes athermal as the temperature drops below about $850^{o}C$, whereas the peak and steady state flow stress continue to rise rapidly due to marked strain hardening. Furthermore, this athermal region starts at a higher temperature for the as-cast alloys than the worked because there is a higher degree of work hardening in the former. While the difference between the yield and steady state stresses becomes very low at high temperature, it is greater for the as-cast because of additional hardening around δ particles.

7. The experimental data across the entire range for all alloys are fitted by the hyperbolic sine function with a constant α, with the stress exponent slightly decreasing as the solute or volume fraction of carbides increases. As a result of an extensive analysis of seventy austenitic stainless steels, the mean value of the stress exponent is about 4.3.

8. In the Arrhenius function the derived activation energies were about 10% higher for the as-cast alloys than for the worked, except 316C. Generally, the activation energy for deformation increases with rise in solute content and δ phase. The present values are in good agreement with the respective means derived from 70 studies of the four alloys. The total data show that the activation energy for deformation has a value consistant with 13.5 kJ/mole for each percent of metallic solute. When correction is made for deformational heating, the activation energy for deformation increases approximately 22% which is recommended for calculation of forces in forming processes. The use of Z to extrapolate or interpolate values of stress was confirmed to be satisfactory.

9. With the relationship of constitutive constants to solute content and grade firmly established, it is possible to compute the flow stress of any austenitic stainless steel from the composition and grain diameter. Such information is needed for calculation of roll separating forces

10. The start and finish of dynamic recrystallization is suitably represented by the Avrami equation with the time exponent 1.3 in close agreement with published microscopic results. From this, it is possible to define the progress of dynamic recrystallization along the flow curve.

11. The dynamic and metadynamic recrystallized grain diameters are related to the steady state flow stress by the -0.75 power. Subgrain diameters are related to the steady state flow stress by a power of -1. Both the steady state grain and subgrain diameters are monotonically dependent on Z.

12. For static recrystallization, the Avrami time exponent is about 1.3 for 304W, declining to about 1.1 as solute rises. The activation energy values for static recrystallization for all alloys are in favorable agreement with those found in the literature.

13. The measurement of fractional softening by comparison of flow stresses before and after an unloaded interval revealed that the rates of static recrystallization after hot deformation decrease with decline in pass strain, strain rate, and temperature and with rise in solute and precipitate levels.

14. Whereas the ductilities of 301W and 304W increase with rising temperature and strain rate, 316W and 317W as well as the as-cast alloys rise with increasing temperature and declining strain rate. Moreover, the as-cast alloys have considerablely lower ductility due to segregated δ phase.

15. Intergranular fissures form randomly in the homogenous austenite. Although impeded by dynamic recrystallization, they increase in number and size and gradually link up, propagating faster as they orient near the plane of maximum shear stress. In the as-cast alloys, δ ferrite generates interphase cracking which tends to eliminate any benefits from enhanced nucleation of dynamic recrystallization.

16. In comparison to a continuous test at a given condition, the ductility in multistage isothermal tests increases if the static restoration between stages cooperates with the dynamic mechanisms in slowing fissure growth.

17. In anisothermal multistage tests, the flow stress in each succeeding pass increases due to both declining temperature and accumulated strain. While the volume fraction recrystallized is about 100% at $1200^{o}C$, it reduces to about 5% at $900^{o}C$. Moreover, the finishing grain diameter is reduced from about 70 to 10μm.

18. The mill power requirements for all alloys determined through torsion simulation are in good agreement with those measured on two planetary mills. These values increase 10 and 18% for 316 and 317 over 304, while that for 301 decreases 2%. In contrast to conventional rolling, these values would increase about twice as much in a finishing pass at 900°C where alloy hardening becomes significant.

19. This research project provides the data needed for modelling of industrial hot forming processes. The stress constitutive equations are useful for determination of forces. The conditions for grain refinement resulting from dynamic recrystallization can be estimated. Knowledge of the dependence of fracture strain on temperature and strain rate permit calculation of forming limits. The rate of static recrystallization and the resulting grain diameters provides the ability to model multistage processes. Mathematical modelling can be confirmed by physical modelling on the torsion machine.

REFERENCES

1 C. Rossard and P. Blain, Flat Rolled Products III, (edited by E.W. Earhart),pp.3-28. Interscience Publishers, Chicago (1962).

2 M.M. Farag, C.M. Sellars and W.J. McG. Tegart, Deformation Under Hot Working Conditions, ISI Pub. 108, pp. 60-67. Iron and Steel Inst., London (1968)

3 H.J. Whittaker, B. Walker and M.A. Adams, Trans. ISIJ, 11 (1971) 662-666.

4 T.B. Vaughan, Deformation Under Hot Working Conditions, ISI Pub. 108, pp. 68-77. Iron and Steel Inst., (1968).

5 R. Moller, A. Gittins and J. Everett, Microstructure and Design of Alloys, CSMA 3, pp. 397-401. Inst. Metals and Iron Steel Inst., London (1973).

6 A. Gittins, R.H. Moller and J.R. Everett, BHP Technical Bulletin, 18 (1974) 2-8.

7 T. Brolin, Paustidewns Inverkan Pa Ductiliteten vid Varmbearbetning, Stockholm (1975).

8 I. Weiss, J.J. Jonas, P.J. Hunt, and G.E. Ruddle, Intl. Conf. Steel Rolling, Vol. 2, ISIJ, Tokyo (1980) 1225-1236.

9 C.G. Radu, E. Soos and C. Teodosiu, Kovove Materialy, 4 (1979) 433-441.

10 J. Sankar, D. Hawkins and H.J. McQueen, Met. Tech, 6 (1979) 325-332.

11 C.G. Radu, C. Teodosiu, E. Soos and T. Dumitrescu, Metalurgia, 31 (1979) 580-584.

12 W. Knudsen, J. Sankar, H.J. McQueen and J.J. Jonas, Hot Working and Forming Processes, (edited by C.M. Sellars and G.J. Davies), pp. 51-56. Metals Society, London (1980).

13 C.M. Sellars and J.A. Whiteman, Met. Sci., 13 (1979) 187-194.

14 B. Migaud, Hot Working and Forming Processes, (edited by C.M. Sellars and G.J. Davies), pp. 67-76. Metals Society, London (1980).

15 J. Everett, A. Gittins, G. Glover and M. Toyama, Int. Conf. on Manufacturing Engineering. pp. 121-127, Melbourne (1980).

16 C.G. Radu, C. Teodosiu, E. Soos and T. Dumitrescu, Kovove Materialy, 6 (1981) 698-708.

17 E. Soos, C. Teodosiu, V. Nicolae, C.G. Radu, Cercetari Metalurgice, 20 (1979) 333-351.

18 E. Soos, C. Teodosiu, V. Nicolae, Rev. Roum. Sci. Techn - Mec,. Appl., 26 (1981) 95-105, 179-191.

19 A.H. Ucisik, I. Weiss, H.J. McQueen and J.J. Jonas, Can. Met. Q., 19 (1981) 351-358.

20 H.J. McQueen and H. Mecking, Creep and Fracture of Engineering Materials and Structures, (edited by B. Wilshire and D.R.J. Owen), pp. 169-184. Pineridge Press, Swansea, (1984).

21 A. Streisselberger, R. Kaspar and O. Pawelski, Metall. Trans A., 16A (1985) 67-73.

22 H.J. McQueen and J.J. Jonas, J. Appl. Met-Work., 3 (1985) 410-420.

23 H.J. McQueen and N. Ryum, Scand. J. Metallurgy, 14 (1985) 183-194.

24 A. Sandberg and R. Sandstrom, Mat. Sci. Tech., 2 (1986) 926-937.

25 W.J. Liu and M.G. Akben, Can. Met. Q., 26 (1987) 145-153.

26 M.G. Akben, W.J. Liu, J.J. Jonas and R.J. Ackert, The Science and Technology of Flat Rolling, pp. F.19.1-10. IRSID, Deauville, France (1987).

27 F. Boratto, S. Yue, J.J. Jonas and T. Lawrence, 1987 COLAM-ABM, Brazilian Society for Metals, San Paulo (1987).

28 T. Chandra, S. Yue, J.J. Jonas and R.J. Ackert, The Science and Technology of Flat Rolling, pp. F18.1-8. Deauville (1987)

29 O. Pawelski and R. Kaspar, Thermec 88, Int. Conf. on Physical Metallurgy of Thermomechanical Processing of Steels and Other Metals, pp. 438-447. ISIJ, Tokyo (1988).

30 W. Roberts, Calculation of Flow Curves Pertinent to Multi-Step Hot-Working OPerations, Rep. IM-2037, pp. 1-43. Swedish Institute for Metals Research, Stockholm (1985).

31 W. Roberts, Strength of Metals ans Alloys, ICSMA 7, (edited by H.J. McQueen et al.), Vol.3, pp. 1859-1891. Pergamon Press, Oxford (1985).

32 J.W. Green and J.F. Wallace, J. Mech. Eng, Sci., 4 (1962) 136-142.

33 E.J. Buckman, BHP Technical Bulletin, 18 (1974) 9-15.

34 W.J. McG. Tegart and A. Gittins, The Hot Deformation of Austenite, edited by J.B. Ballance), pp. 1-46. AIME, N.Y. (1977).

35 I. Weiss, J.J. Jonas, P,J. Hunt and G.E. Ruddle, Int. Conf. on Steel Rolling, Vol. 2, ISIJ, Tokyo (1980) 1225-1236.

36 H.J. McQueen, Can. Met. Q., 21 (1982) 445-460.

37 D.L. Baragar, The Evaluation of Hot Rolling Models Using Can Plastometer Flow Stress Data, Rep: PMRL 85-55(J), pp. 1-10. Phy. Met. Research Lab. (1985).

38 R. Tovini, Sheet Met. Ind., (1960) 488-511.

39 H. Takahashi and J. Kihara, J. JSTP, 27 (1986) 613-619.

40 J.H. Hollomon, Trans. AIME, 162 (1945) 268-290.

41 A. Gueussier and R. Castro, Metal Treatment and Drop Forging, (1959) 255-263, 323-327, 361-366.

42 A. Nicholson, Iron & Steel, 37 (1964) 290-294, 363-367.

43 H.J. McQueen and J.J. Jonas, Metal Forming, (edited by A.L. Hoffmanner), pp.393-428. Plenum Press, N.Y. (1971).

44 R.E. Bailey, R.R. Shring and H.L. Black, Workability Testing Techniques, (edited by G. E. Dieter), pp.73-94. ASM, Metals Park (1984).

45 A.T. Male, and G.E. Dieter, Workability Testing Techniques, (edited by G.E. Dieter), pp.51-72. ASM, Metals Park (1984).

46 D.E.R. Hughes, JISI, 190 (1952) 214-223.

47 K. Tajima and K. Kugai, Tetsu-to-Hagane, 42 (1956) 980-985.

48 T. Morishima, Tetsu-to-Hagane, 44 (1958) 552-559.

49 C. Rossard, Metaux, Corrosion, Industries 35, (1960) 102-115, 140-153, 190-205.

50 F.A. Hodierne, J. Inst. Met., 91 (1962) 267-273.

51 R. Horiuchi, J. Kaneko, A.B. Elsebai and M.M. Sultan, The Characteristics of the Hot Torsion Test for Assessing Hot Workability of Aluminum Alloys, Rep. No. 443, pp. 1-19.Inst. Space Aeronaut. Sci., University of Tokyo, Tokyo (1970).

52 D.R. Barraclough, H.J. Whittaker, K.D. Nair and C.M. Sellars, J. Test. Eval., 1 (1973) 220-226.

53 G.R. Canova, S. Shivastava, J.J. Jonas, and C. G'Sell, ASTM, Spec. Tech. Pub. 753. (1982) 189-210.

54 S.C. Shrivastava, J.J. Jonas and G. Canova, J. Mech. Solids, 30 (1982) 75-95.

55 M.J. Luton, Workability Testing Techniques, (edited by G.E. Dieter), pp. 95-133. ASM, Metals Park (1984).

56 S.L. Semiatin, G.D. Lahoti and J.J. Jonas, ASM Handbook Vol.8, pp. 154-184. ASM, Metals Park, OH (1985).

57 A.T. Cole and G.J. Richardson, Hot Working and Forming Processes (edited by C.M. Sellars and G.J. Davies), pp. 128-132. The Metals Society, London (1980).

58 P. Moore, Deformation Under Hot Working Conditions, ISI Pub. 108, pp. 103-106. Iron and Steel Inst., London (1968).

59 Y. Ohtakara, T. Nakamura and S. Sakui, Trans. ISIJ, 12 (1972) 36-44.

60 T. Nakamura and M. Ueki, Zairyo, 23 (1974) 182-188.

61 T. Nakamura and M. Ueki, Trans. ISIJ, 15 (1975) 185-193.

62 S.L. Semiatin and G.D. Lahoti, Met. Trans, 12A (1981) 1719-1728.

63 A. Nadai and M.J. Manjoine, J. Appl. Mech., 8 (1941) A77-91.

64 C. Zener and J.H. Hollomon, J. Appl. Phys., 15 (1944) 22-32.

65 G.E. Dieter, Fundamentals of Deformation, (edited by W.A. Backofen), pp. 145-182. Syracuse University Press, N.Y. (1964).

66 M. Tsubouchi and H. Kudo, Sosei to Kako, 9 (1968) 332-344.

67 S. Schwandt, Industrie-Anzeiger, 90 (1968) 14-17.

68 H.W. Wagenaar, Deformation Under Hot Working Conditions, ISI Pub. 108, pp. 38-41. Iron and Steel Inst., London (1968).

69 B. Weiss. G.E. Grotke and R. Stickler, Welding Journal Supplement, (1970) 471s-481s.

70 J. Tiberg, Rekristallisation Vid Varmvalsning, Tech. Report D6 (1971) 1-40.

71 G.D. Lahoti and T. Altan, J. Eng. Mat. Tech., (1975) 113-120.

72 J.J. Jonas and M.J. Luton, Advances in Deformation Processing, (edited by J.J. Burke and V. Weiss), pp. 215-243. Plenum Publishing Corp., N.Y. (1978).

73 C. Teodosiu, N. Nicolae, E. Soos and C.G. Radu, Rev. Roum. Sci. Techn - Mec. Appl., 24 (1979) 13-43.

74 D.R. Barraclough and C.M. Sellars, Inst. Phys. Conf. Ser. 21, (1979) 111-123.

75 T. Sheppard and D.S. Wright, Met. Tech., 6 (1979) 215-223.

76 S.L. Semiatin and H.J. Holbrook, Met. Trans., 14A (1983) 1681-1695.

77 R. Colas and C.M. Sellars, Strength of Materials and Alloys, ICSMA 7, Vol. 2, pp. Pergamon Press, Oxford (1985).

78 B. Verlinden, E. Aernoudt, J. Calloens and P. Van Houtte, (1988) personal communication.

79 J. Woolman and R.A. Mottram, The Mechanical and Physical Properities of the British Standard En Steels, Vol.3, pp. 278-279. Pergamon Press, Oxford (1964).

80 Alloy Digest, SS-207 (1968) 1-2.

81 P. Choquet, A. Le Bon, C. Rossard, C. Perdrix and G. Joannes, Physical Metallurgy of Thermomechanical Precessing of Steels and Other Metals, pp.729-736, ISIJ, Tokyo (1988).

82 H.J. McQueen, Trans. JIM, 9, (1968) 170-177.

83 H.J. McQueen, J. Met., 20 (1968) 1-8.

84 J.J. Jonas, C.M. Sellars and W.J. McG. Tegart, Metall. Rev., Vol 1 (1969) 1-24.

85 G. Glover and C.M. Sellars, Met. Trans., 4 (1973) 765-775.

86 H.J. McQueen and J.J. Jonas, "Treatise on Materials Science", Vol. 6: Plastic Deformarion of Materials (edited by R.J. Arsenault), pp. 393-491. Academic Press, N.Y., (1975).

87 L. Fritzemeier, M.J. Luton and H.J. McQueen, Strength of Metals and Alloys, ICSMA 5, Vol.1, pp. 95-100, Pergamon Press, Oxford (1979).

88 H.J. McQueen, Met. Trans., 8A (1977) 807-824.

89 B. Ahlblom and R. Sandstrom, Int. Metall. Rev., 7 (1982) 1-27.

90 H.J. McQueen and J.J. Jonas, J. Appl. MetWork., Pt.B, 3 (1984) 233-241.

91 H.J. McQueen and D.L. Bourell, Inter-Relationship of Metallurgical Structure and Formability IV: Hot Forming, Orlando (1986).

92 H.J. McQueen and D.L. Bourell, J. Met., 39 (1987) 28-35.

93 J.P. Sah and C.M. Sellars, Hot Working and Forming Processes, (edited by C.M. Sellars and G.J. Davies), pp. 62-66. Metals Society, London (1980).

94 P. Richards and T. Sheppard, Mat. Sci. Tech., 2 (1986) 841-846.

95 H.J. McQueen, Metals Forum, 4 (1981) 81-91.

96 D. Hardwick and W.J. McG. Tegart, J. Inst, Metals, 90 (1962) 17-21.

97 M.J. Luton and C.M. Sellars, Acta metall., 17 (1969) 1033-1043.

98 R.W.K. Honeycombe and R.W. Pethen, J. Less-Common Metals ,28 (1972) 201-212.

99 C.M. Sellars, Phil. Trans. R. Soc. Lond. A 288, (1978) 147-158.

100 C.M. Sellars, Metals Forum, 4 (1981) 75-80.

101 W. Roberts, Deformation, Processing and Microstructure, (edited by A.G. Krausz), pp. 1-101. ASM Metals Park, OH (1983).

102 K.J. Irvine, T. Gladman, and F.B. Pickering, JISI, 207 (1969) 1017-1028.

103 F.B. Pickering, Int. Met. Rev. (1976) 227-268.

104 F.B. Pickering, Optimization of Processing, Properities, and Service Performance through Microstructural Control, (edited by H. Abrams et al.,), STP 672, pp. 263-295. ASTM, Philadelphia, Pa (1978).

105 H. K. Ihrig, Trans. AIMME, 167 (1946) 749-790.

106 U. Svennson, The Hot Deformation of Austenite, (edited by J.B. Ballance, pp.499-516. AIME, N.Y. (1977).

107 J. Elfmark, Technical Digest. (SNTL, Prague) 1 (1967) 14-24.

108 F.K. Bloom, W.C. Clarke and P.A. Jennings, Metal Progress, 59 (1951) 250-256.

109 L. Myllykoski and N. Suutala, Met. Tech., 10 (1983) 453-460.

110 O. Hammar and U. Svensson, Intl. Conf. on Solidification Technology, pp. 401-410. The Metals Society, London (1979).

111 V.P. Kujanpaa, N.J. Suutala, T.K. Takalo and T.J.I. Moisio, Metal Construction, 12 (1980) 282-285.

112 N. Suutala and T. Moisio, Solidification Technology in the Foundry and Casthouse, pp. 310-314. The Metals Society, London (1983).

113 U.F. Kocks, Trans. ASME, (1976) 76-85.

114 H. Mecking and G. Gottstein, Recovery and Recrystallization During Deformation, (edited by F. Haessner), pp.195-222. Dr. Riederer Verlag GmbH, Stuttgart, (1978).

115 B. Nicklas and H. Mecking, Strength of Metals and Alloys, ICSMA 5, (edited P. Haasen et al.), Vol.1, pp. 351-356, Pergamon Press, Oxford (1979).

116 G. Gottstein and A.S. Argon, Creep and Fracture of Engineering Materials and Structures, (edited by B. Wilshire and D.R.J. Owen), pp. 15-26. Pineridge Press, Swansea, (1984).

117 H.J. McQueen, Mat. Sci. Eng., 101 (1988) 149-160.

118 G. Gottstein and U.F. Kocks, Acta metall. 31, (1983) 175-188.

119 G. Carfi, C. Perdrix, D. Bouleau and C. Donadille, Strength of Metals and Alloys, ICSMA 7, (edited H.J. McQueen et al), Vol.2, pp. 929-934, Pergamon Press, Oxford (1986).

120 G. Gottstein, Met. Sci., 17 (1983) 497-502.

121 G. Avramovic-Cingara et al., Dispersion Strengthened Aluminum Alloys, (edited by Y. Kim and W. Griffith), pp. 437-450. Met. Soc. AIME, Warrendale, Pa (1988).

122 P. Choquet, B. de Lamberterie, C. Perdrix and H. Biausser, Fast - A New Model for Accurate Prediction of Rolling Force Application on the Solmer Hot Strip Mill, Rep. 1099, pp. 1-8. IRSID, Saint-Germain-en-Laye, (1987).

123 Ch. Perdrix, Charact. d'Ecoulement Plastique du Metal T.A.B. à Chaud (CECA 7210-EA311) IRSID, St. Germaine en-Laye France (1983).

124 M.L. Bernshtein, L.M. Kaputkina, S.D. Prokoshkin and S.V. Dobatkin, Acta metall., 33 (1985) 247-254.

125 M.E. Kassner and A.K. Miller, New Developments in Stainless Steel Technology, (edited R.A. Lula), pp. 19-28. ASM, Metals Park, (1985).

126 C. Donadille, C Rossard and B. Thomas, Annealing Processes: Recovery, Recrystallization and Grain Growth, (edited by N. Hansen et al.), pp. 285-290, Riso Natl. Lab, Roskilde, DK (1986).

127 D. Dulieu and J. Nutting, Metallurgical Developments in High Alloy Steels, Spec. Rep. 86, (1964) 140-145.

128 J.S.T. Van Aswegen, R.W.K. Honeycombe and D.H. Warrington, Acta metall., 12 (1964) 1-13.

129 R. Fawley, M.A. Quader, and R.A. Dodd, Trans. Met. Soc. AIME, 242 (1968) 771-775.

130 I. Kozasu and T. Shimizu, Trans. ISIJ, 11 (1971) 359-366.

131 C.M. Sellars and W.J. McG. Tegart, Int. Metall. Rev., 17 (1972) 1-24.

132 H.J. McQueen and S. Bergerson, Met. Sci. J., 6 (1972) 25-29.

133 T. Sakai and J.J. Jonas, Annealing Processes, Recovery, Recrystallization and Grain Growth, (edited by N. Hansen et al.), pp. 143-165. RISO Nastl. Roskilde, DK. (1986).

134 W. Roberts, H. Boden and B. Ahlblom, Met. Sci., 13 (1979) 195-205.

135 Y. Ohtakara, T. Nakamura and S. Sakui, Trans. ISIJ, 12 (1972) 207-216.

136 T. Sakai and J.J. Jonas, Acta metall., 32 (1984) 189-209.

137 J.J. Jonas and T. Sakai, Deformation, Processing and Microstructure, (edited by G. Krauss), pp. 185-230. ASM, Metals Park, OH (1983).

138 T. Maki, K. Akasaka, K. Okuno and I. Tamura, Trans,. ISIJ, 22 (1982) 253-261.

139 D.R. Barraclough and C.M. Sellars, Met. Sci., 13 (1979) 257-267.

140 M. Ueki and T. Nakamura, Trans. JIM, 17 (1976) 139-148.

141 M. Avrami, J. Chem. Phys., 7 (1939) 1103-1112, 8 (1940) 212-224, 9 (1941) 177-184.

142 J.P. Sah, G.J. Richardson and C.M. Sellars, J. Aust. Inst. Metals, 14 (1969) 292-297.

143 J.J. Jonas, Strength of Metals and Alloys, ICSMA 4, Vol. 3, pp. 976-1002. Laboratoire de Physique du Solide, Nancy (1976).

144 J.P. Sah, G.J. Richardson and C.M. Sellars, Indian J. Techn., 11 (1973) 445-452.

145 L.J. Cuddy, Met. Trans., 1 (1970) 395-401.

146 R. Bhargava , J. Moteff and R.W. Swindeman, Structural Materials for Service at Elevated Temperatures in Nuclear Power Generation, MPC-1 (edited by A.O. Schaefer), pp.31-54. ASME, N.Y. (1975).

147 M. Harris and T.J. Davies, Res Mech., 2 (1981) 175-187.

148 A.M. Ermi and J.Moteff, Met. Trans., 13A (1982) 1577-1588.

149 R. Bromley and C.M. Sellars, Strength of Metals and Alloys, ICSMA 3, pp. 380-385. Pergamon Press, Oxford (1973).

150 D.J. Abson and J.J. Jonas, Met. Sci. J., 4 (1970) 24-28.

151 K. Detert, Zeitschrift fur Metallkunde, 52 (1961) 27-34.

152 C. Ouchi and T. Okita, Trans. ISIJ, 22 (1982) 543-551.

153 C.M. Sellars and W.J. Mc.Tegart, Acta metall., 14 (1966) 1136-1138.

154 J.J. Jonas, Trans. Q. ASM., 62 (1969) 301-303.

155 F. Garafalo, Trans. Metall. Soc. AIME, 227 (1963) 351-355.

156 L.D. Blackburn, The Generation of Isochronous Sress-Strain Curves, ASME, (edited by A.O. Schaefer), pp. 16-48. ASME, N.Y. (1972).

157 H.B. McShane and T. Sheppard, J. Mech. Work. Tech., 9, (1984) 147-160.

158 T. Ikeshima, Nikon Kinsoku Gakkai, 17 (1953) A25-29, A55-58.

159 R. Hinkfoth and H.D. Koing, Neue Hutte, 12 (1967) 212-214.

160 P.N. Cook, The Properities of Materials at High Rates of Strain, pp. 86-97. Inst. Mechanical Engineers, London, (1957).

161 G. Wallquist and J.C. Carlen, Mem. Sci. Rev. Metal., 56 (1959) 268-274.

162 C. Gavrila, Cercetari Metal., 14 (1973) 213-222.

163 J.M. Dhosi, L. Morsing, and N.J. Grant, Proc. 4th Int. Conf. on Mechanical Working of Steel, Vol. 44, (edited by D.A. Edgecombe), pp. 265-283. Gordon and Breach, New York (1965).

164 L. Zela,, J. Fuxa, M. Holler, and L. Maly, Intl. Symp. on Plasticity and Resistance to Metal Deformation, pp. 179-193. Ferrous Metall. Inst., Niksic, Yugoslavoia (1986).

165 S. Hashizume, Sosei-to-Kako, 6 (1965) 71-75.

166 J. Elfmark, Hutnické Listy, 26 (1971) 107-113.

167 H.J. McQueen, R.A. Petkovic, H. Weiss, and L.G. Hinton, Hot Deformation of Austenite, (edited by J.B. Ballance), pp. 113-139. Met. Soc. AIME, (1977).

168 B. Ahlblom, Studies of the Deformation of FCC Materials at Both High and Low Temperatures, IM-1208, Royal Inst. Tech. Stockholm (1977).

169 V.I. Zyuzin, M.Y. Brovman, and A.F. Melynikov, Soprotivenie deformacii, Izdatel'stvo, Metallurgiia, Moscow, (1964) 153-182.

170 V.S. Zotyeyev, Novyie metody ispitanii metallov, Technicheskoe Izdatel'stvo Metallurgiia, Moscow, (1962) 342-348.

171 K. Inouye, Tetsu-to-Hagané, 41 (1955) 15-23.

172 L.D. Sokolov, Chernaia Metal., 7 (1964) 59-63.

173 T.L.F. Muller, Ph.D. Thesis, University of Sheffield (1974).

174 D.R. Barraclough, Ph.D. Thesis, University of Sheffield (1974).

175 C.M. Sellars and W.J. McG. Tegart, Mem. Sci. Rev. Metall., 63 (1966) 731-746.

176 I.J. Tarnovoskij, Cheraia Metallurgiia, 4 (1961) 82-90.

177 K.A. Bywater anf T. Gladman, Met. Tech. 3, (1976) 358-365.

178 Y. Ohtahara, T. Nakamura, and S. Sakui, Trans. ISIJ, 12 (1972) 36-44, 207-216.

179 T. Nakamura, M. Ueki, and Y. Ohtakara, Tetsu-to-Hagané, 58 (1972) A87-90.

180 D. Hengerer, Radex-Rundschau, 1 (1977) 72-82.

181 M. Hildebrand, Neue Hutte, 17 (1972) 724-727.

182 G. Radu, D. Moisescu, C. Vaida, and Ilca, Cercetari Metal., 18 (1977) 239-246.

183 R. McCallum and M.G. Cockcroft, Structure Properities of Warm Extruded γ Stainless Steels, NEL REP. 517, Dept. Trade and Industry, London (1972).

184 H. Suzuki, S. Hashizume et al., Rep. Inst. Sci. Univ. Tokyo, 18 (1968) 1-240.

185 A. Gittins, J.R. Everett, and W.J. McG. Tegart, Met. Tech., 4 (1977) 377-383.

186 M. Zidek and B. Kubickova, Technical Digest (SNTL, Prague), 3 (1968) 154-161.

187 R. Barbosa and Sellars, private communication (1988).

188 K. E. Hughes, K.D. Nair, and C.M. Sellars, Met. Tech., 1 (1974) 161-169.

189 I. Dragon, C.G. Radu, and C. Vaida, Metallurgica, 30 (1978) 439-443.

190 C.M. Young and O.D. Sherby, JISI, 211 (1973) 640-647.

191 C. Teodosiu, V. Nicola, E. Soos, and C.G. Radu, Rev. Roum. Sci. Techn. Mec. Appl., 24 (1979) 13-43.

192 R. Johannson, Clean Steel, 1 (1971) 201-216.

193 K. Nikkila, Scand. J. Metall., 1 (1972) 9-15.

194 A. Tokarz and J. Bik, Intnl. Symp. on Plasticity and Resistence to Metal Deformation, Ferrous Metall. Inst., Niksic, Yugoslavia (1986) 424-433.

195 H. Boden, IM-1233, Swedish Institute for Metals Research, Stockholm (1977).

196 K. Tanaka, T. Nakamura, Y. Hoshida and S. Hara, Res Mech., 12 (1984) 41-57.

197 A. Cingara, L. St-Germain and H.J. McQueen, Processing, Microstructure and Properties of HSLA Steels, (edited by A. Deardo), pp. Met. Soc. AIME, Warrendale, Pa (1987).

198 H. Mecking and U.F. Kocks, Acta metall., 29 (1981) 1865-1875.

199 H.J. McQueen, M.G. Akben and J.J. Jonas, Microstructural Characterization of Materials by Non-Microscopic Techniques, pp. 397-404. RISO, Natl., Lab., Roskilde, DK, (1984).

200 J.J. Jonas, Physical Metallurgy of Thermomechanical Processing of Steels and Other Alloys, (edited by I. Tamura), pp. 59-69. ISIJ, Tokyo, (1988).

201 R.A. Petkovic-Djaic and J.J. Jonas, Metall. Trans., 4 (1973) 622-624.

202 R.A.Petkovic-Djaic and J.J. Jonas, JISI, 210 (1972) 256-261.

203 C.M. Sellars, Hot Working and Forming Processes, (edited by C.M. Sellars and G.J. Davies), pp. 3-15. Metals Society, London (1980).

204 R. Wusatowski, JISI, 204 (1966) 727-736.

205 G. Glover and C.M. Sellars, Met. Trans., 3 (1972) 2271-2280.

206 H. Buhler, D. Bobbert and A. Rose, Stahl und Eisen, 90 (1970) 21-28.

207 T. Sakai and M. Ohashi, Strength of Metals and Alloys, ICSMA 7, (edited by H.J. McQueen et al.), Vol. 2, pp. 917-922. Pergamon Press, Oxford, (1985).

208 A. Sandberg and R. Sandstrom, Mat. Sci. Tech., 2 (1986) 917-925.

209 R. Sandstrom and R. Lagneborg, Acta metall., 23 (1975) 481-488.

210 P.J. Wray, Hot Deformation of Austenite, (edited by J.B. Ballance), pp. 86-112. Met. Soc. AIME (1977).

211 J. Elfmark, Hutnické listy, 25 (1970) 96-102.

212 J. Elfmark, Hutnické listy, 22 (1967) 681-686.

213 G.T. Campbell, E.P. Abrahamson and N.J. Grant, Met. Trans., 5 (1974) 1875-1881.

214 E. Ruibal, J.J. Urcola and M. Fuentes, Z. Metallkde, 76 (1985) 568-576.

215 J. Sankar, M.Eng. Thesis, Concordia University, Montreal (1978).

216 L. Vazquez, H.J. McQueen, M. Charest and G.J.C. Carpenter, Can. Met. Q., 25 (1986) 337-348.

217 H.L. Andrade, M.G. Akben and J.J. Jonas, Met. Trans., 14A (1983) 1967-1977.

218 G.R. Dunstan and R.W. Evans, Metallurgia, (1969) 96-99.

219 C. Ouchi, T. Okita, T. Ichihara and Y. Ueno, Trans. ISIJ, 20 (1980) 833-841.

220 J.O. Tormo and P. Choquet, Int. Symp. on Physical Modelling of Welding, Hot Forming and Casting, Ottawa (1988) in press.

221 C. Rossard, Microstructure and Design of Alloys, ICSMA 3, Vol 2, pp. 175-203. Inst. Metals and Iron Steel Inst., London (1973).

222 C.M. Sellars, Czech. J. Phys., B35 (1985) 239-248.

223 F.N. Rhines and P.J. Wray, Trans. ASM, 54 (1961) 117-128.

224 S.L. Semiatin, J.H. Holbrook and M.C. Mataya, Met. Trans., 16A (1985) 145-148.

225 A. Gittins, L.G. Hinton and W.J. McG. Tegart, Manuf. Eng. Trans., 2 (1973) 199-207.

226 W.J. Mc.G. Tegart, Ductility, pp. 133-177. ASM Metals Park, OH (1968).

227 H.J. McQueen, J. Sankar and S. Fulop, 2 ICM 3, (edited by K.J. Miller and R.F. Smith) pp.675-684. Pergamon Press, Oxford (1979).

228 A. Gittins, Metals Forum, 2 (1979) 98-107.

229 F.E. White, Ph.D. Thesis, Université de Paris, (1967).

230 F.E. White and C. Rossard, Deformation Under Hot Working Conditions, Pub. 108,pp. 14-20. Iron and Steel Inst., London (1968).

231 B. Janzon and A. Omsen, Clean Steel, 1 (1971) 186-200.

232 B. Janzon, JISI, 209 (1971) 826-829.

233 L.A. Norstrom, Scand. J. Metallurgy, 6 (1977) 269-276.

234 I. Dragon, C.G. Radu and C. Vaida, Cercetari Metalurgice, 20 (1979) 353-361.

235 I. Dragon, C.G. Radu and C. Vaida, Metalurgia, 30 (1978) 439-443.

236 T. Kato, T. Kanai and H. Abe, Yawata, On the Hot Workability of Stainless Steel Ingots, Tech. Rep. 231, pp. 3077-3033. Yawata Iron & Steel Co., Ltd., Tokyo, (1960).

237 Y. Uematsu, T. Fujimura and K. Hoshino, A Study of Hot Workability of Continuously Cast Slabs of SUS304 Using High Speed Tensile Testing Machine, Rep. 47, pp. 25-36. Nisshin Steel, Tokyo (1982).

238 L.A. Norstrom and S. Malm, Scand. J. Metallurgy, 8 (1979) 31-33.

239 B. Rogberg, Scand. J. Metallurgy, 12 (1983) 51-66.

240 C.J. Adams, Proc. 45th Conf. Metallurgical Society of AIME, (1962) 290-302.

241 J. H. Decroix, A.M. Neveu, and R.J. Castro, Deformation Under Hot Working Conditions, ISI Pub. 108, pp. 135-144. Iron and Steel Inst., London (1968).

242 H.G. Suzuki, S. Nishmura and S. Yamaguchi, Trans. ISIJ, 22 (1982) 48-56.

243 A. Masi and F. Mancini, Re. Metallurg., 63 (1966) 977-984.

244 R. Castro et R. Poussardin, Etude de la déformabilité à chaud des aciers et alliages au moyen d'essais de traction, pp. 505-527. Centre de Documentation Siderurgique,(1962) 505-527.

245 A. Nicholson and T.W. Moore, Reheating for Hot Working, ISI Pub. 111, pp. 46-54. London (1968).

246 P.J. Wray, J. Appl. Phys., 40 (1969) 4018-4029.

247 L.A. Norstrom and B. Johansson, Scand, J. Metall., 11 (1982) 139-142

248 K. Mayland R.W. Welburn and A. Nicholson, Met. Tech., 3 (1976) 350-357.

249 A. Gittins and C.M. Sellars, Met. Sci. J., (1972) 118-122.

250 M.J. Luton and W.J. McG. Tegart, Met. Sci., 3, (1969) 142-146.

251 J. Elfmark, Czech. J. Phys., B35 (1985) 269-274.

252 J. Elfmark, Czech. J. Phys., B36 (1986) 873-881.

253 H.J. McQueen, Defects, Fracture and Fatigue, pp. 459-471. Marinus Nijhoff Pub., The Hague, DK (1983).

254 C.M. Young and O.D. Sherby, Metal Forming,(edited by A.L. Hoffmanner), pp.429-451. Plenum Press, N.Y. (1971).

255 S. Fulop, K.C. Cadien, M.J. Luton, and H.J. McQueen, J. Test. Eval., 5 (1977) 419-426.

256 E.E. Underwood, Metals Handbook 8th Edition, Metallography, Structures and Phase Diagrams, (edited by T. Lyman et al.) Vol. 8, pp. 3-47. ASM, Metals Park, OH (1985).

257 ASTM Standard E112, Metallography; Nondestructive Testing, Vol. 03.03, pp. 121-155. ASTM, Philadelphia, Pa (1983).

258 P.J. Goodhew, Specimen Preparation for Transmission Electron Microscopy of Materials, Oxford Unuversity Press, Oxford (1984).

259 L. Small, Hardness, Service Diamond Tool Co., Ferndale (1960).

260 M.E. Kassner, A.K. Miller, and O.D. Sherby, Metall. Trans., 13A (1983) 1977-1986.

261 G.W. Powell, E.R. Marshall, and W.A. Backofen, Trans. ASM, 50 (1958) 478-497.

262 T. Nakamura and M. Ueki, Zairyo, 23 (1974) 182-187.

263 M.E. Kassner, J.W. Elmer, and C.J. Echer, Metall. Trans., 17A (1986) 2093-2096.

264 W. Roberts and B. Ahlblom, Acta Metall., 26 (1978) 801-813.

265 D.J. Towle and T. Gladman, Met. Sci., 13 (1979) 246-256.

266 F. Drastik and J. Elfmark, Plastometry a Tvaritelenost Kovu. SNTL. Nakladatelstvi, Praha (1977).

267 N.V. Tikhiy, Ya.I. Spektor, M.I. Sinel'nikov, R.I. Entin and R.V. Yatsenko, Phys. Met. Melallography, 38 (1974) 118-122.

268 Y. Higo and K. Shinoda, Recrystallization in Hot Strip Mill of Austenitic Stainless Steel SUS304, Rep. 44., pp. 10-16. Nisshin Steel, Tokyo (1981).

269 R. Lombry, C. Rossard and B.J. Thomas, Int. Symp. on Metallurgy and Material Science, (edited by N. Hansen et al), pp. 257-262. RISO Natl., Lab., Roskilde, DK, (1980).

270 T.L. Capeletti, L.A. Jackman and W.J. Childs, Metall. Trans., 3 (1972) 789-796.

271 T. Mase, The Sumitomo Search, 3 (1970) 31-38.

272 D.H. Warrington, JISI, 201 (1963) 610-613.

273 K.D. Challenger and J. Moteff, Met. Trans. 3 (1972) 1676-1678.

274 K.D. Challenger and J. Moteff, Met. Trans., 4 (1973) 749-755.

275 K.D. Challenger anf J. Motell, Scripta Metallurgica, 6 (1972) 155-159.

276 C.M. Young and O.D. Sherby, JISI, 211 (1973) 640-647.

277 D.J. Michel, J. Moteff and A.J. Lovell, Acta metall. 21 (1973) 1269-1277.

278 F. Garofalo, C. Richmond, W.F. Domis and F. von Gemmingen, Joint Int. Conf. on Creep, Paper 30, pp.31-39 .The Institution of Mechanical Engineers, London, (1963).

279 T. Sendzimir, Revista Latino Americano de Siderurgia, 7 (1967) 23-36.

280 L.G.M. Sparling, J. Mech. Eng. Sci., 4 (1962) 257-269.

281 R.B. Sims, Proc. Institution Mechanical Engineers, 168 (1954) 191-200.

282 W. Hart, Atlas Steels, Tracy, Quebec, personal connunication.

283 Y. Uda, Nippon Yankin Kogyo Co., Kyobashi, Chuo-Ku, Japan, personal communication.

284 F. Garofalo, Proc. ASTM, 60 (1960) 738-749.

285 T. Hara, M. Takata, K. Ota, and T. Karasudani, Tetsu-to-Hagané, 49 (1963) 1885-1891.

286 S.V. Raj and G.M. Pharr, Mat. Sci. Eng., 81 (1986) 217-237.